UNIVERSITÉ DE GENÈVE
FACULTÉ DES SCIENCES

Section de physique
Professeur Alain Blondel

Département de physique nucléaire et corpusculaire

Measurement of the Water to Scintillator Charged-Current Cross-Section Ratio for Muon Neutrinos at the T2K Near Detector

THÈSE

présentée à la Faculté des sciences de l'Université de Genève
pour obtenir le grade de Docteur ès sciences, mention physique

par

Enrico Scantamburlo

de

Venezia (Italie)

THÈSE N° 5109

DOCTORAT ÈS SCIENCES, MENTION PHYSIQUE

Thèse de Monsieur Enrico SCANTAMBURLO

intitulée :

«Measurement of the Water to Scintillator Charged-Current Cross-Section Ratio for Muon Neutrinos at the T2K Near Detector»

La Faculté des sciences, sur le préavis de Monsieur A. BLONDEL, professeur ordinaire et directeur de thèse (Département de physique nucléaire et corpusculaire), Madame T. MONTARULI, professeure ordinaire (Département de physique nucléaire et corpusculaire), Monsieur M. NESSI, professeur titulaire (Département de physique nucléaire et corpusculaire), Monsieur A. BRAVAR, docteur (Département de physique nucléaire et corpusculaire), Monsieur M. WASCKO, professeur (Department of Physics, Imperial College London, United Kingdom), autorise l'impression de la présente thèse, sans exprimer d'opinion sur les propositions qui y sont énoncées.

Genève, le 6 juin 2017

Thèse - 5109 -

Le Décanat

Résumé

Cette thèse présente une mesure du rapport des sections efficaces sur eau et scintillateur pour les neutrinos muoniques interagissant par courants chargés au ND280, le détecteur proche de T2K. T2K ("Tokai-vers-Kamioka") est une expérience située au Japon, visant à mesurer les paramètres d'oscillation des neutrinos sur une base de 295 km. La mesure précise de ces paramètres nécessite une connaissance approfondie des sections efficaces de neutrinos pour corriger les distorsions introduites par effets nucléaires, inefficacités et résolutions.

Peu de mesures de la section efficace sur l'eau ont été réalisées jusqu'à présent et certainement aucun rapport entre eau et scintillateur dans la gamme d'énergie du flux de T2K. L'extraction des paramètres de mélange de neutrinos et de la phase de violation de CP se faisant en comparant le taux d'interaction de neutrinos de saveurs données dans Super-Kamiokande (SK), le détecteur lontain de T2K, qui est un détecteur Cherenkov d'eau, avec celui qu'on prédit à partir des interactions dans le détecteur proche, qui est en scintillateur : on comprend que ce rapport est essentiel. Ces mesures de section efficaces sont faites dans le detecteur proche de T2K, ND280. Elles nécessitent une connaissance de la saveur et de l'énergie des neutrinos. Les mesures que nous avons faites permettent de contraindre le spectre d'énergie des neutrinos attendus. Cette énergie doit être reconstruite à partir de l'état final des réactions des neutrinos sur des noyaux.

Le détecteur proche, ND280, situé à 280 m de la cible du faisceau de T2K et 2.5° hors axe, contient deux subdétecteurs à grains fins (FGDs) avec des barres scintillantes, masse active pour les interactions des neutrinos. Les deux FGDs sont identiques, sauf le fait que l'un des deux contient également de l'eau, conception qui permet l'extraction de la section efficace sur l'eau par soustraction.

Les faisceaux de neutrinos ne sont pas monochromatiques, et les mesures de la section efficace des neutrinos ont des incertitudes importantes dues à la connaissance limitée du flux. Un rapport des sections efficaces présente l'avantage que ces erreurs systématiques s'annulent largement. En mesurant une section efficace par courants chargés inclusifs de neutrinos muoniques, plutôt que pour un canal d'interaction exclusif, l'erreur statistique est également la plus petite possible.

La mesure est effectuée en sélectionnant des échantillons des interactions par courants chargés dans les deux FGDs, dans une exposition de 5.80×10^{20} protons avec la cible (POT) de données de ND280. Le rapport des sections efficaces entre l'eau et le scintillateur est extrait en bins de $E_{QE}(p_\mu, \cos\theta_\mu)$, la même quantité utilisée dans les analyses d'oscillation de T2K, fonction des propriétés du candidat lepton sortant : l'impulsion p_μ et la direction $\cos\theta_\mu$ du muon. Une excellente simulation de Monte Carlo permet de générer une matrice de réponse du détecteur, qui peut ensuite être inversée et appliquée aux données réelles afin de déplier le flou du détecteur et l'efficience de la reconstruction. Une méthode de déplétisation régularisée est utilisée pour atténuer les problèmes qui accompagnent l'inversion matricielle.

Le rapport des sections efficaces est mesuré dans un espace de phase réduit pour éviter de compter excessivement sur la simulation dans des régions où l'efficience est très faible, soit pour les muons émis vers l'arrière ou avec une faible impulsion ($< 100\,\mathrm{MeV}$). Dans cet espace de phase restreint, le rapport des sections efficaces entre l'eau et le scintillateur est de $1.01 \pm 2.46\%(\mathrm{stat.}) \pm 1.95\%(\mathrm{syst.})$. Les incertitudes statistiques, et les systématiques dues à la description des détecteurs, au flux et à la théorie ont été propagées numériquement aux résultats de la section efficace. La valeur donnée par la simulation de Monte Carlo est 0.962, à un sigma du résultat obtenu.

Le faisceau T2K est en train d'être amélioré pour augmenter sa puissance, et ND280 est programmé pour prendre des données jusqu'à environ quatre fois les POT actuels, donc l'erreur statistique pourrait se voir réduite de moitié dans un proche avenir. Des modèles de section efficace mieux construits entraîneront des incertitudes plus faibles pour les mesures d'oscillation, et en particulier nous donneront une meilleure chance de mesurer la violation du CP dans le secteur leptonique.

Abstract

The T2K (Tokai to Kamioka) experiment is a 295-km long-baseline neutrino experiment which aims at the measurement of neutrino oscillation parameters. Precise measurements of these parameters require accurate extrapolation of interaction rates from the near detector, ND280, mainly made of scintillator, to the Super-Kamiokande, the water Cherenkov far detector. Measurements on water and of the water to scintillator ratio contribute to eliminate the uncertainties arising from carbon/oxygen differences. The ND280 near detector, located at $280\,\mathrm{m}$ from the target of the T2K beam and $2.5°$ off-axis, comprises two fine-grained sub-detectors (FGDs) with scintillating bars, active mass for neutrino interactions. The two FGDs are identical except for the fact that in the downstream one, FGD2, the scintillating layers are interleaved with water-filled modules. By subtraction, this allows extracting the cross section on water, and the ratio of water to hydrocarbon cross section.

The measurement is performed by selecting ν_μ charged-current samples in the two FGDs, in an exposure of 5.80×10^{20} protons on target. The water to scintillator cross-section ratio is extracted in bins of $E_{QE}(p_\mu, \cos\theta_\mu)$, the very quantity which is used in the T2K oscillation analyses, as a function of the outgoing lepton momentum p_μ and polar angle $\cos\theta_\mu$. The cross-section ratio is measured for good acceptance kinematic regions, $\cos\theta_\mu > 0$ and $p_\mu > 100\,\mathrm{MeV}$, avoiding backward-going and low momentum muons.

The integrated ratio, extracted with the help of the SVD-regularised technique, is $1.01 \pm 2.46\%(\mathrm{stat.}) \pm 1.95\%(\mathrm{syst.})$.

To My Muse

Acknowledgements

Grazie agli amici e ai cugini in Italia, per esser sempre presenti nonostante la distanza, e perdonatemi se invece io non son riuscito ad esser presente a molti avvenimenti importanti. Grazie per chiedermi sempre quando torno e dirmi che vi manco, siete come fratelli e sorelle su cui so di poter sempre contare. Grazie anche ai miei nuovi amici a Ginevra, è grazie a voi se adesso mi sento un po' a casa anche in questa città straniera.

Infine i ringraziamenti più importanti: grazie mamma, grazie papà, grazie per avermi sempre supportato (e sopportato) in tutte le avventure in cui mi sono buttato (sì, "buttato" è la parola giusta), compresa questa che mi ha portato lontano, tanto lontano che avete dovuto spolverare il mappamondo che mi avete regalato da piccolo e piazzarlo davanti al televisore... grazie di cuore.

그리고 다시, 가ㅁ사 Jiae, 내 뮤즈, 너를 많이 빚 졌어.

Contents

List of Figures

List of Tables

Glossary

PØD π^0 detector

CC Charged Current

CCinc Charged-Current Inclusive Interactions

COH COHerent Pion Production

CP Charge Parity

CT Current Transformer

DIS Deep Inelastic Scattering

Ds-ECal Downstream ECal module

ECal Electromagnetic Calorimeter

FGDs Fine Grained Detectors

FSI Final State Interactions

Highland HIGH Level Analysis at the Near Detector

INGRID Interactive Neutrino GRID

J-PARC Japan Proton Accelerator Research Complex

LINAC LINear ACcelerator

MC Monte Carlo

MEC Meson Exchange Currents

MIP   Minimum Ionising Particle

MPPC   Multi-Pixel Photon Counter

MR   Main Ring

NC   Neutral Current

ND280   Off-axis Near Detector

PDG   Particle Data Group

PID   Particle IDentification

PMT   Photo-Multiplier Tube

POT   Protons On Target

QE   Quasi-Elastic Interactions

RCS   Rapid Cycling Synchrotron

RES   RESonant Pion Production

RFG   Relativistic Fermi Gas

SK   Super-Kamiokande

SMRDs Side Muon Range Detectors

SVD   Singular Value Decomposition

T2K   Tokai to Kamioka

TPCs   Time Projection Chambers

WLS fibre Wave-Length Shifting fibre

1 Introduction

This thesis presents a measurement of the water to scintillator (hydrocarbon) charged-current cross-section ratio for muon neutrinos at the T2K near detector, ND280.

The Tokai to Kamioka (T2K) experiment is a 295-km long-baseline neutrino experiment which aims at the measurement of neutrino oscillation parameters. Precise measurement of these parameters requires accurate knowledge of neutrino cross sections. Neutrino oscillation experiments rely on the detection of charged particles to infer neutrino interactions. Therefore, the neutrino interaction models need to be extremely well understood to extract the neutrino properties correctly.

Few measurements of the water cross section have been made so far and none of the water to scintillator cross-section ratio in the T2K energy range (200-1200 MeV). The extraction of neutrino mixing parameters and of the CP-violating phase requires knowledge of the neutrino energy, and these measurements have the potential to constrain the expected neutrino event spectrum at Super-Kamiokande, the T2K far detector, it being a water Cherenkov detector.

The ND280 near detector, located at $280\,\mathrm{m}$ from the target of the T2K beam and $2.5°$ off-axis, contains two fine-grained sub-detectors (FGDs) with scintillating bars, active mass for neutrino interactions. They are identical except for the fact that the downstream one also contains water (about half of its mass), design which allows the extraction of the cross section on water by subtraction.

Neutrino beams are not monochromatic, and neutrino cross-section measurements have quite large flux uncertainties. Nonetheless, performing a cross-section ratio has the advantage that the systematics could largely cancel out. Measuring a ν_μ charged-current inclusive cross section, rather than for an exclusive interaction channel, also ensures that the statistical error is the smallest possible.

26 The measurement is performed by selecting ν_μ charged-current samples in the two
27 fine-grained sub-detectors of ND280, with Run II, III and IV of ND280 data, for a
28 total of 5.80×10^{20} protons on target. An excellent Monte Carlo simulation allows to
29 generate a detector response matrix, which can then be inverted and applied to the real
30 data in order to unfold the detector smearing and the reconstruction efficiency. The
31 cross-section ratio result is given in a reduced phase-space to avoid relying completely
32 on the simulation in regions where the efficiency is very low, which is for backward-
33 going and for low momentum ($< 100\,\mathrm{MeV}$) muon candidates. In this restricted phase
34 space the water to scintillator total cross-section ratio is found with 2.5 % of statistical
35 error and 2.0 % of systematics, mostly due to detector uncertainties which don't cancel
36 completely.

1

Neutrinos: a Window Beyond the Standard Model

1.1 Neutrinos in the Standard Model

Neutrinos are fundamental particles of the Standard Model (SM) of particle physics, the theory describing all the fundamental particles and forces in the nature. According to the Standard Model neutrinos are chargeless, colourless and massless, and only undergo the weak interactions. Nevertheless at the end of the 20th century it has been discovered that they have masses, albeit so tiny that we only have upper limits on them, opening new scenarios and theories Beyond the Standard Model (BSM). This discovery is so overwhelming that the Nobel Prize in Physics was awarded to Takaaki Kajita (member of the T2K collaboration [1]) and Arthur B. McDonald in 2015. Moreover, the Breakthrough Prize 2016 in Fundamental Physics [2] was awarded to five experiments currently investigating neutrino oscillations, including the T2K experiment (cf. Chapter 2), considering these particles the "key to understanding the Universe".

The existence of neutrinos was first postulated by Wolfgang Pauli in 1930 [3] to explain the continuous spectrum of β decay. Beta decay is a radioactive decay where a nucleus of atomic number Z transforms to a nucleus of atomic number (Z+1) emitting an electron as:

$$N(Z, A) \rightarrow N^{'}(Z + 1, A) + e^{-} \tag{1.1}$$

where N and $N^{'}$ are two different nuclei. If no other particles are involved, being a two-body decay, the electron energy should be fixed by energy conservation:

$$E_e = \frac{m_N^2 - m_{N'}^2 + m_e^2}{2m_N} \tag{1.2}$$

However, the observed spectrum was continuous, not constant, and not even discrete [4]. In order to satisfy the energy conservation law, Pauli realised there had to be another outgoing particle, and since it was undetected, it had to been neutral and massless. Moreover, in order to conserve the angular momentum, it had to have spin $1/2\ \hbar$.

In 1933 Enrico Fermi baptised this particle as "neutrino", meaning a little neutral object, and included it in his Fermi's Theory of Beta Decays [5, 6, 7, 8]. He suggested the direct couplings of a neutron with an electron and a neutrino with a proton: this was definitely a precursor of the weak interaction.

It took 20 years to demonstrate the existence of this elusive particle: the first measurement of neutrinos in history was by Reines and Cowan in 1952 [9]. They observed anti-neutrinos from the Savannah River reactor through the inverse beta decay:

$$\bar{\nu}_e + p \rightarrow e^{+} + n \tag{1.3}$$

These neutrinos from nuclear fission were detected identifying photons from the annihilation of the emitted positron and two delayed photons from the capture of the neutron in the detector, which had a target of water and $CdCl_2$.

In 1962 L. Lederman, M. Schwartz and J. Steinberger discovered a second type of neutrino [10]: the "muon neutrino". They used the pion decay to produce neutrinos, pions decay to muons and neutrinos in flight

$$\pi^{+} \rightarrow \mu^{+} + \nu \tag{1.4}$$

$$\pi^{-} \rightarrow \mu^{-} + \bar{\nu} \tag{1.5}$$

and they investigated two reactions:

$$\overline{\nu} + p^+ \rightarrow \mu^+ + n \tag{1.6}$$

$$\overline{\nu} + p^+ \rightarrow e^+ + n \tag{1.7}$$

If only one type of neutrino exists, the two reactions should happen equally, but they did not detect electrons. The absence of electron events suggested the existence of another type of neutrino, which should be coupled only with muons and not with electrons. This was the first measurement of the muon neutrino (ν_μ).

As soon as the third lepton τ was discovered in the 1970s, a third neutrino, the tau neutrino (ν_τ), was also postulated to exist. In the following decades several experiments measured its properties, in particular at e^+e^- colliders, but the first interaction of a ν_τ neutrino was observed only in 2000 by the DONUT experiment [11], a challenging test because the τ decays rapidly.

Based on all these discoveries, the Standard Model of particle physics was designed with a lepton family constituted of three massive charged leptons, the electron (e), the muon (μ) and the tau (τ), paired to three massless neutrinos, ν_e, ν_μ and ν_τ, as well as the corresponding three charged anti-leptons and three anti-neutrinos. The number of three for the weakly interacting neutrinos, with mass below the Z mass, has been determined in the LEP experiments [12, 13] ($N_\nu = 2.984 \pm 0.008$), by extracting the invisible decay width from the Z total width and branching ratios.

In Particle Physics, all the particles are divided into fermions and bosons: bosons are particles with a symmetric wave-functions (i.e. they respect the Bose-Einstein statistics) and they can represent the force mediator; fermions are particles with anti-symmetric wave-functions (i.e. they respect Fermi-Dirac statistics), as quarks and leptons. Neutrinos are spin 1/2 fermions, and, as mentioned before, they interact only through the weak force. There are three mediators for this interaction: the charged W^+ and W^- bosons for the charged-current interaction (CC), and the neutral Z boson for the neutral-current (NC) interaction. The weak force couples differently on the two chiral components of a spinor representing a fermion: while the neutral Z boson couples to both left-handed and right-handed components, the charged W^+ and W^- bosons only couple to the left-handed component. In the Standard Model, neutrinos are only left-handed and anti-neutrinos are only right-handed, hence a right-handed neutrino, if

it exists, would not undergo a charged-current interaction. Furthermore, the Standard Model of particle physics relies on a field theory in which, in order to have a mass term in the Lagrangian, both the left-handed and the right-handed components are required. The mass of neutrinos have been questioned since Enrico Fermi developed his theory in 1933 [5, 6, 7, 8]. Several experiments have attempted to measure the mass of neutrinos directly via beta decays, pion decays, and tau lepton decays and cosmological observations, but they did not find any evidence of neutrino mass and could only put some upper limits. Therefore, until the end of the last century, the picture of the observed particles in the Standard Model was the one described in Fig. 1.1 (the Higgs boson[14, 15] is missing as it had not been discovered yet). Nowadays such a picture is changed as in Fig. 1.4, because recent discoveries established that the interacting neutrinos are not in their mass eigenstates, unlike the other quarks and leptons (cf. Section 1.2.4).

The mass matrix in the Lagrangian, in general non-diagonal, can be easily diagonalised by introducing a transformation matrix, and since neutrinos have only the left-handed component, this transformation matrix can be chosen such that the couplings of leptons and weak interaction gauge bosons are isolated for each flavour. This is why flavour mixing is forbidden in lepton sector with massless neutrinos, and why the discovery of the neutrino oscillations, i.e. the transformation from one flavour into another violating the flavour number conservation, directly implicates that neutrinos do have mass. Therefore, investigating neutrino oscillations is another effective way to access the neutrino mass.

Figure 1.1: Particles in the Standard Model of particle physics

1.2 Neutrino Oscillations

The Super-Kamiokande experiment in 1998 [16] and the SNO experiment in 2001 [17, 18] firmly established that neutrinos oscillate and have mass, and for this discovery the Nobel Prize in Physics was awarded to Takaaki Kajita and Arthur B. McDonald in 2015. These measurements eventually solved long-standing problems in neutrino physics, namely the solar neutrino puzzle and the up-down asymmetry in atmospheric neutrinos: for a long time several experiments measured neutrino fluxes in disagreement with the predictions, which were based on the non-oscillating neutrino hypothesis. Neutrino masses and cross sections are so tiny that it took several decades to prove that these disagreements were due to neutrino oscillations.

1.2.1 Solar Neutrinos

Neutrinos are constantly produced in the Sun (mainly from the $p - p$ chain and the CNO cycle) with a net reaction of:

$$4p \rightarrow^4 He + 2e^+ + 2\nu_e + 26.731 \, MeV .$$
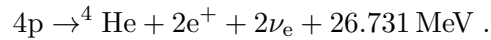
In 1968 the Homestake experiment [19, 20] measured the solar electron neutrino flux and compared the result to the prediction of the Standard Solar Model. They concluded that the flux was between one third and one half of what was expected [21]. This was the first measurement of the solar neutrino problem [22]. More recent experiments, SAGE [23], GALLEX [24] and Kamiokande [25] published results consistent with the Homestake experiment.

This suppression in the electron neutrino flux from the Sun is now explained by the neutrino oscillations and it was finally confirmed in 2001 by the SNO experiment [17, 18]: SNO measured the flux of all the 3 flavours of neutrinos and found consistent results with the prediction of the Standard Solar Model. Fig. 1.2 shows the solar flux result from SNO.

1.2.2 Atmospheric Neutrinos

Primary cosmic rays entering the Earth's atmosphere are mostly made of protons (up to 90 %). When they enter the atmosphere, hadronic interactions produce hadrons such as pions and kaons which decay producing neutrinos. The pions decay into μ
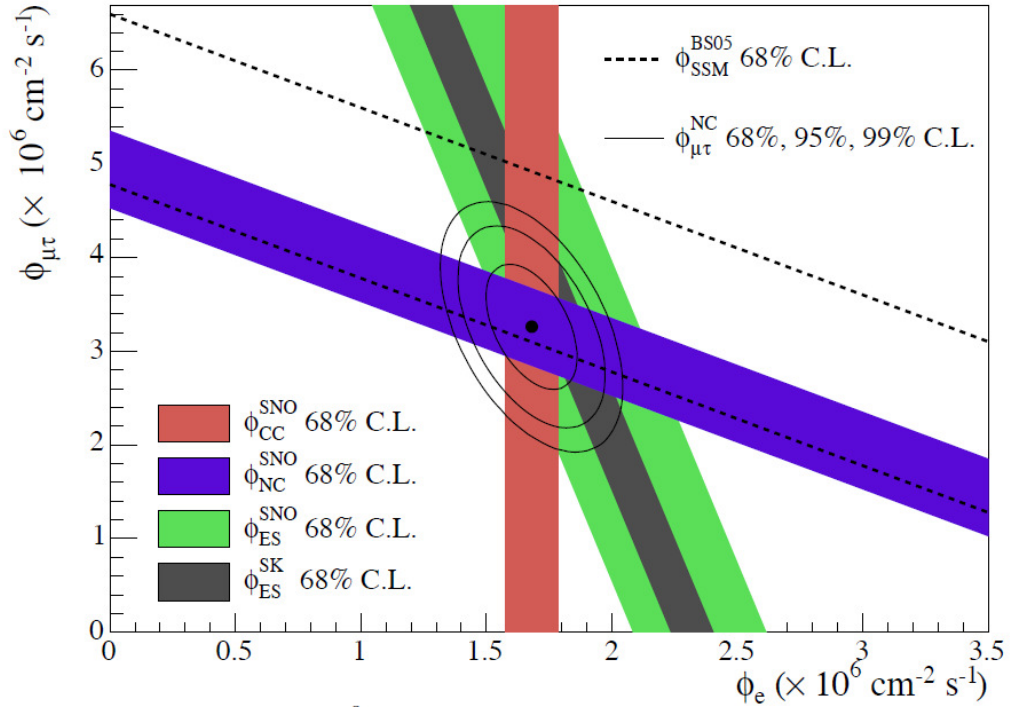
Figure 1.2: Solar neutrino result. The x axis is the flux of ν_e and the y axis is the flux of ν_μ and ν_τ from SNO measurements. The red band is from the SNO CC result. The blue one is from the SNO NC result and the light green is from the SNO elastic scattering result. The dark green band is from the Super-Kamiokande elastic scattering result. The bands represent the 1σ error. The sum of the neutrino fluxes is consistent with the SSM expectation (dashed line) [17, 18],

154 and ν_μ, then subsequently the μ decay into e, ν_e, and ν_μ. These neutrinos are called

155 atmospheric neutrinos.

156   Since the dominant interaction producing neutrinos is the decay chain $\pi^+ \to \mu^+ + \nu_\mu$

157 and subsequently $\mu^+ \to e^+ + \overline{\nu}_\mu + \nu_e$ [26], the amount of $\nu_\mu, \overline{\nu}_\mu$ is approximately twice as

158 much as ν_e, and the ratio of ν_μ flux to ν_e flux should be approximately isotropic, at least

159 for sub-GeV muons (high-energy muons from the zenith might not decay before reaching

160 the detector). Nevertheless in 1998 the Super-Kamiokande experiment measured an

161 anisotropic flux ratio, revealing a zenith angle dependence in the neutrino direction,

162 and proving that the flux depends on how far neutrinos travel. This was the first

163 robust proof of the neutrino oscillations. Fig. 1.3 [16] shows the best-fit with neutrino

164 oscillation is well consistent with the atmospheric neutrino measurements.

165 ### 1.2.3   Neutrino Oscillations in Matter: the MSW Effect

166 While the atmospheric neutrino flux is explained by the neutrino oscillation in vacuum,

167 the solar neutrino flux anomaly is mainly due to the Mikheyev, Smirnov and Wolfenstein

168 (MSW) effect [27, 28], or simply matter effect.

169   When the electron neutrinos travel in matter, they can interact with electrons in

170 matter through both the neutral weak current and the charged weak current, while

171 other flavours of neutrinos only interact through the neutral weak current. Therefore,

172 there will be a phase difference between the components of the different flavours. An

173 effective potential term is added to the Hamiltonian to take into account the MSW

174 effect: this term is proportional to the neutrino energy and the density of electrons in

175 the material it traverses, and it has opposite sign for ν_e and $\overline{\nu}_e$, which will be important

176 to determine the mass hierarchy and to test the lepton CP violation (Section 1.3.2.2).

177 Because of the high density in the core of the Sun, the MSW effect turns a significant

178 amount of electron neutrinos into muon and tau neutrinos.

179 ### 1.2.4   Neutrino Oscillation Framework

180 The very first proposal of a neutrino oscillation framework was formulated in 1957 by

181 Bruno Pontecorvo, imaging the oscillations between neutrinos and anti-neutrinos [29,

182 30]. Few years later, as soon as the muon neutrino was discovered, Pontecorvo also

183 proposed the oscillations between ν_e and ν_μ, further extended into a three neutrino
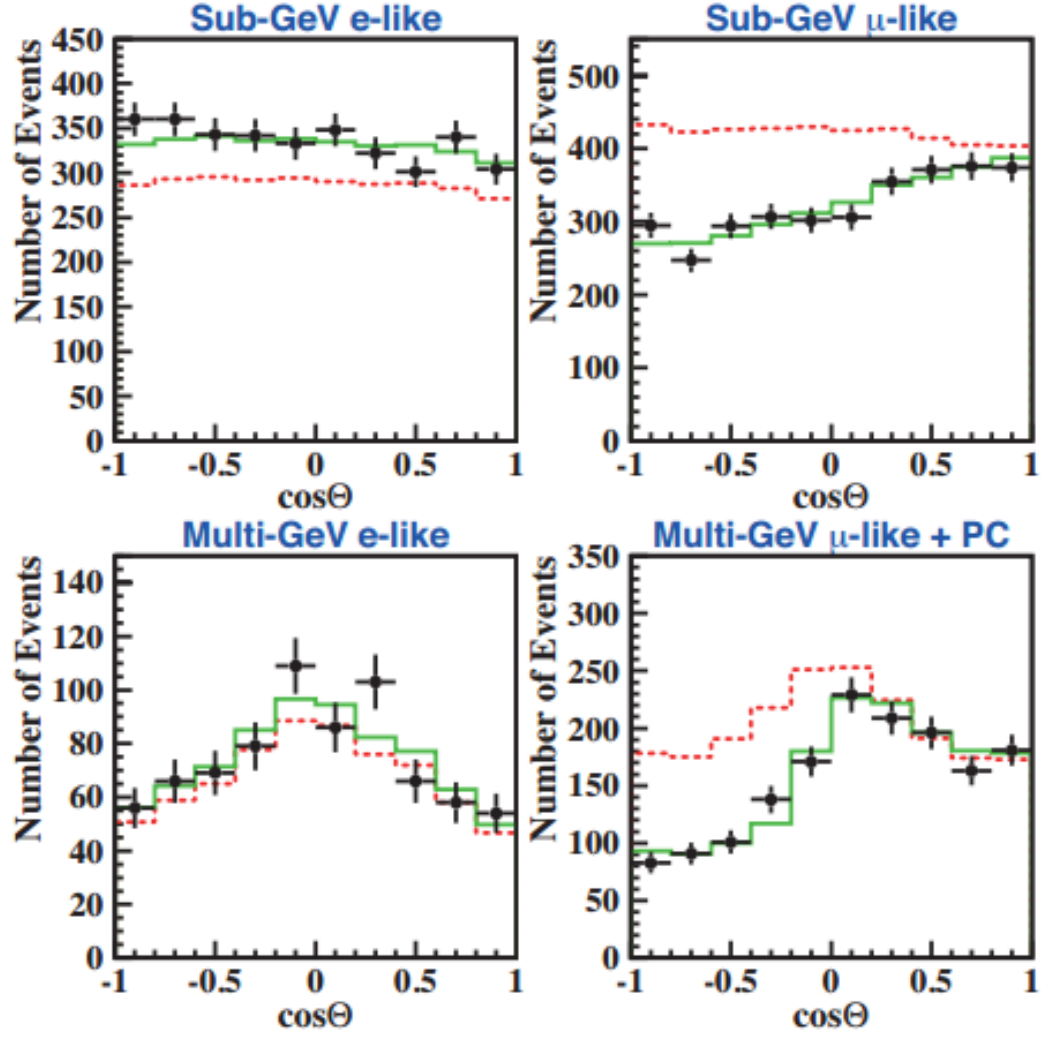
Figure 1.3: Zenith angle distributions: non-oscillated Monte Carlo predictions are in the dotted histograms and the best-fit expectations for ν_μ to ν_τ oscillations are in the solid histograms.

184 oscillation scheme by Z. Maki, M. Nakagawa and S. Sakata in 1962 [31]. Even if
185 the early neutrino experiments discussed in the previous sections were not motivated
186 by this theoretical proposal (or not even aware thereof), the oscillation framework of
187 Pontecorvo, Maki, Nakagawa and Sakata turned out to be the right starting point.

188 As discussed in Section 1.1, neutrino oscillations are a consequence of the non-
189 zero neutrino masses. The fundamental principle of neutrino oscillations is that the
190 neutrino flavour eigenstates, states involved in neutrino interactions (cf. Section 1.4),
191 are not identical to the neutrino mass eigenstates, i.e. the stable energy eigenstates.
192 The flavour eigenstates ν_e, ν_μ and ν_τ are superpositions of the mass eigenstates ν_1, ν_2
193 and ν_3. This implies that neutrinos cannot be massless and that they can change their
194 flavour during propagation (hence the name "neutrino oscillations") [32]. Therefore,
195 the picture of the particles in the Standard Model of particle physics has changed from
196 Fig. 1.1 to Fig. 1.4.
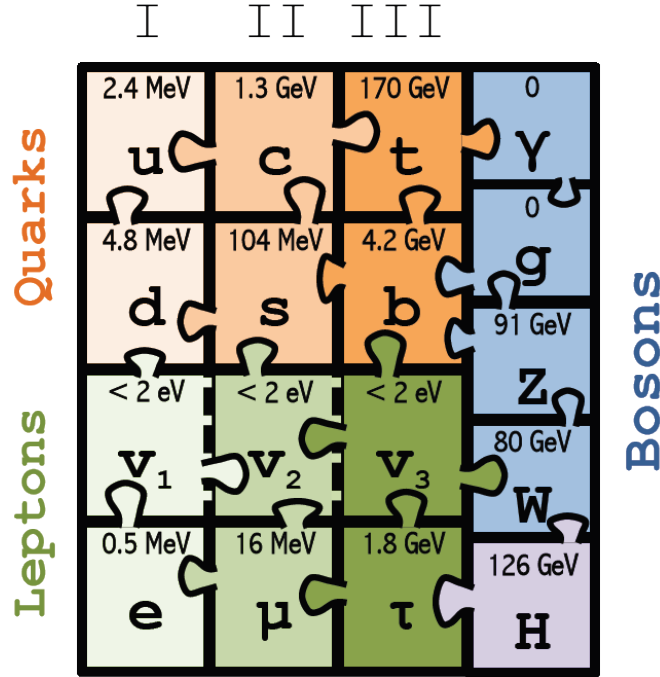
Figure 1.4: Particles in the Standard Model of particle physics

197 The neutrino flavour eigenstates, $|\nu_\alpha\rangle$, can be expressed as a linear combination of
198 mass eigenstates, $|\nu_i\rangle$, $i = 1, 2, 3$, using the unitary matrix U, known as the Pontecorvo-
199 Maki-Nakagawa-Sakata (PMNS) neutrino mixing matrix [33, 34]:

$$|\nu_\alpha\rangle = \sum_{i=1}^{3} U_{\alpha i}^* |\nu_i\rangle \tag{1.8}$$

with $\alpha \in \{e, \mu, \tau\}$. This relation can be represented as a rotation of vectors in a three dimensional space as in Fig. 1.5.
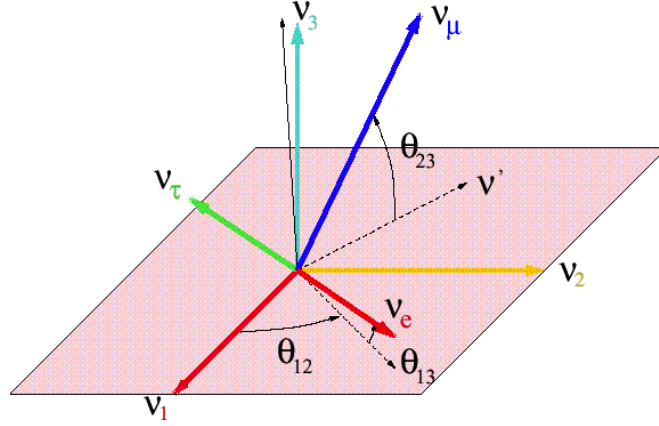
Figure 1.5

The PMNS matrix is a 3×3 complex unitary matrix similar to the Cabibbo-Kobayashi-Maskawa (CKM) matrix in the quark sector [32, 35]. There are many ways to parametrise the PMNS matrix. Usually, it is written in the following extended form which also include the Majorana term (cf. Section 1.3.2.4):

$$U = \begin{pmatrix} 1 & 0 & 0 \\ 0 & c_{23} & s_{23} \\ 0 & -s_{23} & c_{23} \end{pmatrix} \begin{pmatrix} c_{13} & 0 & s_{13}e^{-i\delta} \\ 0 & 1 & 0 \\ -s_{13}e^{+i\delta} & 0 & c_{13} \end{pmatrix} \begin{pmatrix} c_{12} & s_{12} & 0 \\ -s_{12} & c_{12} & 0 \\ 0 & 0 & 1 \end{pmatrix} \begin{pmatrix} 1 & 0 & 0 \\ 0 & e^{i\alpha} & 0 \\ 0 & 0 & e^{i\beta} \end{pmatrix} \tag{1.9}$$

where $s_{ij} = \sin\theta_{ij}$, $c_{ij} = \cos\theta_{ij}$ and θ_{ij} is the mixing angle; δ is a CP-violating phase, and α and β are Majorana phases that have no effect on neutrino oscillations.

If a neutrino is produced at a time $t = 0$ in the state ν_α, the time evolution of neutrino flavour states is given by:

$$|\nu_\alpha(t)\rangle = \sum_{i=1}^{3} U_{\alpha i}^* e^{-iE_i t} |\nu_i\rangle \ . \tag{1.10}$$

Similarly, a mass eigenstate can be expressed as a superposition of the flavour

211 eigenstates

$$|\nu_i\rangle = \sum_\beta U_{\beta i}|\nu_\beta\rangle, \qquad \beta = \mathrm{e}, \mu, \tau \qquad (1.11)$$

212 and the state $|\nu_\alpha(t)\rangle$ can be expressed in the basis of the weak flavour $|\nu_\beta\rangle$

$$|\nu_\alpha(t)\rangle = \sum_\beta \sum_{i=1}^3 U_{\beta i} e^{-iE_i t} U_{\alpha i}^* |\nu_\beta\rangle \qquad (1.12)$$

213 Then, the probability of $\nu_\alpha \to \nu_\beta$ transitions is given by:

$$P(\nu_\alpha \to \nu_\beta) = |A_{\nu_\alpha \to \nu_\beta}(t)|^2 = |\sum_{i=1}^3 U_{\beta i} e^{-iE_i t} U_{\alpha i}^*|^2 . \qquad (1.13)$$

214 As neutrinos are highly relativistic ($E \approx |p|$), this approximation can be made:

$$E_i = \sqrt{p^2 + m_i^2} \approx E + \frac{m_i^2}{2E} \qquad (1.14)$$

215 and the oscillation probability can be re-written as:

$$P(\nu_\alpha \to \nu_\beta) = \sum_{i,j=1}^3 U_{\alpha i}^* U_{\beta i} U_{\alpha k} U_{\beta j}^* e^{-i\frac{\Delta m_{i,j}^2}{2E} t} . \qquad (1.15)$$

216 where $\Delta m_{ij}^2 = m_j^2 - m_i^2$ is the mass squared difference of neutrino mass eigenstates.

217 The T2K neutrino oscillation experiment probes oscillations coming from a muon

218 neutrino beam. The oscillation and survival probabilities are:

$$P(\nu_\mu \to \nu_\mathrm{e}) \simeq \sin^2 2\theta_{13} \sin^2 \theta_{23} \sin^2 \left(1.27 \frac{\Delta m_{32}^2}{(\mathrm{eV}^2)} \frac{L}{(\mathrm{km})} \frac{(\mathrm{GeV})}{E_\nu}\right) , \qquad (1.16)$$

$$P(\nu_\mu \to \nu_\mu) \simeq 1 - \cos^4 \theta_{13} \sin^2 2\theta_{23} \sin^2 \left(1.27 \frac{\Delta m_{32}^2}{(\mathrm{eV}^2)} \frac{L}{(\mathrm{km})} \frac{(\mathrm{GeV})}{E_\nu}\right) , \qquad (1.17)$$

219 where L is the distance travelled by neutrinos in km, E_ν is neutrino energy in GeV,

220 Δm^2 in eV^2, and the factor 1.27 comes from $1/\hbar c$ in the conversion of units to km and

221 GeV. These equations show that the magnitude of the $\nu_\mu \to \nu_\mathrm{e}$ oscillations is governed

222 by the mixing angles θ_{13} and θ_{23}, whereas the frequency of oscillations depends on

223 Δm_{32}^2.

When we measure θ_{23} with the survival probability $P(\nu_\mu \to \nu_\mu)$ which is proportional to $\sin^2 2\theta_{23}$ to first order, there is an octant ambiguity: either $\theta_{23} \leq 45°$ (in the first octant) or $\theta_{23} > 45°$ (in the second octant). By combining the measurements of $P(\nu_\mu \to \nu_\mu)$ and $P(\nu_\mu \to \nu_e)$, future long baseline experiments, like Hyper-Kamiokande [36] and DUNE [37], can reach the necessary sensitivity to determine the θ_{23} octant.

The formal 3-flavour probability for neutrino oscillations in vacuum can be written as:

$$P(\nu_\alpha \to \nu_\beta) = \delta_{\alpha\beta}$$

$$-4 \sum_{i>j} \Re(U_{\alpha i}^* U_{\beta i} U_{\alpha j}^* U_{\beta j}^*) \sin^2[1.27 \Delta m_{ij}^2 (L/E)]$$

$$+ 2 \sum_{i>j} \Im(U_{\alpha i}^* U_{\beta i} U_{\alpha j}^* U_{\beta j}^*) \sin[2.54 \Delta m_{ij}^2 (L/E)] \tag{1.18}$$

where the symbols are those previously defined, and U it the PMNS matrix.

There are 9 oscillation parameters: three mixing angles, three neutrino masses, and one single CP phase and two possible Majorana phases (cf. Section 1.3.2.4). Most of parameters have been measured with certain precision; the latest measurements are discussed in Section 1.3.1. However, there are still missing pieces, described in Section 1.3.2.

1.3 Current Status of Neutrino Physics

1.3.1 Neutrino Oscillation Measurements

Several neutrino oscillation experiments have performed successful measurements and we currently know all the mixing angle $\theta_{12}, \theta_{23}, \theta_{13}$, the mass splitting, Δm_{21}^2, and the absolute value of the other mass splitting $|\Delta m_{32}^2|$. These experiments use sources of neutrinos that are natural, solar and atmospheric, or artificial, from accelerators and reactors. Table 1.1 shows the neutrino oscillation measured parameters from the most recent global analysis performed by the Particle Data Group (PDG) [38] over various neutrino oscillation experiments.

Parameter	best fit
Δm_{21}^2	$7.53 \pm 0.18 \times 10^{-5} eV^2$
$|\Delta m_{32}^2|$	$2.44 \pm 0.06 \times 10^{-3} eV^2$ (normal mass hierarchy)
$|\Delta m_{32}^2|$	$2.51 \pm 0.06 \times 10^{-3} eV^2$ (inverted mass hierarchy)
$sin^2\theta_{12}$	0.304 ± 0.014
$sin^2\theta_{23}$	0.51 ± 0.05 (normal mass hierarchy)
$sin^2\theta_{23}$	0.50 ± 0.05 (inverted mass hierarchy)
$sin^2\theta_{13}$	0.0219 ± 0.0012

Table 1.1: The best-fit values of three-flavour oscillation parameters from the 2016 PDG global fit [38]. For $|\Delta m_{32}^2|$ and $sin^2\theta_{23}$ there are two best fit values depending whether a normal or inverted mass hierarchy is considered; moreover, while the sign of Δm_{21}^2 is known, the sign of Δm_{32}^2 is still unknown (cf. Section 1.3.2.1).

Different sources have different sensitivities to the oscillation parameters.

Solar experiments detect low energy (in the MeV scale) ν_e produced in nuclear reactions in the core of the sun (Section 1.2.1) and they are most sensitive to θ_{12} and Δm_{21}^2 (also called solar mass difference). The best precision of θ_{12} is provided by SNO and SK, while KamLAND gives a better determination of Δm_{21}^2.

Atmospheric experiments detect neutrinos produced by interactions of cosmic rays with nuclei in the upper atmosphere (Section 1.2.2), ν_μ, $\overline{\nu}_\mu$, ν_e and $\overline{\nu}_e$ at energies from MeV to TeV, and they are mainly sensitive to θ_{23} and Δm_{32}^2 (also called atmospheric mass difference).

Long baseline accelerator experiments, like MINOS, T2K and NOνA [39] use GeV muon neutrinos produced by pion decay in an accelerator complex. These experiments are mostly sensitive to θ_{23} and Δm_{32}^2 from ν_μ disappearance, but also to θ_{13}, Δm_{13}^2 and δ_{CP} from ν_e appearance. The determination of $sin^2\theta_{23}$ is mainly from T2K data. The combined results of T2K [40] and MINOS [41] provides the final precision on Δm_{32}^2.

Reactor experiments measure the disappearance spectrum of $\overline{\nu}_e$ at MeV energies produced by nuclear reactors. KamLAND [42] is sensitive to θ_{12} and Δm_{21}^2, whereas

Daya Bay [43, 44], RENO [45] and Double CHOOZ [46] precisely measure θ_{13} and Δm_{32}^2 in the electron channel.

The most recently measured parameter is θ_{13}. Until 2011, only an upper limit of θ_{13} was known. Then T2K reported a non-zero θ_{13} from ν_e appearance [47]. Precise measurements followed from Daya Bay, Double CHOOZ and RENO reactor experiments. The value found for θ_{13} is sufficiently large to make possible the measurement of δ_{CP} (Section 1.3.2.2).

1.3.2 Open Questions in Neutrino Physics

1.3.2.1 Mass Hierarchy

In Equation 1.18, which gives the oscillation probability in vacuum, neutrino masses appear as a mass squared difference Δm_{ij}^2 in the argument of sin^2. Therefore, these processes cannot establish which mass is the largest between m_i and m_j. Nevertheless, this mass hierarchy can be unveiled by studying the propagation of neutrinos in matter (Section 1.2.3): the MSW effect gives an additional phase shift in the oscillation probability which depends on the sign of the mass squared difference (Eq. (1.20)). In the case of solar neutrinos, the matter effect is actually crucial in their oscillation, hence the sign of the solar mass difference Δm_{21}^2 has been determined: $m_1 < m_2$ (cf. Table 1.1). The sign of the atmospheric mass difference Δm_{32}^2 instead is still unknown and its measure is quite challenging, because the only way is to observe the matter effect in Earth and the baseline needs to be very long.

Hence two mass orderings are possible, as shown in Fig. 1.6: *the normal ordering/hierarchy* (NH) where $m_1 < m_2 < m_3$; *the inverted ordering/hierarchy* (IH) where $m_3 < m_1 < m_2$.

The mass hierarchy is one of the missing piece in neutrino physics. Knowing the mass hierarchy will favour or discard some of the new Beyond the Standard Model (BSM) theories, which are being developed to accommodate the neutrino masses and mixing. Moreover, it is important to determine the mass hierarchy in order to measure δ_{CP}, because the matter effect can mimic the CP violation in the oscillation.
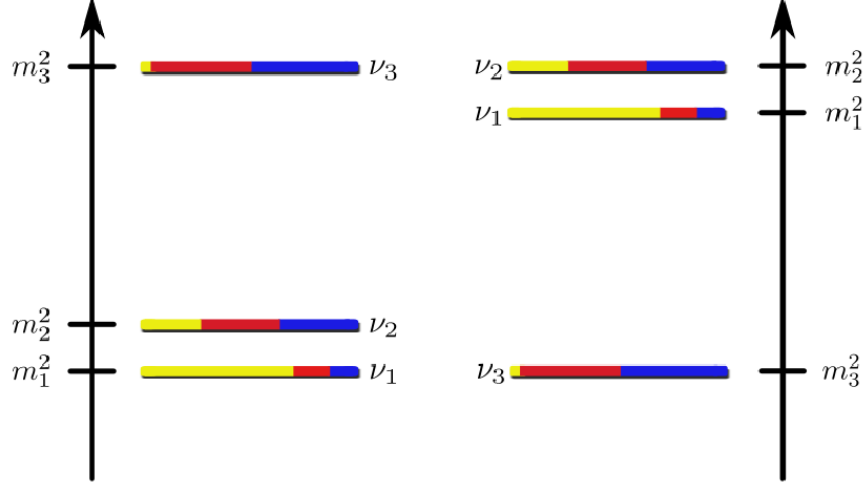
Figure 1.6: Two different mass hierarchies. The left is normal hierarchy, and the right is inverted. ν_1, ν_2 and ν_3 are mass eigenstates and colours represent flavour eigenstates. Yellow is ν_e, red is ν_μ and blue is ν_τ.

1.3.2.2 CP Violation

δ_{CP} is the only unknown parameter to complete the picture of the PMNS matrix (without considering the Majorana term, cf. Section 1.3.2.4). If the CP phase (δ_{CP}) is not zero or π it breaks the CP symmetry, i.e. it violates the invariance under Charge and Parity conjugation (CP) (i.e. the particle interchange with its own anti-particle). This is called CP violation (CPV). CP violation has already been observed in the quark sector, in the CKM matrix [32, 35]. The current explanation of the matter/anti-matter asymmetry in the Universe, by Sakharov [48], requires CP violation, but the one measured in the quark sector is not sufficient. It is natural to expect that matter and anti-matter were generated evenly, but the Universe is basically made of only matter. This can be explained if at some point in the early Universe matter got slightly more abundant over anti-matter, so that the current Universe would be made of what was left after all the anti-matter annihilated. Measuring a δ_{CP} phase different than zero or π would produce CP violation in the leptonic sector, helping to understand the matter/anti-matter imbalance of the Universe.

The CP violation can be observed by the asymmetry between neutrino and anti-neutrino oscillations: in Equation 1.18 neutrinos and anti-neutrinos will give the op-

posite sign for the imaginary part, which will lead to the asymmetry in the oscillation probabilities. Nevertheless, since this measurement needs a long-baseline experiment, the matter effect has to be taken into account because it can mimic the CP violation. Indeed also the shift given by the matter effect has a different sign between neutrinos and anti-neutrinos, and moreover its absolute value depends on the mass hierarchy (Section 1.3.2.1), which limits the precision that can be reached on the CP violation.

All these aspects get more clear writing down the oscillation probability from ν_μ to ν_e, which is the sum of five terms [49] (to the first order in the matter effect):

$$P(\nu_\mu \to \nu_e) = T_{\text{leading}} + T_{\text{CPC}} + T_{\text{CPV}} + T_{\text{solar}} + T_{\text{matter}} \tag{1.19}$$

where T_{leading} is the leading term, T_{CPC} is the CP conserved term, T_{CPV} is the CP violating term, T_{solar} is the CP solar term, and T_{matter} is the matter term. These terms are defined as:

$$
\begin{aligned}
T_{\text{leading}} &= + 4c_{13}^2 s_{13}^2 s_{23}^2 \cdot \sin^2 \Delta_{31} \\
T_{\text{CPC}} &= + 8c_{13}^2 s_{12} s_{13} s_{23} (c_{12} c_{23} \cos \delta_{CP} - s_{12} s_{13} s_{23}) \cdot \cos \Delta_{32} \cdot \sin \Delta_{31} \cdot \sin \Delta_{21} \\
T_{\text{CPV}} &= - 8c_{13}^2 c_{12} c_{23} s_{12} s_{13} s_{23} \sin \delta_{CP} \cdot \sin \Delta_{32} \cdot \sin \Delta_{31} \cdot \sin \Delta_{21} \\
T_{\text{solar}} &= + 4s_{12}^2 c_{13}^2 (c_{12}^2 c_{23}^2 + s_{12}^2 s_{23}^2 s_{13}^2 - 2c_{12} c_{23} s_{12} s_{23} s_{13} \cos \delta_{CP}) \cdot \sin^2 \Delta_{21} \\
T_{\text{matter}} &= - 8c_{13}^2 s_{13}^2 s_{23}^2 \cdot \frac{aL}{4E_\nu} (1 - 2s_{13}^2) \cdot \cos \Delta_{32} \cdot \sin \Delta_{31} \\
&\quad + 8c_{13}^2 s_{13}^2 s_{23}^2 \frac{a}{\Delta m_{31}^2} (1 - 2s_{13}^2) \cdot \sin^2 \Delta_{31} \ ,
\end{aligned}
\tag{1.20}
$$

where Δ_{ij} is $\Delta m_{ij}^2 L/4E_\nu$, and $a[\text{eV}^2] = 7.56 \times 10^{-5} \times \rho[\text{g/cm}^3] \times E_\nu[\text{GeV}]$. The corresponding probability for a $\overline{\nu}_\mu \to \overline{\nu}_e$ transition is obtained by replacing $\delta_{CP} \to -\delta_{CP}$ and $a \to -a$.

T_{CPV}, containing $\sin \delta_{CP}$, is the CP violating term which flips sign between ν and $\overline{\nu}$ and introduces CP asymmetry if $\sin \delta_{CP}$ is non-zero. T_{matter} produces an asymmetry between neutrinos and anti-neutrinos unrelated to CP violation (and proportional to the neutrino energy at a fixed value of L/E_ν). Fig. 1.7 shows the different contributions of each term in the oscillation probability formula.

Assuming $\sin^2 2\theta_{13} = 0.1$, $\sin^2 2\theta_{23} = 1.0$, and $\delta_{CP} = \pi/2$ with normal mass ordering, the effect of the CP violating term can be as large as 27% of the leading term,
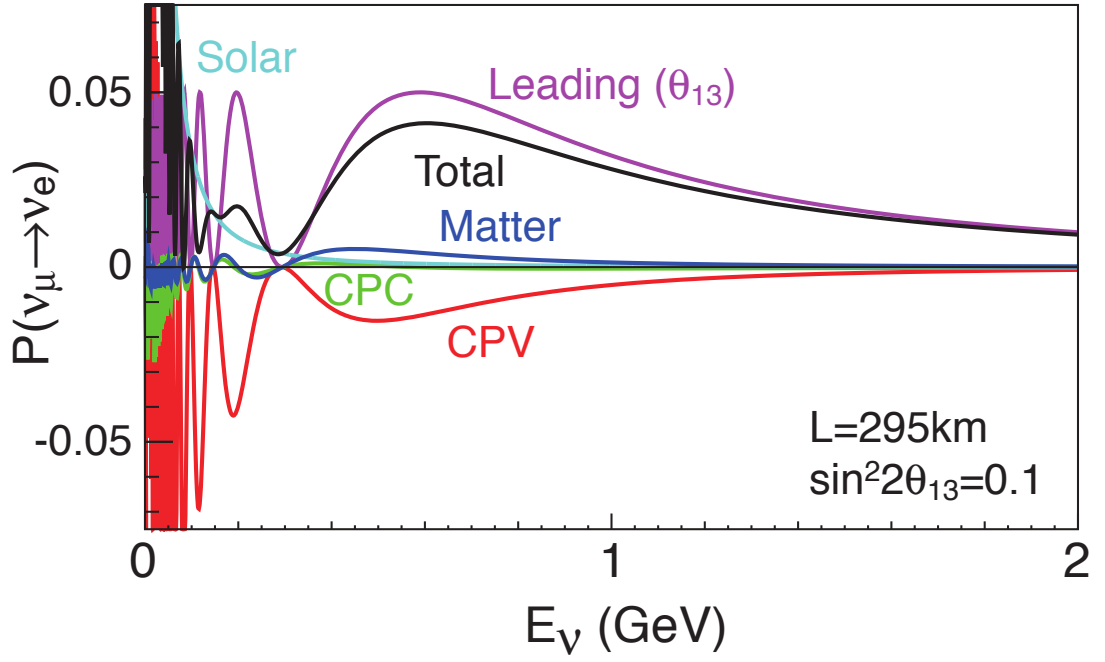
Figure 1.7: Different contributions of the oscillation probability formula for $\nu_\mu \to \nu_e$ transitions as a function of the neutrino energy, as detailed in Equations 1.19 and 1.20. A baseline of $295\,\text{km}$, $\sin^2 2\theta_{13} = 0.1$, $\delta_{CP} = \frac{1}{2}\pi$ and normal mass ordering are assumed.

making long baseline experiments one of the most promising ways of discovering CP violation in the lepton sector. Since when θ_{13} has been precisely measured (Section 1.3), long-baseline experiment programs are focusing on measuring δ_{CP} and determining the mass hierarchy. Current experiments, such as T2K or NOνA, could give some hints on the preferred values of δ_{CP}. Future experiments, like Hyper-K [36] and DUNE [37], will measure δ_{CP} more precisely.

1.3.2.3 Neutrino Masses

As seen in Equation 1.18, the neutrino oscillation probability depends only on the mass squared difference, and not on the absolute masses of neutrinos. Oscillation experiments cannot measure the absolute masses of neutrinos, they can only set some lower limits. Cosmological and astrophysical data can calculate upper bounds on the sum of the masses of the three neutrinos, being the most recent at $0.3 \, \mathrm{eV}$ [50]. Direct neutrino mass measurements are possible by measuring the spectrum of electrons at the end point of Tritium decay $^3\mathrm{H} \rightarrow^3 \mathrm{He} + \mathrm{e}^- + \overline{\nu}_\mathrm{e}$. Several experiments tried this measurement but they could only put quite large upper bounds. The KATRIN [51] experiment will reach the sensitivity of $m(\overline{\nu}_\mathrm{e}) \approx 0.2 \, \mathrm{eV}$.

1.3.2.4 Dirac or Majorana Particles, Sterile Neutrinos

Neutrinos are massless in the Standard Model of particle physics, but since neutrino oscillations have been confirmed by many experiments, a formalism to account for neutrino masses is needed. If neutrinos are Dirac particles, as all known particles, their mass could be generated using the standard Higgs mechanism, therefore requiring a right-handed component of the neutrino field. As these right-handed components do not interact through the weak force, they are also called "sterile neutrinos".

Short baseline neutrino experiments found anomalous oscillation probabilities that could be interpreted with large neutrino mass splittings which are inconsistent with the three-flavour neutrino oscillation framework. They tried to explain the tensions invoking "sterile neutrinos", but different experiments, such as the LSND experiment [52] and MiniBooNE [53, 54], reported different anomalies, inconsistent among each other. It is important to note that these anomalies are rather small, and LSND does not have a near detector. Indeed these anomalies have not been observed by long-baseline

experiments, which normally have both near and far detectors, or an internal normalisation, and which are currently defining more and more stringent limits on the existence of any discrepancy from the three-flavour neutrino oscillation framework (e.g. Super-Kamiokande [55, 56] and MINOS [57], MINOS + Daya Bay [58], Icecube [59]).

If neutrinos are Majorana particles [60], they can be described by a real wavefunction and hence be their own anti-particle. Several experiments are looking for neutrino-less double beta decays, such as SuperNEMO [61], SNO+ [62], GERDA [63], and if such processes are observed, this would qualify neutrinos as Majorana particles. Since the decay rate depends on the neutrino masses, the mass hierarchy plays a key role also to demonstrate this hypothesis.

1.4 Neutrino Interactions

In neutrino experiments, the neutrino flavour and its energy are inferred from the products of the neutrino interactions, therefore it is fundamental to understand the neutrino cross section to extract any neutrino property and interpret the oscillation data. Moreover, the neutrino cross-section measurements can lead to better understanding the nuclear structure and its models. In fact as the target gets heavier, the nuclear effects play more serious role in the measurements.

As previously stated, neutrinos are chargeless, colour-less, and can only interact through the weak force and gravity (which is extremely weak since the mass of neutrinos has an upper limit of $0.3\,\text{eV}$, as seen in Section 1.3.2.3). Weak interactions are mediated by the $W^{\pm}$ boson (Charged-Current interactions, CC) or by the Z boson (Neutral-Current interactions, NC).

CC interactions produce a charged lepton associated with the flavour of the interacting neutrino; detecting this lepton makes it possible to infer the flavour of the neutrino. NC interactions do not involve any charge exchange, hence the outgoing product is still a neutrino, which cannot be directly detected, being electrically neutral: it is impossible to determine the flavour of the incoming neutrino for NC interactions.

Neutrinos can interact with either quarks or leptons. The simplest case of neutrino interactions is neutrino-lepton scattering, which is well predicted by the Standard Model. This is discussed in Section 1.4.1. The other case is the neutrino-nucleon interactions. They are fundamentally neutrino-quark interactions, but because of the colour

390 confinement, they have to be studied as neutrino-nucleon interactions. Furthermore, in
391 order to have a significant event rate, neutrino experiments use heavy nuclei as targets,
392 therefore the nuclear effects plays a crucial role in neutrino-nucleon interactions. This
393 is discussed in Section 1.4.2.

394 1.4.1 Neutrino-Electron Scattering

395 Fig. 1.8 shows the tree level Feynman diagram of neutrino-electron scattering. In this
396 case, the cross section can be precisely evaluated at the tree level by the Standard
397 Model. Indeed, neutrino-electron scattering measurements played a key role to under-
398 stand the Standard Model showing good agreements with the model predictions.
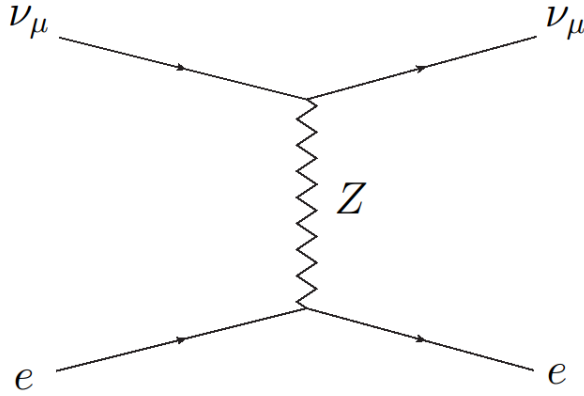
Figure 1.8: Neutrino-electron scattering Feynman diagram

399 The very first experiment was done in 1973 by Gargamelle, a Freon bubble chamber
400 experiment at CERN detecting ν_μ-e scatterings, which proved the existence of the weak
401 neutral current, providing the first demonstration of the Standard Model at the tree
402 level. In the following two decades all possible ν-e reactions have been observed and
403 several experiments have collected many thousands of ν-e events. All the results from
404 these experiments are in very good agreement with the predictions of the Standard
405 Model and the very precise results from LEP experiments. The weak-isospin structure
406 of the Standard Model and the lepton-universality for neutrinos have been verified in
407 the neutral-current sector; furthermore, the ability of the Standard Model to describe

408 very high precision results, using higher order corrections, has been shown, without any

409 deviation from the model.

Experiment		$\sigma(\nu_\mu e)/E_\nu$	$\sigma(\bar{\nu}_\mu e)/E_\nu$	$\sin^2\theta_{\nu e}$
		$(\times 10^{-45}\mathrm{cm}^2\mathrm{MeV}^{-1})$		
Gargamelle (PS)	[18]	< 1.4	$1.0^{+2.1}_{-0.9}$	$0.1 < x < 0.4$
Aachen-Padova (PS)	[31]	1.1 ± 0.6	2.2 ± 1.0	0.35 ± 0.08
Gargamelle (SPS)	[18]	$2.4^{+1.2}_{-0.9}$	< 2.7	$0.12^{+0.11}_{-0.07}$
VMWOF (FNAL)	[32]	$1.4 \pm 0.3 \pm 0.4$		$0.25^{+0.07}_{-0.05} \pm 0.8$
BNL-COL (AGS)	[33]	1.67 ± 0.44		$0.20^{+0.06}_{-0.05}$
15-feet BC (FNAL)	[34]		< 2.1	< 0.37
BEBC-TST (SPS)	[35]		< 3.4	< 0.45
CHARM (SPS)	[20]	$2.2 \pm 0.4 \pm 0.4$	$1.6 \pm 0.3 \pm 0.3$	$0.211 \pm 0.035 \pm 0.011$
BNL E734 (AGS)	[22]	$1.8 \pm 0.2 \pm 0.25$	$1.17 \pm 0.16 \pm 0.13$	$0.195 \pm 0.018 \pm 0.013$
CHARM-II (SPS)[†]	[3]	$1.53 \pm 0.04 \pm 0.12$	$1.39 \pm 0.04 \pm 0.10$	$0.237 \pm 0.007 \pm 0.007$
		$\sigma(\nu_e e)/E_\nu$	$\sigma(\bar{\nu}_e e)$	
		$(\times 10^{-42}\mathrm{cm}^2\mathrm{GeV}^{-1})$	$(\times 10^{-46}\mathrm{cm}^2)$	
Savannah River	[27, 36]		7.6 ± 2.2^a	0.25 ± 0.05
(Reactor)			1.86 ± 0.48^b	
Kurchatov (Reactor)[‡]	[37]		6.8 ± 4.5	0.29 ± 0.10
LAMPF E225 (LAMPF)	[29]	$10.0 \pm 1.5 \pm 0.9$		0.249 ± 0.063

[†] The result on the cross section was derived from the published result on the coupling constants.
[‡] Preliminary result.
[a] Region in visible energy: [1.5..3.0] MeV
[b] Region in visible energy: [3.0..4.5] MeV

Figure 1.9: Compilation of total cross section and $sin^2\theta_{\nu e}$ measurements for all neutrino-electron scattering experiments. Limits are given at the 90% C.L. [64].

1.4.2 Neutrino-Nucleon Scattering

411 In CC neutrino-nucleon interactions the neutrino converts into a charged lepton and a

412 neutron is converted into a proton with the exchange of a W boson (except for coherent

413 pion production, cf. Section 1.4.2.4). The NC neutrino-nucleon interaction is an elastic

414 scattering exchanging a Z boson.

415   It is much easier to detect CC interactions since the outgoing charged lepton pro-

416 vides an evident signature, while in NC the outgoing neutrino is unseen, implying that

the incoming neutrino flavour cannot be identified. Many experiments have measured the charged-current inclusive neutrino interactions (CCinc) on various targets and over broad neutrino energy, as shown in Fig. 1.10.
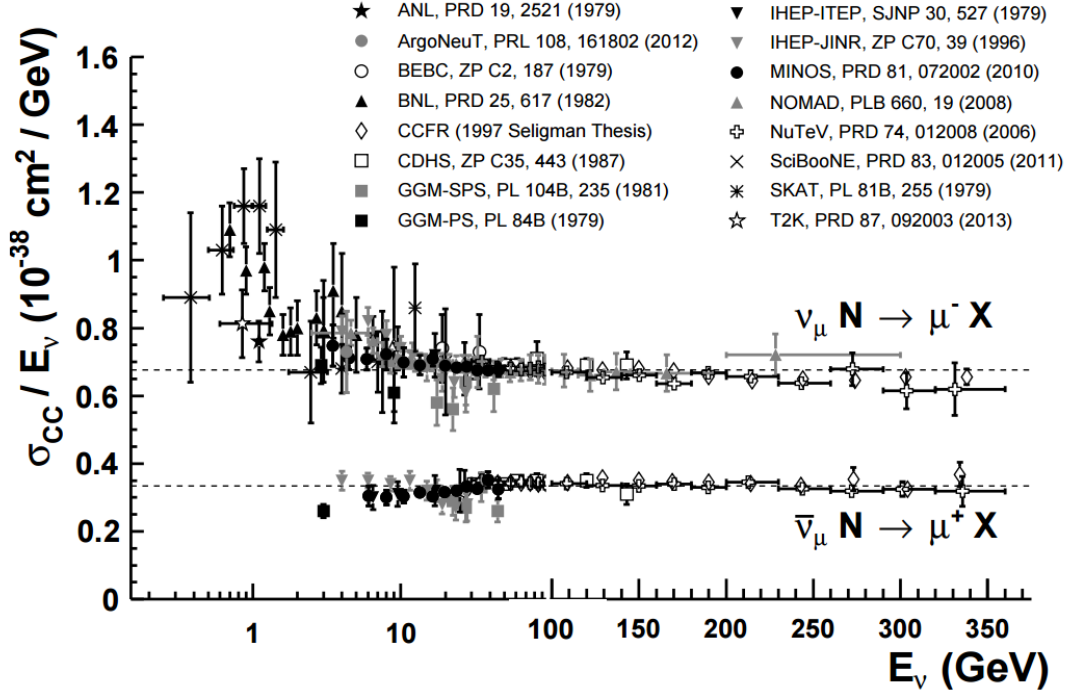
Figure 1.10: Measurements of ν_μ and $\bar{\nu}_\mu$ CC inclusive scattering cross sections as a function of neutrino energy [65].

From the early experiments at BNL and ANL laboratories, which measured the interactions at 1 GeV, to the modern experiments, such as T2K and ArgoNeuT which measured the interactions at even lower energy, and from high energy neutrino experiments such as NOMAD and NuTeV, it has been shown that the CC inclusive cross section depends linearly on the neutrino energy, with good agreement over several quite different experiments. However, there are at least four different types of neutrino-nucleon interactions which contribute to the inclusive cross section, and they are still not completely understood, therefore it is important to study each channel independently. These four channels, either CC or NC, are: Quasi-Elastic (QE), RESonant pion production (RES), COHerent pion production (COH) and Deep Inelastic Scattering (DIS).

431 As for the total interaction rate, the dominant interaction channel depends on the
432 neutrino energy and the transferred energy Q^2. Fig. 1.11 shows some of the most
433 recent neutrino cross-section measurements as a function of the neutrino energy, and
434 the predicted curves for the four interaction channels, which simplify the comparison
435 between experiments using different targets.
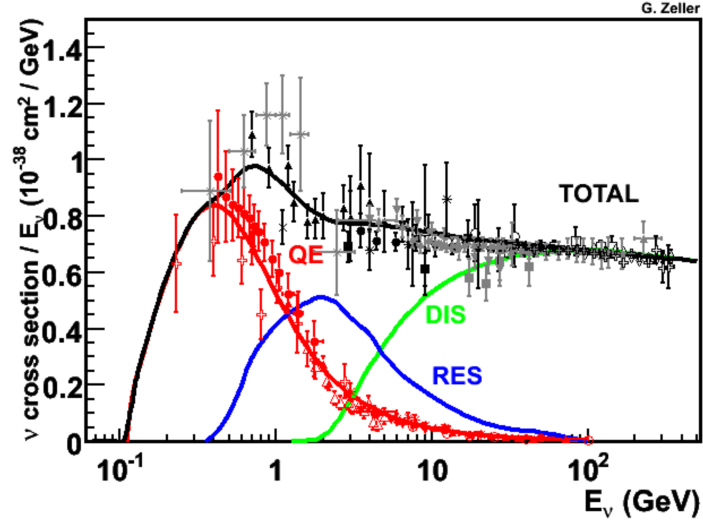
Figure 1.11: Total muon neutrino CC cross sections per nucleon divided by the neutrino energy and plotted as a function of the energy. The CC coherent contribution is not shown as it is negligible compared to the other channels. See Reference [66] for details of the experimental results shown.

436 CCQE and NCQE interactions are the dominant processes for neutrino energies be-
437 low 1 GeV. In QE processes the neutrino interacts with the nucleon as a whole. At neu-
438 trino energies above 1 GeV, the target nucleon can be excited into a baryonic resonance
439 that soon decays into a nucleon and a pion (RES). Even for these resonant processes
440 the neutrino interacts with the nucleon as a whole. Neutrinos can also interact with
441 the entire target nucleus coherently and still produce one single pion in the final state,
442 leaving the nucleus unaltered from its initial state. These coherent neutrino-nucleus
443 processes (COH) can occur in both neutral-current interactions and charged-current
444 interactions, but they are quite rare. Above 5 GeV (large Q^2) the dominant reaction
445 mechanism is the Deep Inelastic Scattering (DIS). In this case the neutrino interacts
446 with an individual quark in the target nucleon and produces a hadronic shower. At

few GeV (low Q^2) there is a region where neither RES nor DIS dominate ("Inelastic Scattering"), a region of transition between processes on the nucleon as a whole and processes on individual quark. This region is currently poorly modelled and additional contributions are believed to come from interactions where the hadronic system is neither completely fragmented nor forms a recognisable resonance.

In Fig. 1.12 the Feynman diagrams for the four CC processes are shown.

(a) Charged-current quasi-elastic (CCQE)

(b) CC resonant pion production (CCRES)

(c) Charged-current coherent (CCCOH)

(d) CC deep inelastic scattering (CCDIS)
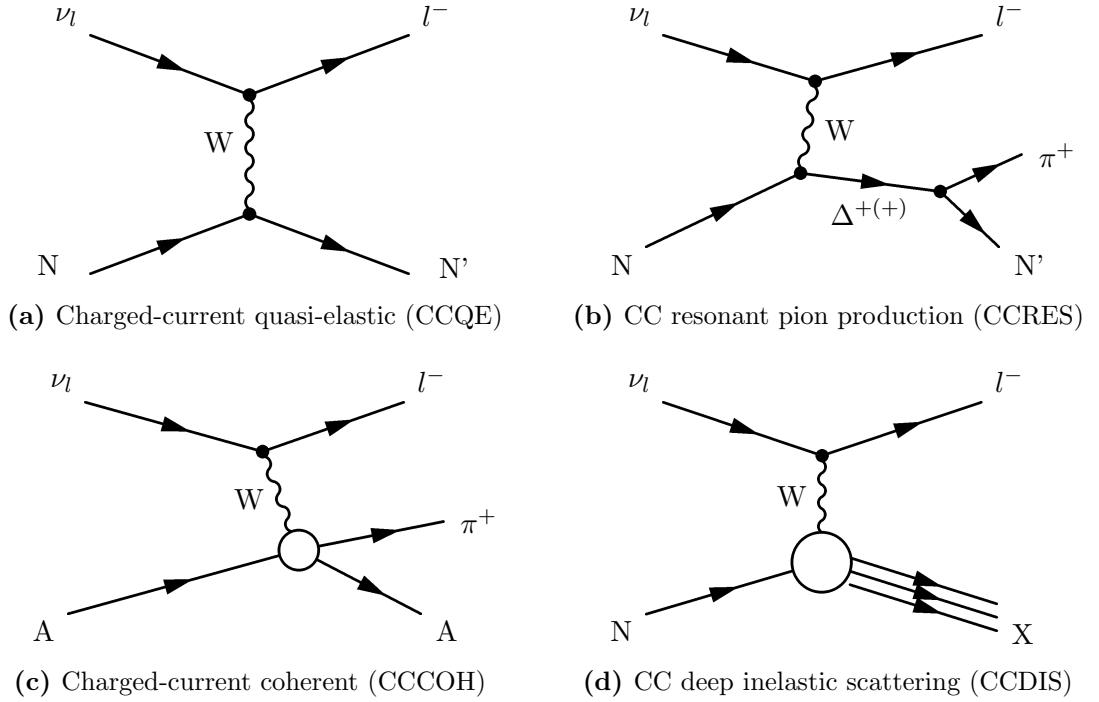
Figure 1.12: Feynman diagrams of the main neutrino-nucleon interactions relevant to the analysis presented in this thesis. N and N' indicate nucleons, A indicates that the reaction happened with the whole nucleus.

The T2K neutrino beam flux peaks at an energy of around $0.6\,\mathrm{GeV}$, hence the main signal is given by CCQE interactions, along with significant amount of CCRES interactions and a small contribution from CCCOH interactions. The QE and RES interaction processes for both CC and NC, typically observed in the T2K experiment, are shown in Table 1.2. The tail of the T2K neutrino energy extends to approximately $30\,\mathrm{GeV}$, covering also the transition between CCRES and CCDIS. High energy cross-section measurements have relatively small errors compared to measurements in the

Channels	
CC quasi-elastic	$\nu_l + n \rightarrow l^- + p$
CC resonant pion production	$\nu_l + p \rightarrow l^- + \Delta^{++} \rightarrow l^- + p + \pi^+$
	$\nu_l + n \rightarrow l^- + \Delta^+ \rightarrow l^- + p + \pi^0$
	$\nu_l + n \rightarrow l^- + \Delta^+ \rightarrow l^- + n + \pi^+$
NC quasi-elastic	$\nu_l + n \rightarrow \nu_l + n$ (not detected)
NC resonant pion production	$\nu_l + p \rightarrow \nu_l + \Delta^+ \rightarrow \nu_l + p + \pi^0$
	$\nu_l + p \rightarrow \nu_l + \Delta^+ \rightarrow \nu_l + n + \pi^+$
	$\nu_l + n \rightarrow \nu_l + \Delta^0 \rightarrow \nu_l + n + \pi^0$
	$\nu_l + n \rightarrow \nu_l + \Delta^0 \rightarrow \nu_l + p + \pi^-$

Table 1.2: List of the QE and RES processes for CC and NC neutrino interactions. The top channels are CC interactions in which a charged lepton emerges. The bottom ones are NC interactions in which a neutrino emerges instead.

0.1-1 GeV region. More interaction cross-section measurements at low energies are necessary to ensure oscillation experiments reach higher sensitivities.

Before describing in detail each of the four processes, we discuss the nuclear effects due to the fact that the nucleon is bound in the nucleus, which complicate the neutrino-nucleon cross-section predictions.

1.4.2.1 Nuclear Effects

Target nucleons in neutrino experiments are usually bound in nuclei: to have a higher event rate, heavier targets are more common than hydrogen or deuterium targets. Plastic scintillators are mainly composed of hydro-carbon, sampling calorimeters mainly contain iron, and Cherenkov detectors mainly use water as a target. This nucleon binding has three consequences. First, the interaction takes place only if the transferred energy is enough to unbound the nucleon (Pauli blocking). Second, once the neutrino has interacted, the products of the interactions travel through the nuclear

medium where they could undergo secondary interactions, such as absorption or scattering, changing their momentum and direction, and possibly generating other particles or kicking other nucleons off the nucleus: these are called Final State Interactions (FSI). Third, neutrinos could interact on multi-nucleon systems. Since the neutrino experiments detect the outgoing particles exiting the nuclei, it is very important to properly model the nuclear medium and the FSI in order to study the primary neutrino interactions.

Nuclear Model
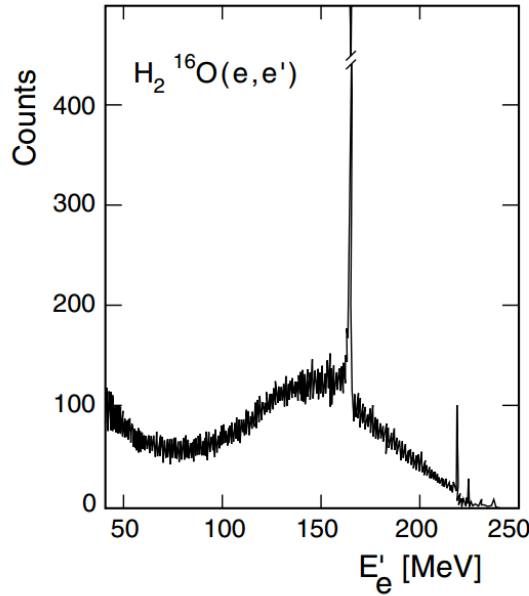
Figure 1.13: Energy spectrum of electrons scattering off a thin H_2O target. The data were taken at the linear accelerator MAMI-A in Mainz at a beam energy of 246 MeV and at a scattering angle of 148.5° [67].

Fig. 1.13 shows the data from electron scattering measurement on H_2O. There is a sharp peak at around 150 MeV which corresponds to quasi-elastic scattering on hydrogen atoms. However, there is a wide energy spectrum overlaid which comes from the scattering on oxygen: the conclusion is that nucleons are not static and fixed in the nucleus but conversely they freely move (Hofstadter, Nobel Prize in Physics 1961). The

Fermi gas model was introduced in the quasi-elastic scattering calculation to describe the nucleons in the nucleus [68], and it describes weakly interacting fermions obeying the Fermi-Dirac statistics. Neutrons in a nucleus, being spin 1/2 fermions, naturally obey Fermi-Dirac statistics; and the same for protons, independently from neutrons: the nucleons in a nucleus could be considered two independent fermion systems. The Fermi gas model assumes the nucleons can freely move inside the nuclear volume with a certain potential which has a shape of well. In this model, protons and neutrons have different values of potentials, but the same radius of the wells. Fig. 1.14 illustrates fermions in the nuclear potential well.
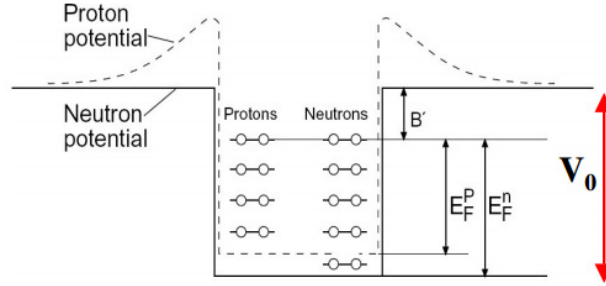
Figure 1.14: Fermions in the nuclear potential well. E_F^p and E_F^n are the Fermi energies of protons and neutrons respectively. V_0 is the binding energy and B is the average binding energy per nucleon [67].

The number of possible states of nucleons depend on the momentum, and in the nuclear ground state the lowest states are all occupied up to the maximum momentum. This is called Fermi momentum and is given as (in a case where the number of neutrons and protons are the same):

$$p_F = \frac{\hbar}{R_0}(\frac{9\pi}{8})^3 \tag{1.21}$$

where R_0 is experimental value obtained from the electron scattering data. The Fermi energy is then:

$$E_F = \frac{p_F^2}{2M} \tag{1.22}$$

where M is the nucleon mass. Only interactions in which the outgoing nucleon has

a momentum higher than p_F are allowed, all other interactions are Pauli blocked. Furthermore, if the transferred energy is larger than the binding energy, the outgoing nucleon is released from the nucleus (consuming some energy), otherwise it is only excited to an higher nuclear energy state.

This model is used to calculate the quasi-elastic scattering and showed good agreement only at the QE peak, but it did not describe well the low momentum transfer. Therefore, other models are being investigated.

Spectral Function (SF) is alternative model to describe a nucleus [69]. It describes the momentum and energy distribution of initial nucleons in a nucleus as a continuous function. In spectral function model, instead of modelling the nucleons with the Fermi-Dirac statistics, the system A-nucleon is described by a non-relativistic Hamiltonian:

$$H_A = \sum_{i=1}^{A} \frac{p_i^2}{2m} + \sum_{j>i=1}^{A} v_{ij} \tag{1.23}$$

where p_i is the momentum of i-th nucleon and v_{ij} is the nucleon-nucleon potential. Therefore, the probability distribution of removing a nucleon with a certain momentum, leaving the residual nucleus with a certain excitation energy, can be calculated. As expected, the SF model shows better agreement with electron scattering data than the Fermi gas model.

Final State Interactions (FSI)

The final state interactions can alter the observed number of hadrons and their kinematics. Pions are particularly sensitive to the FSI effects, therefore the nuclear medium can influence the production of pions or their fate. Once produced, charged pions can either be absorbed, or converted into neutral pions via $n + \pi^+ \rightarrow p + \pi^0$, scatter or also knock out nucleons. To predict FSI, a cascade model is usually implemented in neutrino interaction generators. It considers interactions with nucleons in the nuclear medium as interactions on free nucleons, then integrate over a nucleus assuming they are far enough apart that particles stay on-shell. Fig. 1.15 illustrates how the cascade model works.
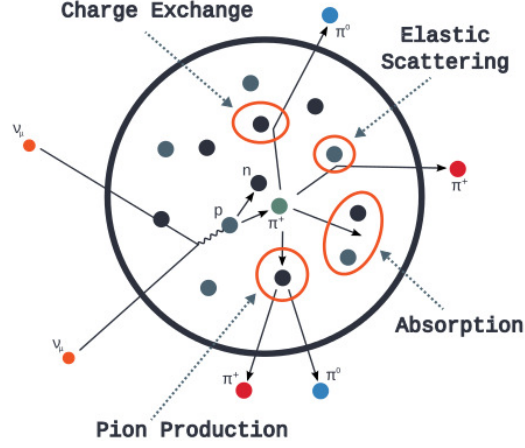
Figure 1.15: This diagram describes the propagation of the particles through a nucleus. It shows all possible FSI modes - pion production, charge exchange, pion absorption and elastic scattering.

Interactions on Multi-Nucleon Systems

In realistic situation, protons and neutrons in a nucleus are not independent, but bound and correlated to each other. Therefore, the interaction cannot be considered as an interaction on a single nucleon. Indeed it is possible that the neutrino scatters off a multi-nucleon system, and it is called n-particles n-holes (np-nh) fluctuation. np-nh means that n particles are in an unbound state with respect to the Fermi Surface to be escaped, and then n holes are left. This is currently interpreted as an alternative explanation to the need of "sterile neutrinos" (cf. Section 1.3.2.4) to explain the tensions reported by MiniBooNE experiment in 2010 [53] (Fig. 1.16). Even if sub-dominant, these processes are becoming important. Indeed, with respect to the same process on a free nucleon, the outgoing lepton gets a different momentum and angle, and it is important to predict these observables correctly because they are used to reconstruct the neutrino energy in oscillation analyses.

Fig. 1.17) shows the Feynman diagrams of neutrino interactions via 2p-2h process. While there is direct evidence of this processes in electron scattering data [71], for neutrinos interactions they are still under investigation. M. Martini and J. Nieves independently developed two models for 2p-2h processes, i.e. neutrino interactions on
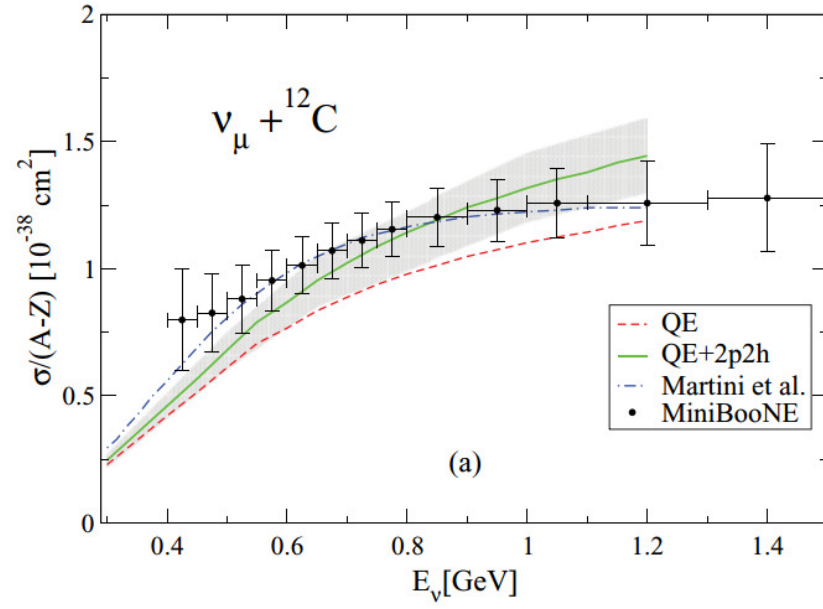
Figure 1.16: MiniBooNE ν_μ CCQE cross-section measurements on carbon as a function of neutrino energy in data points. Theoretical predictions from Martini et. al. (blue dashed) and Nieves et. al. (light green solid) are also shown. Red dashed line is the CCQE cross section.
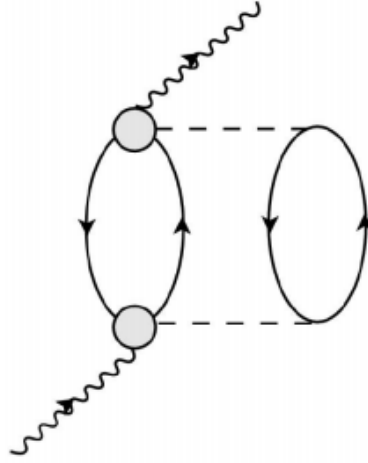
Figure 1.17: MEC interactions are also known as $2p2h$ (two particle two hole), because the calculation of cross sections for these interactions involve the excitation of a pair of particles and holes, which are connected by a meson propagator. Solid lines represent particles or holes, dashed lines represent mesons, wavy lines represent the incoming or outgoing W. Grey circles represent any possible vertex with the corresponding initial/final particles [70].

correlated pairs of nucleons (meson exchange currents, MEC [72, 73]), which are now being tested within the T2K collaboration. Both these models predict that multi-nucleon interactions on carbon at the T2K neutrino energies (peaked at $\approx 0.6\,\mathrm{GeV}$) contribute to a significant fraction of the cross section [74, 75].

1.4.2.2 Quasi-Elastic Interactions (QE)

At T2K, the most significant interaction channel is the charged-current quasi-elastic scattering (CCQE), not only because it is the dominant process at the neutrino energy peak of T2K ($\approx 0.6\,\mathrm{GeV}$), but also because the neutrino energy E_ν can be well reconstructed by two-body kinematics (Fig. 1.12a):

$$E_\nu^{rec} \approx \frac{m_p^2 - (m_n - m_l)^2}{2(m_n - E_l + \sqrt{E_l^2 - m_l^2} \cos\theta_l)} \tag{1.24}$$

with n the incoming neutron, p the outgoing proton, l the outgoing charged lepton and θ_l its polar angle.

The first formulation of CCQE interactions was from Llewellyn Smith [76]. The cross-section matrix is parametrised by a vector form factor $F_V^1(Q^2)$ and and axial form factor $F_A(Q^2)$, a priori unknown, which depends on the transferred momentum between the incident neutrino and the outgoing lepton ($Q^2 = -q^2$). The form factors describe the spatial extension of the nucleus, i.e. the fact that nuclei are not point particle and have a charge distribution. The vector form factor appears in the leading term of the cross section and it is measured from electron scattering data. The axial form factor is defined as a function of the transferred momentum Q^2:

$$F_A(Q^2) = \frac{F_A(0)}{\left(1 + Q^2 / \left(M_A^{QE}\right)^2\right)^2} \ , \tag{1.25}$$

where $F_A(0)$ is the form factor at $Q^2 = 0$ which has been determined from nuclear beta decay measurements, and M_A^{QE} is the "axial mass" which describes how the weak interaction current depends on the electric charge distribution of a target nucleus. M_A^{QE} is the only free parameter and can only be determined by neutrino scattering.

The NOMAD experiment in 2009 [77] and the MiniBooNE experiment in 2010 [53] both measured the *effective* axial mass, due to the nuclear environment where interac-

570 tions take place. NOMAD, using neutrinos with energy between 3 and 10 GeV, reported
571 $M_A^{QE} = 1.05 \pm 0.02(\text{stat}) \pm 0.06(\text{syst})$ GeV, while MiniBooNE, with a mean neutrino
572 energy beam around 0.8 GeV, reported $M_A^{QE} = 1.35 \pm 0.17$ GeV. Fig. 1.18 shows the
573 clear tensions between the model predictions for these values of M_A^{QE} and the NO-
574 MAD and the MiniBooNE data-sets. It should be noticed that the two experiments
575 used quite different detecting strategies, and the explanation of the discrepancy be-
576 tween them might be related to mis-identification of events. As a result, nuclear effects
577 on CCQE interactions have become crucial subject to be investigated, and recent ex-
578 periments started looking at hadronic side as well to have better understanding of this
579 discrepancy.
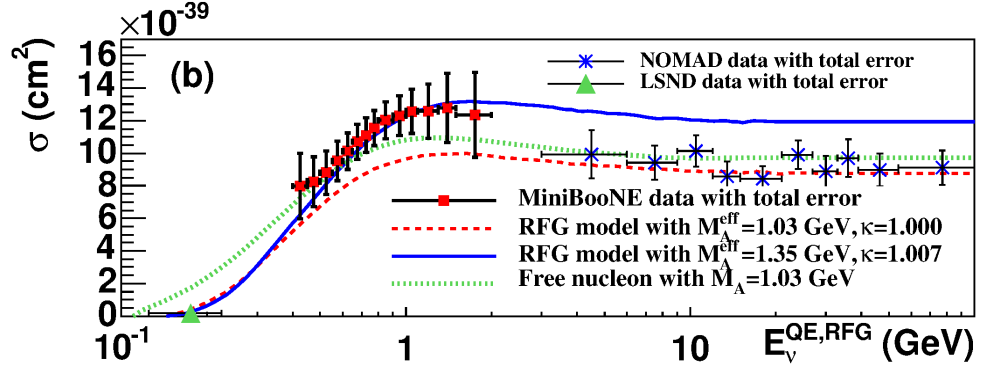
Figure 1.18: Comparison of MiniBooNE and NOMAD ν_μ CCQE cross-section measure-
ments as a function of neutrino energy, and model predictions with M_A^{QE} values that best
describe each data-set.

580 Recently, even the MINERνA experiment [78] found disagreements between the
581 CCQE differential cross-section and the Relativistic Fermi Gas (RFG) model [79]. but
582 their results suggested that a model for the nucleus is necessary in addition to a model
583 of the nucleon. A recent work by the Neutrino Interaction Working Group (NIWG)
584 within the T2K collaboration [70] suggests that adding two nuclear effects in the RFG
585 model would lead to good agreement between the MiniBooNE and MINERνA data.
586 The two effects are the Random Phase Approximation (RPA), a nuclear screening
587 effect due to long range nucleon-nucleon correlations, and the Nieves model for Meson
588 Exchange Currents (MEC), which accounts for interactions between correlated pairs of
589 nucleons inside the nucleus [72] (Fig. 1.17).

The measurement of the axial mass is of extreme importance because of the impact on the model predictions of the interaction rates. More data in this region is necessary to understand the nuclear effects and disentangle the effect of correlations between nucleon pairs from FSI effects. Figure 1.19 shows the latest status of existing measurements of CCQE cross section with theoretical prediction from NUANCE.
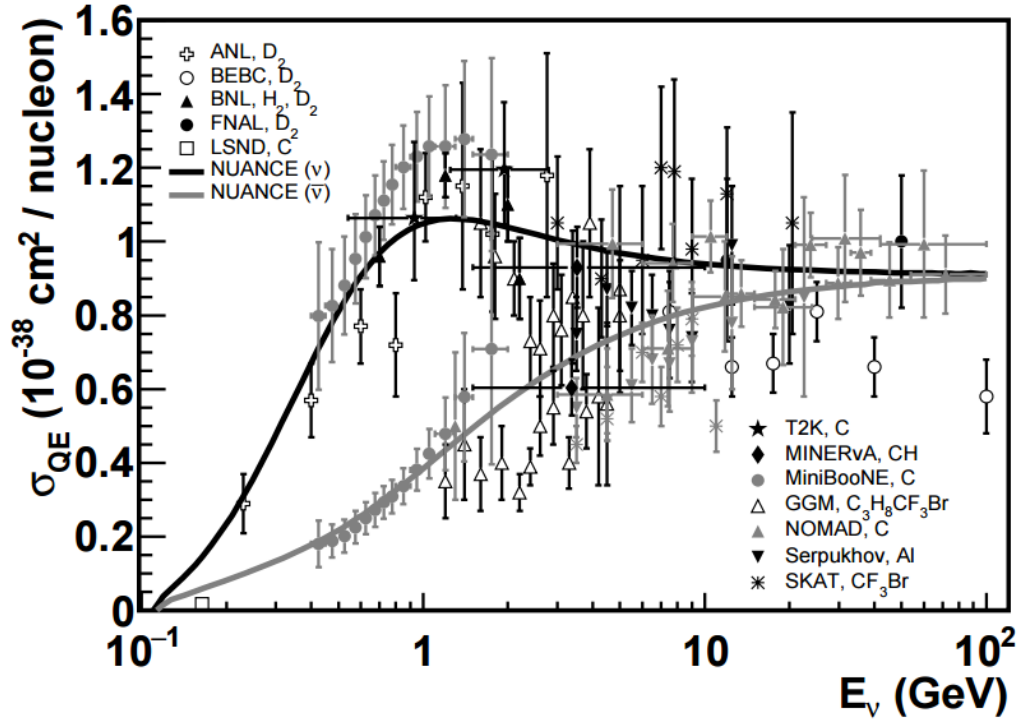
Figure 1.19: Measurements of ν_μ (black) and $\bar{\nu}_\mu$ (red) QE scattering cross sections as a function of neutrino energy. The NUANCE free nucleon scattering prediction assumes $M_A = 1.0$ GeV [65].

1.4.2.3 Resonant Pion Production (RES)

The second largest contribution to the cross section in energies around $1\,\mathrm{GeV}$ is due to CCRES (Fig. 1.11). In resonant interactions the target nucleon is excited into a resonant state (usually $\Delta(1232)$) which decays into a pion and a nucleon (Fig. 1.12b):

$$\nu_\mu + \mathrm{n} \rightarrow \mu^- + \mathrm{n} + \pi^+ \,,$$

$$\nu_\mu + \mathrm{p} \to \mu^- + \mathrm{p} + \pi^+ \,,$$

$$\nu_\mu + \mathrm{n} \to \mu^- + \mathrm{p} + \pi^0 \,.$$

Fig. 1.20 shows the latest status of existing measurements of resonant pion production cross section with theoretical prediction from NUANCE: the data-MC agreement is quite limited, and as for CCQE interactions, it is getting important taking into account the nuclear effects.
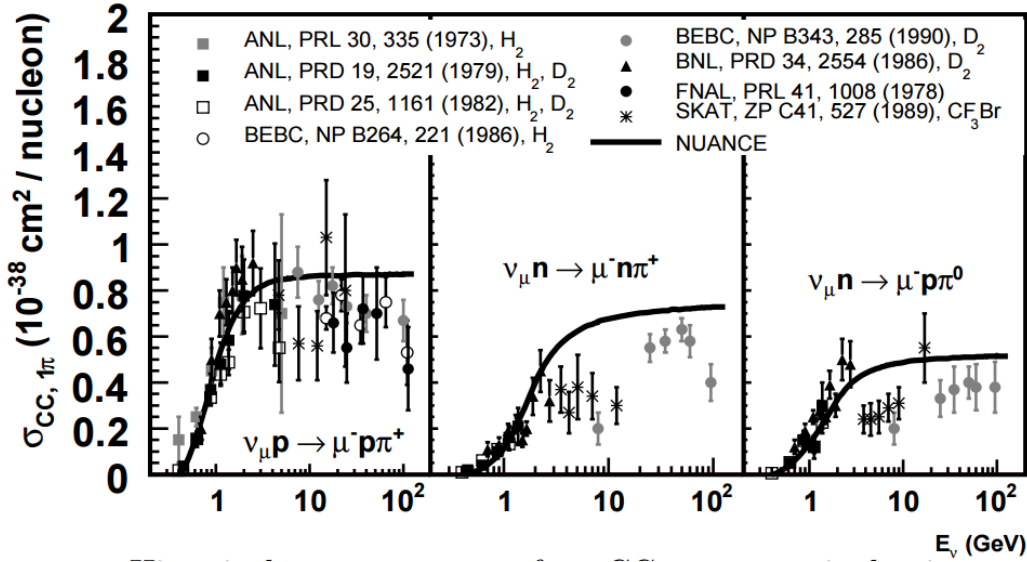
Figure 1.20: Measurements of ν_μ CC resonant single-pion production. The NUANCE free scattering prediction assumes $M_A = 1.1$ GeV.

Most simulations use the Rein-Sehgal model for resonant interactions [80]. In this model all non-strange resonances below 2 GeV are combined to produce the amplitudes of the different pion production channels; moreover, a small non-resonant background is added incoherently to improve the agreement with data. As for CCQE, the cross-section matrix can be written as a function of form factors. Vector and axial-vector form factors have similar forms to those in the quasi-elastic scattering, but there is an additional factor related to the resonance excitation. In this case, M_{RES}^A is the "axial mass" for resonant interactions. Vector form factors are determined from photoproduction and electroproduction data, whereas axial form factors are not well know [81].

₆₁₂ The ANL [82] and BNL [83] bubble chamber experiments both made measurements ₆₁₃ of charged-current resonant pion production on deuterium for muon neutrinos of energy ₆₁₄ about 1 GeV, but their measurements had a long discussed disagreement. Recent re-₆₁₅ analyses of these data [84, 85] produced cross-section ratios for various interaction ₆₁₆ channels and found good agreement between the experiments.

₆₁₇ More recently, experiments, such as MiniBooNE [86] in 2011 and MINERνA [87] ₆₁₈ in 2014, started to measure the CC1π cross-section which is described by the particles ₆₁₉ leaving the nucleus, i.e. one muon, one pion and any number of nucleons. This means ₆₂₀ that CC1π^+ measurements, besides the resonant interactions, contain also coherent ₆₂₁ interactions, DIS interactions where additional pions are absorbed before leaving the ₆₂₂ nucleus, and CCQE interactions where the proton interacts with the nuclear medium ₆₂₃ and produces a positive pion.

₆₂₄ Figure 1.21 shows that the MINERνA and the MiniBooNE $d\sigma/dT_\pi$ data have a ₆₂₅ similar shape above $T_\pi = 100$ MeV, which is where the pion FSI effects are expected to ₆₂₆ be the largest. There are nonetheless significant normalisation and shape discrepancies ₆₂₇ between the two measurements.
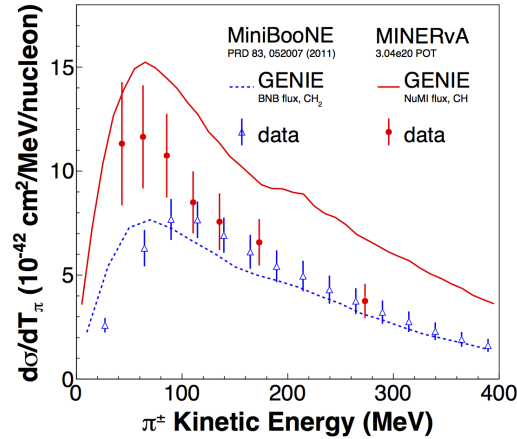
Figure 1.21: Comparison between the MINERνA and MiniBooNE $d\sigma/dT_\pi$ data with the GENIE generator model including FSI treatment [87].

₆₂₈ Currently no theoretical model can explain all the pion production data available. ₆₂₉ Investigating single pion production at energy below 2 GeV is important for under-₆₃₀ standing the neutrino cross section, as well as for reducing the uncertainty related to

pion production in oscillation measurements.

1.4.2.4 Coherent Pion Production (COH)

On targets heavier than hydrogen, neutrinos can coherently scatter from the entire nucleus (Figure 1.12c), producing a pion in the final states, leaving the nucleus unaltered and without detectable recoil. Neutrino interactions depend on the wavelength of the gauge boson, which is determined by the 4-momentum transfer from the leptonic side to the hadronic side. A coherent pion production occurs when this wavelength is much larger than the diameter of the nucleus, which therefore receives a negligible transfer momentum. The emitted pion is more forward-scattered compared to resonant interactions. Coherent pion production is possible in both NC and CC interactions.

At neutrino energies above 2 GeV coherent interactions have been measured precisely and agree quite well with the model predictions [88]. At lower neutrino energies, SciBooNE measured a NC coherent pion production cross-section [89] consistent with the model prediction, but for CC-COH both K2K [90], SciBooNE [91] and more recently MINERνA [92] reported a large deficit compared to the model prediction (Fig. 1.22).
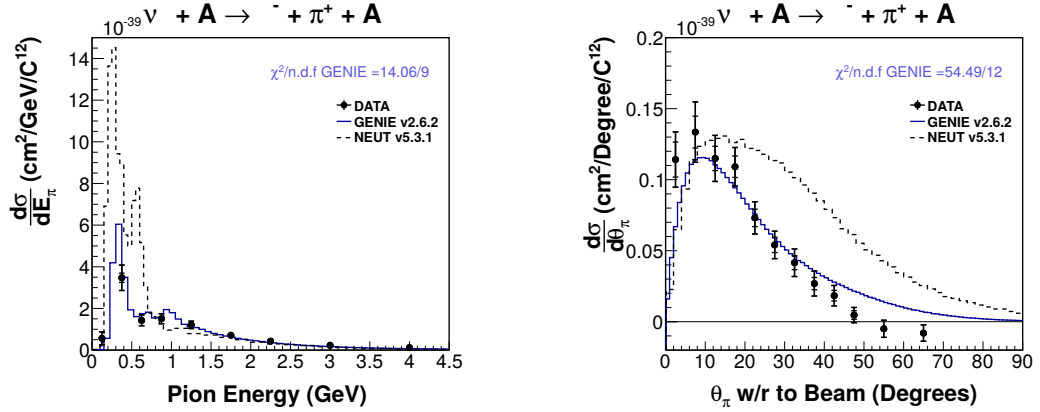
(a) The MINERνA $d\sigma/dE_\pi$ measurement.

(b) The MINERνA $d\sigma/d\theta_\pi$ measurement.

Figure 1.22: Charged-current muon neutrino coherent pion production cross-section measurements released by the MINERνA Collaboration.

1.4.2.5   Deep Inelastic Scattering (DIS)

At the higher neutrino energy Deep Inelastic Scattering is the dominant process (Fig. 1.11). Parton Distribution Functions (PDFs) are used to describe the probability of finding a particle within a certain momentum range [93, 94]. There are several data sets to determine experimentally the parton distribution functions.

2

The T2K Neutrino Oscillation Experiment

The T2K (Tokai To Kamioka) experiment [95]) is a long-baseline neutrino experiment which uses a beam of muon neutrinos to study the neutrino oscillations described in Section 1.1, by measuring the appearance of electron neutrinos and the disappearance of muon neutrinos. T2K is one of the five experiments awarded the 2016 Breakthrough Prize in Fundamental Physics [2] for investigating neutrino oscillations.

A high purity ν_μ or $\overline{\nu}_\mu$ beam is produced at J-PARC (Japan Proton Accelerator Research Complex) in Tokai-Mura (Ibaraki, Japan) from a 30 GeV proton beam. A near detector facility located 280 meters from the proton beam target provides the measurements of the unoscillated neutrino event rates. The Super-Kamiokande (SK) far detector in Kamioka (Gifu), at 295 km from production, detects the oscillated neutrinos. By comparing the near and far detector measurements, the T2K experiment can put stringent constraints on the oscillation parameters.

T2K is the first long-baseline neutrino oscillation experiment using an off-axis configuration (originally proposed in [96]), with the proton beam directed at an angle of $2.5°$ away from the direction towards the far detector. With this off-axis technique the peak of the beam energy spectrum is tuned to the maximum of the $P(\nu_\mu \rightarrow \nu_e)$ oscillation probability, which is at ~ 600 MeV for the T2K baseline of 295 km, enhancing the CCQE interactions and reducing the background contributions from the high energy tail. The schematic layout of the T2K experiment is presented in Fig. 2.1.

42
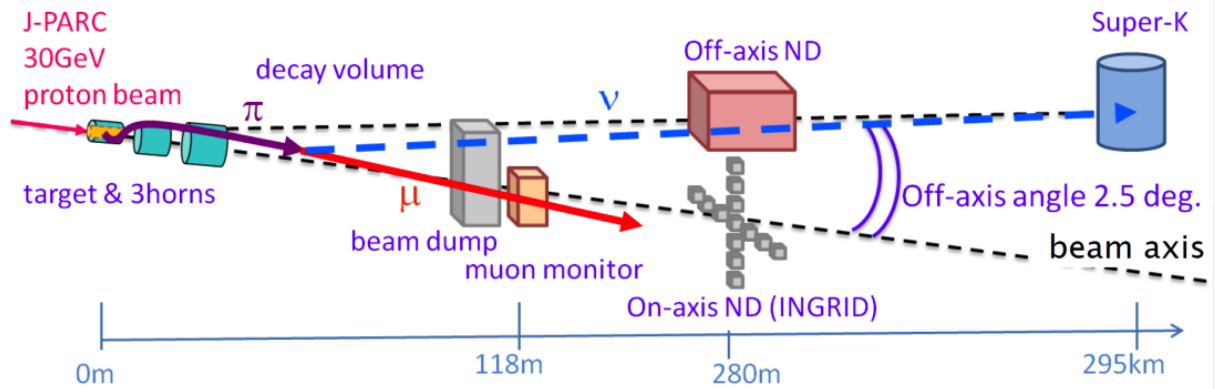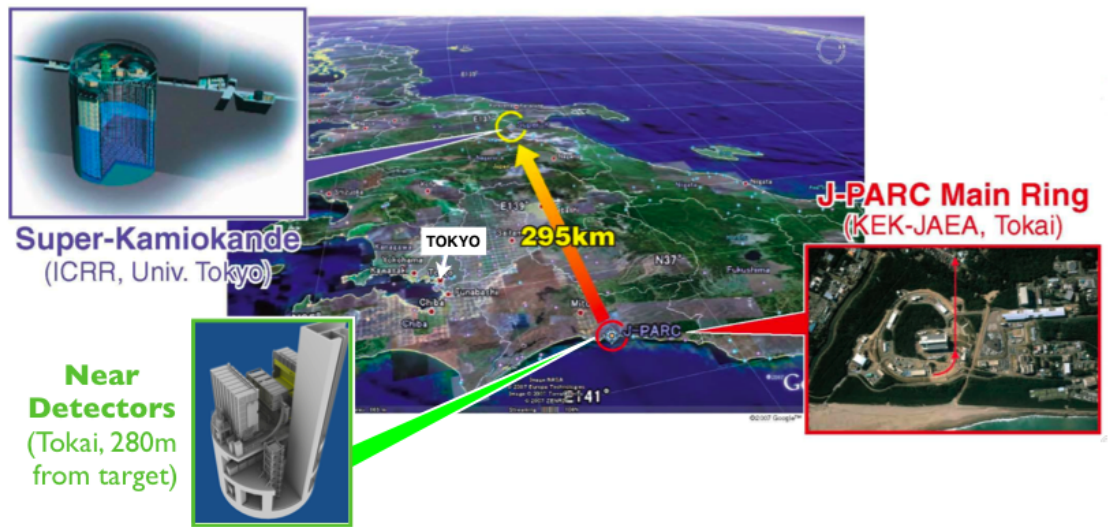
Figure 2.1: Layout of the T2K experiment, showing the position of the J-PARC accelerator facility where the ν_μ beam is produced, the near detectors located at 280 meters from the target and the far detector Super-Kamiokande 295 km away.

₆₇₃ The T2K experiment is the first long-baseline neutrino oscillation experiment pro-
₆₇₄ posed and approved to explicitly look for electron neutrino appearance in a muon
₆₇₅ neutrino beam. The main goals of the T2K experiment were highlighted in the original
₆₇₆ proposal [97] as the discovery of $\nu_\mu \to \nu_e$ oscillations, the precise measurement of ν_μ
₆₇₇ disappearance oscillation parameters and the search for sterile neutrino components
₆₇₈ in the ν_μ disappearance spectrum. T2K was the first experiment to indicate direct
₆₇₉ evidence of $\nu_\mu \to \nu_e$ appearance [47] in 2011, and to measure the mixing angle θ_{13} as
₆₈₀ this parameter affects the leading term of the $P(\nu_\mu \to \nu_e)$ oscillation probability shown
₆₈₁ in Chapter 2, with a sensitivity to the value of $sin^2 2\theta_{13}$ down to 0.006 [98, 99].

$$P(\nu_\mu \to \nu_e) \approx sin^2 2\theta_{13} sin^2 \theta_{23} sin^2 \left(1.267 \frac{\Delta m_{31}^2 L(km)}{E_\nu(GeV)} \right). \qquad (2.1)$$

₆₈₂

₆₈₃ In 2012 the value of θ_{13} was then constrained by $\overline{\nu}_e$ disappearance in the reactor
₆₈₄ experiments of Daya Bay [43] and RENO [45]. In 2013 T2K excluded $\theta_{13} = 0$ at $7.3\,\sigma$
₆₈₅ significance [99].

₆₈₆ The reactor experiments use a different channel to estimate the mixing angle θ_{13}, as
₆₈₇ they perform this measurement in anti-neutrino disappearance. Combining the event
₆₈₈ rates in the T2K experiment with the value of $sin^2 \theta_{13}$ obtained by the reactor experi-
₆₈₉ ments allows to explore in more detail the 3-flavour neutrino paradigm, as probing the
₆₉₀ Dirac CP-violating phase δ_{CP} becomes accessible. The T2K experiment has therefore
₆₉₁ the power to investigate the Charge-Parity (CP) violation in the lepton sector, one of
₆₉₂ the open questions in neutrino physics, and the first hint on the value of δ_{CP} has al-
₆₉₃ ready been obtained. With the current statistics, when analysed in a full framework of
₆₉₄ three neutrinos and anti-neutrino flavours, and combined with measurements of elec-
₆₉₅ tron anti-neutrino disappearance from reactor experiments, the size of the expected
₆₉₆ T2K 90 % confidence interval for δ_{CP} ranges from approximately 2π (i.e. the full range
₆₉₇ of δ_{CP}) to 1π depending on the true value of δ_{CP} and the true mass ordering. The
₆₉₈ actual T2K data yield a 90 % confidence interval for δ_{CP} of [-3.13; -0.39] radians for
₆₉₉ the normal mass ordering and [-2.09 ; -0.74] radians for the inverted mass ordering.
₇₀₀ The CP conserving values ($\delta_{CP} = 0$ and $\delta_{CP} = \pi$) lie outside of this interval.

Furthermore, precise measurements of the atmospheric oscillation parameters $sin^2\theta_{23}$ and Δm^2_{32} can be achieved via ν_μ disappearance analysis [100, 101, 102] as their values determine the leading term of the survival oscillation probability of the muon neutrino shown in Eq. (2.2).

$$P(\nu_\mu \to \nu_\mu) \approx 1 - sin^2 2\theta_{23} sin^2 \left(1.267 \frac{\Delta m^2_{32} L(km)}{E_\nu(GeV)} \right). \qquad (2.2)$$

T2K already provided independent measurements of θ_{23} and Δm^2_{32} [103], and is expected to reach a precision of $\delta(\Delta m^2_{32}) \sim 10^{-4} eV^2/c^4$ and $\delta(sin^2 2\theta_{23}) \sim 0.01$ with the approved exposure of 7.8×10^{21} POT. Furthermore, T2K will have good sensitivity on the octant of the mixing angle θ_{23} and some sensitivity to the mass hierarchy determination.

At the near detector facility there are two detectors: the on-axis INGRID and the $2.5°$ off-axis ND280. These two near detectors produced a series of cross-section measurements [104, 105, 106, 107], and more are being worked on, which are important to reduce the systematic uncertainties in the oscillation analysis, and can help to constrain the neutrino interaction models. Other studies, such as the search for sterile neutrinos via electron neutrino disappearance and the search for exotic processes, are being performed in the ND280 detector.

The T2K collaboration is formed by about 500 physicists from 59 institutions in 11 countries.

2.1 Neutrino Beam

At J-PARC [108] a proton synchrotron produces a proton beam which is fast-extracted in a single turn and fired against a graphite target to produce pions and kaons. Electromagnetic horns focus these hadrons into the decay pipe, where they decay producing muon neutrinos.

2.1.1 Proton Accelerators

The J-PARC accelerator facility is a system of three accelerators, commissioned in April 2009. A schematic view of the J-PARC accelerator facility is shown in Fig. 2.2.

⁷²⁷ There are three accelerator phases: the linear accelerator (LINAC), the rapid-
⁷²⁸ cycling synchrotron (RCS), and the main ring synchrotron (MR).

Figure 2.2: Schematic view of the J-PARC accelerator facility. The three accelerator phases are highlighted (LINAC, RCS and MR), as well as the beamline (NU) and the location of the near detector facility.

⁷²⁹ Firstly, an H^- beam is accelerated by the 300 meters LINAC. Upgrades have been
⁷³⁰ recently performed in the LINAC by installing Annular-ring Coupled Structure (ACS)
⁷³¹ cavities in its drift tube to reach the design 400 MeV power. The H^- beam is then
⁷³² converted to an H^+ beam by charge-stripping foils at the RCS injection and accelerated
⁷³³ by the rapid-cycling synchrotron up to 3 GeV with a 25 Hz cycle. About 5% of the spills
⁷³⁴ accelerated at the RCS are injected to the main ring (the rest supplies other facilities
⁷³⁵ at J-PARC). The main ring, with a circumference of 1567 meters and a nominal design
⁷³⁶ beam power of 750 kW, accelerates the protons up to 30 GeV. The spills are then
⁷³⁷ fast-extracted in a single turn by a set of five kicker magnets, and are directed down
⁷³⁸ the neutrino beamline (NU) to the target.

₇₃₉ Each spill lasts less than $5\,\mu s$ and consists of 8 bunches, each containing $\approx 3 \times 10^{14}$
₇₄₀ protons and lasting 58 ns. The short duration of the spill is critical to reject background
₇₄₁ events, including cosmic rays, at both near and far detectors. Recently the J-PARC
₇₄₂ MR has achieved a world record for beam intensity reaching a beam power of 470 kW.

₇₄₃ ## 2.1.2 Neutrino Beamline

₇₄₄ The neutrino beamline is divided into two sequential steps: the primary beamline which
₇₄₅ transports the protons from the MR to the target, and the secondary beamline which
₇₄₆ handles the secondary pions that are focused by magnetic horns before they decay into
₇₄₇ neutrinos (cf. [95]).
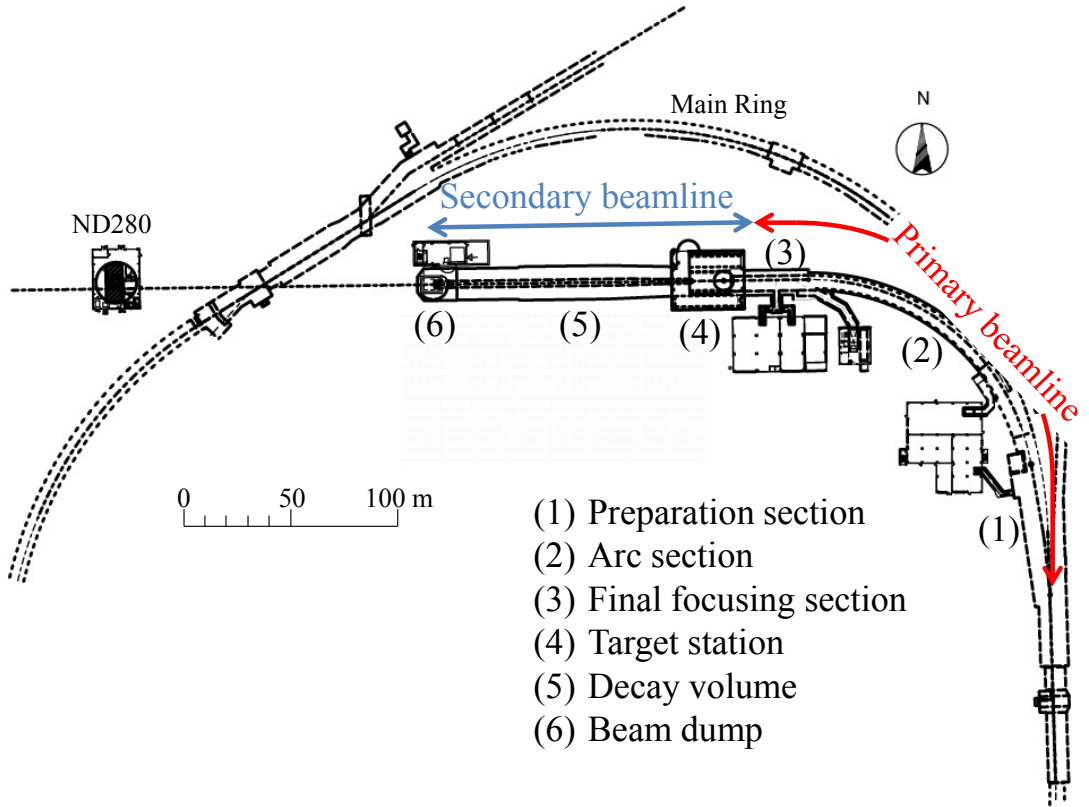
Figure 2.3: Schematic view of neutrino beamline at J-PARC.

₇₄₈ Fig. 2.3 shows the primary beamline which consists of a preparation section, an
₇₄₉ arc section and a final focusing section. In the preparation section the proton beam
₇₅₀ is tuned and aligned by normal conducting magnets for entering the arc section. In

the arc section superconducting magnets direct the protons at 2.5° away from Super-Kamiokande. The final focusing section aligns the beam for entering the secondary beamline.

In order to produce a stable neutrino beam it is essential that the proton beam is well-tuned and precisely monitored. The primary beamline is equipped with several instruments for measuring the position, intensity, profile and loss of the beam. A set of 21 ElectroStatic Monitors (ESMs) surrounding the proton orbit oversee the beam centre position by measuring top-bottom and left-right asymmetry of the current induced by the beam on the electrodes. A set of 19 Segmented Secondary Emission Monitors (SSEMs) are used during beam tuning (and removed during beam operations since they cause beam losses) to monitor the beam profile by measuring the currents induced by the interactions of protons with titanium foil strips. A set of 50 Beam Loss Monitors (BLMs), which are proportional counters filled with a Ar-CO_2 gas, are installed at different places along the primary beamline to measure the beam loss. A set of 5 Current Transformers (CTs), which are 50-turns toroids around the beam pipe, monitor the beam intensity by measuring the current by the proton beam passing through the coils. The induced current is measured for each bunch and is converted into the number of protons in the spill.

The final CT, namely CT5, is located just before the protons reach the target, and it is used to determine the number of protons on target (POT) delivered. Fig. 2.4 shows the total POT delivered by the neutrino beamline since the start of the experiment. From March 2010 to March 2017, 2.045×10^{21} good POT has been delivered to the T2K target, of which 12.83×10^{20} good POT in neutrino running and 7.62×10^{20} good POT in anti-neutrino running. The analysis described in this Thesis only uses T2K Run II-IV which corresponds to 5.80×10^{20} good POT in neutrino running mode.

In the secondary beamline, the proton beam is guided onto a graphite target where kaons and pions are produced and then focused by magnetic horns to finally decay into neutrinos; after the decay tunnel a beam dump absorbs the non-neutrino products. The secondary beamline is then constituted of three parts, all contained inside a helium vessel at 1 atm: the target station, the decay volume and the beam dump. A schematic view of the secondary beamline is presented in Fig. 2.5.

The target station is separated from the primary beamline by a beam window and a baffle acting as a collimator to protect the horns. Just before the collision onto
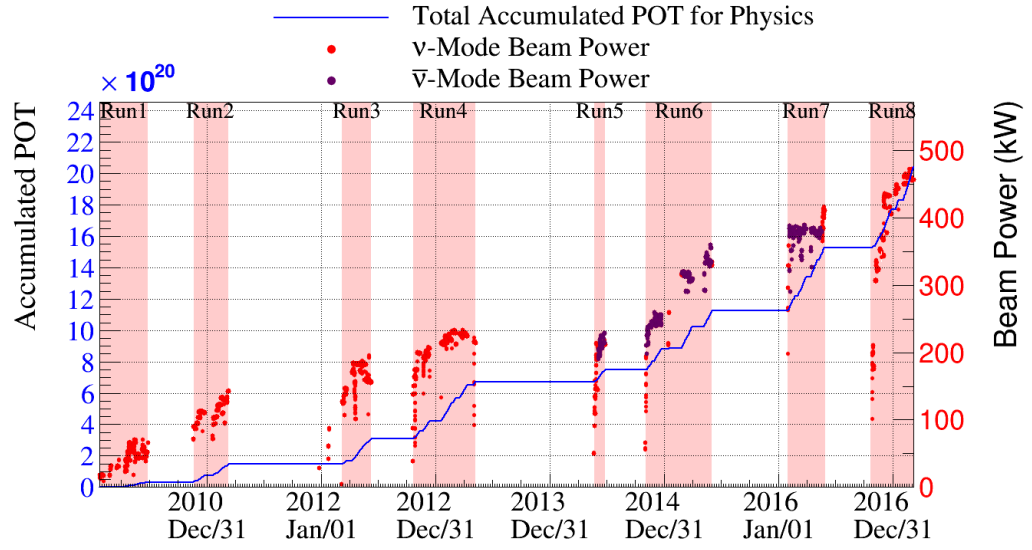
Figure 2.4: Accumulation of protons on target (POT) delivered to the neutrino beam line from January 2010 to March 4th, 2017 (Run I - Run VIII). The red and purple dots show the beam power during neutrino running and anti-neutrino running, respectively. The first long break is related to the damages from the 2011 Great Tohoku earthquake, the second long break was due to a radiation accident in the J-PARC hadron hall.
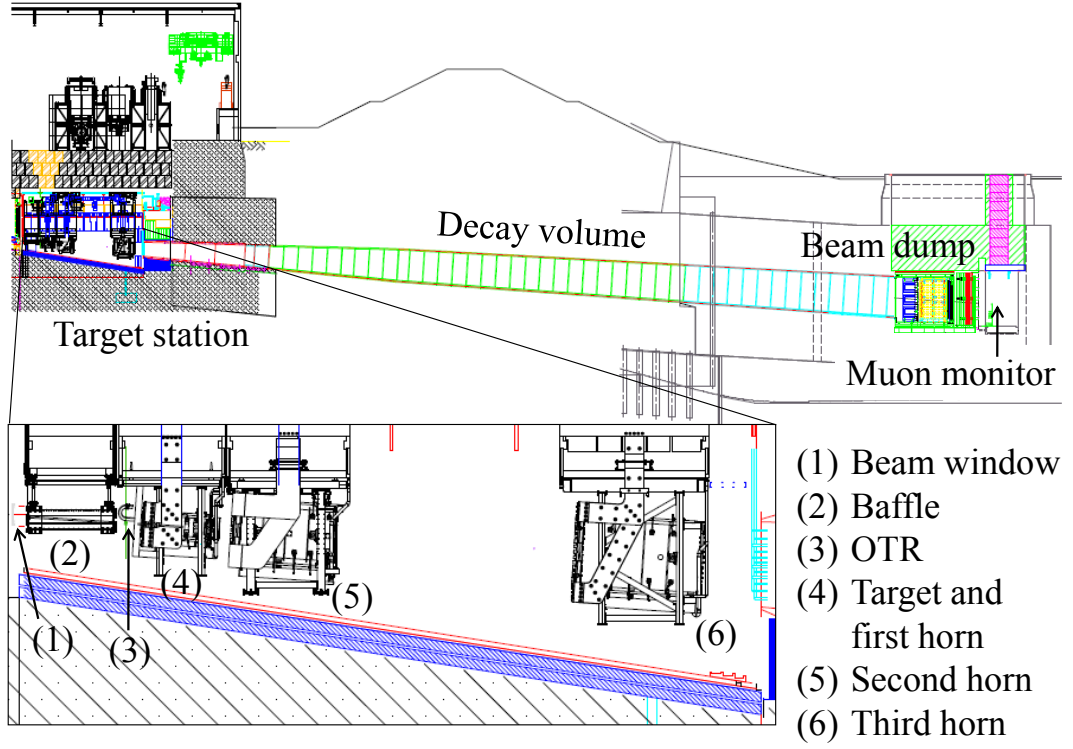
Figure 2.5: Schematic view of the T2K secondary beamline, divided in three sections: target station, decay volume and beam dump. The proton beam enters the target station and interacts with the graphite target. In neutrino beam mode, positive hadrons produced in the interaction are focused by the three horns and directed to the decay volume, where pions mainly decay into muons and muon neutrinos. At the end of the decay volume there is a beam dump made of graphite and iron plates.

784 the target, the proton beam is monitored by an Optical Transition Radiation monitor
785 (OTR). The target is composed of a graphite rod of 2.6 cm in diameter, 91.4 cm long
786 and 1.8g/cm^3 of density, surrounded by a graphite tube 2 mm thick and a 0.3 mm
787 titanium case. At the design beam power of 750 kW the temperature at the target
788 centre is expected to reach 700° C; helium gas is flown through the assembly to cool
789 the target.

790 Protons interacting with the graphite produce charged pions and kaons, which are
791 focused by three magnetic horns. Each horn consists of two coaxial conductors which
792 produce a toroidal magnetic field inversely proportional to the distance from the beam
793 axis. The charged particles are either focused or deflected depending on the charge
794 of the particle and the direction of the current. For Run I-IV T2K focused positive
795 hadrons and defocus negative hadrons, which lead to the production of mainly μ^+ and
796 ν_μ, for Run V-VII negative hadrons were focused and positive hadrons defocused, which
797 lead to the production of mainly μ^- and $\overline{\nu}_\mu$.

798 Hadrons travel through a decay volume, a 96 m long steel tunnel filled with helium.
799 The hadrons decay in flight producing neutrinos (or anti-neutrinos), mainly through
800 $\pi^+ \to \mu^+ \nu_\mu$. When T2K runs in neutrino mode, the majority of pions decay through
801 $\pi^+ \to \mu^+ + \nu_\mu$ producing a 93.3% pure ν_μ beam. The main backgrounds are the $\overline{\nu}_\mu$
802 (5.6%), which are produced by forward going π^- that are defocused ($\pi^- \to \mu^- + \overline{\nu}_\mu$),
803 and ν_e (1.1%), which are mainly produced by muon decay $\mu^+ \to e^+ + \overline{\nu}_\mu + \nu_e$. The
804 purpose of the helium, filling the vessel, is to reduce pion absorption and to suppress
805 the production of unwanted elements like tritium and NO_X. Fig. 2.6 (right) shows the
806 predicted flux at ND280 broken down by neutrino type.

807 At the end of the decay tunnel, closing the secondary beamline, there is a beam
808 dump which is constituted of a core of 75 tons of graphite and iron plates (3.2 meters of
809 graphite and 2.4 meters of iron) inside and outside the vessel. The beam dump absorbs
810 all the the hadrons, charged leptons and other by-products, except muons with energy
811 higher than 5.0 GeV which reach the muon pit.

812 ### 2.1.3   Muon Monitor

813 Behind the beam dump, there is a muon monitor (MUMON) that monitors the prop-
814 erties of the beam on a bunch-by-bunch basis by detecting the muons that were not

51
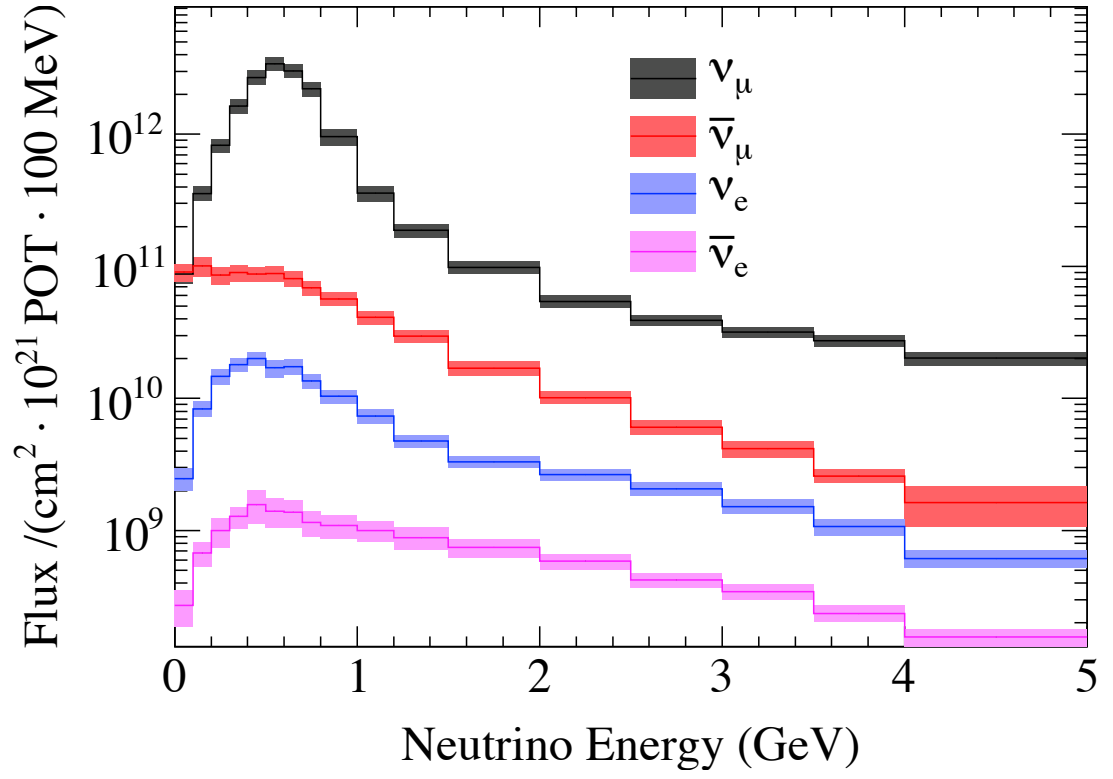
Figure 2.6: Expected T2K flux broken down by neutrino type composition.

815 absorbed (cf. [109]). Since muons are mainly produced along with neutrinos in the pion

816 two-body decay described through $\pi^+ \to \mu^+ \nu_\mu$, the measurement of the muon profile

817 centre (with a precision better than 3 cm) determines the neutrino beam direction (with

818 a precision better than 0.25 mrad), calculated as the direction between the target and

819 the centre of the muon profile. The MUMON also monitors the neutrino beam intensity

820 with a precision better than 3%. An emulsion tracker, composed of nuclear emulsion

821 films, is installed downstream of the muon monitor and measures the absolute muon

822 flux and the distribution of momenta of the muons via multiple Coulomb scattering.

823 2.1.4   Off-Axis Configuration

824 T2K is the first long-baseline neutrino oscillation experiment with an off-axis config-

825 uration. In the T2K beamline design the neutrino beam direction does not coincide

826 exactly with the direction to Super-Kamiokande, but forms an angle away from the

827 direction towards the far detector. Such off-axis angle can be adjusted from a mini-

828 mum of $\sim 2°$ to a maximum angle of $\sim 2.5°$. The T2K baseline and off-axis angle were

829 precisely measured by a GPS survey [95]: the measured distance from the graphite

830 target to the centre of Super-Kamiokande is 295335.2 ± 0.7 meters and the measured

831 angle is $2.504 \pm 0.004°$. With this off-axis technique, due to the kinematics of pion

832 decay, the neutrino energy spectrum at Super-Kamiokande presents a narrower band

833 (cf. [110]) and its high energy tail is minimised due to the reduction of the dependency

834 of the neutrino energy with the energy of the parent pion. This translates into a reduc-

835 tion of the high-energy unoscillated ν_μ background at the far detector which improves

836 the sensitivity to both ν_μ disappearance and ν_e appearance. Furthermore, the peak

837 neutrino energy is lower, which gives a lower intrinsic ν_e background. This effect is

838 illustrated in Fig. 2.7, in which the distributions are calculated with two-body decay

839 kinematics for different angles. The off-axis angle is chosen such that the peak of the

840 neutrino energy spectrum at Super-Kamiokande corresponds to the energy at which

841 the oscillation probability $P(\nu_\mu \to \nu_e)$ is maximised and the oscillation probability

842 $P(\nu_\mu \to \nu_\mu)$ is minimised: in this way the sensitivity for the oscillation parameters is

843 enhanced (Fig. 2.8).

844   For the T2K baseline of 295 km and assuming $\Delta m_{32}^2 = 2.4 \times 10^{-3} eV^2/c^4$, this energy

845 peak is around 600 MeV. Fig. 2.8, left side, shows the effect on the neutrino energy
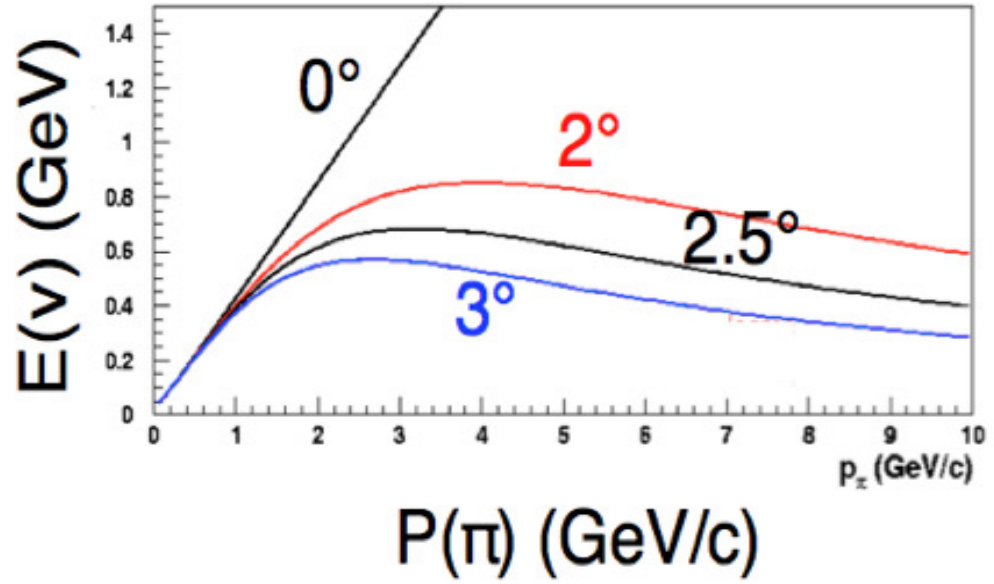
Figure 2.7: Neutrino energy versus parent pion momentum (two-body decay kinematics) for different off-axis angles: it shows that the dependency of the neutrino energy on the parent pion momentun is reduced using an off-axis angle. (cf. [111]).

54
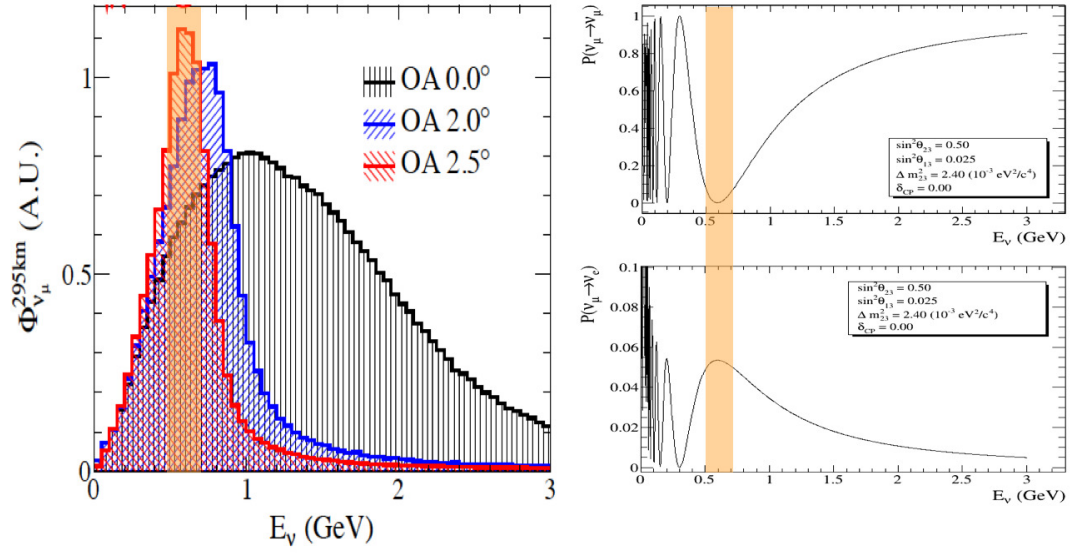
Figure 2.8: On the left, effect of an off-axis configuration on the neutrino energy spectrum for different off-axis angles: the neutrino energy spectrum is narrower for larger off-axis angles (cf. [112]). On the right: the maximum of the $P(\nu_\mu \to \nu_e)$ oscillation probability and the minimum of the $P(\nu_\mu \to \nu_\mu)$ oscillation probability lay both in an energy band around 600 MeV.

spectrum of an off-axis configuration for different off-axis angles: the neutrino energy spectrum becomes narrower for larger off-axis angles, increasing the flux at the peak, even though reducing the total integrated flux. The right side of Fig. 2.8 shows that with an off-axis angle of $\sim 2.5°$, the maximum of the $P(\nu_\mu \to \nu_e)$ oscillation probability and the minimum of the $P(\nu_\mu \to \nu_\mu)$ oscillation probability lay both in an energy band around 600 MeV.

The charged-current quasi-elastic (CCQE) interaction channel described by $\nu_l + n \to l + p$ (where $l = e^-$ or μ^-) is used in Super-Kamiokande and in ND280 to reconstruct the neutrino energy. This channel allows a full neutrino energy reconstruction through the formula (assuming that the target neutron is at rest):

$$E_\nu = \frac{(m_N - E_B)E_l - m_l^2/2 + m_N E_B - E_B^2/2 + (m_P^2 - m_N^2)/2}{m_N - E_B - E_l + p_l \cos\theta_l} \qquad (2.3)$$

where m_N, m_P and m_l are respectively the masses of the neutron, proton and lepton created in the neutrino interaction, E_B is the binding energy and E_l, p_l and θ_l are the energy, momentum and angle of the lepton. As shown in Fig. 2.9, the energy band at ~ 600 MeV for T2K, with an off-axis angle of $\sim 2.5°$, enhances the CCQE channel and reduces the backgrounds induced by neutrinos in the high energy tail of the beam (charged-current non quasi-elastic and neutral-current processes). On the other hand, some shape information is lost with the narrower beam as it can be observed in Fig. 2.8 by comparing the widths of the oscillation and the flux peaks. However, the important shape information for the oscillation analyses, around the oscillation maximum and minimum, is retained in the narrower beam, and improved with the more accurate energy reconstruction using CCQE events.
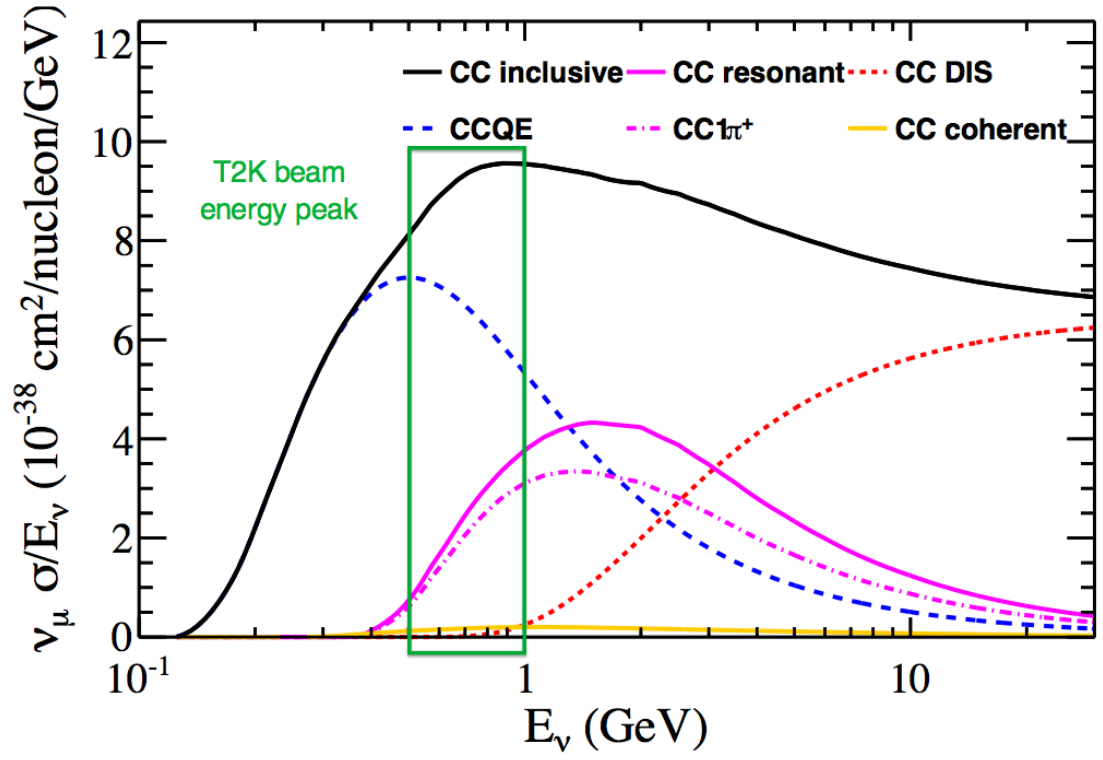
Figure 2.9: NEUT cross sections per nucleon for charged-current interactions of ν_μ on carbon as a function of neutrino energy, with the T2K energy band overlaid: the CCQE channel is enhanced and the backgrounds are reduced.

2.2 Super-Kamiokande, the Far Detector

Neutrino oscillations are measured at Super-Kamiokande (SK), the T2K far detector, after neutrinos have travelled a distance of 295 km. Super-Kamiokande is the largest land-based water Cherenkov detector in the world, located 1 km underground in the Mozumi zinc mine (Gifu prefecture), within the Kamioka Observatory. The 1000 meters of rock above the detector corresponds to 2700 meters of water equivalent, which reduce the rate of cosmic rays by about five orders of magnitude compared to that on the surface of the Earth.

Super-Kamiokande [113] is a cylindrical detector 42 meters high and with a diameter of 39 meters, filled with 50 kton of pure water. Its walls are covered with about 13,000 Photo-Multiplier Tubes (PMTs), which serve to image neutrino interactions. Fig. 2.10 shows the design and location of the Super-Kamiokande detector.
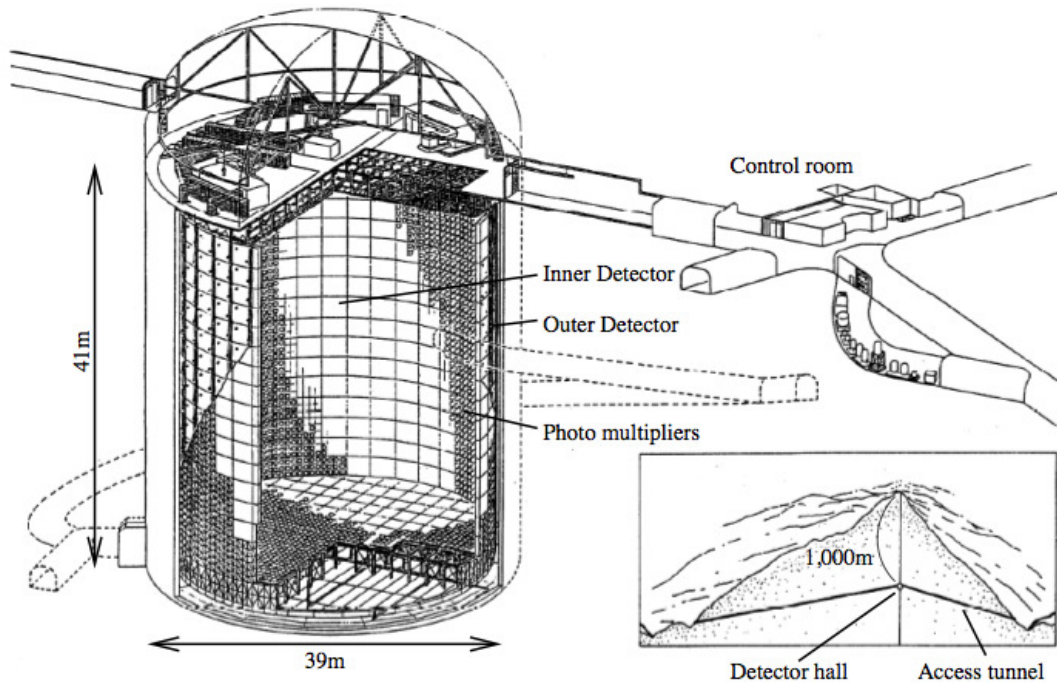
Figure 2.10: Design and location of the Super-Kamiokande detector, a cylindrical Cherenkov detector filled with 50 kton of pure water, instrumented with Photo-Multiplier Tubes (PMTs) covering its walls and placed 1 km deep within the centre of Ikenoyama mountain in the Kamioka Observatory.

Super-Kamiokande consists of two major volumes, an inner detector volume contained inside an outer detector volume (OD). These two volumes are separated by a cylindrical structure of about 50 cm of width, a stainless steel scaffold covered by plastic sheets that serve to optically separate the two volumes. The inner detector volume, 36.2 meters high and with 33.8 meters of diameter, incorporates in its walls 11,129 PMTs. The PMTs have a diameter of 50 cm and they are placed on a regular square grid with 71 cm step, providing an effective 40% PMT cathode surface coverage. The outer detector volume surrounds the inner one with a depth of 2 meters and is instrumented with 1,885 outward facing 20 cm diameter PMTs. The outer detector serves as an active veto counter against incoming particles, as well as a passive shield for neutrons and γ rays from the surrounding rocks. A set of horizontal and vertical Helmholtz coils reduces the Earth magnetic field to below 50 mG, such that the PMTs are not affected by it. In Fig. 2.11 is shown a schematic drawing of the two volumes, a picture of the inner detector and a picture of a PMT.
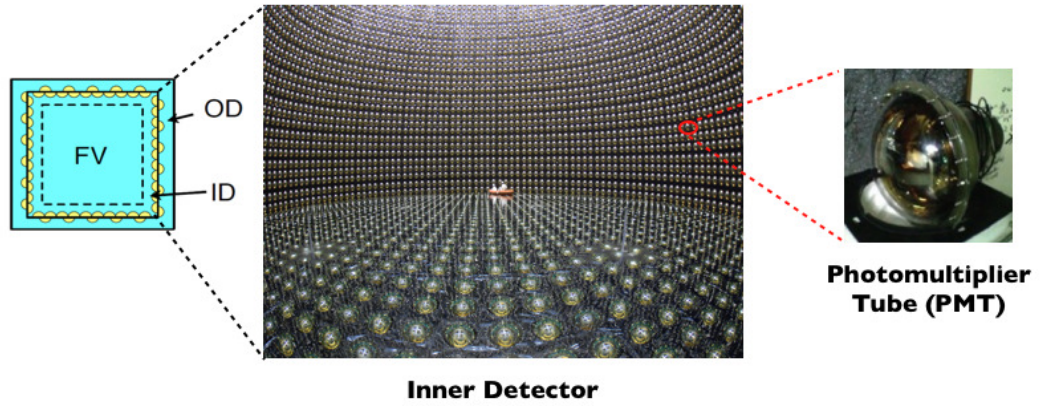
Figure 2.11: Schematic drawing of the division of Super-Kamiokande into inner and outer detector (left), picture of the inner detector (middle) showing the walls instrumented with PMTs and picture of one of the photo-tube (right).

The detector is located in a large cylindrical cavity with an hemispherical dome ceiling. In order to keep radon out of the area, the ceiling is covered by the so-called Mineguard, a spray-applied polyurethane membrane. Radon constitutes a significant background in low energy analysis (solar neutrinos), but it is less important for the

high energy analysis.

Water Cherenkov detectors use Cherenkov light [114] to detect the charged particles produced by CC interactions. When a charged particle travels faster than the speed of light in a medium, it polarises the molecules of the medium, which then turn back rapidly to their ground state, emitting prompt radiation (called Cherenkov radiation). The speed of light in a medium is c/n where c is the speed of light in vacuum and n is the refractive index of the material ($n \approx 1.33$ in water). At every point along the particle path, the emitted light forms a coherent wave front at an angle of $\cos\theta = 1/(n\beta)$, where $\beta = v/c$ with v speed of the particle in the medium, effectively forming a cone of light. For relativistic particles in water with $v = c$, the opening angle is $42°$. When charged particles with speed above c/n are created in neutrino interactions in Super-Kamiokande, they generate Cherenkov radiation as they cross the water filling. As the charged particles travel through the medium, they lose energy and stop emitting once the speed decreases below c/n. The Cherenkov photons reach the PMTs in the walls of the detector producing a ring-shaped hit pattern: the PMTs act as imaging pixels, detecting the light and giving information about the vertex position, the type of charged particles and their momenta. A particle identification (PID) likelihood can be used to distinguish electrons and muons looking at the charge collected in the hit PMTs, the timing and the patterns: while muons generate a single ring with a well defined shape, electrons undergo multiple-scattering producing a fuzzy ring. The e/μ separation is quite net: less than 1% of muons are mis-identified as electrons. With this information, charged-current quasi-elastic (CCQE) interactions for muon neutrinos and for electron neutrinos can be distinguished and compared to the expected ones to measure the neutrino oscillations.

Super-Kamiokande has been running since 1996 over four running periods:

- SK-I, April 1996 - July 2001, ended with an accident that destroyed most of the photo-tubes;

- SK-II, December 2002 - October 2005, started after a year of rebuilding the detector, with half of the previous tube density;

- SK-III, October 2006 - August 2008, with restored full photo-tube density;

- SK-IV (current), from 2009, including the T2K experiment and with upgraded PMT readout electronics and data acquisition that allow a higher data processing rate.

Super-Kamiokande has studied oscillations in atmospheric, solar and accelerator-produced neutrinos: it confirmed the solar neutrino deficit [115], provided the first strong evidence of oscillation in atmospheric neutrinos [116] for which the 2015 Nobel Prize in Physics was awarded to Takaaki Kajita, and verified the oscillations in an accelerator-produced beam (K2K experiment [117]). Moreover, it has performed studies on the proton decay, setting limits on partial lifetimes for processes such as $p \rightarrow e^+\pi^0$ and $p \rightarrow \bar{\nu}K^+$ [118, 119].

2.3   Near Detectors

In order to study neutrino oscillations between the production point and the far detector, it is essential to characterise the unoscillated beam with a precise measurement of the neutrino energy spectrum, the flavour content and the interaction rates before oscillating. In the T2K experiment, these measurements are performed by a set of detectors located in a facility at 280 m from the target station. There is an on-axis detector (INGRID) and an off-axis detector (ND280) as shown in Fig. 2.12. Both are in a pit, ND280 is about 24 m below the surface and INGRID is just below. The ND280 detector is actually composed of many sub-detectors and is described in Chapter 3: the analysis of this thesis is based on data acquired with ND280.

2.3.1   INGRID, the On-Axis Detector

Interactive Neutrino GRID (INGRID) is the on-axis near detector, located at 280 m from the target. The main purpose of INGRID is to monitor the neutrino beam rate, profile, and centre, by detecting neutrino interactions in iron. INGRID is composed of 14 identical modules arranged in two identical groups of 7 modules, one along the horizontal axis and one along the vertical axis, forming a cross, with 2 extra off-diagonal modules, as shown in Fig. 2.13. With this structure, INGRID is designed to sample the beam in a transverse section of 10 m × 10 m, sufficiently covering the neutrino
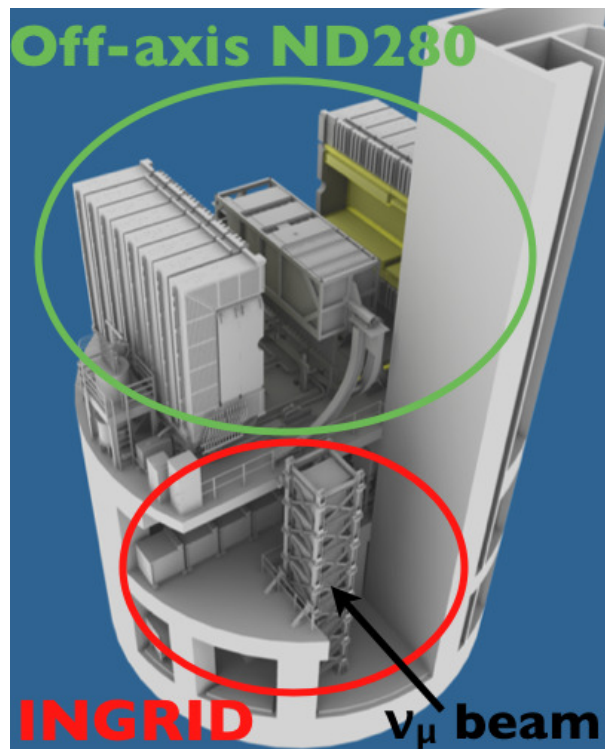
Figure 2.12: The near detector facility located 280 m from the target station: the off-axis detector ND280 is located in the upper level (about 24 m below the surface); the on-axis detector INGRID is located on the level below (about 33 m deep for the horizontal modules).

beam profile. The centre of the INGRID cross coincides with the centre of the neutrino beam, defined as 0° with respect to the proton beamline.
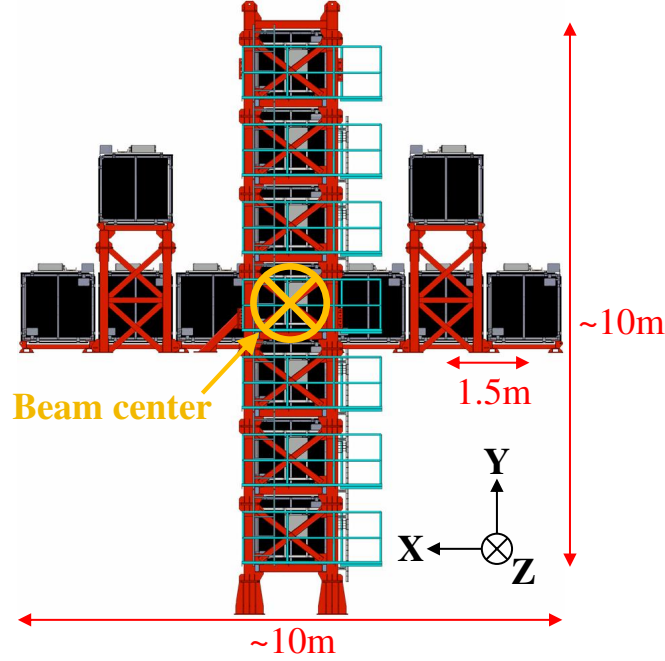
Figure 2.13: Schematic view of the INGRID on-axis detector: the centre module of the vertical row and of the horizontal row corresponds to the neutrino beam centre.

Each module consists of eleven tracking scintillator planes interleaved with nine iron target plates. Fig. 2.14 shows a drawing of one INGRID module (left side), where the blue planes are the iron layers and the greys are the tracking planes. The ensemble of iron and scintillator planes is surrounded by veto scintillator planes to reject charged particles that enter the modules from outside (Fig. 2.14, right side). Each iron plate is a square of 124×124 cm^2 and 6.5 cm thickness, with a total of 7.1 tons of iron mass serving as neutrino target per module. Each tracking plane is composed of 24 scintillator bars in the horizontal axis and 24 in the vertical axis. Scintillation light produced by muons from charged-current interactions is collected from each bar and transported to a photo-detector with a wavelength shifting fibre (WLS fibre). The light is read out by a Multi-Pixel Photon Counter (MPPC) attached to an end of the WLS fibre. Tracking scintillator layers in alternating orientations enable 3D reconstruction of the muon paths.

An extra special module, called Proton Module, is located between the central module of the horizontal group and the central module of the vertical group. This module is composed of 34 scintillator planes (without iron) which allow 3D tracking of low energy particles. Detecting low energy particles, as protons, allows a better understanding of the neutrino interactions in INGRID, and consequently of the neutrino beam properties.
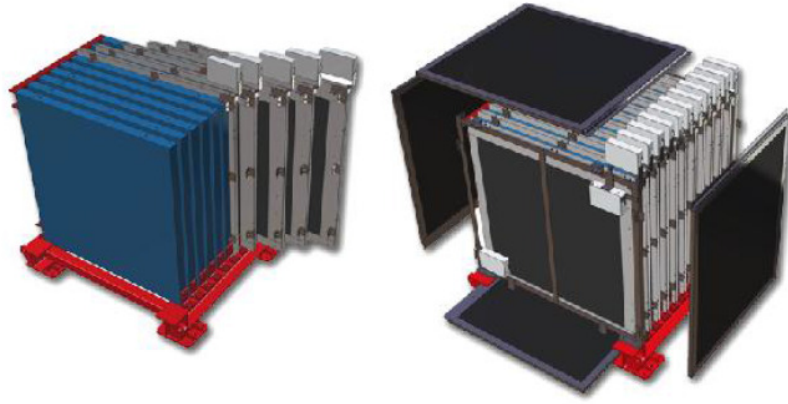
Figure 2.14: Drawings of an INGRID module (left side): eleven tracking scintillator planes (blue) interleaved with nine iron plates (grey). The ensemble of iron and scintillator planes is surrounded by veto scintillator planes (right side, black).

A typical neutrino event in the INGRID detector is shown in Fig. 2.15: the neutrino enters from the left, interacts in the Proton Module (left module) producing charged particles whose tracks are shown as red circles (different sizes depending on the strength of the generated signal); the green lines are scintillator planes, the blue lines are veto scintillator planes and the grey boxes are the iron plates; the long track exiting the Proton Module corresponds to a muon while the short one corresponds to a proton.

The beam centre is measured counting the number of observed charged-current neutrino events in each module (identified by detecting muon tracks). The precision of the measurement of the beam centre is better than 10 cm (0.4 mrad precision), defined by the systematic error due to the uncertainty on the neutrino event rate, and stable within the statistical error of ~ 2 cm. The observed profiles (number of events versus position from the INGRID centre) in the x and y directions are fitted with Gaussian
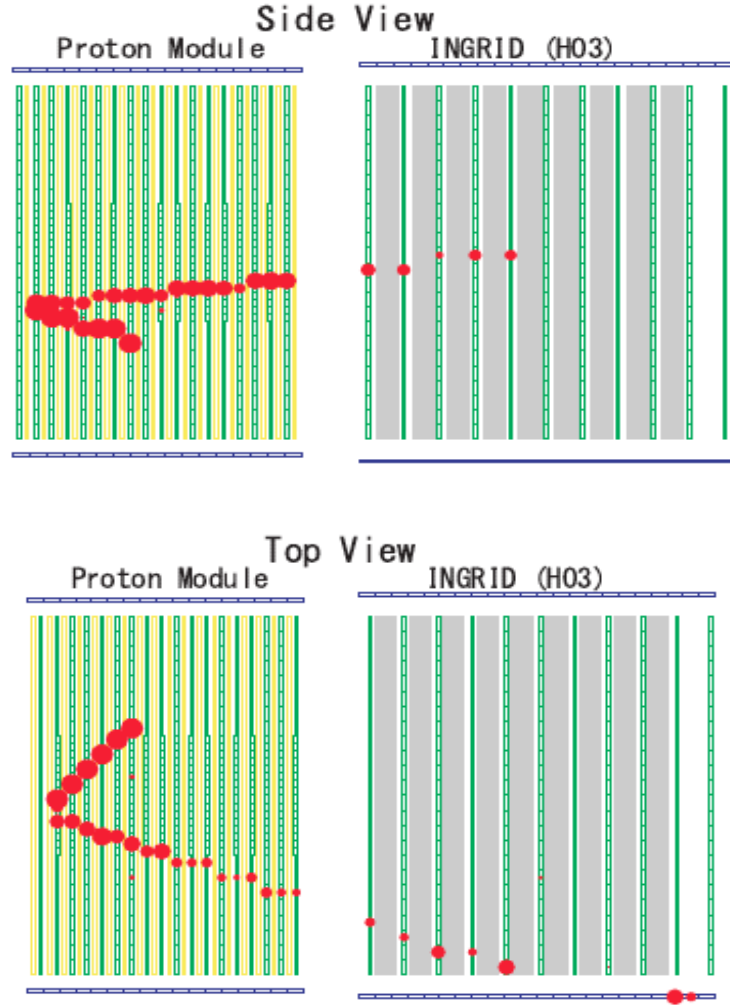
Figure 2.15: Typical neutrino event in the INGRID detector: the neutrino enters from the left, the interaction happens in the Proton Module (left module), producing charged particles whose energy deposition is shown as red circles.

functions, and the beam centre is defined as the peak of the fit. The two modules off the main cross are used to check the axial symmetry of the neutrino beam. Cosmic ray data and beam data were used for the calibration of the INGRID detector. INGRID measurements shows that the neutrino beam intensity and direction have always been stable along the different data taking periods. More details about the performance, calibration and simulations for INGRID can be found in [120].

3

The Off-Axis Near Detector: ND280

3.1   ND280 in T2K Oscillation Analyses

The neutrino event rate observed at Super-Kamiokande depends on the oscillation probability, the neutrino flux, the neutrino interaction cross-section, and the detection efficiency. The model of the neutrino flux, the cross-section and the detection efficiency need to be well understood to reach high sensitivity in the oscillation measurements. In fact the largest contributions to the error of the oscillation analyses come from the knowledge of the flux at SK and from the theoretical cross-section parameters used in the simulation model. The neutrino cross-section model must include the dependence on the neutrino energy, the kinematics of the outgoing lepton, and the kinematics of final state hadrons.

Several ν_μ CC samples from the ND280 detector are currently used in a fit to the T2K oscillation model, separately for neutrino beam runs and anti-neutrino beam runs. The samples from the ND280 detector are selected by looking at the particles leaving the nucleus:

- The $CC0\pi$ sample requires one muon, no pions, any number of nucleons in the final state. This sample is enhanced in the CCQE interactions.

- The $CC1\pi^+$ sample requires one muon, one positive pion, any number of nucleons in the final state. This sample is enhanced in the CCRES interactions.

- The *CCother* sample requires one muon, at least one negative pion or at least one neutral pion or more than one positive pion, and any number of nucleons in the final state. This sample is enhanced in the "inelastic" interactions.

These samples are selected in the tracker of ND280 where there are both water and scintillators as target volumes, hence an uncertainty needs to be considered to account for the fact that in Super-Kamiokande there is only water. Furthermore, SK has a 4π coverage, while these samples only consider interactions with forward muons: future improvements of this fit will include other samples to increase the coverage.

3.2 The ND280 Design

ND280 is the off-axis near detector, located at $280\,\mathrm{m}$ from the target and 2.5° off-axis. It serves to characterise the neutrino beam before the oscillations, by measuring the energy spectrum and the flavour composition of the neutrino beam, and by providing measurements of the different interaction channels.

Fig. 3.1 shows the sub-detectors that compose ND280. The ND280 tracker volume contains two Fine-Grained Detectors (FGDs [121]) which are used as the neutrino interaction target, sandwiched between three gaseous Time Projection Chambers (TPCs [122]) which are used to track charged particles. Upstream of the tracker there is a π^0 Detector (PØD [123]), consisting of scintillator, water and brass layers. As the FGDs, also the PØD is an active target mass, and it is optimised to reconstruct neutral pions. Both the tracker and the PØD detector are inside a metallic container (*basket*) with dimensions of 6.5 m $\times$ 2.6 m $\times$ 2.5 m. The Electromagnetic Calorimeter (ECal [124]), made of layers of lead and scintillator bars, surround the tracker and the PØD. The refurbished UA1/NOMAD magnet surrounds the entire detector to create a uniform magnetic field of $0.2\,\mathrm{T}$. Plastic scintillators in the magnet return yoke form the Side Muon Range Detectors (SMRDs [125]). The coordinate convention is also indicated in Fig. 3.1: the y axis is vertical and the x and z axes are in the horizontal plane. The origin is at the centre of the magnet and the magnetic field is along the $+x$ direction. The z axis is the direction to SK projected onto the horizontal plane.
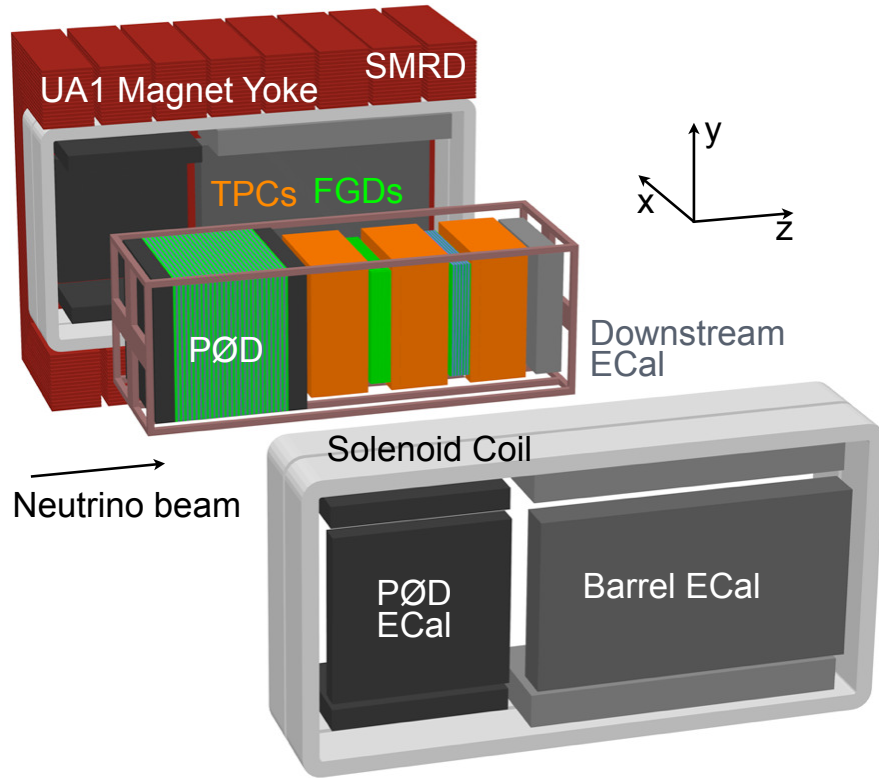
Figure 3.1: Exploded view of the ND280 sub-detectors: the PØD detector, optimised to reconstruct neutral pions; the tracker composed of time projection chambers (TPCs) interleaved with fine-grained detectors (FGDs); the Electromagnetic Calorimeters (ECal) surrounding the basket which contains the tracker and the PØD; the refurbished UA1/NOMAD magnet with the side muon range detector (SMRD) inserted in its air gaps.

3.2.1 Tracker

The three TPCs interleaved with the two FGDs form the ND280 tracker, designed to study charged and neutral-current neutrino interactions and optimised to measure charged-current quasi-elastic (CCQE) processes, which are the dominant at the T2K neutrino beam energy and which is the channel that allows an exact kinematic reconstruction of the neutrino energy. The ND280 tracker is therefore the key element to reconstruct tracks of charged particles, such as the outgoing muon, their momenta, angles and vertices.

Fig. 3.2 shows the event display of a candidate neutrino interaction occurred in FGD2, where two reconstructed tracks originate from the same vertex in FGD2 and go through TPC3 and the ECal detector. In Fig. 3.3 the signature of a muon track crossing all the different ND280 sub-detectors can be appreciated, it enters via the upstream side of the P∅D, continues through the tracker (TPCs and FGDs) and interacts producing secondary particles in the last TPC, which are then stopped in the ECal detectors.

| Event number : 23394 | Partition : 63 | Run number : 4173 | Spill : 0 | SubRun number :5 | Time : Sat 2010-03-20 06:45:45 JST |Trigger: Beam Spill
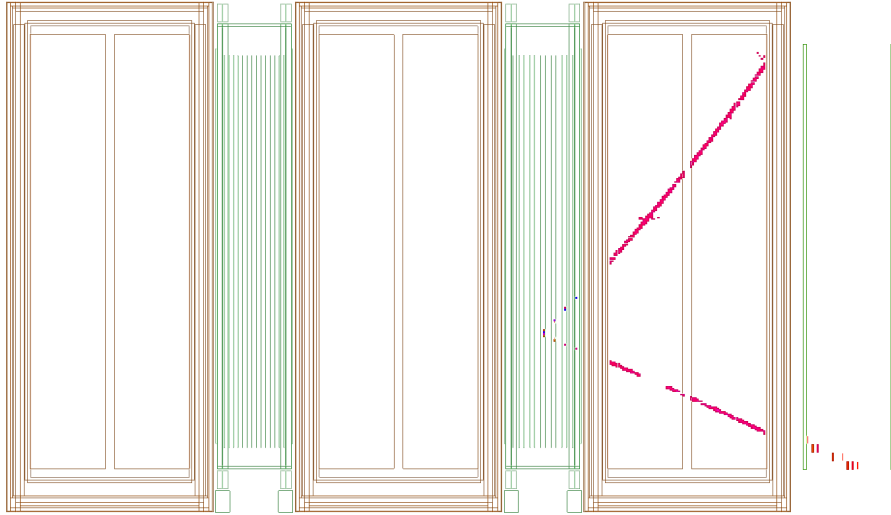
Figure 3.2: Event display of a candidate neutrino interaction occurred in FGD2, where two reconstructed tracks originate from the same vertex in FGD2 and go through TPC3 and the ECal detector.
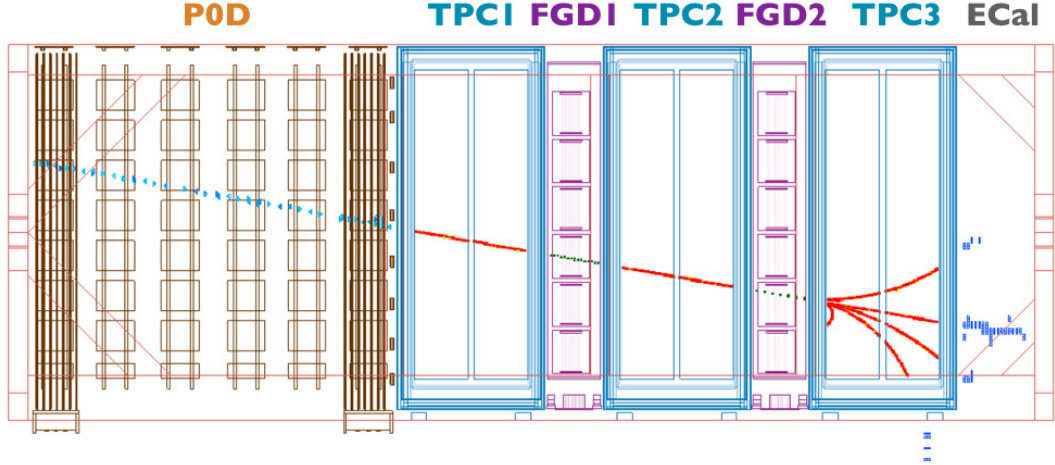
Figure 3.3: Example of event display where a muon track crosses the different sub-detectors composing ND280: it enters via the upstream side of the P∅D, continues through the tracker (TPCs and FGDs) and interacts producing secondary particles in the last TPC which are stopped in the ECal detectors.

3.2.1.1 Fine-Grained Detectors (FGDs)

There are two Fine-Grained Detectors (FGDs) in the inner part of the ND280 detector, placed in between the three TPCs. The two FGDs have the same overall geometry, the same mounting and the same readout technologies. The most upstream FGD, namely FGD1, primarily consists of extruded polystyrene scintillator bars (5760 in total), CH (1%-doped with $C_{15}H_{11}NO$): most of the interactions in FGD1 are on carbon nuclei. 192 scintillator bars ($1x1x186\,\mathrm{cm}^3$ each) are glued together to form a layer. The layers are oriented perpendicularly to the beam direction, alternately in the x and y direction (*X layers* and *Y layers*), allowing 3D tracking of charged particles. Every X layer is glued to an Y layer to form a stand-alone *XY module* of about $2\,\mathrm{cm}$ of width, along the beam direction, and about $2\,\mathrm{m}$ of height and $2\,\mathrm{m}$ of depth, orthogonal to the beam direction. FGD1 is composed of 15 XY modules, providing a target mass of $1.1\,\mathrm{ton}$.

The downstream FGD, namely FGD2, has a similar structure, but its 7 XY modules are interleaved with 6 water layers to allow the measurement of neutrino interactions on water. The width of each water module is about $2.8\,\mathrm{cm}$. The water layers are non-active target materials, but when a charged-current interaction occurs, the outgoing charged

lepton is tracked in the scintillator layers. As the far detector is a water Cherenkov detector, the cross-sections on water are extremely important to be understood. By comparing interaction rates obtained in the two FGDs, a subtraction method can be used to determine the cross sections separately on carbon and water [126].

A schematic drawing of the layer structure of the two FGDs is shown in Fig. 3.4.
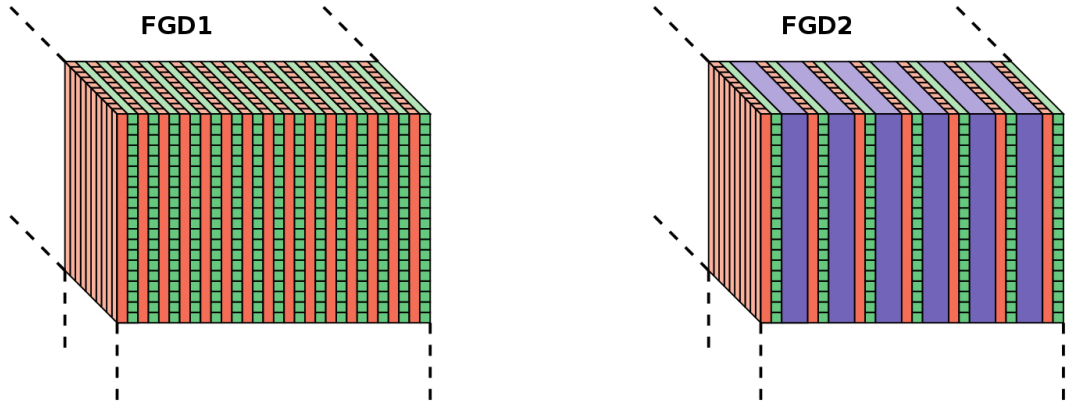
Figure 3.4: Schematic drawing of the layer structure of the two FGDs: in red the vertical bars that form the X layers, in green the horizontal bars that form the Y layers, and in blue the water layers. The neutrino beam goes from left to right.

Each scintillator bar has dimensions $9.61\,\mathrm{mm} \times 9.61\,\mathrm{mm} \times 1864.3\,\mathrm{mm}$, and has a hole (1 mm wide) in the middle where a Wave-Length Shifting (WLS) fibre is inserted. The emission spectrum of the plastic scintillator is centred at 420 nm, the WLS fibre has an absorption spectrum centred at 430 nm, and the WLS fibre emission spectrum is centred at 476 nm. The small overlap between the emission and absorption spectra creates a small self-absorption as the light travels along the fibre. One end of the fibre is attached to an MPPC (Fig. 3.5), and the other end is coated with aluminium to form a mirror.

The MPPC consists of 667 individual pixels covering an area of $1.3 \times 1.3\,\mathrm{mm}^2$. Each pixel in its detection surface is treated as a binary (i.e. hit or not-hit) element that is insensitive to the incident amplitude in that particular pixel. When a photon from the fibre strikes a pixel, an avalanche is created and the signal is counted. The MPPC signal is a linear sum of the number of fired pixels. The size of the signal depends on the over-voltage applied to the MPPC, and a careful calibration is required
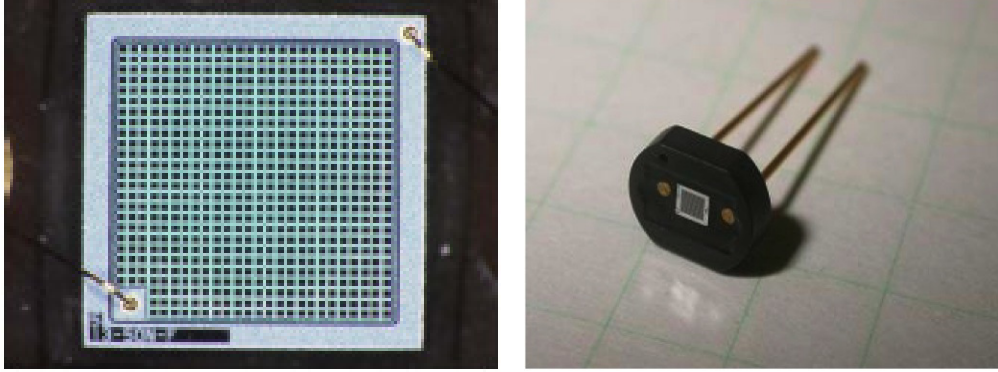
Figure 3.5: Photographs of a 1.3×1.3 mm^2 MPPC and the packaging in which it is mounted.

to normalise the response of each bar to the same level. Individual pixels can generate a signal when there is no incident photon, this is called "dark noise", and it is ignored when trying to reconstruct particle tracks. An example signal demonstrating the single photon resolution of a standard MPPC is shown in Fig. 3.6.
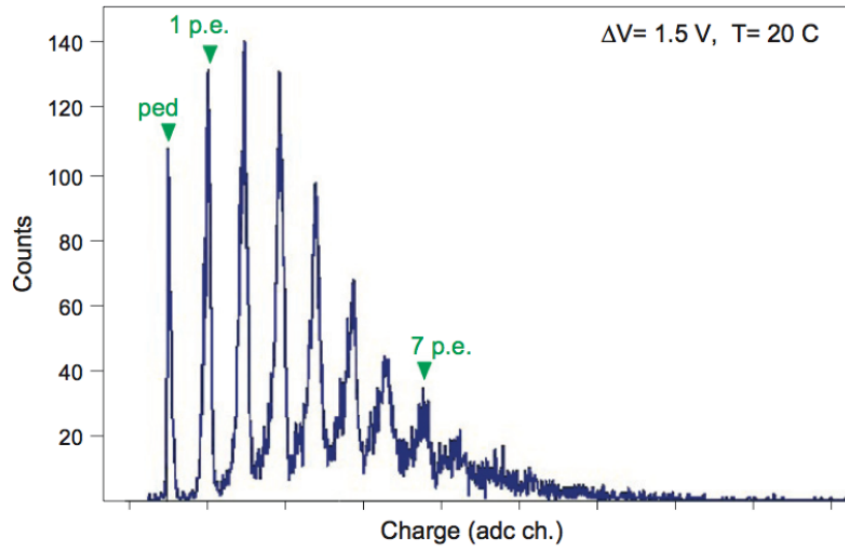
Figure 3.6: MPPC performance: example of charge amplitude spectrum measured with an LED source demonstrating the single photon resolution of MPPCs.

Each FGD is inside a light-tight dark box where the readout electronics are mounted. The width of each FGD in the beam direction is 33 cm, hence most of the penetrating particles produced in neutrino interactions, especially muons, pass through the TPCs. The fine granularity of the FGDs allows to resolve individual tracks of short-ranged particles, such as recoil protons, although the analysis of this Thesis does not use them.

In addition, the energy loss in the FGD scintillator bars can be used to identify the particle creating a track stopping in an FGD: comparing the measured total energy deposited by a particle for a given range in the FGD to the theoretical expected curves, muons, protons and pions can be distinguished. This is shown in Fig. 3.7, where the deposited energy distribution as a function of the range for particles stopping in FGD1, calculated with T2K Run1-2 data, is compared to the expected curves from MC for protons, muons and pions, using neutrino beam (left) and cosmic rays data (right) [127].
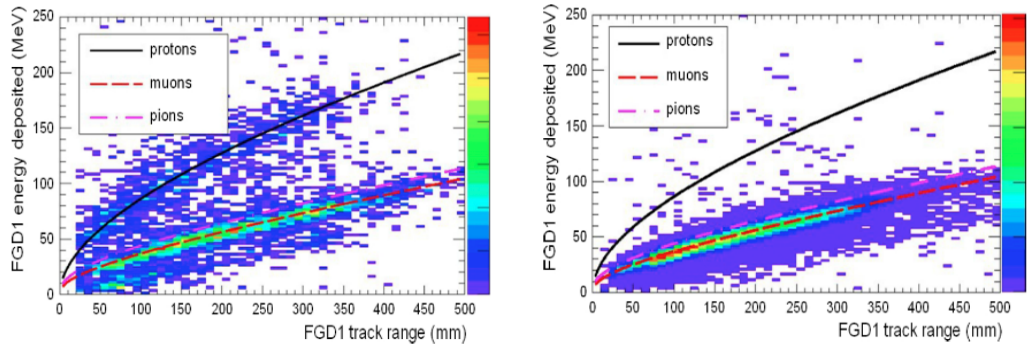
Figure 3.7: Example of the deposited energy distribution calculated with T2K Run1-2 data as a function of the range for particles stopping in FGD1, compared to the expected curves calculated with MC for protons, muons and pions, using neutrino beam data (left) and cosmic rays data (right).

Studies for Michel electrons have been performed in the FGDs. Low energy muons which stop in the FGDs are likely produced in pion decays. When the muon stops, it decays into an electron (Michel electron), which produces a signal, delayed with respect to the initial neutrino interaction. The identification of Michel electrons is important to detect events with pions, in order to measure the rate of CC1π interactions. The Michel electron tagging efficiency, computed with cosmic rays, is estimated to be $\sim$61% for MC and $\sim$58-59% for data (more details can be found in References [127, 128]).

See Reference [121] for more information on the FGDs.

3.2.1.2   Time Projection Chambers (TPCs)

The excellent imaging capabilities of the TPCs makes them a tool for the event reconstruction.

Each of the three ND280 TPCs consists of an inner box that holds an argon-based drift gas contained within an outer box that holds CO_2 as an insulating gas (provides the electrical insulation between the inner box and ground, and excludes atmospheric oxygen from entering the inner volume). The drift gas mixture is $Ar:CF_4:C_4H_{10}$ in 95:3:2 proportions of volumes and it was chosen for its high drift speed, its low diffusion and its good performance with MicroMEGAS (MM) detectors. A gas system connected to the TPCs is designed to maintain a stable mixture in the inner volume and a positive pressure with respect to the outer volume. An electric field parallel to the $0.2\,T$ magnetic field is created from a central vertical cathode at -25 kV to the anodes at each side of the TPC. Copper strips on the inner box walls pattern a field cage which shapes a uniform electric field in the active drift volume. When a charged particle travels through the TPC it ionises the gas and the ionised electrons drift to the anodes. Each inner side facing the cathode is instrumented with 12 MicroMEGAS modules [129] (MM) which amplify and sample the signal from the drifting electrons before being recorded. A schematic drawing of the TPC structure is presented in Fig. 3.8.

The MicroMEGAS modules are arranged in two vertical columns with a small offset between them so that inactive regions are not aligned. Each MicroMEGAS module is divided into 1728 pads ($7.0\,mm \times 9.8\,mm$) arranged in 48 rows and 36 columns. Before installing the TPCs, a dedicated test bench was designed and operated at CERN to characterise the MM modules, i.e. to build a gain map of each MM and to measure their energy resolution. It consisted of a small drift chamber with a MM implemented on one side and a cathode on the other side. An automated X-Y scanning system allowed to measure the response of individual pads when illuminated by a collimated ^{55}Fe source ($185\,MBq$).

Each drift time measurement is triggered by signals from all the other sub-detectors.Some monitor chambers in the ND280 facility are continuously monitoring the gas entering and exiting the TPCs, measuring the drift velocity and the gas amplification.

75
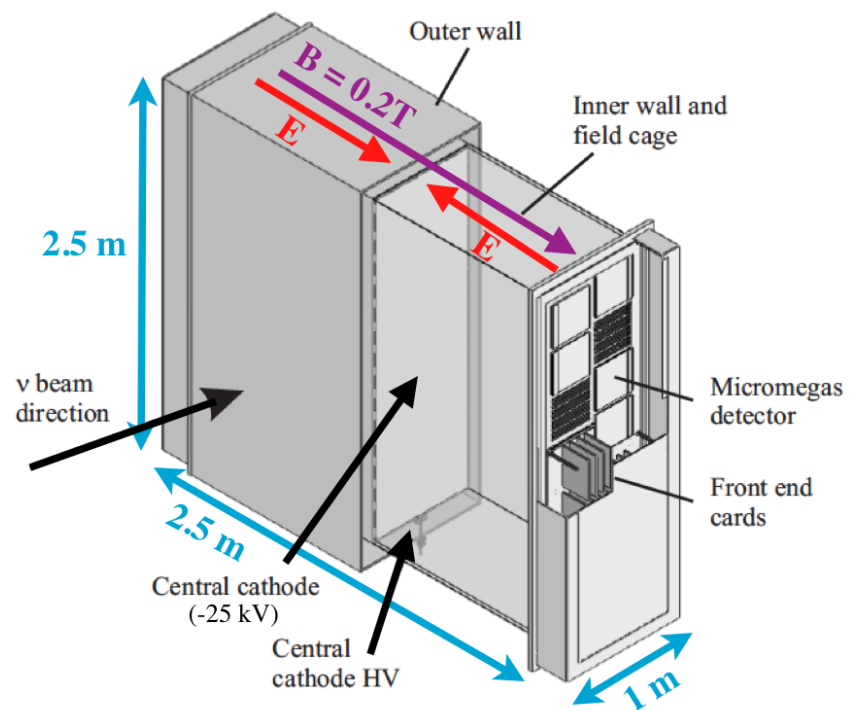
Figure 3.8: Schematic drawing of the TPC structure. The cathode is in the middle of each TPC and ionisation electrons drift to the anodes on the side.

1147   The TPCs provide excellent tracking, since it can provide 3D hit position, whereas

1148   the FGD can only provide alternating xz and yz information: the MM pads give the

1149   hit position in the yz plane, and the x coordinate is determined by the time difference

1150   between the hits. The spatial resolution of the TPCs depends on the drift distance and

1151   it is always lower or ≈ 1 mm. Determining precisely the number of charged particles and

1152   their directions allows the selection of samples of different neutrino interactions with

1153   a very high purity. The curvature due to the magnetic field provides measurements of

1154   the particle momentum and charges. The momenta can then be used to measure the

1155   event rate as a function of the neutrino energy for the different neutrino interaction

1156   processes. The relative momentum resolution of the TPCs is 0.1 $p_T/(GeV/c)$. Particle

1157   identification is also possible: different charged particles can be distinguished combining

1158   the measured momenta with the amount of energy deposited by the ionisation of each

1159   particle. The resolution of the deposited energy for minimum ionising particles is

1160   7.8±0.2% and it allows distinguishing muons from electrons.

1161   See Reference [122] for more information on the TPCs.

3.2.2   Pi-Zero Detector (P∅D)

1162

1163   The Pi-zero Detector (P∅D) is located inside the magnet, upstream of the tracker. The

1164   active volume of the P∅D consists of structural elements called P∅Dules: they are made

1165   of two perpendicular arrays of doped polystyrene triangular scintillator bars, one in the

1166 x direction and one in the y direction, which are sandwiched between sheets of high-

1167   density polyethylene forming a plane. Each bar is read out by a WLS fibre attached to

1168   MPPC photosensors, Between the P∅Dules there are lead and brass sheets, and water

1169   bags which can be filled and emptied.

1170   The P∅D has been optimised for π^0 detection and its main goal is to precisely

1171   measure the neutral-current process $\nu_\mu + N \rightarrow \nu_\mu + N + \pi^0 + X$. An accurate mea-

1172   surement of the cross section for this process is of high importance because events

1173   containing π^0's are one of the main backgrounds of the $\nu_\mu \rightarrow \nu_e$ appearance signal at

1174   Super-Kamiokande. As the P∅D operates with the water target bags filled or emptied,

1175   a subtraction method can be used to determine the cross section for the neutral-current

1176 π^0 interactions on water [130].
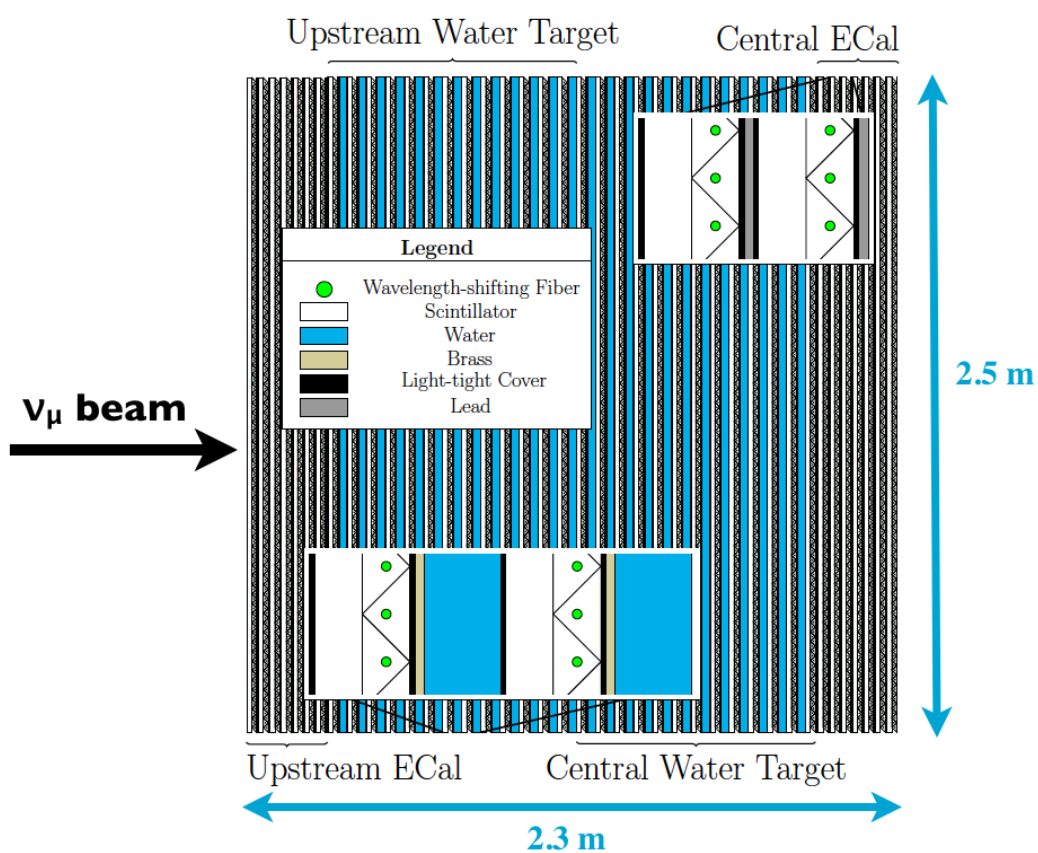
Figure 3.9: Schematic view of the P∅D design. The beam direction is left to right.

The PØD detector has been calibrated using minimum ionising particles from cosmic ray muons. More details about its design, performance and calibration can be found in Reference [131].

3.2.3 Electromagnetic Calorimeter (ECal)

The ND280 Electromagnetic Calorimeter consists of layers of plastic scintillator bars, serving as active material, interleaved with lead absorber sheets. It uses the same scintillator technology as the FGDs, but the granularity is coarser: each bar is $1\,\text{cm}\times4\,\text{cm}$, and the lead sheets are $1.75\,\text{mm}$ thick. The ECal plastic scintillator bars are made of doped polystyrene and they are read by WLS fibres connected to one or two MPPCs depending on the length of the bar. The lead layers are used to contain electromagnetic showers and to increase the probability for a photon conversion. The ECal provides a near-hermetic coverage for the particles exiting the inner detector volume, which includes the PØD, the TPCs and the FGDs. The ECal can also provide complementary information and additional particle identification for regions of phase space where the TPC cannot distinguish between particles.

The ECal is composed of 13 independent ECal modules separated in 3 groups arranged as shown in Fig. 3.1: six PØD-ECal modules surround the PØD detector and six Barrel-ECal modules surround the tracker volume, covering the four sides parallel to the neutrino beam axis; one downstream module (Ds-ECal) covers the downstream exit of the tracker volume. On top and bottom the modules are split in two following the magnet division in two halves, to allow the opening and access to the inner sub-detectors. The 6 Barrel-ECal modules consist of 32 layers each for a total thickness of 9.7 radiation lengths ($9.7\,X_0$). The bars running on the z direction are read out by two MPPCs at the end of the fibre; the other bars are much shorter and are read out by one MPPC, with the other end coated with aluminium to form a mirror. The Ds-ECal consists of 34 layers for a total thickness of $10.6\,X_0$, and each bar is read out by two MPPCs. A drawing of a completed module is shown in Fig. 3.10.

The ECal energy resolution is 10% for particles with momentum higher than $1\,\text{GeV}$, 10-15% for particles with momentum 0.5-$1\,\text{GeV}$, and 15-20% for particles with momentum lower than $0.5\,\text{GeV}$.
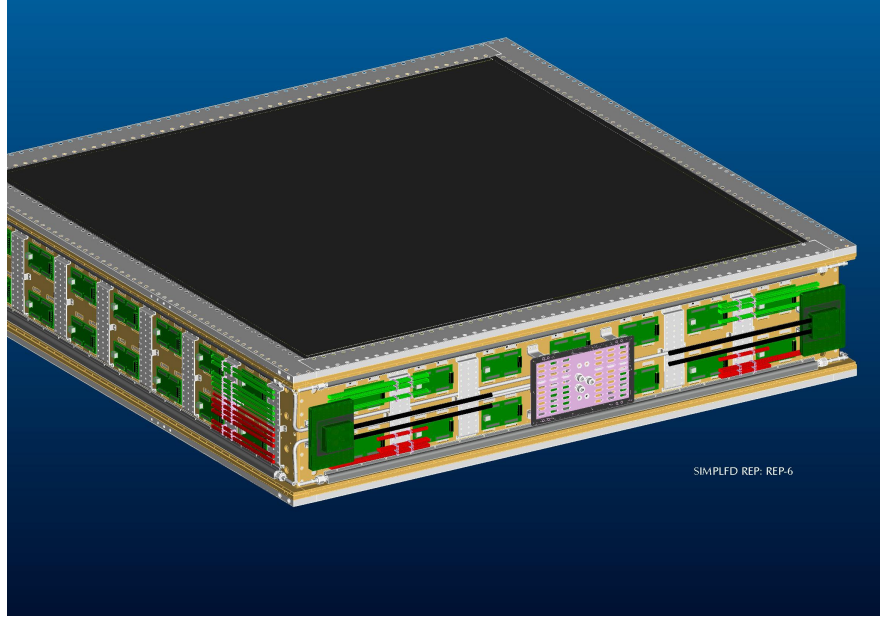
Figure 3.10: External view of one ECal module.

The main goal of the ECal is the detection of photons, primarily from π^0 production, and the measurement of their energy and direction: the ECal is a key element in the reconstruction of neutral pions produced in neutrino interactions in the tracker.The PØD-ECal serves as a veto for entering particles and complements the PØD reconstruction with information on escaping energy, detecting muons and photons exiting the PØD without being reconstructed. The ECal detector also provides information on charged particles, complementing the TPC dE/dx particle identification to distinguish electrons, muons and pions.

See Reference [124] for more information on the ECal.

3.2.4 UA1 Magnet and Side Muon Range Detector (SMRD)

The off-axis ND280 detectors are enclosed by the refurbished CERN UA1/NOMAD magnet. This magnet consists of two mirror-symmetric halves composed of water-cooled coils made of aluminium bars and a return yoke which serves as mechanical support for the coils, electrically isolated from them. The magnet generates an horizontal uniform dipole magnetic field of 0.2 T (with a current of 2900 A) which allows

to measure with good resolution the momenta and the signs of the charged particles produced in the neutrino interactions.

A dedicated mapping procedure was performed using Hall probes to precisely measure the magnetic field of the ND280 magnet. This measurement is specially important in the region of the TPCs in order to understand and correct the spatial distortions that could appear in the reconstruction of the charged particle tracks. Fig. 3.11 shows an example of a slice of the magnetic field mapped in one TPC at $\sim 0.07\,\mathrm{T}$: the field is very homogeneous in the centre of the magnet but it varies more and more as it gets closer to the edge of the TPC region (downstream).
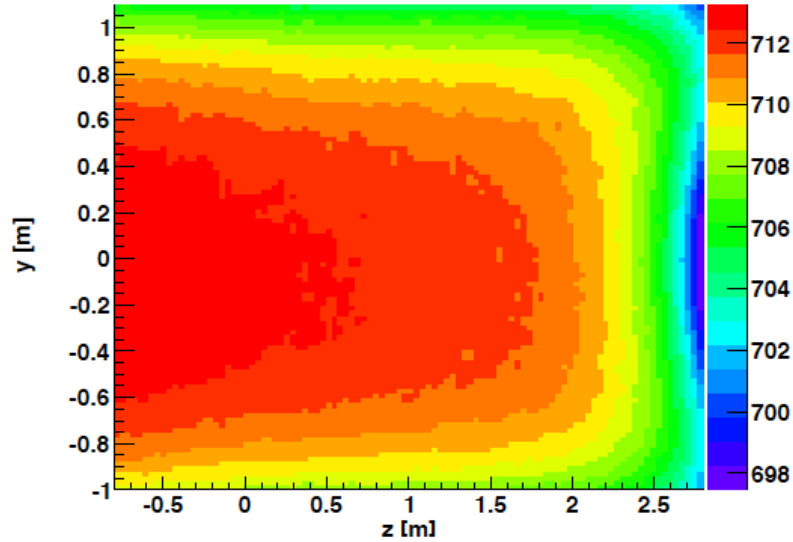
Figure 3.11: Slice of the magnetic field mapped in one TPC at $\sim 0.07\,\mathrm{T}$ (colours represent the magnetic field in units of Gauss): the field is very homogeneous in the centre of the magnet but it varies more and more as it gets closer to the edge of the TPC region (downstream).

The magnet yokes consist of 16 iron plates spaced with $17\,\mathrm{mm}$ air gaps. In these air gaps, 440 polystyrene-based scintillator modules are inserted, forming the Side Muon Range Detector (SMRD). Each module incorporates a wavelength shifting fibre connected to an MPPC. The main goal of the SMRD is to detect muons produced in the neutrino interactions that escape the inner detectors at large angles with respect to the

beam direction, also measuring their momenta. Furthermore, the SMRD provides a trigger for cosmic rays entering the ND280 detector and helps identifying background events from beam neutrino interactions occurring in the magnet or in the surrounding walls. MC studies shows that a significant fraction of the muons produced in CCQE interactions are emitted with larger angles and reach the SMRD [132]. Muons emitted with large angles often leave a short track or no tracks in the TPCs, but their momenta and direction can be measured by the SMRD plastic scintillator counters.

3.3 The ND280 Simulation

The analyses performed using the near detector depend on the ND280 software, which includes different tools for data collection, simulation and analysis. The ND280 software is based on ROOT [133] and GEANT4 [134] and is responsible for producing processed output from either data or MC input. For Monte Carlo (MC), the output from a neutrino generator is processed as follows:

1. GEANT4 detector geometry

2. GEANT4 energy deposition simulation;

3. electronics simulation;

4. digitisation;

5. detector calibration;

6. event reconstruction.

The aim of this software chain is to create MC data sets which are representative as much as possible of the real data (a comparison is shown in Section 5.2.1). In fact the raw MIDAS files of real data are processed through the same software chain, except for the simulation steps, thus digitisation, detector calibration and event reconstruction. After the last step, the truth and reconstructed MC information, as well as real data information, are summarised into a format ready for analysis.

Fig. 3.12 is a visual overview of the ND280 software suite showing the process flow.
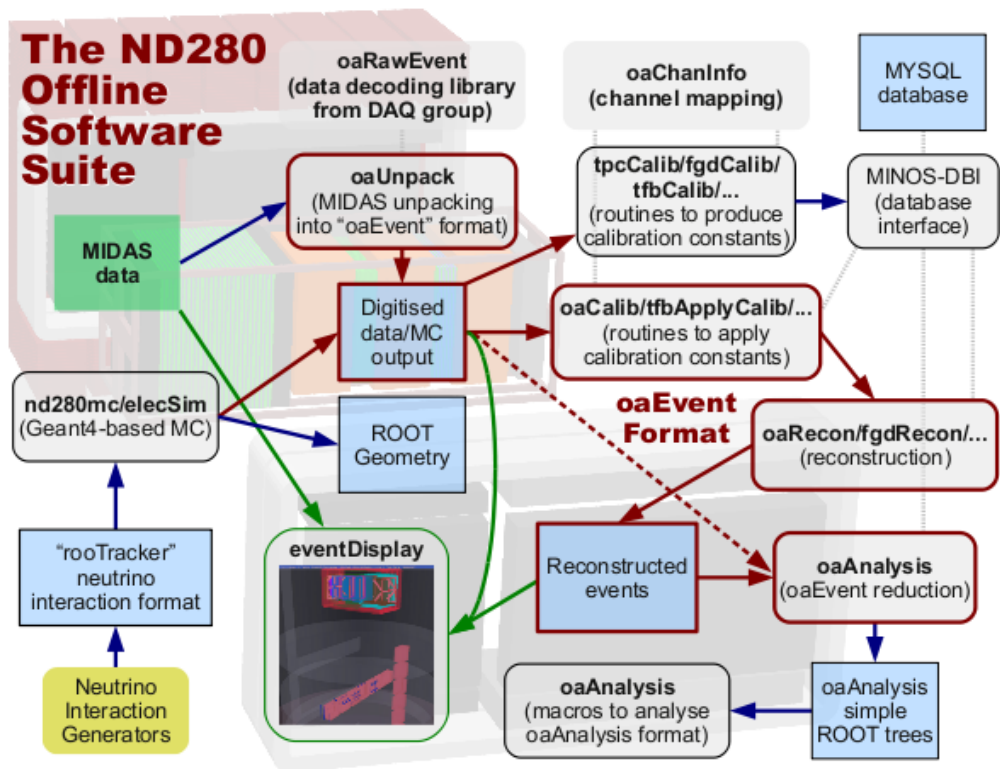
Figure 3.12: Overview of the ND280 software suite showing the process flow.

3.3.1 MC Event Simulation

An initial prediction of the neutrino beam flux is obtained by using FLUKA2008 [135] to simulate the 30 GeV protons in the primary beamline and on the target, and GEANT3 to propagate the by-products in the decay volume. The initial prediction is tuned using both beamline measurements and data from NA61/SHINE, a dedicated hadron interaction experiment at CERN [136]. The differences between the measured and simulated beam profile in each T2K run are used to reweigh the flux (cf. Section 6.3.1).

Official MC event generators used in T2K are NEUT [137] and GENIE [138].

3.3.1.1 The NEUT Event Generator

The NEUT [137] event generator is used to simulate neutrino interactions on all the elements of ND280, including the magnet yoke. In reality, interactions can also happen in the concrete wall of the pit or the sand surrounding it: a separate "sand MC sample" is produced to estimate the contribution of these events in the analyses.

Events are simulated from a few MeV to hundreds of GeV, following the input given by the beam group to better model the energy, position, direction and flavour of the produced neutrinos. Considering the geometry of ND280, NEUT can track the neutrinos and also the interaction probability on all the materials that they cross. A pseudo-random number generator determines whether an interaction happens or not.

The simulation of neutrino interactions follows a chosen nuclear model (to describe the movement of the nucleons in the nucleus), integrates it to the neutrino interaction with the target nucleon, and then propagates the products in the nuclear medium (final state interactions) until they exit the nucleus.

The version of NEUT used in this analysis is 5.3.2 [139]. For simulating the initial neutrino-nucleon interaction, Spectral Function model [69] (SF) is used as a nuclear model for quasi-elastic interactions, and the Relativistic Fermi Gas model (RFG) [79] otherwise. Nevertheless, event-by-event weights can be calculated and applied to effectively modify the simulated nuclear model. This is actually the case for this analysis, as explained in Section 6.4.1. For the pion production, NEUT implements the Rein-Sehgal model [80]. It also generates multi-nucleon neutrino interactions with an implementation of the Nieves model [140].

Final State Interactions (FSI) are simulated with a *cascade model* (cf. Section 1.4.2.1). Each particle is propagated inside the nucleus with steps determined by the mean free path. The mean free path depends on the position inside the nucleus and the momentum of the particle. At each step the probability of interaction (such as charge exchange, absorption or scattering) is calculated. If an interaction occurs, the resulting particles are used for stepping through the rest of the nucleus. This process continues until all particles are either absorbed in the nucleus or escape it. Data from several pion scattering experiments are used to tune this model.

3.3.1.2 The GENIE Event Generator

While NEUT is the "official" generator, GENIE [138] is also used as an alternative neutrino event generator. Since GENIE provides a general framework valid over a large range of experiments, targets and neutrino energies, it is often used as a baseline to compare results from experiments with different neutrino flux or targets.

The version of GENIE used in this analysis is 2.8.0. As shown in Table 3.1, GENIE uses essentially the same models as NEUT, but with important differences in the implementation and the parametrisation, hence also the predicted cross-sections differ.

Generator	Nuclear Model	FSI	Pion Production	2p2h
NEUT	RFG and SF	Cascade	Rein-Sehgal	Nieves
GENIE	Bodek-Ritchie FG	Cascade	Rein-Sehgal	N/A

Table 3.1: MC event generators comparisons

The Bodek and Ritchie Fermi Gas model [141] is an extension of the Relativistic Fermi Gas (RFG) model which considers a longer energy tail compared to NEUT. The value of the axial masses for QE and RES interactions are also different: M_A^{QE} is 1.21 GeV/c^2 in NEUT and 0.99 GeV/c^2 in GENIE, and M_A^{RES} is 1.21 GeV/c^2 in NEUT and 1.12 GeV/c^2 in GENIE.

3.3.1.3   Detector Simulation and Electronics Response

NEUT and GENIE only simulate individual neutrino interactions. The ND280 detector simulation groups them in spills and simulates the passage through the detector by using GEANT4 [134]. GEANT4 provides the complicated detector geometry and tracks the particles through the given geometry. It accounts for energy loss and deposition due to passing through particles in the detector materials.

Eventually, the response of the electronics is simulated for sub-detectors by modelling detection components. In the scintillator sub-detectors (FGDs, ECals, PØD), the simulation describes: the light emitted in response to the energy deposition, the transportation of the light through the bar to the optical fibres, the response of the MPPCs. For the TPCs, the simulation describes the electron drifts, the MicroMEGAS response, and the electronics chain afterwards.

The simulation of the passage through the detector and electronics response produces an output which is in the same format as the real data.

3.3.2   Detector Calibration

The calibration of ND280 events is done using calibration constants that are valid for specific periods of data.

For the scintillator-based detectors, "pedestal" triggers and "cosmic" triggers are used to calibrate the light yield and time of hits. Pedestal triggers measure the dark noise of the MPPCs, whereas cosmic triggers can be used to calibrate the response of different bars to minimally ionising particles (MIPs). Timing calibration accounts for both bar-to-bar variations and delays introduced by readout electronics. Since there is no precise inter-detector time calibration, delays up to 10 ns are observed between TPCs and ECals.

For the TPCs, a dedicated laser system is used to calibrate the drift velocity, the gain of the electric field, and the energy deposited in the gas by charged particles.

3.3.3   Event Reconstruction

The event reconstruction happens in two phases: local reconstruction by each sub-detector and then global reconstruction.

Each sub-detector gathers hits, coming from MPPCs or MicroMEGAS pads, together to form tracks or showers (local reconstruction). The global reconstruction propagates the TPC reconstruction to the other sub-detectors to form a complete picture of the event.

Even though an attempt to evaluate a global particle identification (PID) is made, it is more powerful to use PID information from each sub-detector separately (e.g. this analysis uses the TPC PID).

The momentum of each global track is reconstructed according to different particle hypotheses (electron, muon, proton), and a backward going track can be recognised from the timing recorded in each sub-detector.

3.3.4 Corrections

Highland (High Level Analysis at the Near Detector) is a set of global tools developed for all analyses at ND280. Within this framework, before any selection is performed, a set of corrections are applied to both data and MC samples in order to reduce the discrepancies between them. These corrections are either based on known hardware failures or the result of studies using control samples (samples not used in the analyses, e.g cosmic muons), This is the list of the corrections applied (more details can be found in [142]).

- **Ignore right ECAL correction**: ignore right-side Barrel ECAL for T2K runs 3 and 4 as part of it was broken. During the Great Tohoku earthquake in March 2011, two of the electronics boards in the right-side Barrel ECAL were damaged. One of these boards (TFB 25) handles data from bars near FGD2 that only have an MPPC at one end, thus these bars are now dead. These missing bars affect the reconstruction, PID and energy estimation of any particles entering that region, but the simulation does not currently reproduce these dead channels. Rather than applying a large systematic uncertainty to account for this, the right-side Barrel ECAL are entirely ignored for Runs III and IV. This correction is applied to both data and MC by removing from global tracks all right ECAL segments.

- **dE/dx DATA correction**: a correction is applied to the measured dE/dx for each TPC. The correction factor is evaluated for each TPC and each running period, and is always close to one within few %.

- ***dE/dx* MC correction**: studies on control samples showed that the MC over-estimates the energy loss of true electrons by 1%. A reduction factor of 1.01 is applied to the measured dE/dx of all true electrons in the MC.

- ***dE/dx* expected correction**: use a more accurate method to estimate the expected dE/dx for a given particle type and momentum than the one in the event reconstruction (Section 3.3.3). Studies done a posterior have shown that the average dE/dx for a true given particle type and true momentum do not coincide with the values assumed during the track reconstruction process.

- **Pile-Up MC correction**: applies a weight (smaller than one) to all MC events to account for the coincidence between beam neutrino interactions in the tracker and sand muons events, which do not occur in the MC because neutrino interactions within the magnet and sand muons are simulated separately. This effect is explained in detail in Section 6.2.4.3. The correction depends on the beam intensity and therefore on the running period, and also on the FGD where the reconstructed vertex is.

Another set of corrections is applied only to the MC samples when propagating the systematic errors.

- **Momentum resolution MC correction**: an x dependent smearing factor up to almost 40% is applied to the inverse transverse momentum of all TPC and global tracks, in order to account for the difference in momentum resolution between data and MC. Those factors are computed comparing the momentum in two consecutive TPCs, using control samples of tracks that cross multiple TPCs. The same study is also used to evaluate the uncertainty on the TPC momentum resolution (cf. Section 6.2).

- **TPC PID MC correction**: a further effective correction on the measured dE/dx in the TPCs is applied when propagating the corresponding systematic error in order to have pulls centred at 0 (Section 6.2.2).

Eventually, two corrections are applied to the MC samples to fix two known issues in NEUT.

- NEUT version 5.3.2 (and previous versions) contains a bug resulting in incorrectly simulating coherent interactions on hydrogen; these interactions are removed from the MC sample.

- In the list of true vertices generated by NEUT there are also the interactions that actually didn't take place because of Pauli blocking. These vertices don't have any outgoing particles, nevertheless they are removed from the MC sample in order to evaluate the efficiencies correctly.

4

Cross-Section Measurements

4.1 Why Cross Sections Are Important

Neutrino oscillation experiments measure the charged-current and neutral-current event rates in their detectors, which can generically be expressed as

$$R(\vec{x}) = \sum_i^{\text{process}} \sum_j^{\text{target}} \Phi(E_\nu) \times \sigma_i(E_\nu, \vec{x}) \times \epsilon(\vec{x}) \times T_j \times P(\nu_A \to \nu_B) \qquad (4.1)$$

where $R(\vec{x})$ is the total event rate for all processes as a function of the reconstructed kinematic variables $\vec{x}$, $\Phi_\nu(E_\nu)$ is the neutrino flux as a function of the neutrino energy E_ν, σ_i is the neutrino cross section for a particular interaction process, ϵ is the detection efficiency and T_j is the number of target nuclei in the detector fiducial volume for target type j. It is obvious from this equation that in order to measure the neutrino oscillation probability $P(\nu_A \to \nu_B)$, the unoscillated flux must be well measured, the neutrino cross section must be known, and the detector efficiency must be understood. Any assumptions in the neutrino oscillation model must also be well tested. If any of these components is not well modelled, the final oscillation measurement may be biased. Large uncertainties on any of these components will limit the sensitivity of an experiment.

In reality, not all interaction processes are signal for each experiment, the other processes become backgrounds, which must be taken into account if they can mimic the signal in the detector. For T2K, the dominant interaction process is Charged-Current

Quasi-Elastic scattering (CCQE), as shown in Fig. 4.1. Although this implies that CCQE is the most important process for the T2K oscillation analysis, there are significant contributions from resonant pion production (RES) and deep inelastic scattering (DIS), which have to be well modelled as these will produce significant contributions. Note that Fig. 4.1 shows the cross sections divided by the neutrino energy, so the cross section for the tail of the T2K flux is significantly larger than at the peak.

(a) $\nu_\mu - {}^{12}\text{C} \ (/E_\nu)$ **(b)** $\bar{\nu}_\mu - {}^{12}\text{C} \ (/E_\nu)$
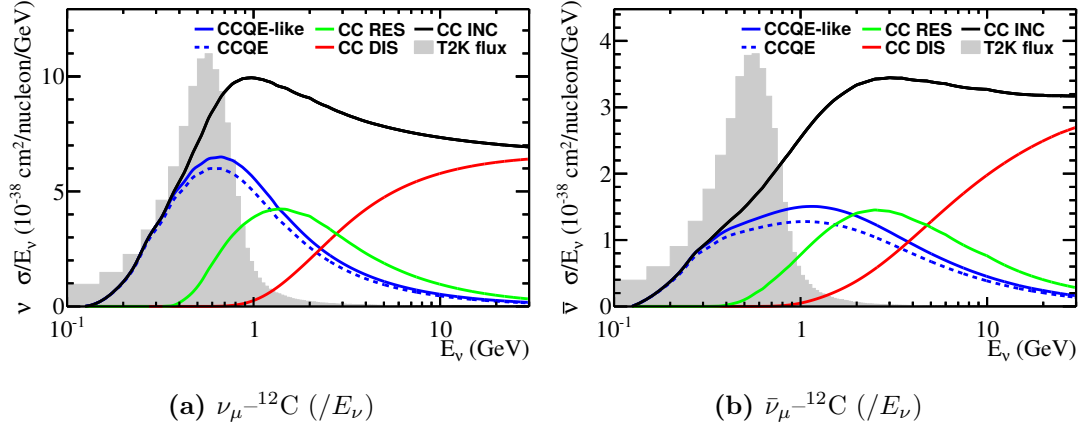
Figure 4.1: NEUT v5.3.3 ν_μ and $\overline{\nu}_\mu$ cross-section predictions after NIWG 2014 tuning (Section 6.4.1), divided by neutrino energy for both neutrino mode and anti-neutrino mode running.

4.1.1   What Can Be Measured

In Eq. (4.1), $\sigma_i(E_\nu, \vec{x})$ is the contribution from the ith interaction process. Examples of interaction processes on nucleons are:

- Charged-Current Quasi-Elastic (CCQE):

$$\overset{\scriptscriptstyle(-)}{\nu_l} + n(p) \rightarrow l^{-(+)} + p(n) \tag{4.2}$$

- Neutral-Current Single π^0 (NC1π^0):

$$\overset{\scriptscriptstyle(-)}{\nu_l} + n, p \rightarrow \overset{\scriptscriptstyle(-)}{\nu_l} + n, p + \pi^0 \tag{4.3}$$

Unfortunately, we do not observe interaction processes on nucleons. Instead, we can only see final state topologies on nuclear targets. After a neutrino interacts inside

a nucleus, the particles produced at the vertex have to propagate through the dense nuclear medium, where many (if not the majority) outgoing hadrons will re-interact ("final state interactions" or "FSI"). So instead of CCQE events, all we can observe are events with a topology of a single charged lepton, and no pions and any number of nucleons (CC0π). However, in the case of a charged-current inclusive analysis, i.e. considering all the charged-current interaction processes rather than an exclusive one, detecting the presence of a muon is an unquestionable signature (production of lepton-pairs in the final state is very unlikely at the T2K flux).

The cross-section terms which enter into Eq. (4.1), $\sigma_i(E_\nu, \vec{\mathbf{x}})$, for oscillation experiments are a function of true kinematic variables, and the neutrino energy. Unfortunately, we cannot reconstruct the neutrino energy or other quantities like four momentum transfer, Q^2, on an event by event basis. The available observables are only the final state particle kinematics, smeared by the detector resolution; the relationship to true quantities is an assumption of our underlying simulation.

So we cannot measure the cross section, $\sigma_i(E_\nu, \vec{\mathbf{x}})$, for the ith interaction process as is required for oscillation analyses. Instead, we measure some topology-based cross section $\widetilde{\sigma}_k$, which is integrated over the T2K flux, as a function of some outgoing particle kinematics, $\vec{\mathbf{x}}$:

$$\widetilde{\sigma}_k(\vec{\mathbf{x}}) = \sum_i \int_{E_{min}}^{E_{max}} \sigma_i(E_\nu, \vec{\mathbf{x}}) dE_\nu \tag{4.4}$$

where σ_i is the contribution of true interaction process i to the final state topology k.

Theorists and other users of the data (for example the T2K's Neutrino Interactions Working Group [143]) want to compare and constrain their $\sigma_i(E_\nu, \vec{\mathbf{x}})$ with data from $\widetilde{\sigma}_k(\vec{\mathbf{x}})$. Because of the complexity of that comparison, they need a lot of data, ideally from multiple experiments. What the cross-section community most desperately lacks at the moment is high quality data free of model-dependence. Without new data, it will not be possible to develop new interaction models ($\sigma_i(E_\nu, \vec{\mathbf{x}})$) or parametrise cross-section uncertainties well enough to make high precision measurements of oscillation parameters (Eq. (4.1)).

4.1.2 Reconstructed Energy from Lepton Kinematics

In Section 4.1.1 we stated that the true neutrino energy cannot be reconstructed on a event by event basis. In general, the energy can be reconstructed in two ways: calorimetrically or kinematically. For a calorimetric reconstruction, all the involved particles should be fully contained in the detector, which is not the case for ND280. For a kinematic reconstruction, angles and momenta of all the particles produced in the neutrino-nucleon interaction should be known, but even in a 100 % efficient detector, we can only measure those observables after they get possibly modified by the final state interactions, as explained in Section 4.1.1.

Nevertheless, in the case of a CCQE process (Eq. (4.2)), the only outgoing particle is a lepton, which being a minimum ionising particle, it is assumed not to interact before exiting the nucleus, i.e. it is unaffected by FSI. Therefore, for a CCQE process from a ν_μ, the true neutrino energy can be easily found knowing the muon momentum p_μ and the angle θ_μ between the directions of the incoming neutrino and the outgoing muon:

$$E_\nu = \frac{m_p^2 - m_\mu^2 - (m_n - V)^2 + 2 \cdot E_\mu \cdot (m_n - V)}{2 \cdot ((m_n - V) + p_\mu \cdot \cos\theta_\mu - E_\mu)} \tag{4.5}$$

where $m_n = 1232$ MeV, $m_p = 938.27$ MeV and $m_\mu = 105.66$ MeV are the masses of the neutron, the proton and the muon respectively; V is the binding energy (in MeV); E_μ is the energy of the muon, i.e. $\sqrt{p_\mu^2 + m_\mu^2}$.

However, we can only select a sample of CC0π events rather than of CCQE events, again because of the final state interactions, as explained in Section 4.1.1. Since the CCQE processes are dominant in a CC0π selection, and even in a CC-inclusive selection below 1 GeV (Fig. 4.1), in these cases the distribution of a quantity defined in the same way of Eq. (4.5), namely $E_{QE}(p_\mu, cos\theta_\mu)$, is still a fair approximation of the true neutrino energy distribution:

$$E_{QE}(p_\mu, cos\theta_\mu) = \frac{m_p^2 - m_\mu^2 - (m_n - V)^2 + 2 \cdot E_\mu \cdot (m_n - V)}{2 \cdot ((m_n - V) + p_\mu \cdot \cos\theta_\mu - E_\mu)} \simeq E_\nu \tag{4.6}$$

Even if $E_{QE}(p_\mu, cos\theta_\mu)$ does not correspond to the true neutrino energy (except for CCQE processes), it can always be interpreted simply as a function of the muon kinematics, thus model-independent, also on a event-by-event basis. With respect to

p_μ, $E_{QE}(p_\mu, cos\theta_\mu)$ is more sensitive to the detector smearing, thus also to model discrepancies, as a reconstruction shift is more likely to be washed out in p_μ than in $E_{QE}(p_\mu, cos\theta_\mu)$. Indeed $E_{QE}(p_\mu, cos\theta_\mu)$ is related to the flux shape, which is very sensitive to the beam geometry. Furthermore, $E_{QE}(p_\mu, cos\theta_\mu)$ has the advantage of having less migrations among bins in the smearing matrix, which helps the unfolding to resolve the detector smearing (Section 7.1). Given its excellent resolution, $E_{QE}(p_\mu, cos\theta_\mu)$ is the quantity more sensitive to any shifts in the Monte Carlo simulation. Eventually, the T2K oscillation analyses at the far detector Super-Kamiokandeare performed as a function of this same quantity E_{QE}.

For these reasons, the cross-section results presented in this thesis are performed as a function of $E_{QE}(p_\mu, cos\theta_\mu)$.

4.2   Extracting a Cross Section

Simplifying Eq. (4.1), the number of true neutrino interactions in the near detector as a function of the reconstructed kinematic variables $\vec{\mathbf{x}}$ is defined as:

$$N_{\text{true}}(\vec{\mathbf{x}}) = \sigma_{true}(E_\nu, \vec{\mathbf{x}}) \times \epsilon(\vec{\mathbf{x}}) \times T \times \Phi(E_\nu) \tag{4.7}$$

where $\Phi_\nu(E_\nu)$ is the neutrino flux as a function of the neutrino energy E_ν, σ_{true} is the exclusive or inclusive (i.e. integrated over certain interaction processes) true neutrino cross section, ϵ is the detector efficiency and T is the total number of targets.

Because of the detector smearing, what we actually measure is $N_{\text{observed}}(\vec{\mathbf{x}})$, which is related to $N_{\text{true}}(\vec{\mathbf{x}})$ through the detector efficiency $\epsilon(\vec{\mathbf{x}})$ and the so called "unsmearing matrix", which account for the events migration among bins. The detector efficiency might be incorporated in the unsmearing matrix, which is then called "unfolding matrix". Unfolding, or deconvoluting, is the procedure for removing the detector smearing from results [144]. Building the unfolding matrix and properly handling the uncertainties is tricky, since it requires a matrix inversion, which usually leads to large oscillations in the unfolded result, as noise in the smeared signal is blown up in the inverse. Various regularising methods for smoothing the unfolded distributions exist, where a pseudo-inverse matrix $\widetilde{U}_{ij}^{-1}$ is calculated. Unfolding methods are discussed further in Chapter 7.

The estimated number of true neutrino interactions in the bin i of a certain kinematic variable can be written as

$$\hat{N}_i = \frac{1}{\epsilon_i} \cdot \sum_j \widetilde{U}_{ij}^{-1} \left(N_{\text{observed},j} - B_j \right) \simeq N_{\text{true},i} \tag{4.8}$$

where B is the estimated background (predicted by the MC or estimated from a control sample) and the hat denotes the fact that $\hat{N}$ is only an estimation of N_{true}, since it relies on the efficiency predicted by the Monte Carlo and on the unfolding matrix $\widetilde{U}_{ij}^{-1}$. There are other ways of dealing with the background events and they are discussed in Section 7.4: even using a different method, all the following arguments would stand.

Using the estimated number of events $\hat{N}$, Eq. (4.7) becomes

$$\hat{N}(\vec{\mathbf{x}}) = \sigma(E_\nu, \vec{\mathbf{x}}) \times T \times \Phi(E_\nu) \tag{4.9}$$

from which the cross section $\sigma(E_\nu, \vec{\mathbf{x}})$ can be measured.

If we could access the true neutrino energy, we could simply measure the total cross section as a function of the true neutrino energy E_ν (from Eq. (4.7) and Eq. (4.8)):

$$\sigma(E_\nu) = \frac{\hat{N}}{T \, \Phi(E_\nu)} \tag{4.10}$$

Since this is not possible without relying heavily on the Monte Carlo, as explained in Section 4.1.1, model-independent cross sections need to be differential in some final state kinematic variables $\vec{\mathbf{x}}$ and normalised by the total flux in each bin.

Using Eq. (4.7) and Eq. (4.8), the flux-integrated differential cross section in the ith bin of a true final state kinematic variable x is

$$\frac{d\sigma}{dx_i} = \frac{\sum_j \widetilde{U}_{ij}^{-1} \left(N_{\text{observed},j} - B_j \right)}{\epsilon_i \, T \, \Phi_\nu \, \Delta x_i} \tag{4.11}$$

where Φ_ν is the total flux and Δx_i is the width of the true bin. The flux and other kinematic variables have been integrated over.

Normalising in each bin for the total flux is one of three possible choices.

- "Flux-unfolded" cross section: normalise by $\int_{E_\nu^{min}(i)}^{E_\nu^{max}(i)} w_i(E_\nu)\Phi(E_\nu)dE_\nu$ evaluated in each bin i. In this case the neutrino energy distribution in each bin, $w_i(E_\nu)$, needs to be known. The measurement depends strongly on the particular model

used to apply this correction; on the other hand the result can be directly compared between different experiments, since it has been fully corrected for the flux.

- "Flux-folded" cross section: normalise by $\int_{E_\nu^{min}(i)}^{E_\nu^{max}(i)} \Phi(E_\nu)dE_\nu$ evaluated in each bin i. This method produces a result which is experiment-dependent, since the result has not been fully unfolded for the particular neutrino flux in each bin, and it is also still model-dependent since an assumption on $E_\nu^{min}(i)$ and $E_\nu^{max}(i)$ for each bin needs to be done to evaluate the average flux normalisation.

- "Flux-integrated" cross section[1] : normalise the same $\Phi_\nu = \int \Phi(E_\nu)dE_\nu$ in each bin. This is the method used in Eq. (4.11) and it is completely model-independent, since no assumptions need to be made on the particular neutrino energy distribution in each bin. As for the 'flux-folded" cross section, also in this case the result is experiment-dependent, since there is no a bin-by-bin flux correction, but being model-independent it has the advantage that another model could be convoluted with the T2K flux and compared with the result.

In the case of a cross-section ratio between two samples where the flux is the same, the flux normalisation, no matter which, cancels out. The water to scintillator cross-section ratio studied in this thesis, as a function of $E_{QE}(p_\mu, cos\theta_\mu)$ which has been defined in Eq. (4.6), is given by

$$\frac{\sigma_{\text{water}}(E_{QE}(p_\mu, cos\theta_\mu))}{\sigma_{\text{scint}}(E_{QE}(p_\mu, cos\theta_\mu))} = \frac{\hat{N}_{\text{water}}/T_{\text{water}}}{\hat{N}_{\text{scint}}/T_{\text{scint}}} \tag{4.12}$$

where T_{water} and T_{scint} are the number of targets for the water and the scintillator volumes respectively, and $\hat{N}_{\text{water}}$ and $\hat{N}_{\text{scint}}$ are the estimated number of events in water and scintillator respectively, obtained by Eq. (4.8). Being water a passive material, evaluating $\hat{N}_{\text{water}}$ is not obvious and it is discussed in Section 4.3.

---

[1]There is no well defined convention for how to refer to the flux integral in the extraction of the cross section. MiniBooNE referred to their work as "flux integrated", but MINERνA used "flux average" to refer to the same thing.

4.3 Cross-Section on Water and the Water to Scintillator Ratio

As seen in Section 4.2, cross-section measurements have the potential to reduce the interaction model systematics in neutrino oscillation experiments such as T2K, and in particular cross sections on water and water to scintillator ratios, to further constrain the expected neutrino energy spectrum at Super-Kamiokande, it being a water Cherenkov detector. Such measurements should also be useful for future experiments such as the proposed Hyper-Kamiokande [145].

No measurements of the water cross section in the T2K energy range have been made so far, except for a recent T2K paper: "First measurement of the muon neutrino charged-current single pion production cross section on water with the T2K near detector" [146]. In that paper, one of the main uncertainties is the flux systematic, which is hard to reduce because it is correlated with the neutrino interaction model uncertainties: it is impossible to distinguish between a higher cross section and a higher initial flux.

Nevertheless, flux systematics almost completely cancel in a $\sigma_{\text{water}}/\sigma_{\text{scint}}$ cross-section ratio as it will be shown in this chapter (Eq. (4.19)). Moreover, a CC inclusive analysis, rather than $CC1\pi$, has the advantage that also the statistics uncertainty will be small.

In ND280, such a $\sigma_{\text{water}}/\sigma_{\text{scint}}$ ratio cross-section can be measured by comparing FGD1 (scintillator-only) and FGD2 (scintillator+water). Thanks to the ND280 design, most of the systematic uncertainties are highly correlated between FGD1 and FGD2 and largely cancel in the ratio. There are two identical TPCs placed after each FGD with exactly the same relative position, and also the two FGDs are identical, except for the target material. This allows to select a sample in FGD1 (scintillator-only) and a sample in FGD2 (water+scintillator) with exactly the same acceptance.

4.3.1 Extraction of the Cross Section on Water with the FGDs

An FGD XY module is composed of 86.1 % of carbon, 7.4 % of hydrogen and 3.7 % of oxygen (cf. [147]). Therefore, a cross section on an XY module is almost a cross-section

on pure carbon (the cross section on hydrogen is negligible, and cannot be QE as there are no neutrons).

By contrast however, a cross section on a water module is far from being a cross section on pure water, because its structure contains a significant amount of carbon, which accounts for 15.1 % of the mass of a water module.

Nevertheless the structure of the water modules has been carefully chosen to match the elemental composition of the XY modules. This matching is the key for extracting the cross section on water (cf. [148]).

The water in a water module accounts for 79.5 % in mass, and it is contained in a framed polycarbonate panel. Two polypropylene sheets are glued on each face of the panel using Crosslink Technology CLR 1390/CLH 6025 epoxy (Fig. 4.2). Their dimensions and densities were specifically chosen in order to obtain the elemental matching with the XY modules. In fact, considering together the polypropylene sheets, glue, polycarbonate panel, and a number of G10 spacers among the panels, the total number of carbon, hydrogen and oxygen nuclei are in the same ratio as they are in an XY module ("virtual XY"), plus some remaining hydrogen and oxygen nuclei which are in a 2:1 ratio ("virtual water").

Thus a water module is actually composed of 79.5 % water, 17.5 % "virtual XY" and 3.0 % "virtual water". Liquid water and "virtual water" together are called "water-like", and sum up to 82.5 % of the water module. The whole FGD2 can be considered as composed of two components:

- a *"water-like" component*, the sum of the "water-like" components of the 6 water modules;

- an *"XY-like" component*, the sum of the "virtual XY" components of the 6 water modules plus the actual XY modules in the FGD2 fiducial volume.

Note that these components are not two physically-separated volumes. Nevertheless, this can be written in terms of number of targets T:

$$T_{\mathrm{FGD2}} = T_{\mathrm{FGD2water}} + T_{\mathrm{FGD2scint}} \qquad (4.13)$$

where $T_{\mathrm{FGD2water}}$ is the number of targets in the "water-like" component and $T_{\mathrm{FGD2scint}}$ is the number of targets in the "XY-like" component. FGD2 is essentially composed of 409.4 kg of H_2O plus a portion of FGD1.
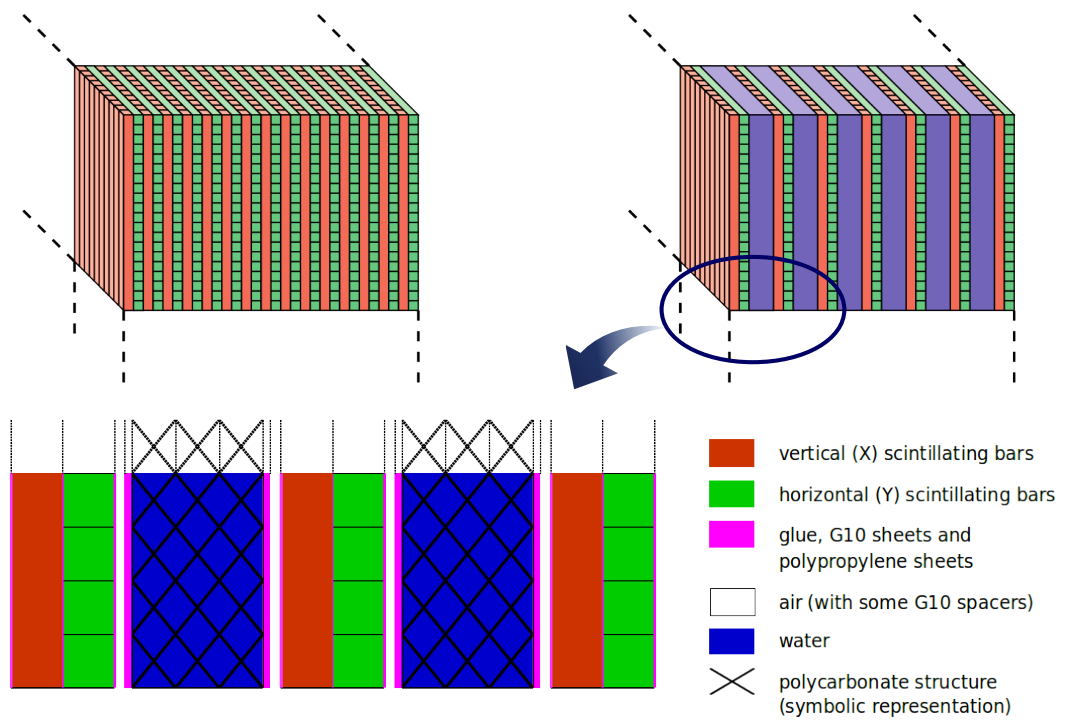
Figure 4.2: Schematic view of FGD2

Thanks to this design, the cross section on pure water can be obtained by subtracting the cross section on the "XY-like" component [1] (estimated in FGD1) from the cross section on the whole FGD2.

Nota bene: from now on we will refer to the "cross section on water" as the cross section of the "water-like" component, composed only of atoms of hydrogen and oxygen in the ratio 2:1.

4.3.2 Water to Scintillator Cross-Section Ratio in $E_{QE}(p_\mu, \cos\theta_\mu)$

Since the whole FGD2 can be considered as composed of two components, "water-like" (pure water) and "XY-like" (scintillators), as described in Section 4.3.1, the estimated number of true events in the whole FGD2 can be written as the sum of the events in the two components:

$$\hat{N}_{\text{FGD2}} = \hat{N}_{\text{FGD2water}} + \hat{N}_{\text{FGD2scint}} \tag{4.14}$$

where $\hat{N}_{\text{FGD2water}}$ is the estimated number of events in the "water-like" component and $\hat{N}_{\text{FGD2scint}}$ is the estimated number of events in the "XY-like" component. The hat in $\hat{N}$ denotes that this is an estimation of the number of true events, and as explained in Section 4.2 it can be inferred from the number of observed events N through Eq. (4.8), i.e. by correcting for:

- the reconstruction efficiency;

- event migrations between bins (unfolding).

Unfolding methods are discussed further in Section 7.1.

From Eq. (4.9), the expected number of events in the "XY-like" component can be written as

$$\hat{N}_{\text{FGD2scint}} = \sigma_{\text{scint}}(E_{QE}) \cdot T_{\text{FGD2scint}} \cdot \Phi_{\text{FGD2}} \tag{4.15}$$

where $T_{\text{FGD2scint}}$ is the number of targets in the "XY-like" component as in Eq. (4.13), Φ_{FGD2} is the flux (no matter whether integrated or folded, since it will cancel, as

---

[1]Note that the cross section on the "virtual XY" component or on the "XY-like" component simply corresponds to the cross section on an XY module properly scaled by the number of targets, since they all have the same elemental composition.

anticipated in Section 4.2) and $\sigma_{\text{scint}}(E_{QE})$ is the cross section on scintillator as a function of $E_{QE}(p_\mu, \cos\theta_\mu)$ defined in Eq. (4.6).

The cross section on scintillator $\sigma_{\text{scint}}(E_{QE})$ can be estimated using FGD1:

$$\sigma_{\text{scint}}(E_{QE}) = \frac{\hat{N}_{\text{FGD1}}}{T_{\text{FGD1}} \cdot \Phi_{\text{FGD1}}} \tag{4.16}$$

The cross section on water is a little trickier as it requires subtraction. Using Eq. (4.14), Eq. (4.15) and Eq. (4.16), the expected number of events in the "water-like" component can be written as

$$
\begin{aligned}
\hat{N}_{\text{water}} &= \hat{N}_{\text{FGD2}} - \hat{N}_{\text{FGD2scint}} \\
&= \hat{N}_{\text{FGD2}} - \sigma_{\text{scint}}(E_{QE}) \cdot T_{\text{FGD2scint}} \cdot \Phi_{\text{FGD2}} \\
&= \hat{N}_{\text{FGD2}} - \frac{\hat{N}_{\text{FGD1}}}{T_{\text{FGD1}} \cdot \Phi_{\text{FGD1}}} \cdot T_{\text{FGD2scint}} \cdot \Phi_{\text{FGD2}}
\end{aligned} \tag{4.17}
$$

Therefore, the cross section on water can be written as:

$$
\begin{aligned}
\sigma_{\text{water}}(E_{QE}) &= \frac{\hat{N}_{\text{water}}}{T_{\text{FGD2water}} \cdot \Phi_{\text{FGD2}}} \\
&= \frac{\hat{N}_{\text{FGD2}}}{T_{\text{FGD2water}} \cdot \Phi_{\text{FGD2}}} - \frac{\hat{N}_{\text{FGD1}}}{T_{\text{FGD1}} \cdot \Phi_{\text{FGD1}}} \cdot \frac{T_{\text{FGD2scint}}}{T_{\text{FGD2water}}}
\end{aligned} \tag{4.18}
$$

where $T_{\text{FGD2water}}$ is the number of targets in the "water-like" component as in Eq. (4.13), and Φ_{FGD2} cancels in the second term.

The water to scintillator cross-section ratio is finally obtained dividing Eq. (4.18) by Eq. (4.16)

$$\frac{\sigma_{\text{water}}(E_{QE})}{\sigma_{\text{scint}}(E_{QE})} = \frac{\hat{N}_{\text{FGD2}}/T_{\text{FGD2water}}}{\hat{N}_{\text{FGD1}}/T_{\text{FGD1}}} \cdot \frac{\Phi_{\text{FGD1}}}{\Phi_{\text{FGD2}}} - \frac{T_{\text{FGD2scint}}}{T_{\text{FGD2water}}} \tag{4.19}$$

Note that having a larger fraction of water in FGD2, relative to the scintillator component, would decrease the second term $(-T_{\text{FGD2scint}}/T_{\text{FGD2water}})$, giving a smaller fractional error for $\sigma_{water}/\sigma_{scint}$.

Regarding $\frac{\Phi_{\text{FGD1}}}{\Phi_{\text{FGD2}}}$, it can be safely assumed that the flux shape cancels and only a normalisation correction shall be considered: being that $\Phi \propto 1/r^2$ (in the approximation of a point-like neutrino source), and that FGD1 is placed at 245.83 meters from the

mean position of the neutrino's parent decay points and FGD2 is at 247.19 meters, it follows that

$$\frac{\Phi_{\text{FGD1}}}{\Phi_{\text{FGD2}}} = \frac{247.19^2}{245.83^2} = 1.011 \tag{4.20}$$

which indicates that the flux in FGD2 is 1.1 % lower than in FGD1.

4.3.3 Calculation of the Number of Target Nucleons

The results of this analysis are cross sections per nucleon, thus both protons and neutrons contribute to the number of targets T.

T2K-TN-198 [148], T2K-TN-122 [149] and T2K-TN-091 [147] provide the areal densities of the different components of the FGDs as built, considering all the materials present in the FGD's fiducial volume and taking also into account the natural abundance of their isotopes. The relevant areal densities are summarised in tab. 54 of T2K-TN-212 [142]. The number of targets for FGD1 and for the "water-like" component and the "XY-like" component of FGD2 are obtained multiplying these areal densities by the fiducial area (XY-plane area of the fiducial volume defined in Section 5.2) and by the Avogadro number:

$$T_{\text{FGD1}} = 30.058 \text{ g/cm}^2 \cdot 29584 \text{ cm}^2 \cdot N_{\text{A}} = 5.35510 \cdot 10^{29}$$
$$T_{\text{FGD2}} = 29.651 \text{ g/cm}^2 \cdot 29584 \text{ cm}^2 \cdot N_{\text{A}} = 5.28259 \cdot 10^{29}$$
$$T_{\text{FGD2water}} = 13.838 \text{ g/cm}^2 \cdot 29584 \text{ cm}^2 \cdot N_{\text{A}} = 2.46536 \cdot 10^{29}$$
$$T_{\text{FGD2scint}} = 15.813 \text{ g/cm}^2 \cdot 29584 \text{ cm}^2 \cdot N_{\text{A}} = 2.81723 \cdot 10^{29}$$

$$\tag{4.21}$$

In the chosen fiducial volume (Section 5.2) the water is the 47 % in mass of the whole FGD2.

5

Samples

The aim of the analysis described in this thesis is the measurement of the water to scintillator ratio for ν_μ charged-current cross sections. This is achieved by performing the subtraction explained in Section 4.3.1 between an inclusive sample of ν_μ charged-current interactions in scintillators and an inclusive sample of ν_μ charged-current interactions in scintillator plus water.

The two ν_μ charged-current samples are selected by looking for a negative muon candidate exiting FGD1 or FGD2 respectively, in the T2K near detector.

5.1 Data and MC Samples

The data-set includes the Run II-IV ND280 events that pass the standard beam quality and ND280 data quality checks. Run I was excluded because of issues with the calibration of this run, and because of the small amount of statistics that Run I represents ($0.17 \cdot 10^{20}$). As a result of different beam and detector conditions, the Monte Carlo is separated into different samples and scaled to the equivalent POT of each run, as shown in Table 5.1. The main configuration differences between each run are:

- The PØD contains water bags that were filled with air or water depending on the run period.

- The beam power was increased over time, and three separate beam powers were considered in the simulation.

103

T2K run	horn current	PØD status	Data POT	MC POT
Run II	250 kA	water	$0.43 \cdot 10^{20}$	$11.87 \cdot 10^{20}$
Run II	250 kA	air	$0.36 \cdot 10^{20}$	$9.24 \cdot 10^{20}$
Run III b	205 kA	air	$0.22 \cdot 10^{20}$	$4.48 \cdot 10^{20}$
Run III c	250 kA	air	$1.36 \cdot 10^{20}$	$26.32 \cdot 10^{20}$
Run IV	250 kA	water	$1.64 \cdot 10^{20}$	$34.98 \cdot 10^{20}$
Run IV	250 kA	air	$1.78 \cdot 10^{20}$	$35.00 \cdot 10^{20}$
Total			$5.80 \cdot 10^{20}$	$121.88 \cdot 10^{20}$

Table 5.1: Definition of T2K runs and their amount of data POT and of Monte Carlo POT (generated to model the data). The first two columns show the horn current and whether there was water or air in the PØD (irrelevant for this analysis).

- In Run IIIa, the magnetic horns that focus the beam were switched off, hence the data from this period is not used.

- In Run IIIb, the magnetic horns were operating at a current of 205 kA, rather than the nominal 250 kA.

Overall, the MC statistics are more than 20 times larger than the data statistics. As explained in Section 3.3.1, NEUT version `5.3.2` was used to generate the MC sample, and the beam flux was tuned based on measurements made by the Beam Group, as explained in Section 6.3.1.

For studies of particles originating outside of the ND280 detector, separate samples are produced using a description of the concrete that forms the detector pit and the surrounding sand. The sand muon production corresponds to $1.12 \cdot 10^{21}$ POT (i.e. two times the data taken during Runs II-IV). The sum of the events coming from the interactions with the sand and with the detector are what is really observed. Anyhow the contribution of sand muons to this analysis is negligible.

5.2 ν_μ Charged-Current Inclusive Selection in FGDs

The selection used in this analysis is identical to the ν_μ CC inclusive selection developed for the oscillation analyses ([142, 150]), except for a small change in the fiducial volume of the FGDs. The goal of the selection criteria is to identify a sample of neutrino interactions which originate in the FGD1 or FGD2 detector and contain a reconstructed muon track of negative charge crossing the following TPC.

The fiducial volume used in References [142, 150] is slightly different between FGD1 and FGD2. However, for this analysis the same fiducial volume has been applied for both FGDs, in order to ensure the same acceptance for the two selections. In the coordinates orthogonal to the beam direction (x and y) the fiducial volume begins 72.17 mm inward from the edges of the FGDs. In the coordinate parallel to the beam direction (z) the fiducial volume begins 10.125 mm inward from the edges of the FGDs, which corresponds in discarding the first and the last scintillator layers.

	FGD1	TPC2	FGD2	TPC3
Size in X [mm]	1864.34	2300	1864.34	2300
Size in Y [mm]	1864.34	2400	1864.34	2400
Size in Z [mm]	331.75	974	333.75	974

Table 5.2: FGDs and TPCs positions in the ND280 coordinate system. Very small asymmetries: FGD2 is 2 mm larger than FGD1 in Z; the FGD2-TPC3 gap is 1 mm smaller than the FGD1-TPC2 gap (25.625 mm and 26.625 mm respectively); in X the FGDs are exactly centred with respect to the TPCs, but in Y they are 25 mm off.

As described in Section 2.1, the T2K beam spill is constituted of eight bunches, separated by 0.6 μs. The selection is performed over the tracks grouped together in bunches according to their timing, i.e. occurring within the time windows of the beam bunches. The selection criteria allow to select only one event per bunch, either in FGD1 or in FGD2. The probability of having more than one event per bunch is very low, anyhow a pile-up systematic uncertainties is evaluated to account for it (Section 6.2.4.3).

The ν_μ CC-inclusive selection criteria are as follows.
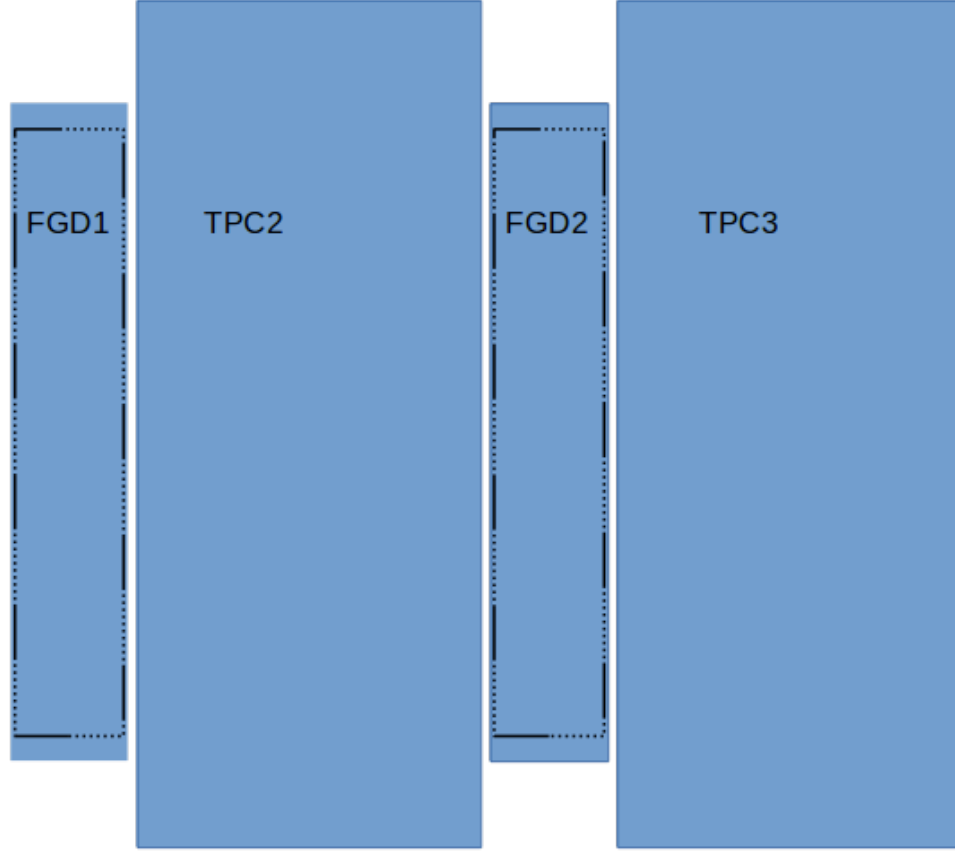
Figure 5.1: FGDs and TPCs relative positions in the yz plane (drawing to scale). The centres of the FGDs and of the TPCs are almost aligned (only 25 mm off); in the xz plane instead they are exactly aligned. The dashed line shows the fiducial volume.

1. *Data quality flag.* The full spill must have a good global ND280 data quality flag.

2. *Muon candidate identification.* The muon candidate is chosen as the highest momentum track (if any) among those satisfying the following criteria:

   (a) start position inside the FGD fiducial volume (FV);

   (b) negatively charged (according to its curvature in the magnetic field);

   (c) have more than 18 clusters in the TPC ("TPC track quality" requirement to reject short tracks for which the reconstruction is less reliable).

3. *External veto.* Some reconstruction failures can lead to a muon candidate track starting in the FGD fiducial volume even if the real muon started far upstream. For example a muon originating in the PØD and undergoing a large scatter in FGD1 may be reconstructed as two tracks (one PØD-TPC1-FGD1, and the other FGD1-TPC2). In order to exclude such events, if there is a TPC track with higher momentum than the muon candidate and starting more than 150 mm upstream (outside the FV) the event is rejected. Additionally, for FGD2 selection, the event is vetoed if there is a potential muon candidate in FGD1 fiducial volume.

4. *Broken track veto.* A TPC-FGD track is first reconstructed in the TPC and then projected to the FGD to match its hits incrementally. Matching failures are more likely to happen in the first matched hits, resulting in a broken track starting at the end of the FGD and crossing the TPC, which might be taken as muon candidate even though the other part of the broken track was starting outside the fiducial volume. To avoid this, the *broken track veto* rejects events with the muon candidate starting in the last XY module of the FGD and with another FGD track starting outside the fiducial volume (and not reaching the TPC).

5. *Muon PID cut.* The particle identification procedure (PID) is applied to the muon candidate based on the dE/dx distribution measured in the TPC. The energy deposit in the TPC is compared with the energy deposit expected under the assumption of four particle hypothesis: muon, pion, electron and proton. Based on that, a discrimination function is applied.

   The dE/dx is estimated as a truncated mean of the energy released in the TPC. Pulls are calculated as:

$$\text{Pull}_i = \frac{(dE/dx_{\text{measured}} - dE/dx_{\text{expected},i})}{\sigma_{(dE/dx_{\text{measured}} - dE/dx_{\text{expected},i})}} \tag{5.1}$$

   where $dE/dx_{\text{expected},i}$ is the value of the truncated mean for the particle hypothesis $i = \mu^-, \pi^{+/-}$ or p. For each hypothesis the likelihood L_{particle} is defined as:

$$L_i = \frac{e^{-\text{Pull}_i^2}}{\sum_l e^{-\text{Pull}_l^2}} \tag{5.2}$$

107

Electrons, which are not minimum ionising particles (MIP), are rejected by requiring that:

$$L_{\text{MIP}} = \frac{L_\mu + L_\pi}{1 - L_p} > 0.8 \tag{5.3}$$

applied only for tracks with $p < 500$ MeV/c. A further cut removes protons and pions:

$$L_\mu > 0.05 \tag{5.4}$$
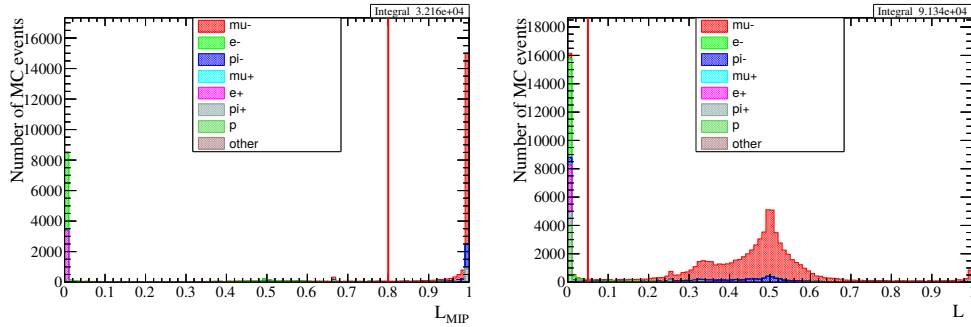
Figure 5.2: Distributions of L_{MIP} (Eq. (5.3)) and L_μ (Eq. (5.2)). The red lines show the cut value decided to enhance the muon candidate purity of the sample.

Fig. 5.2 shows the distributions of L_{MIP} and L_μ. The red lines show the cut value decided to enhance the muon candidate purity of the sample.

Events passing these criteria define the ν_μ CC-inclusive selection either in FGD1 or in FGD2.

5.2.1 Data-MC Comparison

Fig. 5.3 shows the data-MC comparison for the ν_μ CC inclusive selections in FGD1 and in FGD2, as a function of the reconstructed energy evaluated with the kinematic formula of Eq. (4.6): for both selections the MC simulation well agrees with the data; the mean reconstructed energy is well reproduced by the MC at the level of $1.5 \pm 3.1 / 650$ MeV. The momentum is measured in the TPC and extrapolated at the

beginning of the track, correcting for the energy lost in the FGD. For a muon origi-
nated in the water of FGD2 the track length between the vertex and the first hit in
the nearest scintillating bar, is not taken into account. This might be the reason, or at
least part of it, why the average reconstructed energy for the FGD2 selection is slightly
lower than the FGD1 selection, as can be seen in Fig. 5.3. Anyway, considering that
the energy loss for a minimum ionising particle in water is about $2\,\mathrm{MeV}$ per cm, and
that the water modules have a width of only $2.5\,\mathrm{cm}$, the correction would be very small.
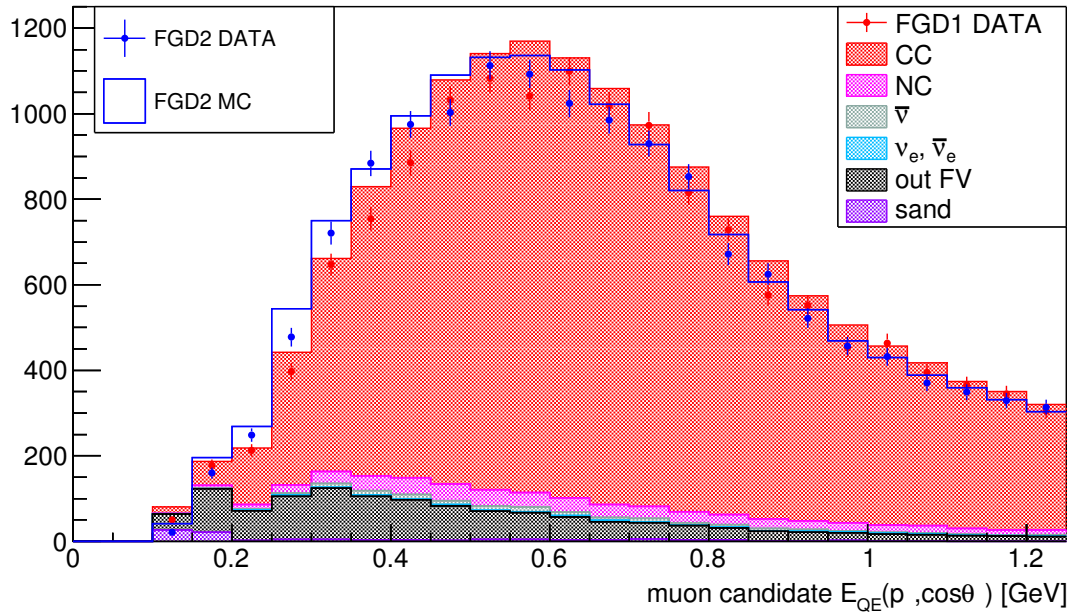
Figure 5.3: Data-Monte Carlo comparison of the reconstructed energy distribution for both the FGD1 and the FGD2 selections. Red and blue circles (with statistical error bars) are the data points for FGD1 and FGD2 respectively. The coloured area is the MC distribution for FGD1, broken down by the predicted NEUT reactions, whilst the blue line is the FGD2 MC.

5.2.2 Efficiency, Purity and Background

The efficiency is defined as:

$$\epsilon = \frac{N_{\text{selected | generated}}}{N_{\text{generated}}} \tag{5.5}$$

1792 where $N_{\text{generated}}$ is the number of interactions generated by the MC and N_{selected} — generated

1793 represents how many of them were reconstructed and selected.

1794 Note that with this definition, the efficiency includes also the selection acceptance.

1795 Fig. 5.4 shows the efficiency evaluated at each step of the selection described in

1796 Section 5.2, for both selections, in FGD1 (red) and in FGD2 (blue). For the number

1797 of generated interactions, all the ν_μ CC interactions predicted by NEUT in the fiducial

1798 volume are considered (cf. Section 7.3). The final efficiency predicted by NEUT, after

1799 the last cut, is 53.66 % for the selection in FGD1 and 53.85 % for the selection in FGD2.
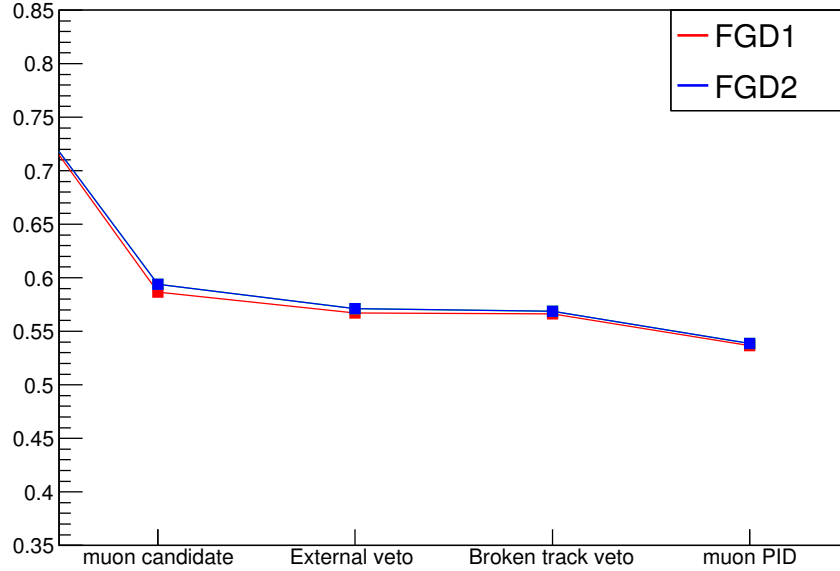
Figure 5.4: Efficiency evaluated at each step of the selection described in Section 5.2 for both selections, in FGD1 (red) and in FGD2 (blue).

1800 Fig. 5.5 shows the efficiency as a function of the true muon direction, in terms

1801 of the θ angle respect to the neutrino direction (the lepton produced by the neutrino

1802 interaction associated to the selected muon candidate). The requirement of crossing

1803 a TPC (cf. Section 5.2) significantly limits the efficiency at high angles. Timing

1804 information of tracks crossing both FGDs can tell whether the particle is going from

1805 FGD1 towards FGD2 or vice versa. This helps the reconstruction of backward-going

1806 tracks originating in FGD2, and explains the better efficiency of the selection in FGD2

for negative $cos\theta$. Nevertheless the fraction of reconstructed events with a backward-going muon, shown as well in Fig. 5.5, is quite negligible.
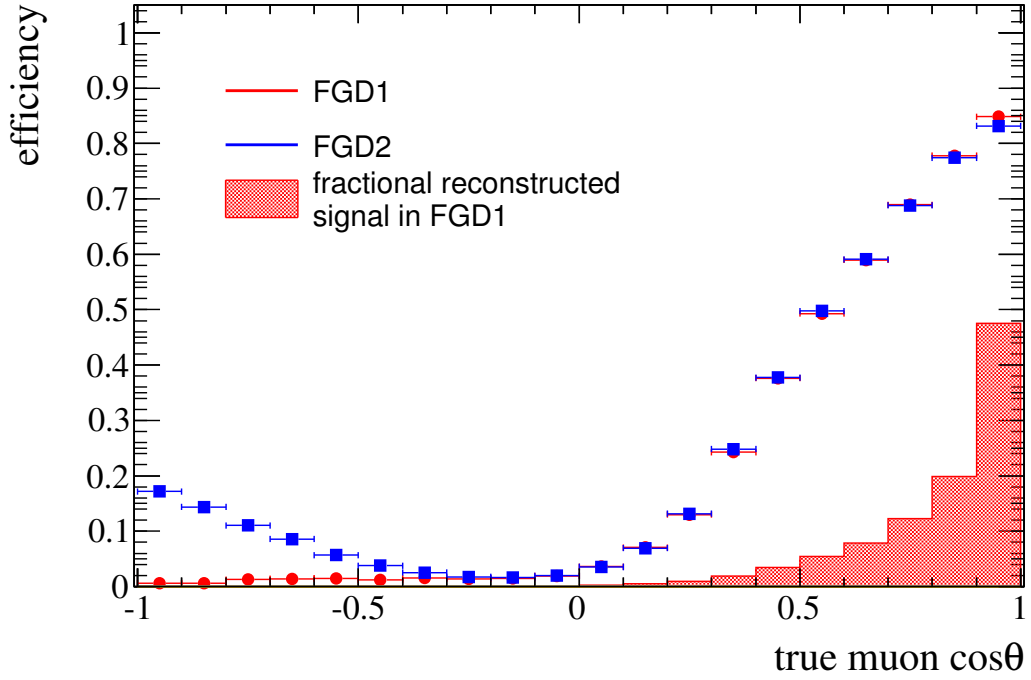
Figure 5.5: Efficiency as a function of the true muon direction, in terms of the θ angle respect to the neutrino direction, for both selections, in FGD1 (red) and in FGD2 (blue). Statistical error bars are shown, but small. The fractional distribution of the reconstructed events in FGD1 is shown as well.

Fig. 5.6 shows the true muon $(p_\mu, cos\theta)$ phase space predicted by NEUT for ν_μ-CC interactions in FGD1 and in FGD2 fiducial volumes. High energy muons are more likely to be in the forward direction, where the detector efficiency is high. On the contrary, muons scattered at high and negative angles, where the detector efficiency is low, always have a relatively low momentum. This explain why the efficiency as a function of the true muon momentum decreases below 1 GeV, as it can be seen in Fig. 5.7. Considerations on the phase space are discussed in Section 7.3.

The purity is defined as:

$$\text{purity} = \frac{N_{\text{selected}} - N_{\text{background}}}{N_{\text{selected}}} \tag{5.6}$$
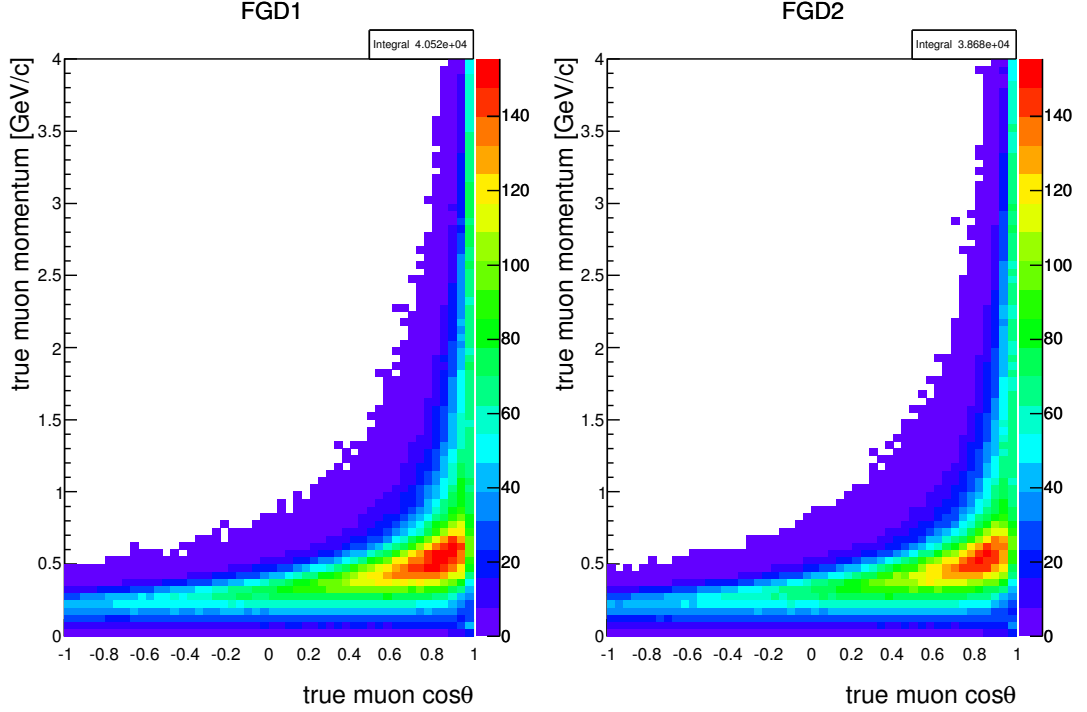
Figure 5.6: $(p_\mu, cos\theta)$ phase space of the true muons from ν_μ-CC interactions predicted by NEUT in FGD1 (left) and FGD2 (right) fiducial volumes.
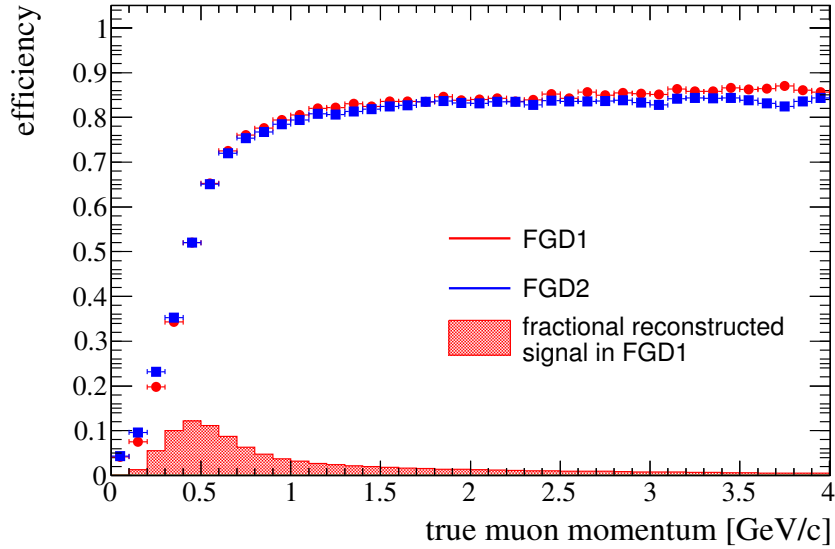
Figure 5.7: Efficiency as a function of the true muon momentum, for both selections, in FGD1 (red) and FGD2 (blue). Statistical error bars are shown, but small. The fractional distribution of the reconstructed events in FGD1 is shown as well.

1817 where $N_{\text{selected}} - N_{\text{background}}$ is the number of signal events among the selected ones.

1818 The purity predicted by NEUT after the last cut is 90.31 % for the selection in FGD1
1819 and 88.65 % for the selection in FGD2. The reconstructed momentum and direction
1820 distributions of the muon candidates are shown in Fig. 5.8 for both the FGD1 and
1821 the FGD2 selections, broken down by the predicted NEUT reactions. The sources of
1822 background are:

1823 1. *out of fiducial volume* (main background): ν_μ-CC interactions happening outside
1824   the fiducial volume of FGD1 or FGD2 respectively;

1825 2. *non ν_μ-CC interactions*: these are neutral-current (NC), $\bar{\nu}_\mu$ and ν_e interactions,
1826   where a π^- (in most cases) is mis-identified as the μ^- candidate (cf. Fig. 5.9).
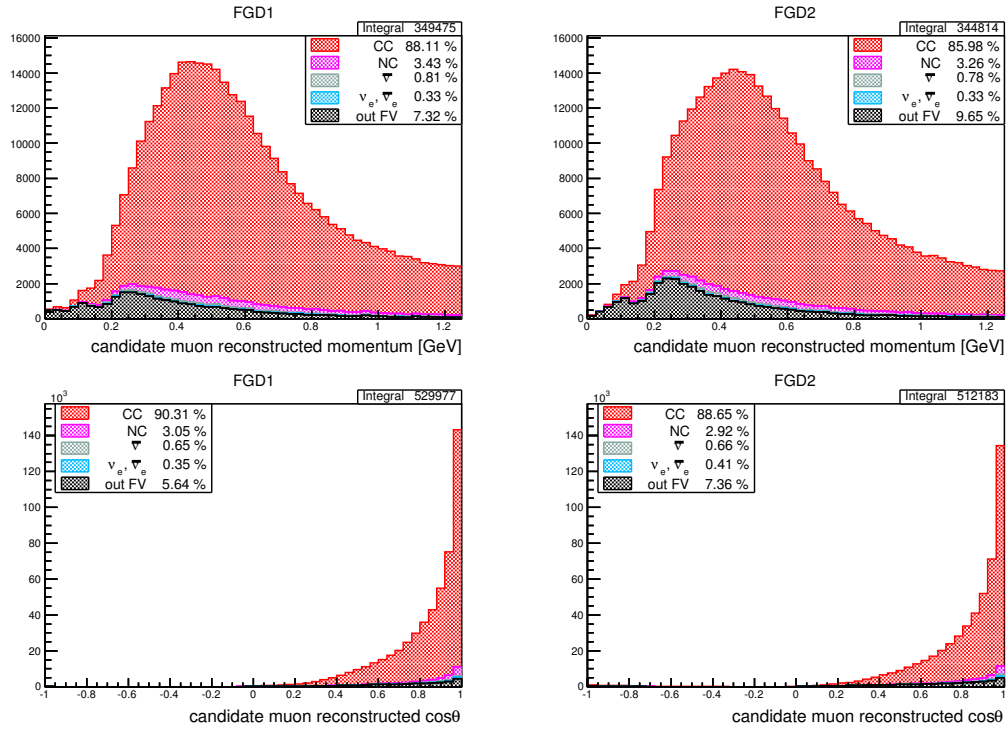
Figure 5.8: Reconstructed momentum (top) and direction (bottom) distributions of the muon candidates for both the FGD1 (left) and the FGD2 (right) selections, broken down by the predicted NEUT reactions. "out FV" are the events occurred out of the fiducial volume. The percentages on the legend are the fractions of each component in the whole plotted distribution.

Fig. 5.9 shows again the reconstructed momentum and direction distributions but broken down by the true particles associated to track chosen as muon candidate. In a non-negligible fraction of events the chosen track is not associated to the true muons, but most of them are background events: this can be seen in Fig. 5.10 where it is shown the same distributions after removing the background events. The remaining $\sim 2\%$ of non-true muons in CC signal events is not considered background, nor in the T2K oscillation analyses neither in this analysis, hence it is considered as a reconstruction inefficiency (which might cause events being reconstructed in a wrong bin). Note that events where a pion is selected as muon candidate affect the secondary interaction pion systematics (cf. Section 6.2.3.1).
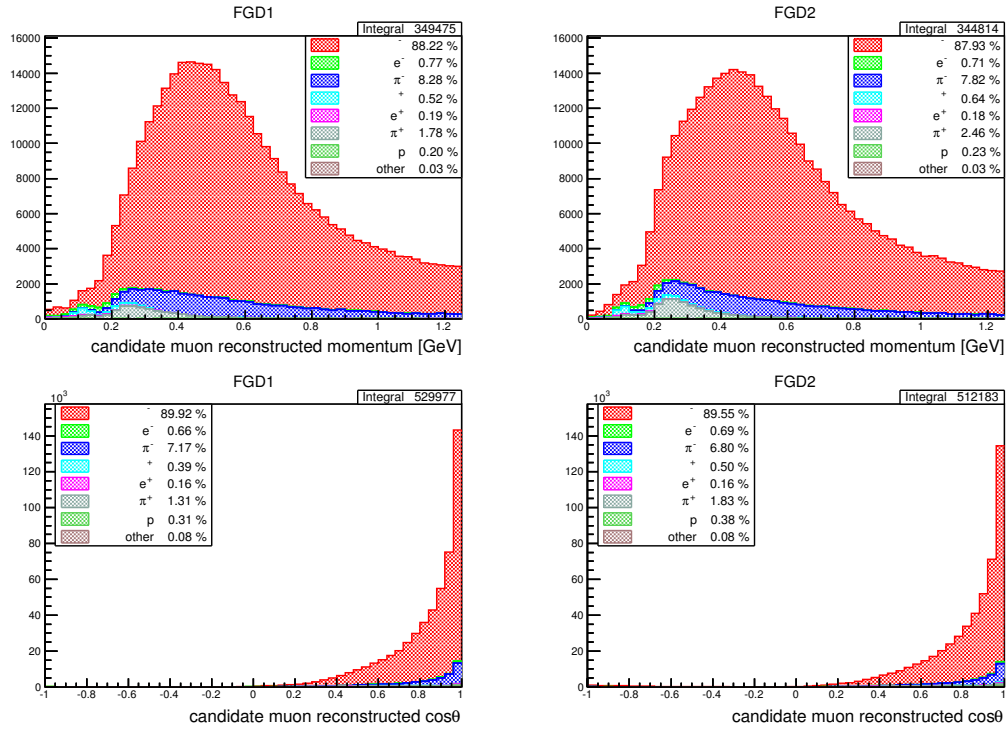
Figure 5.9: Reconstructed momentum (top) and direction (bottom) distributions of the muon candidates for both the FGD1 (left) and the FGD2 (right) selections, broken down by the true particles associated to the muon candidate (as predicted by NEUT). The percentages on the legend are the fractions of each component in the whole plotted distribution.

Fig. 5.11 shows again the reconstructed momentum and direction distributions but broken down by the target nucleus elements where the true neutrino interaction oc-
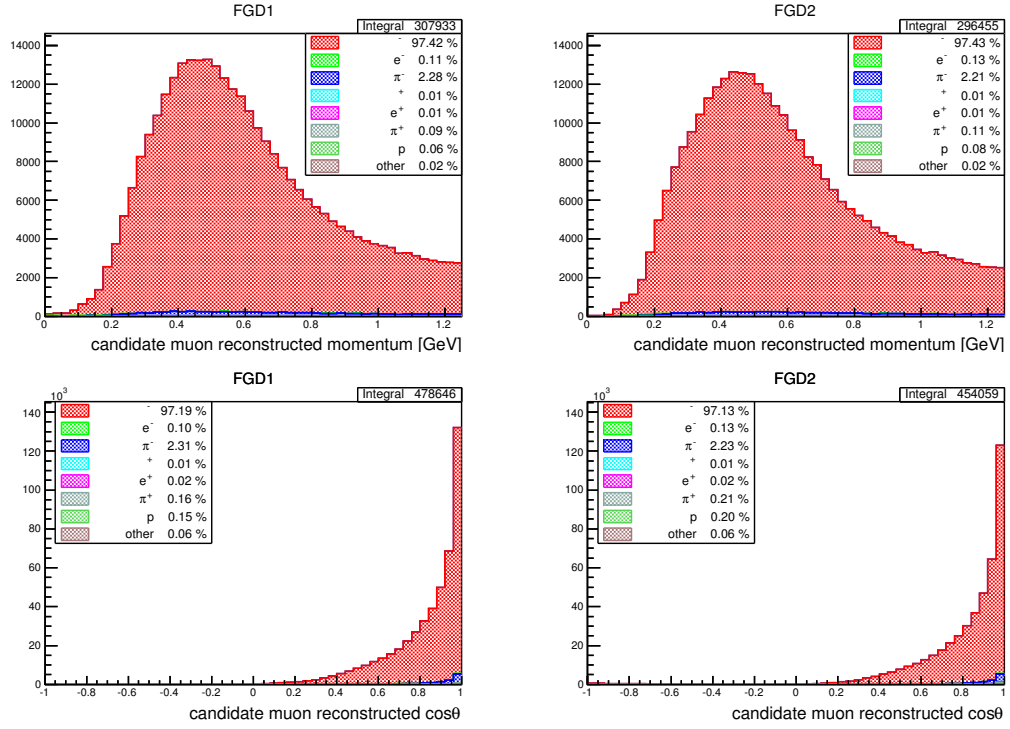
Figure 5.10: Reconstructed momentum (top) and direction (bottom) distributions of the muon candidates for both the FGD1 (left) and the FGD2 (right) selections, without the background events, broken down by the true particles associated to the muon candidate (as predicted by NEUT). The percentages on the legend are the fractions of each component in the whole plotted distribution.

1839 curred. There are non-negligible contributions from heavy targets, but they are actu-
1840 ally background events occurred out of the fiducial volume ("out FV"), as it can be
1841 seen in Fig. 5.12, where it is shown the same distributions after removing the "out FV"
1842 background events. This allows assuming that any interaction model uncertainties on
1843 heavy targets is covered by the out of fiducial volume systematics (Section 6.2.4.1).
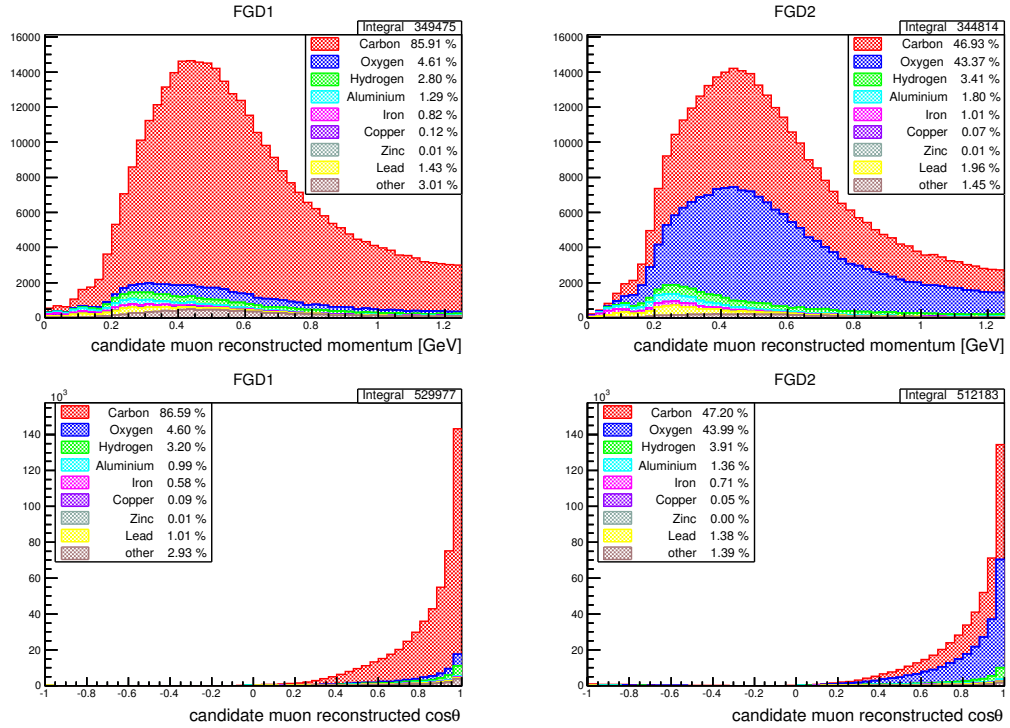
Figure 5.11: Reconstructed momentum (top) and direction (bottom) distributions of the muon candidates for both the FGD1 (left) and the FGD2 (right) selections, broken down by the target nucleus elements where the true neutrino interaction occurred (as predicted by NEUT). The percentages on the legend are the fractions of each component in the whole plotted distribution.
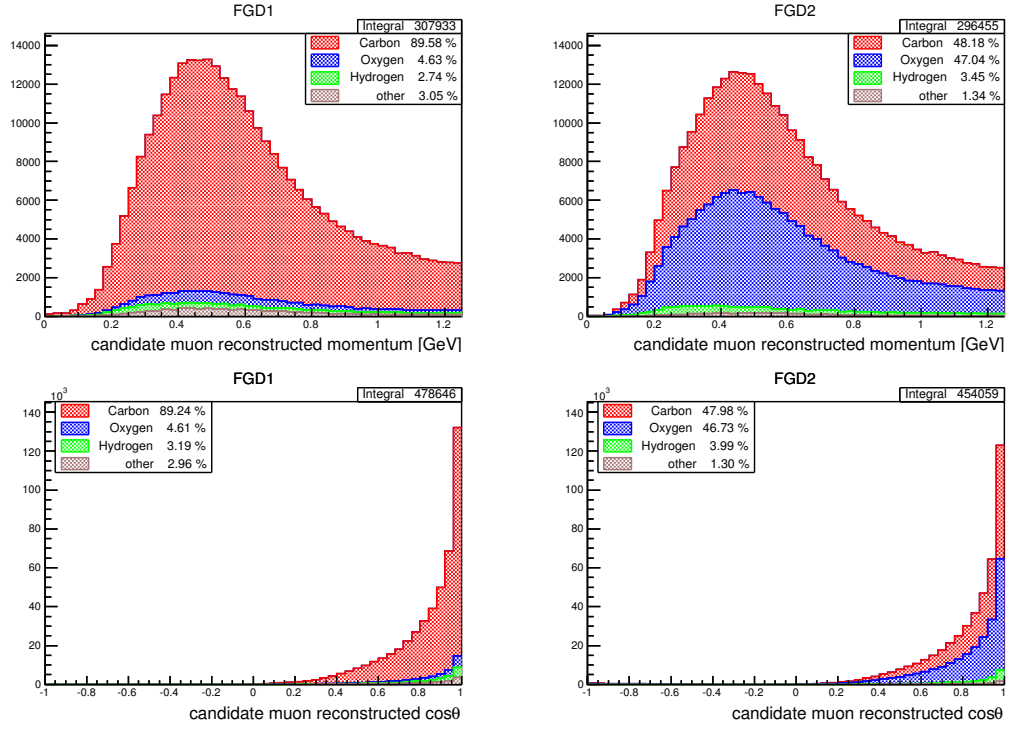
Figure 5.12: Reconstructed momentum (top) and direction (bottom) distributions of the muon candidates for both the FGD1 (left) and the FGD2 (right) selections without the "out FV" background events, broken down by the target nucleus elements where the true neutrino interaction occurred (as predicted by NEUT). The percentages on the legend are the fractions of each component in the whole plotted distribution.

117

6

Estimation of Uncertainties

Since most of the systematics uncertainties cancel in the ratio, the largest uncertainty in the cross-section ratio of this thesis is the statistical error.

The systematic uncertainties can be grouped in detector, beam flux and model uncertainties, and they are detailed in Section 6.2, Section 6.3 and Section 6.4 respectively. Since the flux and the model uncertainties cancel to a very good degree in the ratio, the detector systematics is the largest systematics, in particular due to the secondary pion interactions (Section 6.2.3.1) and secondarily because of the mass systematics (Section 6.2.3.2). The detector systematics are well understood, which is important to legitimate the unfolding procedure.

The full ND280 MC software performs a complex and thorough simulation which includes the flux generation, the neutrino-nuclear interaction, the ND280 detector simulation and track propagation. Ideally any uncertainties would be treated with a full re-simulation across the entire MC chain but this is unfeasible due to CPU limits. The alternative is studying the effect of altering the input parameters and applying weights.

Uncertainties could be propagated traditionally but an approach of throwing toys and calculating the resulting covariances is more durable given the often non-linear response functions. In general, the value of a systematic parameter is thrown according to its expected prior probability distribution, and the effect on the observables is propagated to the cross-section measurement to evaluate the systematic error; the propagation is described in Section 6.1.

6.1 Uncertainties Propagation to the Cross-Section Results

All uncertainties are numerically calculated throwing toys which generate pseudo-experiments that go through the unfolding framework. To evaluate the effect of a systematic uncertainty, the extracted cross section must be recalculated for each toy of the systematic parameters. For the data statistical uncertainty only the actual data selection is varied. For all the other error sources the MC selection (truth and reconstructed) and the flux are variate while the actual data selection is kept unaltered. This means that the unfolding matrix (Section 4.2) efficiency, purity, and flux may change depending on which error source is being propagated. Therefore, each pseudo-experiment corresponds to an alternative hypothesis and gives a different cross-section result.

For each independent error source, a covariance matrix is built across the bins in which the cross-section measurement is made. The covariance for bins (i, j) is defined as:

$$cov_{i,j}^{s} = \frac{1}{N_s - 1} \sum_{n_s = 1}^{N_s} (\sigma_{i,n_s} - \overline{\sigma}_{i,n_s})(\sigma_{j,n_s} - \overline{\sigma}_{j,n_s}) \tag{6.1}$$

where σ_{i,n_s} and σ_{j,n_s} are the measured cross-section values in bins i and j for throw n of source s, N_s is the total number of throws, and the overline denotes the sample mean across all throws.

When sources are independent these covariance matrices can be added to form the final overall covariance matrix which is then used to extract the overall uncertainty across bins. The diagonals of the covariance matrix gives the variance for each bin.

The cross-section results of this analysis are given by the formulas derived in Section 4.3.2. Eq. (4.19) is evaluated for each throw to build the covariance matrix. This means that the number of events of FGD1 and in FGD2 in each bin, as they appear in the formulas, are evaluated at each throw, preserving the correlations between the FGDs in the propagation.

Different runs may have different flux properties (Section 5.1), thus they need to be handled separately for measuring the cross section. Nevertheless all uncertainties

have to be treated as completely correlated across runs, and this is done by ensuring identical seeding for all throws.

Uncertainties can be categorised into five categories, assumed to be independent: [1]

- statistical, for data and for MC

- detector

- flux

- cross-section model

    - neutrino interaction model

    - final state interaction model ("FSI")

The way of propagating the uncertainties onto the cross-section results presents some differences among these error categories. Statistical uncertainties are evaluated using 10000 pseudo-experiments for both data and MC, with poissonian variations. Propagation of systematics is much more CPU intensive, so a smaller number of throws, 500, was used.

6.1.1   Propagation of Statistical Errors

While all the other systematic uncertainties are treated on a event-by-event basis, the statistical uncertainties are performed on a bin-by-bin basis. All the bins are assumed independent of each other and are smeared under the Poisson $\sqrt{N}$ assumption. Statistical errors affect both MC and data in the same way. To evaluate the data statistical uncertainties, each pseudo-experiment only varies the data reconstructed distribution. To evaluate the MC statistical uncertainties, each pseudo-experiment varies the MC reconstructed and truth distributions, implying also a new unfolding matrix, efficiency, and background in each throw. The selections in FGD1 and in FGD2 are designed such that an event can only pass one of them, ensuring the two samples are statistically uncorrelated.

---

[1]In general, if control samples are used to constrain the background, systematic errors from different sources would become correlated and could not be thrown independently. However, in this analysis the background is relatively small (Section 5.2.2) and control samples are not used.

6.1 Uncertainties Propagation to the Cross-Section Results

In an analysis which performs the background subtraction (Section 7.4) the MC background and the measured data are independent, thus when propagating the data statistical uncertainties the subtracted MC background is kept constant over throws. This means that the variation on the data distribution is the same with or without background subtraction:

$$\text{Var}[N_{\text{data}} - N_{\text{background}}] = \text{Var}[N_{\text{data}}] = \sigma^2[N_{\text{data}}] \tag{6.2}$$

This implies that the background-subtracted result carries a larger fractional uncertainty:

$$\frac{\sigma^2[N_{\text{data}}]}{N_{\text{data}} - N_{\text{background}}} > \frac{\sigma^2[N_{\text{data}}]}{N_{\text{data}}} \tag{6.3}$$

In an analysis which corrects the data distribution by the purity instead of subtracting the background, N_{data} is simply scaled, which preserves the fractional error.

The fact of throwing toys instead of calculating analytically the statistical uncertainties guarantees of handling properly the FGDs subtraction (Eq. (4.17)) and the water to scintillator ratio (Eq. (4.19)) together with the background subtraction and the unfolding. Since the data statistical uncertainty is the largest in this analysis, it is worth to give an estimation.

The variance of a cross-section ratio R which has been defined in Eq. (4.19) is:

$$\text{var}(R) = (\frac{T_{\text{FGD1}}}{T_{\text{FGD2water}}} \cdot \frac{\Phi_{\text{FGD1}}}{\Phi_{\text{FGD2}}})^2 \cdot [(\frac{1}{\hat{N}_{\text{FGD1}}})^2 \cdot \text{var}(\hat{N}_{\text{FGD2}}) + (-\frac{\hat{N}_{\text{FGD2}}}{(\hat{N}_{\text{FGD1}})^2})^2 \cdot \text{var}(\hat{N}_{\text{FGD1}})]$$

$$= (\frac{T_{\text{FGD1}}}{T_{\text{FGD2water}}} \cdot \frac{\Phi_{\text{FGD1}}}{\Phi_{\text{FGD2}}})^2 \cdot [\frac{\hat{N}_{\text{FGD2}}}{(\hat{N}_{\text{FGD1}})^2} + \frac{(\hat{N}_{\text{FGD2}})^2}{(\hat{N}_{\text{FGD1}})^3}]$$

$$= (\frac{T_{\text{FGD1}}}{T_{\text{FGD2water}}} \cdot \frac{\Phi_{\text{FGD1}}}{\Phi_{\text{FGD2}}})^2 \cdot (\frac{\hat{N}_{\text{FGD2}}}{\hat{N}_{\text{FGD1}}})^2 \cdot [\frac{1}{\hat{N}_{\text{FGD2}}} + \frac{1}{\hat{N}_{\text{FGD1}}}] \tag{6.4}$$

Choosing a simple case where there are exactly the same number of events in FGD1 and in FGD2 ($\hat{N}_{\text{FGD1}} = \hat{N}_{\text{FGD2}} = \hat{N}$), the statistical error would be:

$$\sqrt{\text{var}(R)} = \frac{T_{\text{FGD1}}}{T_{\text{FGD2water}}} \cdot \frac{\Phi_{\text{FGD1}}}{\Phi_{\text{FGD2}}} \cdot \sqrt{\frac{2}{\hat{N}}} \simeq \frac{1}{0.46} \cdot 1.011 \cdot \sqrt{\frac{2}{\hat{N}}} \simeq \frac{3.1}{\sqrt{\hat{N}}} \tag{6.5}$$

where 0.46 is the ratio between the number of targets $T_{\text{FGD2water}}$ and T_{FGD1} calculated in Section 4.3.3, and 1.011 is the flux normalisation ratio estimated in Eq. (4.20).

In reality FGD1 and FGD2 don't have exactly the same number of events, nevertheless from Eq. (6.5) we can estimate that for a ratio $R \sim 1$, in a bin with $\hat{N}_k = 2000$ events the fractional error should be around 7%, and for $\hat{N} = 20000$ events the fractional error should be around 2.2%. Because of Eq. (6.3), the amount of background increases these values.

6.1.2 Propagation of Detector Errors

All detector uncertainties are treated on a event-by-event basis, some of them via reweighting ("weight systematics"), other varying some kinematic variables and redoing the selection ("variation systematics"). Both types of systematics can affect the MC by altering the unfolding matrix, the efficiency and the background. All detector systematics are thrown simultaneously, allowing correlations among them.

A detailed discussion of individual systematics is discussed in Section 6.2.

The central value of the final cross-section results includes some cross-section model corrections discussed in Section 6.4.1) ("NIWG tuning"), which are not taking into account when the detector systematics are propagated (for software limitations). On the other hand, the covariance matrix Eq. (6.1) associated with detector uncertainties is evaluated using the average of detector throws as a reference. This implies that the variance in each diagonal bin is related to the average of the throws, but not to the final result. Nevertheless, the fractional error is preserved, thus it is easy to extrapolate the absolute error on the tuned final result.

6.1.3 Propagation of Flux and Theory Errors

Flux and cross-section model errors are all handled by altering a set of parameters (or dials), discussed in Section 6.3 and Section 6.4 respectively. Correlations between parameters are taken into account using the covariance matrix provided by the T2K's NIWG group. Gaussian throws are performed using this covariance matrix across the three groups, flux, neutrino interaction model, and FSI model, via the Cholesky decomposition method: for each group, the parameters within that group are simultaneously varied while the other parameters are kept to their nominal value. A reweighting procedure is then run across all the events to generate event-by-event weights for each value of each altered parameter.

6.2 Detector Uncertainties

The ND280 detector consists of many sub-detectors, hence there are a large number of sources of systematic uncertainties. Thanks to the design of ND280 (Section 3.2.1), all the systematics can be evaluated in the same way for both FGD1 and FGD2 selections.

Some derived parameters which directly affect the event selection are used to describe the uncertainties on MC (e.g. reconstruction efficiencies or mean and resolution of some reconstructed observables). In practice, the uncertainty on a given observable is quantified by evaluating the data to MC differences in an ad-hoc control sample (samples not used for the analysis).

These systematic uncertainties on physical parameters are then propagated to the number of events passing the selection cuts. This propagation is performed in three different ways according to the nature of the variables to be propagated.

- **Variation systematics** This concerns all the reconstructed quantities on which we have uncertainties. For these variables, the propagation consists in altering their values, and re-processing the selection for every pseudo-experiment: some events might migrate in a different bin or being selected/discarded depending on the applied variations.

- **Weight systematics** In this case, the selection does not need to be re-processed since the propagation is performed by reweighting the events: an event-by-event weight is computed for each pseudo-experiment, and it is used to increase or reduce the contribution of each event to the selection.

  - **Efficiency-like systematics** This concerns all the variables that correspond to a reconstruction/detection efficiency, from which event-by-event weights are evaluated.

  - **Normalisation systematics** This generally concerns sub-samples of the selection associated to a given systematics source, which can affect the total event normalisation. The uncertainties on a certain sub-sample of the selection is used to calculate the weight which scales only the events associated to the sub-sample.

In all cases, a Probability Density Function (PDF) must be assumed: all systematic sources are assumed to be Gaussian except the B-field distortion, for which a uniform PDF is used.

For some sources of uncertainties, discrepancies between data and MC are observed either in the resolution or in the mean value of the observables. In these cases, a correction is applied to take into account the discrepancies. Details can be found in the descriptions of each single systematics, in the following sections.

Table 6.1 details the list of the detector systematic uncertainties considered in this analysis, as well as the corresponding error propagation model and PDF assumed, and whether or not a correction has been applied.

6.2.1 Correlations Among Variation and Weight Systematics

All systematics are numerically calculated generating a large number of pseudo-experiments with altered parameters. While the "weight systematics" are considered independent among themselves (there is not a correlation matrix applied), the "variation systematics" affect each others, and they also affect some of the weight systematics. To take into account this correlations, all the detector systematics are applied in conjunction, and in each pseudo-experiment the weight systematics are evaluated after having applied the variation systematics, i.e. after having altered the concerned observables. Nevertheless, the framework allows to alter each systematics individually, in order to obtain an individual error for each source. Being that there are no systematics anti-correlated, the sum in quadrature of the individual errors is larger than the one obtained applying all systematics at once. The error given applying all the systematics in conjunction is the error quoted on the final results, since it properly takes into account the correlations among them.

6.2.2 TPC-Related Systematics

The TPC and FGD systematic uncertainties have been studied in depth by the NuMu ND280 working group, and are described in detail in Reference [142, 151]. These systematic uncertainties are studied with a control sample of particles that cross all three TPCs, unless otherwise stated.

Systematic error source	Propagation model	PDF	Correction applied
TPC related			
Magnetic Field distortions	Variation	Flat	no
TPC momentum resolution	Variation	Gaus	yes
TPC momentum scale	Variation	Gaus	no
TPC PID	Variation	Gaus	yes
TPC cluster efficiency	Efficiency-like	Gaus	no
TPC tracking efficiency	Efficiency-like	Gaus	no
TPC charge ID efficiency	Efficiency-like	Gaus	no
TPC-FGD matching efficiency	Efficiency-like	Gaus	no
MC modelling related			
Pion secondary interactions	Normalisation	Gaus	no
FGD mass	Normalisation	Gaus	no
Background related			
Out FV background	Normalisation	Gaus	no
Sand muon background	Normalisation	Gaus	no
Pile-up	Normalisation	Gaus	yes

Table 6.1: List of detector systematic uncertainties and their treatment.

Magnetic field distortions give anomalous curvatures of the particles crossing the detector, affecting the measurements of their momentum and charge. The distortions, unavoidable near the field edges, were measured with a Hall probe before the detectors were installed, and the reconstruction accounts for these measured deviations from the ideal field. The systematic uncertainty is evaluated by looking at the difference in reconstructed momentum turning on/off the magnetic field corrections.

TPC momentum resolution is studied on a sample of tracks that cross multiple TPCs, by comparing the reconstructed momentum in each TPC after correcting by the energy loss in the FGDs. Their difference should follow the Gaussian distribution centred at 0 and its standard deviation is the momentum resolution. The uncertainty is given in bins which represent the x coordinate of the track, and they are assumed to be fully correlated among themselves since they do not originates from different sources of uncertainty. No angle dependence was found. The inverse momentum resolution is found to be better in MC than in data: to account for this, a correction is applied to the MC as a function of the transverse momentum. It might be that the observed discrepancy is caused by the magnetic field distortion, thus this uncertainty would be double counting. In fact the cause could be the electric field distortions together with the magnetic field and the MicroMEGAS/TPC alignment. Nevertheless this is not clearly understood and a conservative approach requires to include both errors. However, the correlation between this uncertainty and the magnetic field distortions, which are variation systematics, is taken into account by applying them in conjunction, as explained in Section 6.2.1.

TPC momentum scale depends on the overall magnetic field strength because there is a calibration mapping between the curvature and the momentum of the tracks. Uncertainties in the magnetic field strength lead to an uncertainty on the momentum scale of 0.6%, which is confirmed using a control sample of cosmic muons passing through both FGDs.

TPC PID depends on dE/dx measurements, which depend on a particle hypothesis: the uncertainties mainly come from the difficulty of particle separation. Mis-

identification of muons (more probable at high momentum) can cause events migration between signal and background. The systematics is evaluated by comparing the energy deposit of data and MC in high-purity control samples of electrons, muons and protons. The muon control sample is composed of through-going sand muons; the electron control sample is based on a γ conversion sample studied by the NuE group; the proton control sample is found by selecting positive tracks with $0.3 < p < 1.1\,\mathrm{GeV}$. Pull distributions are calculated for both data and MC and the differences are taken to correct the MC. The uncertainty is evaluated as a function of momentum, pull's mean and pull's sigma for each particle type and for each TPC. Being the three control samples very pure, the parameters for a particle types are assumed to be fully uncorrelated from those of another particle type. The correlation between this uncertainty and the momentum uncertainties, which are variation systematics, is taken into account by applying them in conjunction, as explained in Section 6.2.1.

TPC cluster efficiency describes the efficiency of reconstructing a cluster where one is expected; it is found to better than 99%. This systematics is evaluated as a function of the horizontal and the vertical clustering, which are assumed to be fully correlated, because they have the same underlying uncertainty, namely the hit efficiency.

TPC tracking efficiency is estimated from the difference observed between data and MC in the tracking efficiency of a control sample of through-going muons. In all three TPCS, the efficiency is found to be better than 99% for both data and MC (for tracks with 16 clusters or more) without any dependence on angles, momenta, track lengths or number of clusters. The inefficiency due to the overlap from a second nearly collinear track is found to be negligible for both data and MC.

TPC charge ID efficiency is calculated studying how often the assigned charge is wrong, by comparing the charge assignment in each TPC. The charge of a track is determined from its curvature in the magnetic field. This uncertainty is found to be less than 1% for momenta less than $5\,\mathrm{GeV}$. For larger momenta the uncertainty increases because the tracks are more and more straight. In the very low momentum bins (i.e. $p < 0.3\,\mathrm{GeV}$), the uncertainty can get up to a few %,

because low momentum particles are less likely to cross the three TPCs, and mis-matching of tracks belonging to different particles is more likely to happen. This uncertainty depends on the error on the momentum provided by the likelihood fit of the track, therefore it depends on the momentum systematics. The correlation between this uncertainty and the momentum systematics, which are variation systematics, is taken into account by the fact that in each pseudo-experiment this uncertainty is applied on top of the altered momentum systematics, as explained in Section 6.2.1.

TPC-FGD matching efficiency is evaluated with a control sample of through-going muons from cosmics and sand muons. A muon passing through two near TPCs should also cross the FGD in between: if the event contains a TPC-FGD segment, then it is considered a good match. The difference between data and MC is found to be negligible and the matching efficiency is found to be 100% for both FGDs, in both MC and data. However, this does not represent the whole uncertainty: efficiency to match short tracks generated close to the edge of the FGD has to be taken into account. This uncertainties on short tracks is estimated from the FGD hit efficiency of the last two layers. A matching failure can also lead to including out of fiducial volume events, but this issue is evaluated in the out of fiducial volume systematics.

6.2.3 MC Modelling-Related Systematics

6.2.3.1 Pion Secondary Interactions

Pion secondary interactions refer to any interactions that pions can undergo once they have left the nucleus. The most significant interactions are *absorption* (the pion is completely absorbed by the nucleus), *charge exchange* (the pion interacts with the nucleus and creates a π^0), *quasi-elastic scattering* (the pion scatters off the nucleus without producing any additional pions). While, absorption and charge exchange do not affect this analysis, quasi-elastic scattering can cause a change in the momentum or direction of the track which might alter the selection. Although these interactions are modelled in GEANT4 (Section 3.3), the predictions have been found to be significantly different from the available external data. A correction is therefore calculated to take

into account for this discrepancy, The systematic uncertainty is propagated by looking at all the pions associated to each event and generating weights from the uncertainty in the external data. Details can be found in Reference [152].

6.2.3.2   FGD Mass

The FGD mass systematics is evaluated from the uncertainty on the density of the scintillator and water modules. The FGD1 consists overall of 15 scintillator modules (each one composed of two layers of scintillating bars), while the FGD2 is overall composed of 7 scintillator modules interleaved with 6 water modules. The mass uncertainties are propagated either for a scintillator module or for a water module, according to whether the true interaction occurs in the former or in the latter. When the FGDs have been assembled, each component has been carefully measured, which allow to have the uncertainties 'as built'. The density of a scintillator module has been evaluated with a 0.6% uncertainty, and the densities of the water modules with a 0.55% uncertainty (dominated by the uncertainty on the masses of plastic and glue). More details can be found in Reference [153].

6.2.4   Background-Related Systematics

Background-related systematic uncertainties are due to interactions occurring outside the fiducial volume. Interactions in the sand around ND280 are also studied (in a separated MC sample), since they produce muons which can cross the detector. In any case, these interaction can produce a muon track that can be mis-identified as a ν_μ CC candidate in the fiducial volume. Moreover, they can also trigger the veto cut in the selection, which might prevent a true ν_μ CC events to be selected (pile-up). Therefore, the background-related systematic uncertainties can be divided in:

Out of fiducial volume : due to interactions in the ND280 detector but outside the fiducial volume, which mimic an event inside the fiducial volume.

Sand muons : due to interactions outside the ND280 detector, which mimic an event in the fiducial volume.

Pile-up : due to any pile-up which prevents a true ν_μ CC events to be selected.

6.2.4.1 Out of Fiducial Volume

"Out of fiducial Volume" events ("out FV") are interactions reconstructed as originating in the FGD fiducial volume while the true vertex is outside. The "out FV" event rate has been found to be 5% of CC-inclusive events selected in FGD1 and 7.5% in FGD2. Two uncertainties are assigned to this systematics: an uncertainty on the rate and an uncertainty on the reconstruction.

The rate uncertainty is assigned to each "out FV" event depending on the sub-detector in which the event occurred (i.e. in SMRD, ECal, PØD, in the magnet or electronics). Disentangling the sources in this way, rather than using an average value, gives a smaller overall rate uncertainty.

The reconstructions uncertainty is calculated by splitting this background into 9 categories of events, and using the true information contained in a MC sample of CC-inclusive FGD events. These categories are:

- Interactions in the FGD (but outside the fiducial volume);

- Interactions in the tracker, upstream of FGD;

- Interactions in the tracker, downstream of FGD;

- From neutral parent;

- Backward-going tracks [1];

- High-angle tracks; [2];

- Last module failure [3];

- Double skipped layers [4];

---

[1]E.g. events in FGD or TPC walls with a backward-going track which is reconstructed as part of the main forward-going particle. MC does not behaves as data, therefore an uncertainty has been associated to this effect.

[2]When a track is bent too much, the reconstruction fails and the track is broken, appearing as a track starting inside the FGD fiducial volume (FV) even though it is not the case.

[3]The last module failure events are due to events missing hits in all X or Y planes, causing the reconstruction to break in the last module. This failure is mainly explained by readout issues for which all the hits in the X or Y plane were not properly reconstructed.

[4] When matching FGD hits to TPC tracks, the matching algorithm ignores a single missed layer, but if two layers in a row lack FGD hits, the matching routine gives up and the track is broken,

2167 • Hard scattering [5].

2168 Details can be found in [154].

2169 As explained in Section 5.2.2, being the fraction of predicted interactions on heavy
2170 nuclei very small (Fig. 5.12), it is assumed that any interaction model uncertainties on
2171 these targets is covered by the "out of fiducial volume" systematic (Section 6.2.4.1).

2172 6.2.4.2 Sand Muons

2173 The particles produced by neutrinos interacting in the pit walls and the surround-
2174 ing sand and entering the ND280 region are simulated by a separate MC simulation.
2175 They can produce tracks which mimic the neutrino interactions. The process of such
2176 simulation is described in detail in [155].

2177 A sample of sand MC was used to estimate the contamination of sand interactions
2178 to the selected neutrino events. The size of sand MC corresponds to $6.78 \cdot 10^{20}$ POT,
2179 which is the 118% of data taken during Runs II-IV.

2180 The ν_μ-CC selection in FGD1 and in FGD2 was applied to the sand MC samples.
2181 The number of events passing the selection, scaled to the POT number in data, gives
2182 an estimated contamination from sand interactions of 0.6% in FGD1 and 0.33 % in
2183 FGD2.

2184 Details can be found in Reference [142, 151].

2185 6.2.4.3 Pile-Up

2186 When two interactions occurs in the same bunch, a signal event can be rejected by the
2187 external veto cut (cf. Section 5.2), triggered by activity in the upstream TPC. This is
2188 more likely to happen because of interactions occurring upstream of the detector (sand
2189 muons), rather than because of a TPC tracks from another interaction in ND280.

2190 Since the beam spill MC sample and the sand muon MC sample are simulated
2191 separately, when the selection is processed on the beam spill MC sample, it does not

---

appearing as a track starting inside the FGD fiducial volume (FV) even though it is not the case. The
FGD hit efficiency is almost 100%, nevertheless there can be horizontal tracks which pass through the
dead coating material between scintillator bars, skipping more than one layer in a row. The MC doesn't
reproduce very well this effect, therefore an uncertainty has been associated to this effect.

[5]A muon which has a hard scatter in the FGD is difficult to reconstruct.

include the effect of the veto due to coincidence with a sand muon, while instead it does happen processing the real data. To take this into account, a correction is applied to the simulated events.

The correction is evaluated for each run separately, as the pile-up depends on the beam intensity, and it is defined as:

$$C_{\text{pile-up}} = \frac{N_{\text{TPC}} \cdot I_d}{POT_{\text{sand}} \cdot N_b} \, , \tag{6.6}$$

where N_{TPC} is the number of TPC events in the sand muon MC that trigger the veto cut, $I_d = POT_{\text{beam}}/nSpills$ is the beam intensity, POT_{sand} is the POT in the sand muon MC, and N_b is the number of bunches per spill (8 bunches in the runs considered in this analysis, i.e. Run II, III and IV).

The uncertainty on this systematics is computed by comparing N in data and simulation, where the MC is weighted to the beam intensity, and the sum of the beam spill and sand MC samples is used for the comparison. The difference between data and MC is taken as the systematic uncertainty. If the data-MC difference is less than $0.1 \cdot C_{\text{pile-up}}$, then the uncertainty considered is just $0.1 \cdot C_{\text{pile-up}}$, because there is a 10% normalisation uncertainty on the sand muon MC.

Details can be found in [142].

6.2.5 Correlations Between FGD1 and FGD2 Selections

Globally the detector systematic uncertainties for FGD2 selection are very similar to the FGD1 selection, although this is the result of averaging over all systematic together. Both are dominated by the secondary pion interactions. The other systematics are second order uncertainties, with small differences between the FGD1 and FGD2 selections, as shown in Section 7.7.5. This is not necessarily true for their ratio: the more important systematics will be the ones with less cancellations. In particular, the FGD mass uncertainties, which are quite different between FGD1 and FGD2, are not expected to cancel in the ratio, because the uncertainty on the scintillator modules and on the water modules have been evaluated independently, as explained later in this section.

The systematic uncertainty for the "out of fiducial volume" events is smaller for FGD1, due to the fact that the reconstruction uncertainties assigned for it are generally

smaller. The sand muon differences is easily explained by the fact that the veto cut of FGD2 is more strong than the FGD1 veto.

In order to have the uncertainties properly cancelling in the cross-section ratio, correlations between FGD1 and FGD2 systematics must be taken into account. All systematics are numerically calculated generating a large number of pseudo-experiments with altered parameters (Section 6.1), hence it is important to throw them at the same time for the two selections, within a unique machinery/framework.

Since most of the systematic uncertainty parametrisations are done via parameters that are correlated together such as momentum binning, FGD scintillator bars, and TPCs, most of the systematic uncertainties can be assumed fully correlated.

This is the list of assumptions which have been made.

- The magnetic field distortion uncertainty represents the difference in momentum between a rough corrected MC with the nominal one. If there is any correlation between different TPCs, the used method should already take them correctly into account without further assumptions.

- Regarding the TPC PID uncertainty, the three TPC are assumed to behave similarly, hence they are considered fully correlated among themselves. The three TPCs are expected to behave in the same way also for the δ ray production, which is the only source of uncertainty not well reproduced by the MC, and which affect the charge deposition.

- The TPC tracking efficiency systematics is assumed to be fully correlated among TPCs, because the main source of the data-MC difference should be the δ rays production that add hits along the track, spoiling the reconstruction.

- As explained in Section 6.2.2 the TPC-FGD matching efficiency systematics is mostly due to tracks generated close to the edge of the FGD. Being the last modules of FGD2 a scintillator module, identical to the modules of FGD1 (Section 3.2.1.1), the associated parameters for FGD1 and FGD2 are assumed to be fully correlated.

- Regarding the out of fiducial background, each category listed in Section 6.2.4.1 has a different source of systematic error, unrelated to the sources of the other categories. Nevertheless these sources are the same in the two FGDs, thus the

categories are assumed to be fully uncorrelated among themselves, but the same category is assumed to be fully correlated between FGD1 and FGD2.

- For the pion secondary interactions systematics, the uncertainties depend on the target nuclei, thus the correlations are expected to be limited.

- For the mass systematics (Section 6.2.3.2), the masses have been calculated independently for the water and the scintillator modules. The mass uncertainties are propagated either for a scintillator module or for a water module, according to whether the true interaction occurs in the former or in the latter. This means that they will be fully correlated between FGD1 and a scintillator module of FGD2, while they will be fully uncorrelated for a water module.

6.3 Beam Flux Uncertainties

The ND280 Beam Group evaluates the flux uncertainties and provides the flux corrections, or tuning, and the covariance matrix to propagate the uncertainties. The flux systematics is parametrised in bins of true E_ν (variable binning between 0 GeV and 30 GeV) and neutrino flavours (ν_μ, $\overline{\nu}_\mu$, ν_e and $\overline{\nu}_e$).

The neutrino flux prediction is affected by uncertainties on different parts of the ND280 MC simulation (Section 3.3.1), taking into account: kaon production multiplicity, pion production multiplicity, proton beam, off-axis angle, horn angular alignment, horn field asymmetry, production cross sections, horn absolute current, target alignment, secondary nucleon production, near detector phase space, proton beam intensity.

The hadron production uncertainties are constrained with external data from a dedicated experiment at CERN (NA61/SHINE) [136]. Uncertainties related to the proton beam, including the beam profile and alignment, are constrained by T2K data for each run. The uncertainties on the alignment of the target and magnetic horns are studied by rotating the target and shifting the horns in the simulation. Similarly, the uncertainties on the horn current and magnetic field are varied in the MC.

Fig. 6.1 shows the ND280 ν_μ flux uncertainty as a function of the neutrino energy. The hadron production uncertainties are dominant especially at low neutrino energy. For future analyses this uncertainty will be significantly reduced by using a NA61 data samples using a T2K replica target.
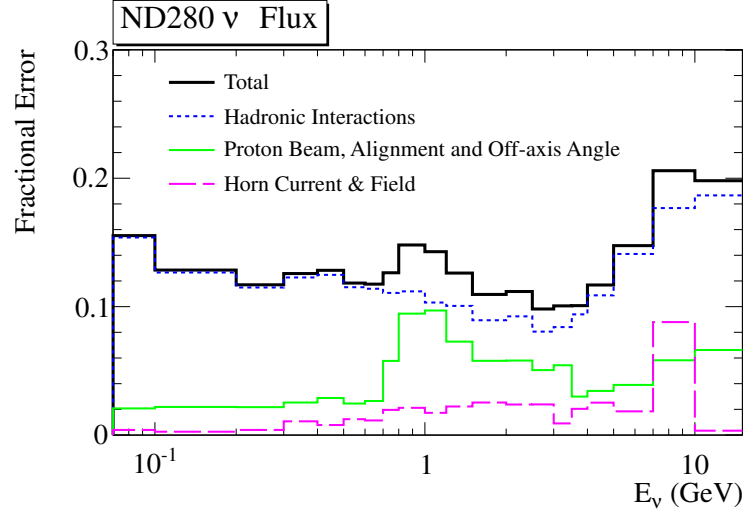
Figure 6.1: Fractional flux uncertainty on the ND280 ν_μ flux prediction [156].

6.3.1 Beam Flux Tuning

The nominal flux prediction is subject to large hadron production uncertainties and hence corrections are often applied after additional analyses of external data or more accurate measurements along the beam line are performed. Tuned versions of the flux can then be used to reweigh events after the fact. This analysis uses the most up to date flux tuning (`tuned13av1.1`) to reweigh events as a function of true E_ν. Corrections are applied to all true and selected events in the MC, as well as on the flux itself which is needed for the flux normalisation in the denominator of the cross-section formulas.

The flux tuning and uncertainty parametrisation are described in details in [157].

6.4 Model Uncertainties

A good analysis should have a very minimal dependence on the signal model, but the uncertainties on it still have to be considered. Anything that could introduce a bias on the extracted cross section needs to be parametrised as a systematic uncertainty. Dependence on the signal model generally enters into the measurements through the signal efficiency and purity. This might have different effects on carbon and oxygen, but the differences should be small, and in fact these uncertainties well cancel in the ratio as expected.

The neutrino interaction model parameters account for: the values of the axial mass for quasi-elastic and for resonant pion production; the Fermi momentum and the binding energy; the normalisation for CC-ν_{e}, DIS, CC-Coherent, NC-Coherent, NC-Other and 2p2h processes; the scaling of the $I = 1/2$ background and of the axial form factor at $Q^2 = 0$ GeV/c^2 ($C_5^A(0)$) for resonant pion production. The Fermi momentum, the binding energy and the normalisation for 2p2h processes are parametrised separately for carbon and oxygen.

The FSI model parameters describe the uncertainties on what happens to the pions before leaving the nucleus, where the following reactions can happen after the neutrino interacts: pion production, pion absorption, energy charge exchange and inelastic re-scattering.

The neutrino interaction and the FSI model uncertainties affect both the background, which contaminates the samples, and the signal, which is used to estimate the efficiency of the selection. They are parametrised either based on the internal NEUT parametrisation or based on some template reweighting scheme from T2K's Neutrino Interactions Working Group (NIWG [143]), which provides the uncertainties for the oscillation analysis. A detailed description is given in [158] and [150].

Performing fits to external neutrino interactions and pion scattering data (Mini-BooNE), the T2K's NIWG (Neutrino Interaction Working Group) constrains the neutrino interaction and FSI model parameters, as described in Reference [150]. T2K's NIWG group provides the best fit values for the relevant parameters ("NIWG tuning", Section 6.4.1), along with their errors and the covariances across them, which are used for the propagation (Section 6.1.3).

6.4.1 NIWG Tuning

NEUT is the MC event generator used by T2K oscillation analyses. Recent versions of NEUT use the spectral function (SF) model for CCQE interactions on carbon and oxygen (cf. Section 1.4.2.1). Prior versions of NEUT relied on a more simplistic Fermi gas (RFG) model. While the SF model is supposed to be a more accurate representation than RFG of nucleon momenta distributions within a nucleus, there is no random phase approximation correction (RPA, cf. Section 1.4.2.2) available for SF and there are

inconsistencies between the 1p1h (SF) and 2p2h calculations. As it currently stands, both SF and RFG are known to be imperfect models.

The NIWG set out to perform a fit of three models (SF+2p2h, RFG+rel.RPA+2p2h, and RFG+non-rel.RPA+2p2h) implemented in NEUT to external MINERνA and MiniBooNE CCQE measurements [158]. Results from these fits show that none of the models adequately describes all of the data. The best fit model was the RFG+rel.RPA+2p2h and the NIWG recommends using this for cross-section measurements. The best fit values for RFG+rel.RPA have

$$M_{\mathrm{A}} = 1.15 \pm 0.03 \text{ GeV}/c^2$$

$$p_{\mathrm{F}} = 223 \pm 5 \text{ MeV}/c$$

$$\text{2p2h normalisation} = 27 \pm 12 \text{ \%}$$

This analysis follows the NIWG recommendations in [158]. The default NEUT MC simulation uses the SF model, but setting the proper dials in the framework for the error propagation, the MC is reweighted to RFG+rel.RPA model. Moreover, the NEUT nominal values for M_A, p_F, and 2p2h normalisation are tuned to the NIWG best fit: those are the values upon which their associated errors should be centred against.

7

Measurement of the Water to Scintillator Charged-Current Cross-Section Ratio

This section first discusses the water to scintillator cross-section ratio as a function of the reconstructed energy $E_{QE}(p_\mu, \cos\theta_\mu)$ defined in Eq. (4.6). We find, and discuss, significant dependence of the result upon the unfolding method and propose a result on the basis of an assumption of a smooth energy dependence. Then we perform the integrated measurement which is far less dependent on this assumption.

The cross-section ratio is evaluated with Eq. (4.19), obtained in Section 4.3.2 and reported here for convenience:

$$\frac{\sigma_{\text{water}}(E_{QE})}{\sigma_{\text{scint}}(E_{QE})} = \frac{\hat{N}_{\text{FGD2}}/T_{\text{FGD2water}}}{\hat{N}_{\text{FGD1}}/T_{\text{FGD1}}} \cdot \frac{\Phi_{\text{FGD1}}}{\Phi_{\text{FGD2}}} - \frac{T_{\text{FGD2scint}}}{T_{\text{FGD2water}}} \tag{7.1}$$

where $\hat{N}_{\text{FGD1}}$ and $\hat{N}_{\text{FGD1}}$ are the estimated numbers of true events in FGD1 and in FGD2 respectively, in each bin of $E_{QE}(p_\mu, cos\theta_\mu)$. As explained in Section 4.2, $\hat{N}_{\text{FGD1}}$ and $\hat{N}_{\text{FGD2}}$ are related to the number of observed events, i.e. the number of events in FGD1 and FGD2 selections described in Chapter 5, through Eq. (4.8); as anticipated, the handling of the background in this formula might be different, and alternatives methods are discussed in Section 7.4.

In general, the number of observed events differs from the expectation for an ideal detector mainly because of three effects:

1. detector effects: the event properties such as momentum or direction are measured only with finite precision and limited efficiency, therefore events may be reconstructed in the wrong bin or may get lost;

2. statistical fluctuations: the number of observed events is drawn from a Poisson distribution, the measurement provides an estimate of the Poisson parameter μ;

3. background: events similar to the signal may be produced by other processes.

The process of extracting information about the true content of the measurement bins, given the observed measurements, is referred to as "unfolding".

7.1   Unfolding Techniques

In order to remove the detector smearing, one could simply invert the smearing matrix $U_{i,j}$, obtaining $U_{i,j}^{-1}$, and calculate the estimated cross section in the true variables. Indeed $U_{i,j}^{-1}$ and the detector efficiency relate $N_{\mathrm{observed}}(\vec{\mathbf{x}})$ to $N_{\mathrm{true}}(\vec{\mathbf{x}})$. This method is called "matrix inversion" and leads to unbiased results but typically suffers from large bin-to-bin correlations, oscillation patterns, and huge uncertainties, as noise in the smeared signal is blown up in the inverse. Indeed the problem belongs to a class of ill-posed problems, which are unstable against small variations in the initial system. Various regularising techniques for smoothing the resulting unsmeared distributions exist, where a pseudo-inverse matrix $\widetilde{U}_{i,j}^{-1}$ is calculated.

Reference [159] provides an overview of the unfolding techniques mostly used in high energy physics, pointing out their limitations: a (constrained) "template fit", being equivalent to a "matrix inversion", gives also unbiased results but wildly oscillating and with large uncertainties; the "bin-by-bin method" replaces the smearing matrix by a diagonal approximation, leading to MC biased results; other unfolding methods use regularisation techniques, such as "Tikhonov regularisation" and "iterative methods", to reduce oscillations and bin-to-bin correlations via damping the fluctuations, at the cost of introducing some biases. The iterative methods start from a fully biased result and the number of iterations required to reach the unbiased result is a priori unknown.

Methods with Tikhonov regularisation use parameters which have to be tuned to obtain a good compromise between bias and damping, with the advantage that there is a natural transition to unbiased results, by properly setting the parameters. In general, over-regularisation biases the unfolded spectrum towards the Monte Carlo input, while under-regularisation leads to large fluctuations in the result. In order to minimise the bias, the regularisation should be controlled via data-driven methods, relying the least possible on the MC.

In this thesis, the water to scintillator cross-section ratio as a function of $E_{QE}(p_\mu, \cos\theta_\mu)$ is obtained unfolding the ND280 data with two methods: a simple (unregularised) matrix inversion, and the regularised SVD-based unfolding technique described in Section 7.7.1.

7.2 Blind Analysis and Fake-Data Studies

To reduce the risk of biasing the final results by looking at the data, even unintentionally, the analysis have been kept blind and developed with fake data studies. There is quite a lot of literature on blind analyses and their benefits (see for example Reference [160]). In order to keep the data blind the MC needs to be used, and it is very important then that it is correctly reweighted to take into account known factors like flux, detector corrections, neutrino generator updates and any other possible factor.

Performing the analysis with a fake data-set is a good way to check that the unfolding procedure is working properly, the uncertainties are consistent and the bias is small. A good fake data-set can be obtained using a MC sample produced with an alternative neutrino generator. As discussed in Section 3.3.1, NEUT is the official generator in T2K and GENIE is an alternative one, hence GENIE 2.8.0 has been used to generate a fake data-set. Moreover, once applied the NIWG tuning discussed in Section 6.4.1, via event-by-event reweighting, the obtained simulation is significantly different from the original one, as it can be seen in Fig. 7.5. Indeed this reweighting changes even the nuclear model, from the original spectral function model in NEUT 5.3.2 to the RFG+rel.RPA model (cf. Section 6.4.1). Therefore, the original NEUT SF 5.3.2 simulation gives another reasonable fake-data distribution.

7.3 True Signal Definition and Phase Space Restriction

The selections used for the analysis presented in this thesis are the ν_μ CC inclusive selections in FGD1 and in FGD2 as described in Section 5.2. Therefore, the definition of the true signal is true ν_μ CC inclusive interactions, as predicted by the Monte Carlo simulation, occurred in the fiducial volume of FGD1 or FGD2 respectively. A selected event is a signal event if the true vertex of the particle associated to the muon candidate is:

- generated by a muon neutrino (PDG code 14);

- due to a charged-current interaction (NEUT reaction code between 1 and 30);

- occurred inside the fiducial volume.

As the muon is not affected by FSI (cf. Section 1.4.2.1), the topology of these true interactions is one negative muon in the final state and any number of any other particles. For a cross-section measurement, even though this true signal definition is straightforward for ν_μ CC inclusive selections, considerations on the phase space needs to be done. Indeed limited acceptance of a detector can also compound limited phase space (acceptance) of outgoing particles.

Contrary to the T2K far detector which has a 4π acceptance, the ND280 angular coverage is quite limited. The efficiency for forward muons in ND280 is very good, while it is lower or zero for backward tracks (cf. Section 5.2.2). In such a case it is appropriate to quote the measurements with a phase space restriction. Indeed, if the measurement is differential, it is straightforward to report results only for bins where efficiency is high. Even for a "total" (full phase space) cross section, if no such restriction is applied, the measurement would include a correction for the unmeasured region which biases the measurement towards the simulation signal model used: integrating over all bins would include bins driven by the data and bins filled according to the Monte Carlo, creating artificial agreement with the MC signal model, and perhaps artificial disagreements with other measurements which may rely on alternate signal models or MCs. Restricted phase space measurements can be compared to the MC signal process to understand deficiencies, and also compared to other experiments.

The cross-section ratio presented in this thesis is evaluated as a function of $E_{QE}(p_\mu, \cos\theta_\mu)$, defined in Eq. (4.6), hence it is an analysis in two dimensions (momentum and angle)

projected into 1 dimensions. As a result, each bin would contain contributions from events with different muon kinematics.Therefore, a phase space restriction based on the efficiency in $E_{QE}(p_\mu, \cos\theta_\mu)$ bins would not necessarily get rid of the contributions from $(p_\mu, cos\theta_\mu)$ bins where nothing was measured: the phase space restriction has to be guided by the underlying kinematics.

In general, the phase space should be restricted to a region where the efficiency is flat (as much as possible): if the efficiency of the selection changes rapidly over a kinematics variable, it is unlikely to be well modelled by the Monte Carlo simulation, which would introduce model dependence on the signal or on the background. Nevertheless, in the case of a ratio measurement, as far as the efficiencies of numerator and denominator are adequately similar, as they are in this analysis (cf. Section 5.2.2), it can be genuinely assumed that eventual model dependencies introduced by steep behaviour of the efficiencies, cancel out. Therefore, in order to keep the highest possible statistics and obtain the smallest statistical error, the phase space has been restricted only to further reduce the difference between the efficiencies in the two selections, in FGD1 and in FGD2, and to discard regions where there are no reconstructed events.

By looking at Fig. 5.5 it is clear that the backward-going muon should not be considered, as in FGD1 there are almost no candidates. Fig. 7.1 shows the efficiencies as a function of the momentum considering only the forward muons: with respect to the same plot for the whole sample, Fig. 5.7, even the small differences at low momentum between the selection in FGD1 and the selection in FGD2 disappear. In the same figure, the fraction of reconstructed events as a function of momentum is also shown. Below 100 MeV of momentum there are very few muon candidates and they are reconstructed with very low efficiency. Fig. 7.2 shows the simulated muon candidate $(p_\mu, cos\theta)$ phase space for true ν_μ-CC interactions, and it can be seen that the low momentum threshold is slightly different for the two selections. From these reasons, it is sensible to restrict the phase space to forward muons above 100 MeV.

The chosen restricted phase space is therefore

$$cos\theta_\mu > 0, \quad p_\mu > 100 \text{ MeV} \tag{7.2}$$

and the final true signal definition is: true ν_μ CC inclusive interactions in the fiducial volume, where the outgoing muons have $cos\theta_\mu > 0$ and $p_\mu > 100$ MeV. The events
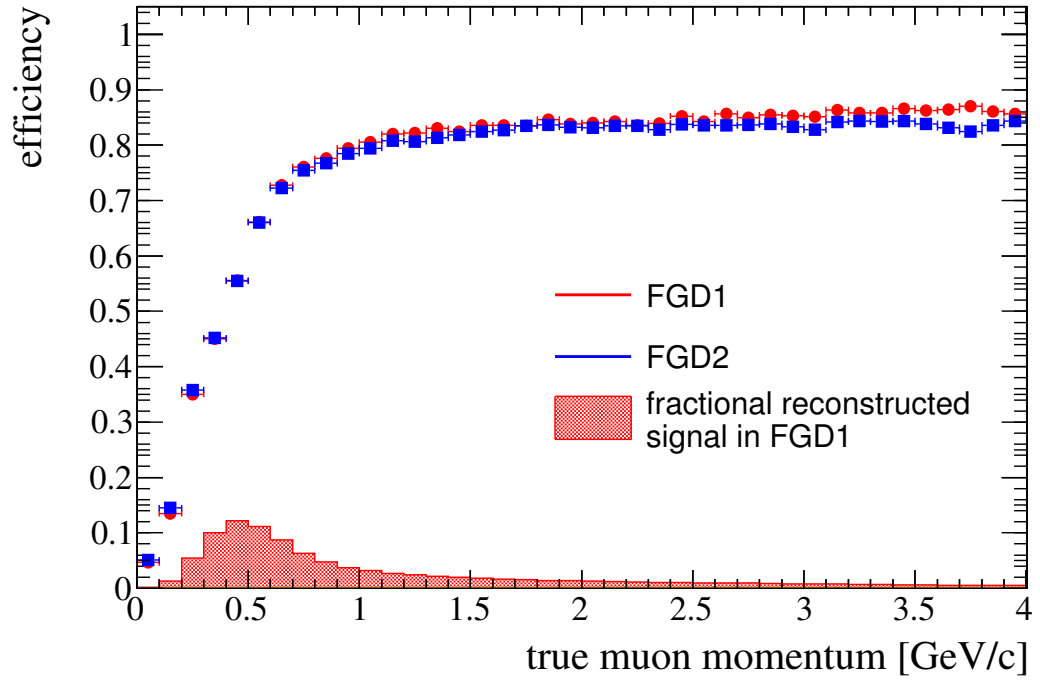
Figure 7.1: Efficiency as a function of the true muon momentum, for both selections, in FGD1 (red) and in FGD2 (blue), with $cos\theta_\mu > 0$. Statistical error bars are shown, but small.
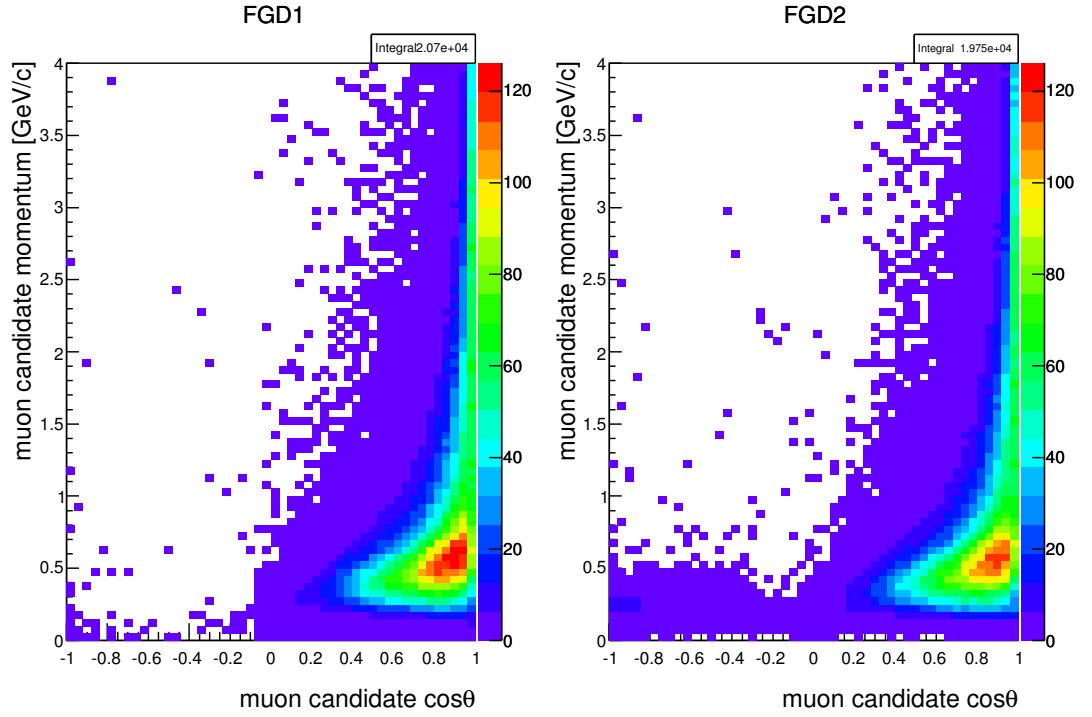
Figure 7.2: (p_μ,$cos\theta$) phase space of the muon candidates for both selections, in FGD1 (left) and in FGD2 (right).

₂₄₇₈ excluded by this phase space restriction are quite few, compared to the full statistics,
₂₄₇₉ therefore it is reasonable to simply treat them as background.

₂₄₈₀ The efficiency as a function of $E_{QE}(p_\mu, \cos\theta_\mu)$ is shown in Fig. 7.3; the lowest energy
₂₄₈₁ bins are empty because of the phase space restriction.
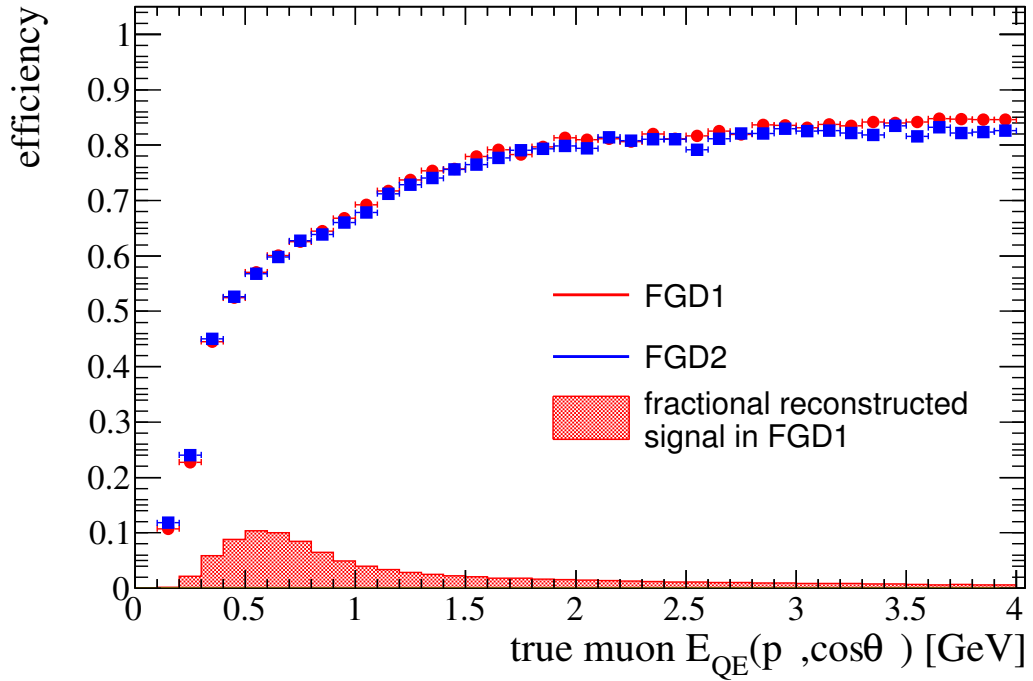
Figure 7.3: Efficiency as a function of the true muon $E_{QE}(p_\mu, \cos\theta_\mu)$, for both selections, in FGD1 (red) and in FGD2 (blue), with $p_\mu > 100$ MeV and $cos\theta_\mu > 0$. Statistical error bars are shown, but small.

₂₄₈₂ ## 7.4   Background Treatment

₂₄₈₃ It is not possible to have a perfectly pure selection, so some fraction of any selection will
₂₄₈₄ be due to background processes. These may be from other interactions misidentified
₂₄₈₅ as signal or interactions happening outside the fiducial volume, due to reconstruction
₂₄₈₆ inefficiencies.

₂₄₈₇ In the assumption that the efficiency is correctly modelled in the Monte Carlo, the
₂₄₈₈ background can be simply removed from the observed distribution, without introducing

any assumptions between the signal and the background. This "background subtraction" method is the one used to define the estimated number of events in Eq. (4.8), where B is the simulated background scaled down to correspond to the protons on target in the data sample (cf. Chapter 5):

$$B = B_{\mathrm{MC}} \cdot \frac{\mathrm{POT}_{\mathrm{data}}}{\mathrm{POT}_{\mathrm{MC}}} \qquad (7.3)$$

Alternatively, one could assume that the signal/background ratio is correctly modelled in the Monte Carlo, and perform a "purity correction": the background is removed based on a scaling from the MC. This method reflects the correlation between the signal model and the background, but it explicitly uses the signal MC model, which may be an unwanted assumption when trying to measure a model independent cross section.

While a cross section with the background subtraction is defined as

$$\sigma = \frac{N_{\mathrm{observed}} - B}{\epsilon \, T \, \Phi} \qquad (7.4)$$

a cross section with the purity correction is defined as

$$\sigma = \frac{p \, N_{\mathrm{observed}}}{\epsilon \, T \, \Phi} \qquad (7.5)$$

where N_{observed} is the number of observed events, T is the number of targets, Φ is the flux, ϵ is the efficiency and p is the purity (defined in Eq. (5.5) and Eq. (5.6)). Implications on statistical uncertainties have been already discussed in Section 6.1.1, showing that the background-subtracted result carries a larger fractional uncertainty:

$$\frac{\sigma^2[N_{\mathrm{data}}]}{N_{\mathrm{data}} - N_{\mathrm{background}}} > \frac{\sigma^2[N_{\mathrm{data}}]}{N_{\mathrm{data}}} \qquad (7.6)$$

The estimated number of true events $\hat{N}_i$ is defined in Eq. (4.8) for the background subtraction method. Similarly, for the purity correction method it is given by:

$$\hat{N}_i = \frac{1}{\epsilon_i} \cdot \sum_j \widetilde{U}_{ij}^{-1}(p_j \cdot N_{\mathrm{observed},j}) \simeq N_{\mathrm{true},i} \qquad (7.7)$$

In order to reduce as much as possible the assumptions on the model, the results of this analysis are given with the background subtraction method.

146

An even better handling consists in adding the background in the smearing matrix as an extra bin, and subtracting it after the unfolding by simply removing this bin. In this way the background is unfolded along with the signal, allowing the migration of signal events into the background bin and vice versa.

In order to minimise assumptions based on the Monte Carlo, an independent sample of background events (also called "sideband sample") could be used to constraint the background. This control sample should have no overlap with the signal selection, without much contribution from the true signal, and with a similar phase space coverage as the background in the signal region. Anyway the model dependence is not completely removed, as the model is still used to extrapolate the constraint from the data in the control sample into the background in the signal region. For the ν_μ-CC selections described in Chapter 5 there is no obvious control sample to constrain the background. Moreover, these selections are quite pure, as shown in Section 5.2.2, and the MC well agrees with the data, as seen in Section 5.2.1. Therefore, the cross-section ratio presented in this analysis is evaluated relying on the Monte Carlo simulation of the background.

For the results with the regularised SVD-based unfolding, the background B (Eq. (7.3)) is unfolded along with the signal, adding an extra bin in the smearing matrix in both dimension (reconstructed and truth). When not using a sideband, this introduces a whole column of empty elements, which makes the smearing matrix not invertible. For this reason in the results with the (unregularised) matrix inversion the background B is simply subtracted before unfolding.

7.5 Binning, Distributions, Detector Response and Smearing Matrix

The total number of events in FGD1 and in FGD2, selected as described in Section 5.2, in the real ND280 data and in the NEUT-NIWG Monte Carlo simulation (scaled down to the data POT), are reported in Table 7.1. Note that, as anticipated in Section 7.3, both the non-CC events and the small fraction discarded by the phase space restriction contribute to the background.

7.5 Binning, Distributions, Detector Response and Smearing Matrix

Selection	ND280 data	NEUT-NIWG (with background)	Background	Purity (Eq. (5.6))	Efficiency (Eq. (5.5))
FGD1	24190	22943	2477	89.2 %	62.8 %
FGD2	23494	21906	2671	87.8 %	61.6 %
Water	10908	9968	1383		

Table 7.1: Number of selected events in real ND280 data and in NEUT-NIWG Monte Carlo (POT scaled), expected background, purity and efficiency, for both the FGD1 and the FGD2 selections. In the last row the expected number of events in water is reported.

The number of expected events in water is calculated with Eq. (4.17), using the values evaluated in Eq. (4.21) for the number of targets T and the value in Eq. (4.20) for the flux ratio $\frac{\Phi_{\text{FGD2}}}{\Phi_{\text{FGD1}}}$:

$$\hat{N}_{\text{water}} = \hat{N}_{\text{FGD2}} - \hat{N}_{\text{FGD1}} \cdot \frac{T_{\text{FGD2scint}}}{T_{\text{FGD1}}} \cdot \frac{\Phi_{\text{FGD2}}}{\Phi_{\text{FGD1}}} = \hat{N}_{\text{FGD2}} - \hat{N}_{\text{FGD1}} \cdot 0.526 \cdot \frac{1}{1.011} \quad (7.8)$$

The selection statistics and the resolution of the chosen variable affect the binning choice. Because the data is finite, arbitrarily fine binning would result in huge statistical errors. A good rule of thumb is that it is desirable to have the systematic and statistical errors approximately the same. The other consideration is that it is pointless to bin so finely that the detector smearing will introduce very strong bin to bin correlations.

In the cross-section ratio presented in this thesis, systematic uncertainties are relatively small, therefore the binning should be thick enough to have statistical errors of the same size. Note that because of the subtraction between the two FGDs, as seen in Section 6.1.1, a bin with 2000 events should have a statistic error around 7%. The binning is chosen evenly populated, so that all the bins have similar statistic errors, and at the same time it ensures a finer binning in the more interesting region, i.e. around the peak of the T2K neutrino flux.

The chosen binning for $E_{QE}(p_\mu, \cos\theta_\mu)$ is

$$[0.2, 0.45, 0.55, 0.65, 0.75, 0.9, 1.25, 2, 4, 14] \text{ GeV.} \quad (7.9)$$

7.5 Binning, Distributions, Detector Response and Smearing Matrix

Below 170 MeV there are no events as they are cut out by the phase space restriction (cf. Section 7.3). Above 1.25 GeV the bin width has to be large to compensate the low statistics and the worse resolution. An extra bin, for a total of 10 bins, handle the eventual "out of range" events (below 200 MeV and above 14 GeV), which allows event migration over the full spectra in the unfolding. The more interesting region is below 1.25 GeV, as it is the range in which the T2K oscillation analyses are performed.

Fig. 7.4 shows again the efficiency as a function of $E_{QE}(p_\mu, \cos\theta_\mu)$, as in Fig. 7.3, but using the chosen binning.
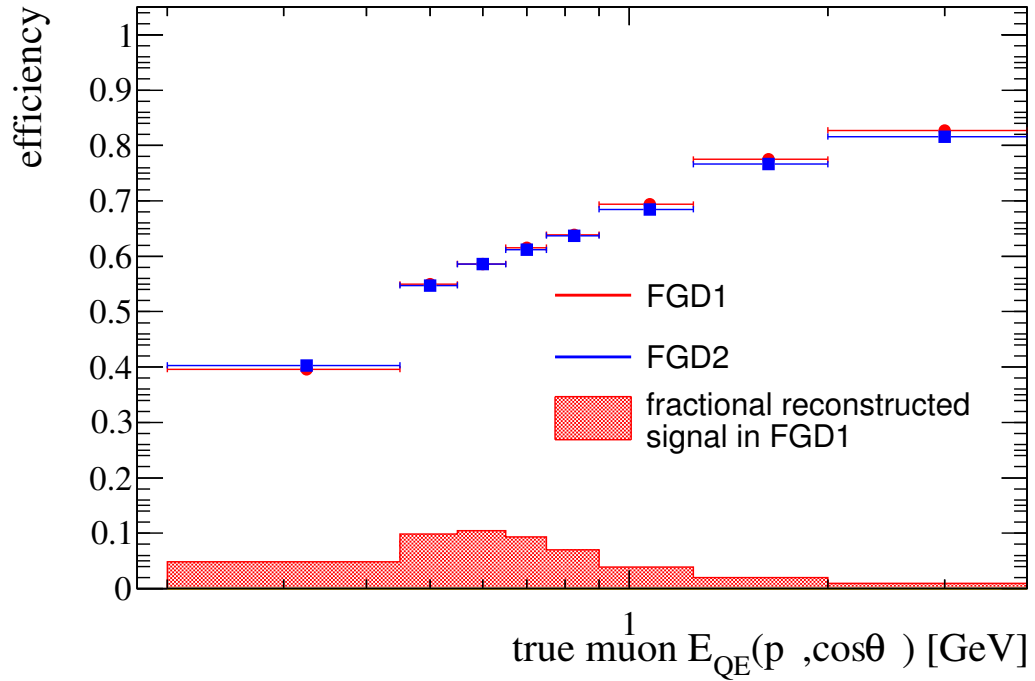
Figure 7.4: Efficiency as a function of the true muon $E_{QE}(p_\mu, \cos\theta_\mu)$ in the chosen binning, for both selections, in FGD1 (red) and FGD2 (blue), with $p_\mu > 100 MeV$ and $cos\theta_\mu > 0$.. Statistical error bars are shown, but small. The fractional distribution of the reconstructed events in FGD1 is shown as well.

Fig. 7.5 presents the distribution of events as a function of $E_{QE}(p_\mu, \cos\theta_\mu)$ in the chosen binning, for both FGD1 and FGD2 selections. Beside the real ND280 data distribution, both NEUT and GENIE Monte Carlo simulations are shown (properly

scaled to the data POT for comparison). For each simulation it is also shown the background prediction, which includes both the background described in Section 5.2.2 and the events excluded by the phase space restriction (cf. Section 7.3). The number of events in each bin is reported in Table 7.2.
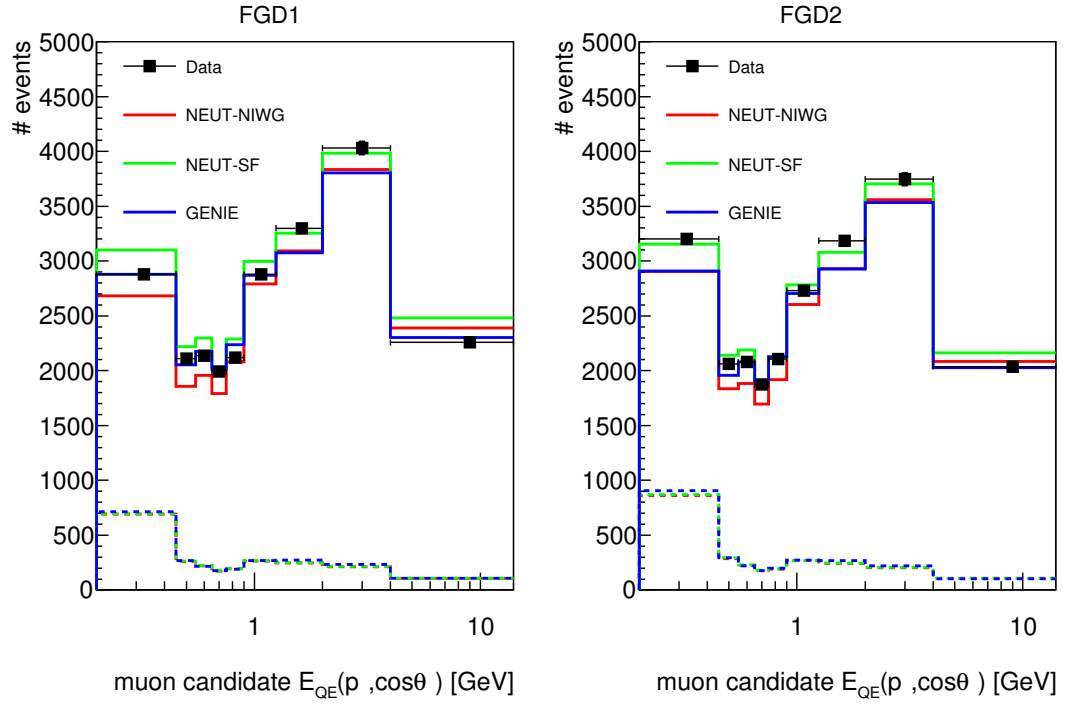
Figure 7.5: Distribution of events as a function of $E_{QE}(p_\mu, \cos\theta_\mu)$ in the chosen binning, for both FGD1 and FGD2 selections. The real ND280 data distribution is compared to three different Monte Carlo simulations. The nuclear model in GENIE is the Bodek and Ritchie Fermi Gas model (cf. Section 3.3.1.2) while NEUT-SF uses the Spectral Function model (cf. Section 3.3.1.1); NEUT-NIWG is reweighted with the NIWG tuning which effectively turns SF into the RFG+rel.RPA nuclear model (cf. Section 6.4.1).

Fig. 7.6 shows the NEUT-NIWG signal distributions and the real ND280 data after subtracting the background predicted by the Monte Carlo. As discussed in Section 7.4, these are the distributions which are used for the unfolding with the (unregularised) matrix inversion, while for the results with the regularised SVD-based unfolding, the background is not subtracted from the real data distribution, but instead it is added as an extra bin in the smearing matrix and unfolded along with the signal.

Bin range [GeV]	Selected events in FGD1	Selected events in FGD2	Expected signal events in FGD1	Expected signal events in FGD2
$< 0.2 \,\&\, > 14$	492	474	378.53	357.51
$[0.20, 0.45]$	2879	3201	2188.93	2341.41
$[0.45, 0.55]$	2109	2064	1850.13	1777.95
$[0.55, 0.65]$	2138	2078	1916.98	1853.55
$[0.65, 0.75]$	1991	1874	1818.96	1697.86
$[0.75, 0.90]$	2118	2106	1925.97	1916.07
$[0.90, 1.25]$	2877	2729	2613.32	2462.83
$[1.25, 2.00]$	3298	3185	3050.51	2940.97
$[2.00, 4.00]$	4030	3745	3817.54	3541.83
$[4.00, 14.0]$	2258	2038	2152.06	1932.62
Total	24190	23494	21713	20823

Table 7.2: Number of selected events (real ND280 data) in each bin of Fig. 7.5 for both FGD1 and FGD2 selections; in the last two columns the NEUT-NIWG predicted background has been subtracted.
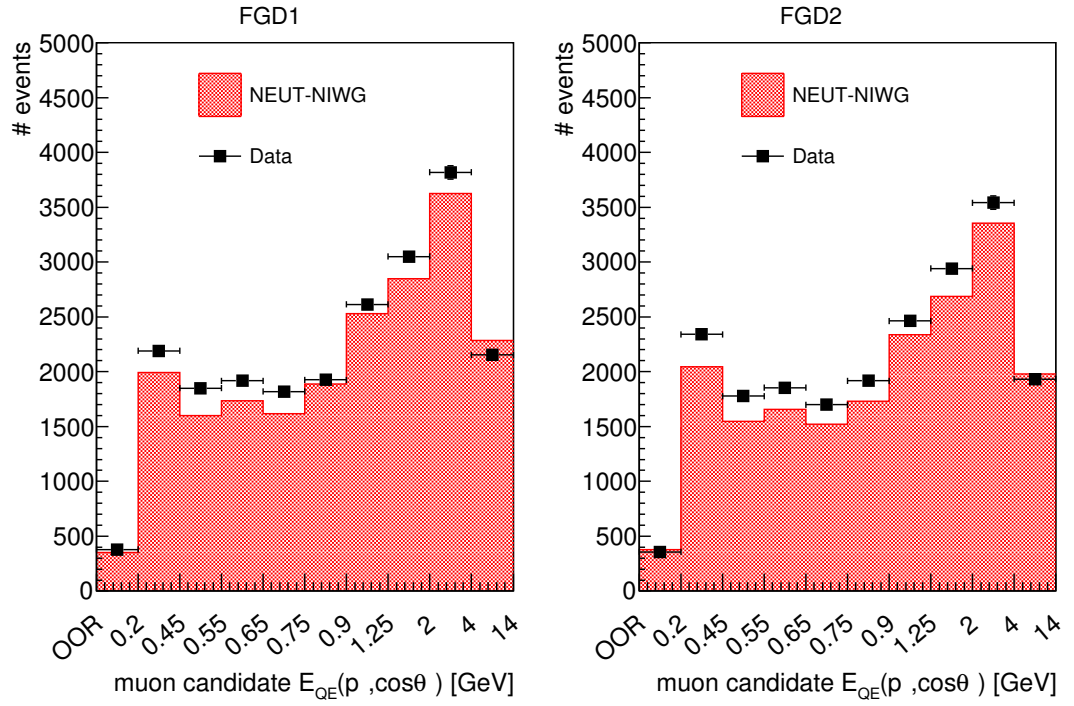
Figure 7.6: Comparison of real ND280 data and NEUT-NIWG distributions after subtracting the background predicted by the Monte Carlo, for both FGD1 and FGD2 selections.

7.5 Binning, Distributions, Detector Response and Smearing Matrix

Fig. 7.7 presents the detector response and the folding matrix for both FGD1 and FGD2 selections, relating the reconstructed MC simulation and the NEUT-NIWG distributions shown in Fig. 7.6. The detector response matrix describes the event migrations, in terms of number of events. The folding matrix is the detector response divided by the true spectrum (as simulated by the neutrino generator), and represents the probability of reconstructing a true event of a true bin i in a reconstructed bin j, accounting for both the migration probability and the reconstruction efficiency. Note how these matrices are mostly diagonal, and off-diagonal bins other than the first are basically empty: events migrate only to adjacent bins.
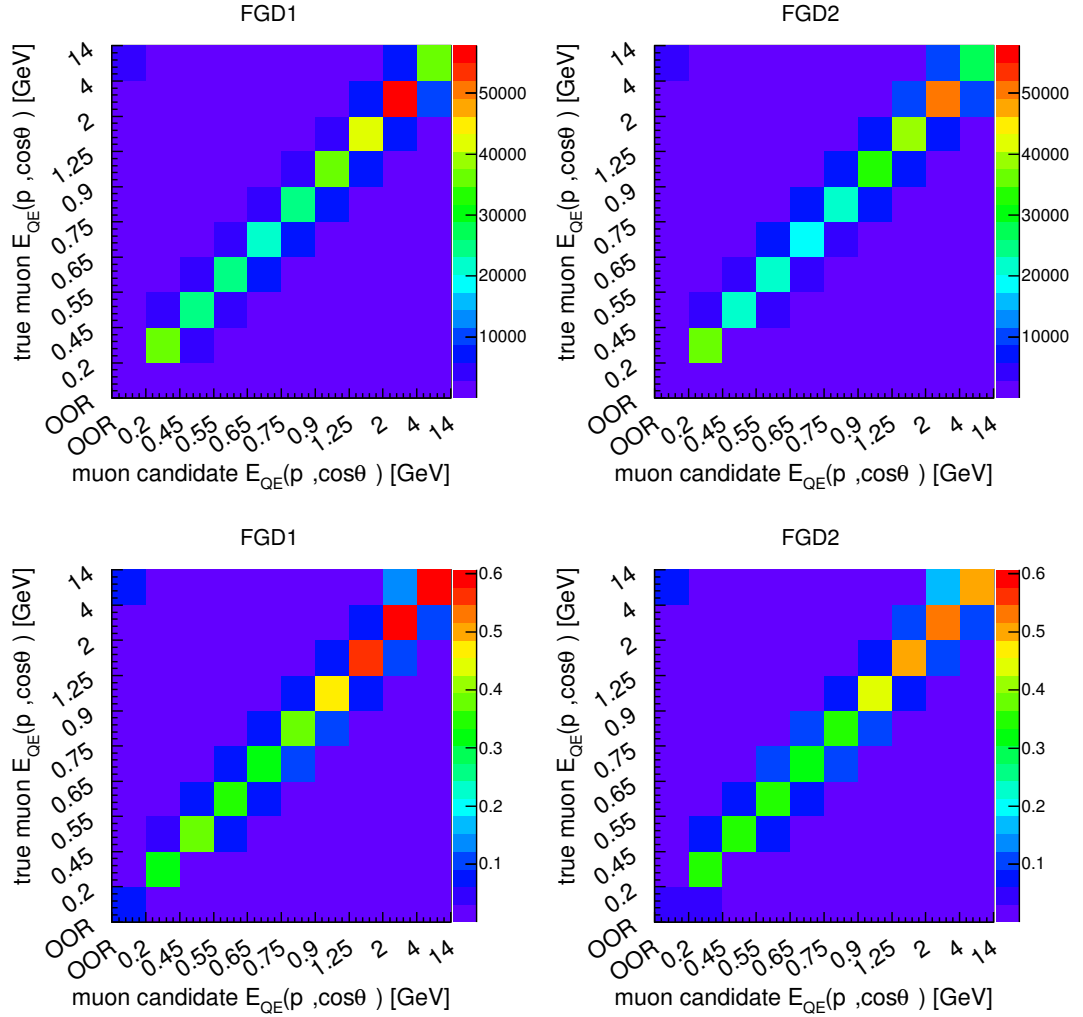
Figure 7.7: Detector response (top) and folding matrix (bottom) for FGD1 (left) and FGD2 (right) selections, showing the correlations between $E_{QE}(p_\mu, \cos\theta_\mu)$ with the true muon's kinematic variables and $E_{QE}(p_\mu, \cos\theta_\mu)$ with the muon candidate's reconstructed variables.

7.6   Unregularised Results

This section presents the water to scintillator cross-section ratio as a function of $E_{QE}(p_\mu, \cos\theta_\mu)$, unfolding the ND280 data with the (unregularised) matrix inversion method. As seen in Section 7.1, simply inverting the smearing matrix leads to unbiased results, even though with large uncertainties and bin-to-bin correlations. For these unregularised results, the unfolding is performed after subtracting the background predicted by the NEUT-NIWG simulation, as discussed in Section 7.4.

A good preliminary closure test consists in performing the unfolding process on the same MC sample used to evaluate the smearing matrix of Fig. 7.7. This means that the reconstructed MC spectrum and the fake-data spectrum do correspond, and the unfolded cross section should exactly match the one from the MC truth, as it corresponds to the fake-data truth. This test would reveal eventual pathological problems in the unfolding process or in the evaluation of the systematics. As can be seen in Fig. 7.8 the unfolding behaves as expected.

Fig. 7.9 (top figure) is a fake-data study where GENIE is used as fake-data sample, showing the cross-section ratio as a function of $E_{QE}(p_\mu, \cos\theta_\mu)$ (top), with uncertainties for the six error sources (assumed independent, cf. Section 6.1). Fig. 7.9 (bottom figure) is the correspondent overall correlation matrix, considering all the error sources. The correlation matrix is an easier way to look at the correlations among bins, other than the covariance matrix, as each of its elements is defined as

$$\text{correl}_{i,j} = \frac{\text{cov}_{i,j}}{\sqrt{\text{cov}_{i,i} \cdot \text{cov}_{j,j}}} \tag{7.10}$$

where $\text{cov}_{i,j}$ is the element (i, j) of the covariance matrix defined in Eq. (6.1).

The χ^2 per degrees of freedom N_{dof} is given by

$$\chi^2/N_{\text{dof}} = \frac{1}{N_{\text{dof}}} \sum_{i,j} [(\sigma_i - \sigma_j^{\text{true}}) \cdot \text{cov}_{i,j}^{-1} \cdot (\sigma_j - \sigma_i^{\text{true}})] \tag{7.11}$$

where $\text{cov}_{i,j}^{-1}$ is the element (i, j) of the inverse of the covariance matrix (Eq. (6.1)), and N_{dof} corresponds to the number of bins. The χ^2/N_{dof} between the unfolded result and the fake-data truth (GENIE), evaluated for the overall covariance matrix (which takes into account all the error sources), is 0.1.
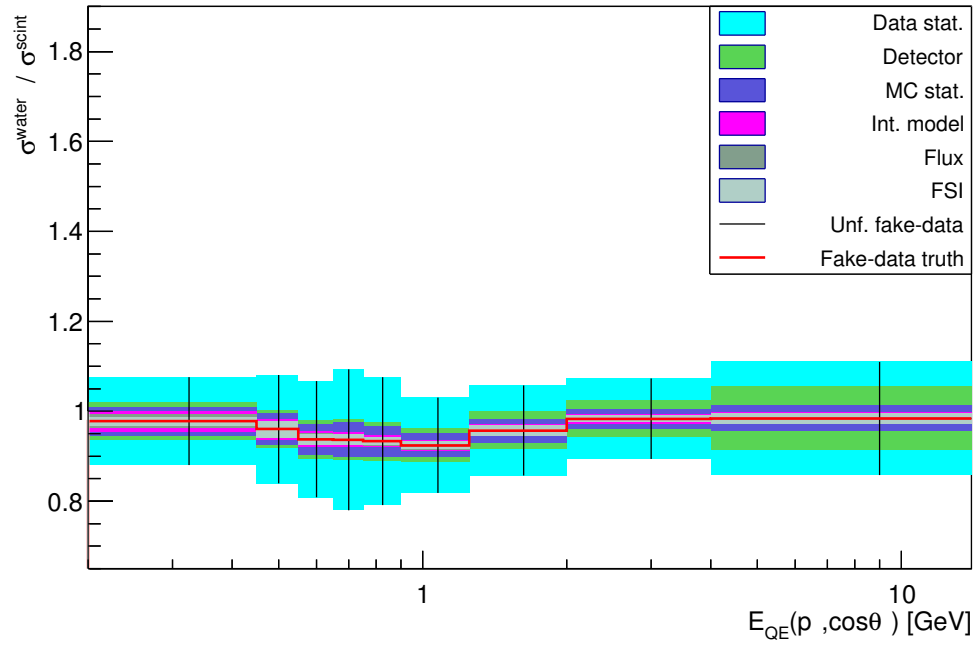
Figure 7.8: Water to scintillator cross-section ratio as a function of $E_{QE}(p_\mu, \cos\theta_\mu)$ unfolding the NEUT-NIWG fake-data distribution with the inverted smearing matrix built from the NEUT-NIWG simulation: the unfolded results exactly match the fake-data truth cross-section ratio (closure test).

Figure 7.9: Water to scintillator cross-section ratio as a function of $E_{QE}(p_\mu, \cos\theta_\mu)$ (top) and its correlation matrix (bottom), unfolding the GENIE fake-data distribution with the inverted smearing matrix built from the NEUT-NIWG simulation.

The water to scintillator cross-section ratio as a function of $E_{QE}(p_\mu, \cos\theta_\mu)$, unfolding the ND280 data with the (unregularised) matrix inversion method, is shown in Fig. 7.10 (top figure). The uncertainties have been propagated to the cross-section result using toy experiments, as described in Section 6.1. In Fig. 7.10 (bottom figure) is reported the overall correlation matrix. The χ^2/N_{dof} (Eq. (7.11)) between the unfolded result and the NEUT-NIWG truth, evaluated for the overall covariance matrix (which takes into account all the error sources), is 0.8.

As expected, and anticipated in Section 7.1, there are unphysical bin-to-bin correlations, which could be removed using a regularised unfolding technique.
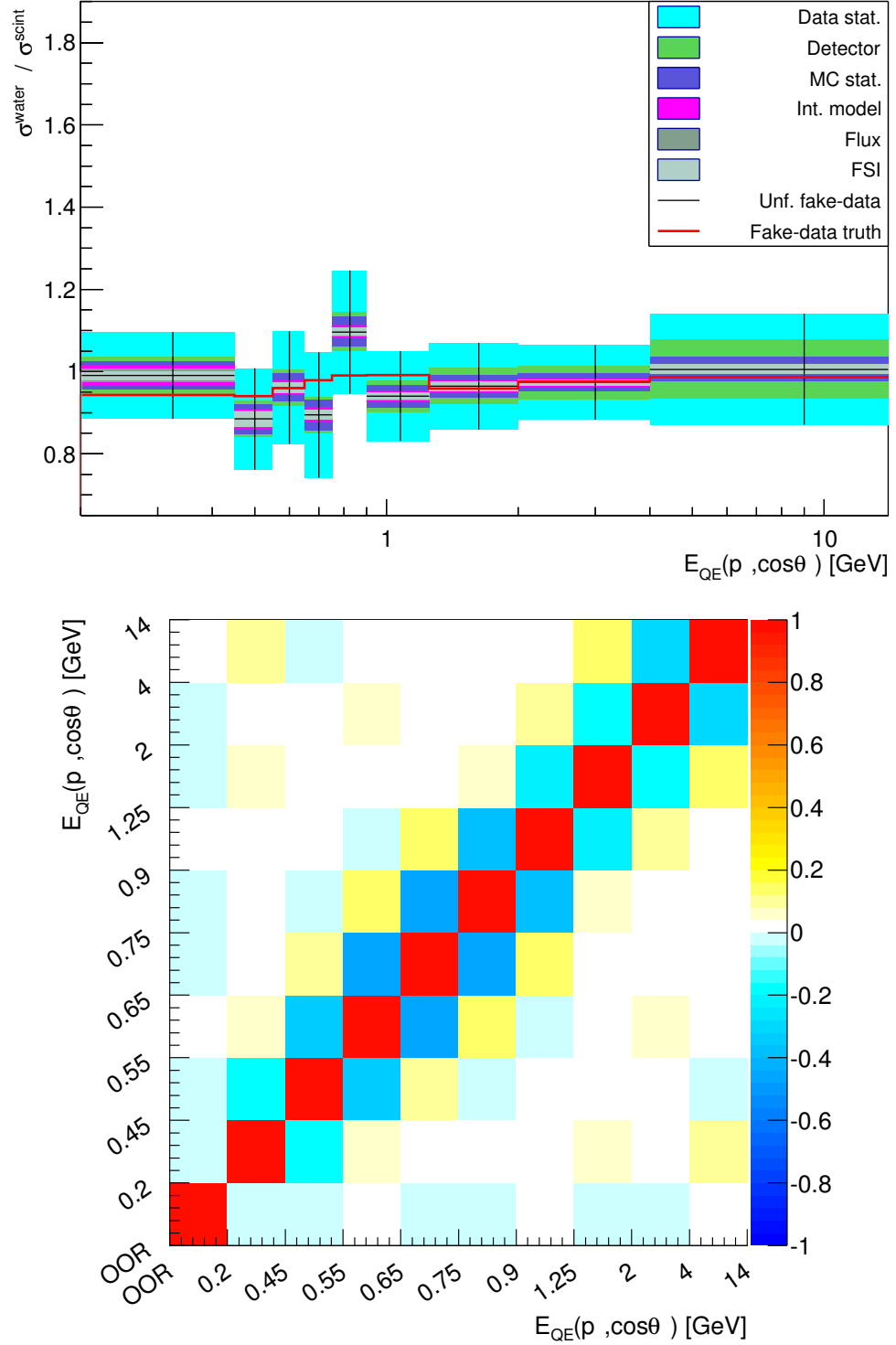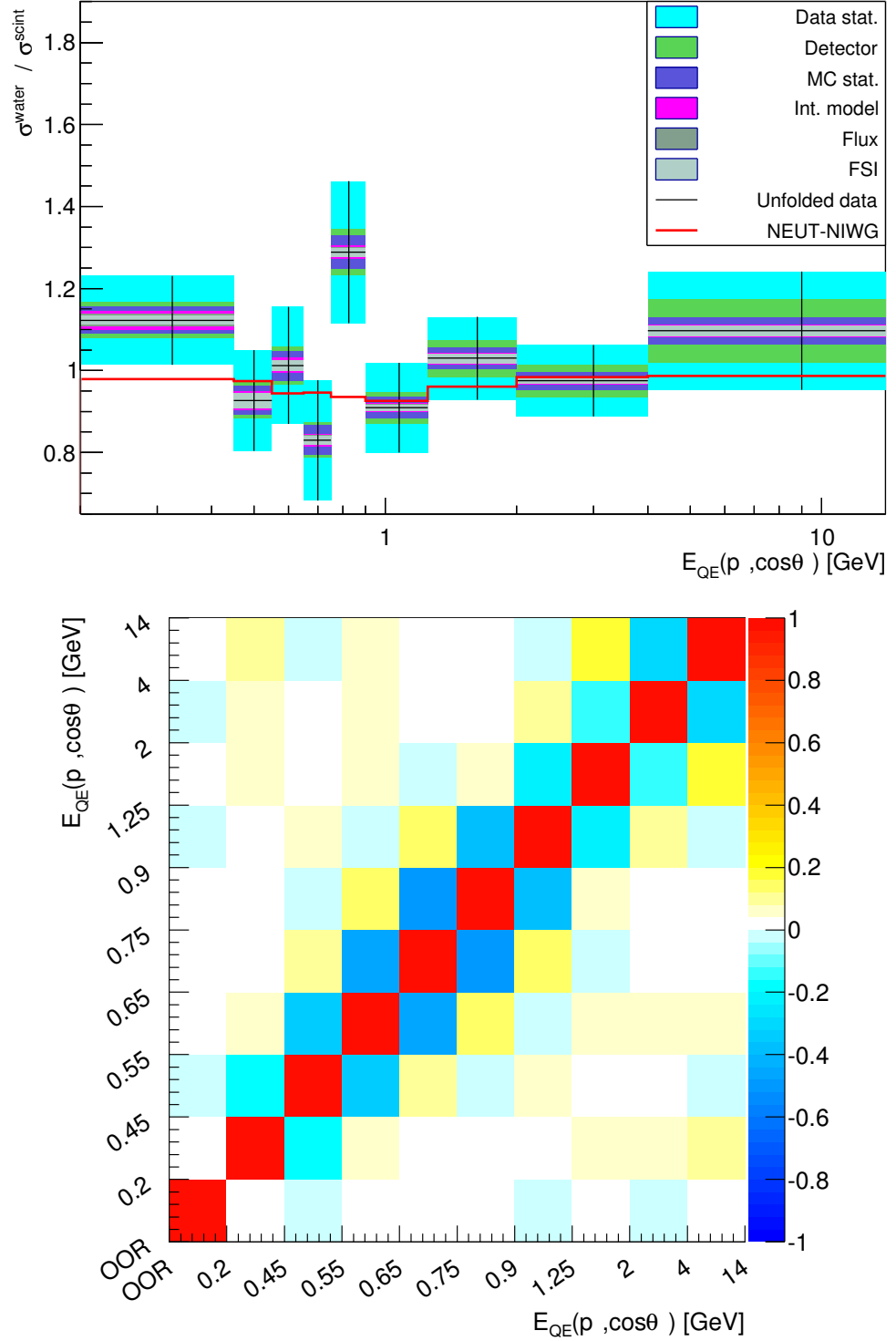
Figure 7.10: Water to scintillator cross-section ratio as a function of $E_{QE}(p_\mu, \cos\theta_\mu)$ (top) and its correlation matrix (bottom), unfolding the ND280 data ν_μ-CC inclusive selection (Section 5.2) with the inverted smearing matrix built from the NEUT-NIWG simulation.

7.7 SVD-Regularised Results

A relatively simple, fast and robust unfolding technique is the "SVD-based unfolding" [161], where a Tikhonov regularisation is re-formulated in terms of the Singular Value Decomposition (SVD) of the smearing matrix. This technique has been already used in several analyses in Particle Physics (for example [162]).

As discussed in Section 7.4, the background is treated differently from the unregularised results given in Section 7.6: instead of simply subtracting the background before performing the unfolding, the background is added as an extra bin in the smearing matrix, to take into consideration also the event migration between signal and background.

7.7.1 SVD-Unfolding

The SVD-based unfolding is basically a regularised matrix inversion, equivalent to a regularised template fit, as the regularisation matrix has a structure which mimics second derivatives. It is based on a loop-free linear algorithm and the regularisation leads to a smooth unfolded distributions, which has the smallest possible curvature among the solutions satisfying the initial linear system in the least squares sense. Unlike matrix inversion, in SVD the matrix is inverted through singular value decomposition, which allows to introduce a regularisation parameter: a normalised smearing matrix is decomposed into singular values and the regularisation parameter defines the level at which they are deemed to be due to statistical fluctuations, granting to suppress their contributions. The SVD-based unfolding naturally implements a data-driven method for determining the optimal value of the regularisation parameter. The regularised solution contains as much statistically significant information from the measured data as possible, simultaneously suppressing spurious, wildly oscillating components. Being a regularised matrix inversion, this unfolding method can only unfold N measurements to N truth parameters. Another limitation is that empty bins are bound to fail, and also Poisson distributed measurements might have issues with this technique. This is not a problem for this analysis since the data samples described in Chapter 5 contains thousands of events, and the binning can be chosen such that all bins are well populated. A C++ implementation of the SVD-based unfolding is provided by `TSVDUnfold`, which is part of the ROOT analysis framework [133].

Singular Value Decomposition and Regularisation of Fluctuations

Very valuable information about the properties of a matrix can be inferred decomposing it into singular values. If, for example, the matrix is orthogonal, all its singular values are equal to 1. On the contrary, a degenerate matrix will have at least one zero among its singular values, which makes the linear system ill-posed and difficult to solve. Even matrices with nearly-zero singular values, or just significantly smaller than others, behave like degenerate ones. Indeed, small singular values, which are often present with detector smearing matrices, are found to greatly enhance statistical fluctuations in the measured distribution. The SVD analysis sheds light on the underlying instability of the problem and locates the difficulty: Reference [161] shows that the fluctuations are due to non-significant contributions, and that the solution depends on the CPU accuracy, which obviously does not make any sense. This allows for a physically motivated regularisation via a discrete minimum-curvature condition on the ratio of the unfolded distribution and a simulated truth distribution, by retaining only the statistically significant contributions, which are found to be related to the larger singular values.

A singular value decomposition (SVD) of a real $m \times n$ matrix A is its factorisation in the form

$$A = U\ S\ V^{T} \tag{7.12}$$

where U is an $m \times m$ orthogonal matrix, V is an $n \times n$ orthogonal matrix, while S is an $m \times n$ diagonal matrix with non-negative diagonal elements. The diagonal elements s_i of S are called `singular values` of the matrix A and they form a non-increasing sequence. If A is a probability matrix with m reconstructed bins and n true bins, very valuable information about the reasons for the apparent instability of its inversion can be inferred from its singular values and from the rotated right-hand-side (r.h.s.) vector d:

$$d = U^{T}\ b \tag{7.13}$$

where U^{T} is the orthogonal matrix in Eq. (7.12) and the vector b, which has dimension m, is the measured spectrum in the m reconstructed bins.

2675 Reference [161] shows that if all the components d_i of the rotated r.h.s. vector d are
2676 statistically significant and if neither one of the singular values is too small, the system
2677 can be easily solved. Otherwise, the problem becomes ill-posed, and when in addition
2678 the r.h.s. is affected by measurement errors, the exact solution usually does not make
2679 any sense. In this case conventional methods of solving linear systems do not work and
2680 usually cannot even detect the problem.

2681 The SVD-based method suppresses the spurious oscillatory component using some
2682 a priori knowledge about the solution, and uses a discrete analogue of the minimum
2683 curvature condition to stabilise the unfolded solution. Technically this can be achieved
2684 by adding a regularisation term to the expression to be minimised, effectively working
2685 as a cutoff for a low-pass filter, if Fourier-transform terminology is used. The common
2686 belief is that the solution should be smooth, with small bin-to-bin variation.

2687 Very important and interesting information about the whole problem can be dis-
2688 closed by plotting $\log|d_i|$ against i. For reasonably smooth measured distributions, only
2689 the first few (say, k) terms of the decomposition are expected to be significant, while
2690 the contribution of quickly oscillating basis vectors (with $i > k$) should be compatible
2691 with zero, well within the statistical errors in d_i (which are equal to 1 for all i). Thus
2692 on the plot one should see two separate patterns: for small i, d_i should be statisti-
2693 cally significant, with $|d_i| >> 1$, falling gradually (usually exponentially) towards a
2694 gaussian-distributed random value for large i. The critical value $i = k$, after which
2695 d_i are non-significant, determines the effective rank of the system.This critical value is
2696 where the behaviour of d_i changes from exponentially falling to a constant and usually
2697 it can be clearly seen on the plot of $\log|d_i|$ against i. The analysis of d_i reveals the
2698 actual level of understanding the measurement errors in the experiment described by
2699 the smearing matrix A in Eq. (7.12).

7.7.2 Regularisation Strength

2701 As explained in Section 7.7.1, the SVD-based unfolding should be regularised by ne-
2702 glecting the insignificant terms of the singular values decomposition, which should be
2703 evident examining $\log|d_i|$ against i, where d_i is the rotated right-hand-side (r.h.s.) vec-
2704 tor defined in Eq. (7.13). This can be seen in Fig. 7.11 where the black solid line shows
2705 the r.h.s. vector for the smearing matrix of Fig. 7.7, i.e. using real ND280 data and the

NEUT-NIWG simulation, for both FGD1 and FGD2 selections. As recommended in the SVD-based unfolding paper [161], the regularisation parameter is to be chosen from this plot at the end of the exponentially falling distribution, which represents the number of significant terms in the decomposition, whilst the following gaussian-distributed random values (around 1) are the singular terms to be neglected. This is clearly on bin 5 for the real ND280 data r.h.s. vector (solid black line), for both FGD1 and FGD2 selections. The dashed lines show the r.h.s. vector when the data distribution is replaced by the GENIE or the NEUT-SF simulation (fake-data). The same could be said looking at the r.h.s vector with GENIE as fake data (dotted blue line), whilst there are less significant terms with NEUT-SF as fake data (dashed red line), which is expected as in this case the Monte Carlo model (NEUT-NIWG) and the fake data model (NEUT-SF) are quite similar.
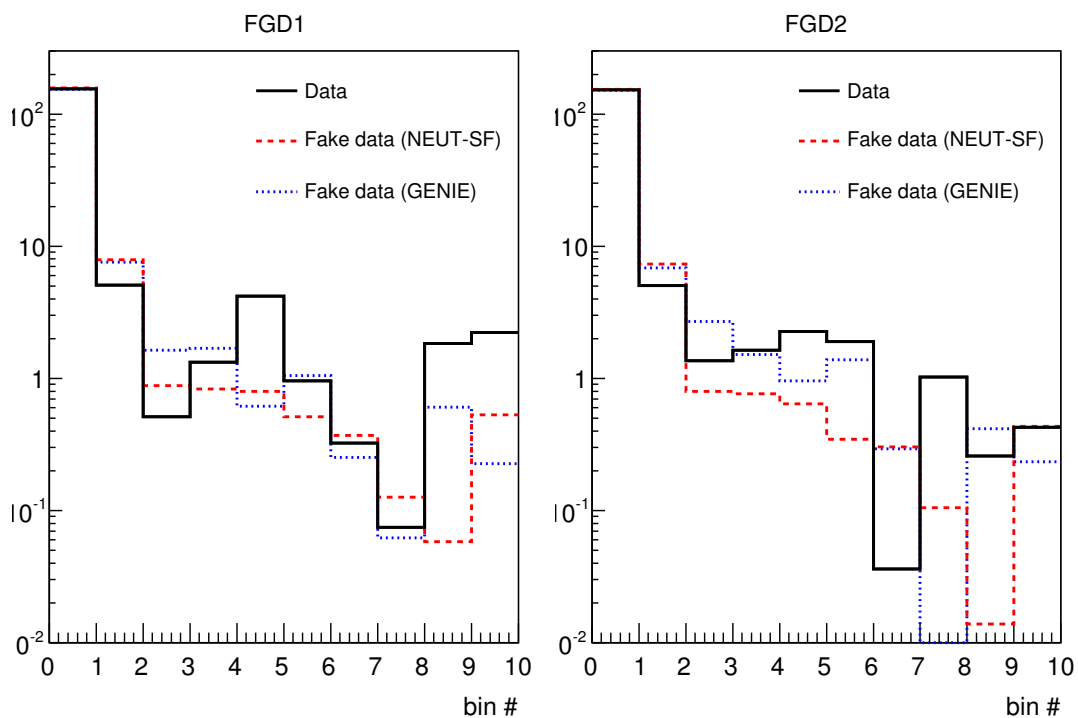
Figure 7.11: Rotated right-hand-side vector (r.h.s., defined in Eq. (7.13)), in solid black using real ND280 data, in dashed red using NEUT-SF as fake data, in dotted blue using GENIE as fake data.

7.7.3 Bias Study with Fake-Data Samples

Unfolding the same MC distribution used to build the detector response matrix, instead of the real ND280 data, the unfolded result should exactly match the cross section given by the MC truth, as it corresponds to the fake-data truth. This preliminary closure test is shown in Fig. 7.12.
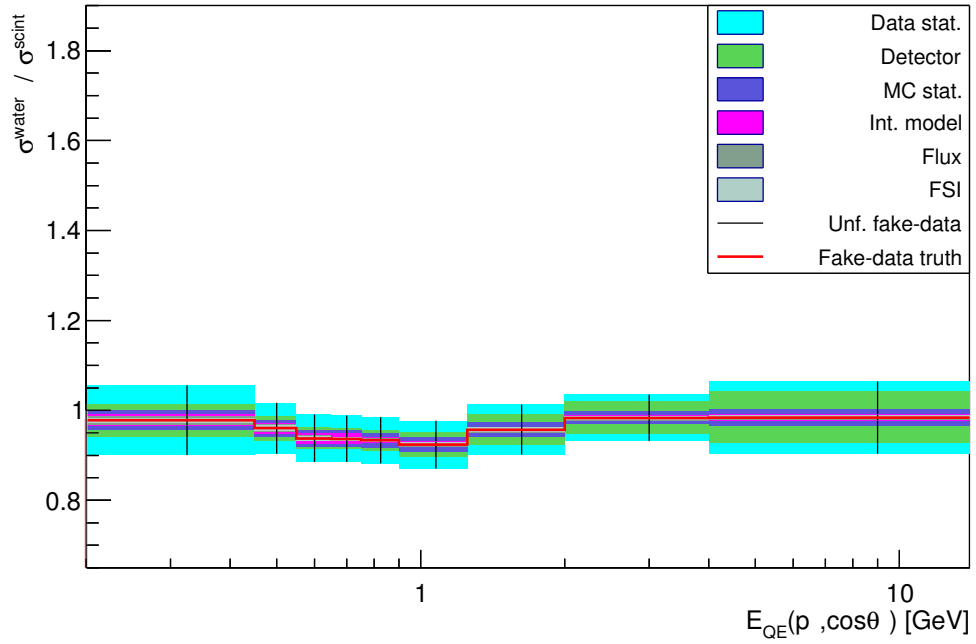
Figure 7.12: Water to scintillator cross-section ratio as a function of $E_{QE}(p_\mu, \cos\theta_\mu)$ unfolding the NEUT-NIWG fake-data distribution with the SVD-regularised technique: as expected the unfolded result exactly matches the fake-data truth cross-section ratio (closure test).

Fig. 7.13 is a fake-data study where GENIE is used as fake-data sample, showing the cross-section ratio as a function of $E_{QE}(p_\mu, \cos\theta_\mu)$ (top figure), with uncertainties for the six error sources (assumed independent, cf. Section 6.1). The error bars are stacked in quadrature: each colour represents how much the correspondent uncertainty contributes to the total error. It can be seen that even though in Fig. 7.5 the differences between NEUT and GENIE are quite evident, they become quite small in the cross-section ratio.

Fig. 7.13 (bottom figure) is the correspondent overall correlation matrix, considering

Figure 7.13: Water to scintillator cross-section ratio as a function of $E_{QE}(p_\mu, \cos\theta_\mu)$ (top) and its correlation matrix (bottom), unfolding the GENIE fake-data distribution with the SVD-regularised technique.

all the error sources. The correlation matrix is an easier way to look at the correlations among bins, other than the covariance matrix, as each of its elements is defined in Eq. (7.10). The χ^2/N_{dof} (Eq. (7.11)) between the unfolded result and the fake-data truth (GENIE), evaluated for the overall covariance matrix (which takes into account all the error sources), is 0.3.

7.7.4 Regularised Results with ND280 Data

The water to scintillator cross-section ratio as a function of $E_{QE}(p_\mu, \cos\theta_\mu)$, unfolding the ND280 data with the SVD-regularised technique, is shown in Fig. 7.14 (top figure). The uncertainties have been propagated to the cross-section result using toy experiments, as described in Section 6.1. The error bars are stacked in quadrature: each colour represents how much the correspondent uncertainty contributes to the total error. Fig. 7.15 shows instead the fractional error of each uncertainties in each bin. The larger uncertainty is the data statistics, which is not supposed to cancel in the ratio, and which is in agreement with the estimation discussed in Section 6.1.1. The systematics uncertainties instead cancel quite nicely in the ratio, thanks to effort spent to correlate and propagate them properly. In the following section, where a total cross-section ratio is evaluated, each detector systematics is detailed. In Fig. 7.14 (bottom figure) is reported the overall correlation matrix. The χ^2/N_{dof} (Eq. (7.11)) between the unfolded result with the ND280 data, and the NEUT-NIWG truth, evaluated for the overall covariance matrix (which takes into account all the error sources), is 0.5.
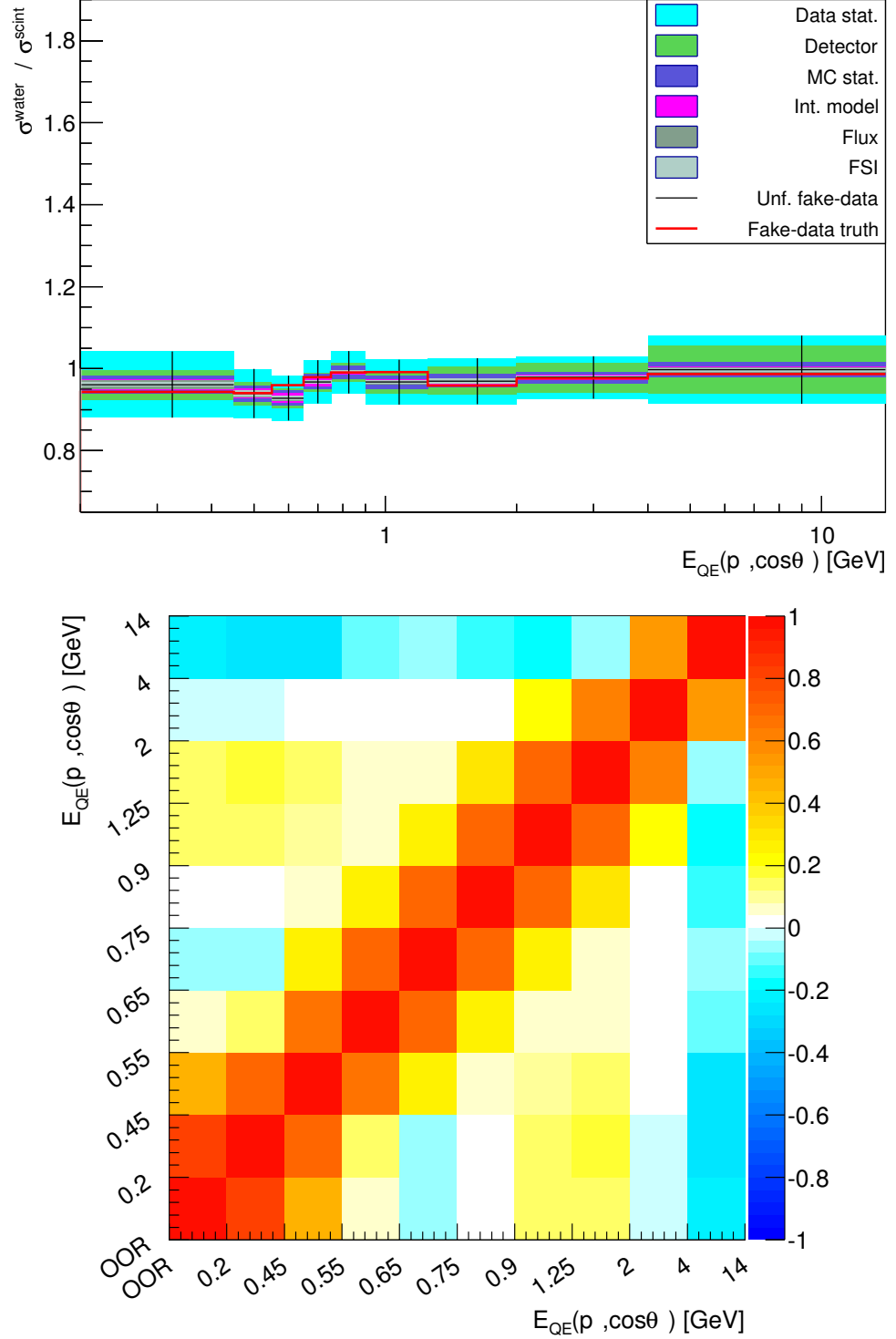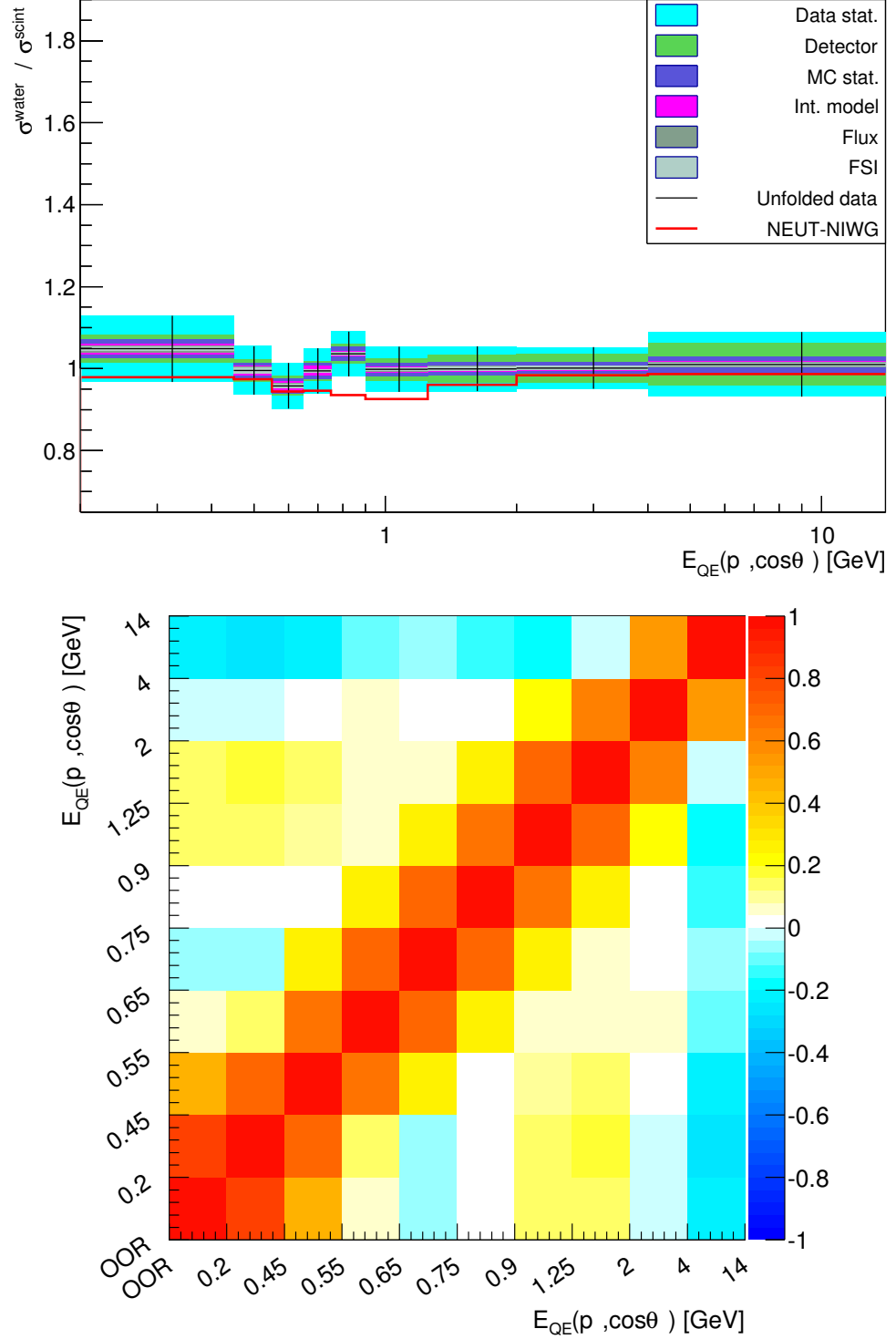
Figure 7.14: Water to scintillator cross-section ratio as a function of $E_{QE}(p_\mu, \cos\theta_\mu)$ (top) and its correlation matrix (bottom), unfolding the ND280 data ν_μ-CC inclusive selection (Section 5.2) with the SVD-regularised technique.
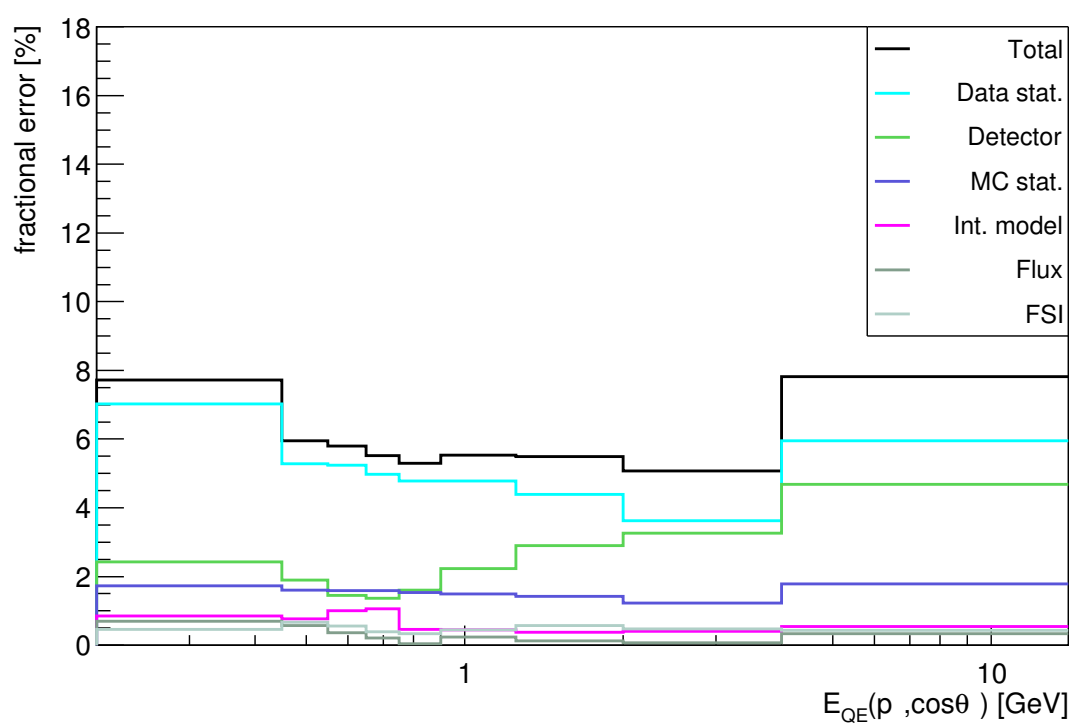
Figure 7.15: Fractional errors of the water to scintillator cross-section ratio in Fig. 7.14 for the corresponding unfolding bins.

7.7.5 Total Cross-Section Ratio

The total cross section is usually found by summing over bins. For the MC truth, this gives the same result of evaluating the cross section from the total number of events, i.e. replacing the estimated number of events $\hat{N}_{\text{FGD1}}$ and $\hat{N}_{\text{FGD2}}$ in Eq. (7.1) with the predicted ones. For the reconstructed data instead, the result would be different: applying the efficiency correction bin by bin gives a more correct result than applying an average efficiency correction to the whole number of events. In the case of a ratio, the sum over bins has to be computed separately for the numerators and the denominators, and the total cross section is the ratio of the two sums.

In the restricted phase space (Eq. (7.2)) the water to scintillator total cross-section ratios predicted by the three generators considered in this analysis (cf. Section 7.2), are:

	Predicted $\sigma^{H_2O}/\sigma^{CH}$
NEUT-NIWG	0.962
NEUT-SF	0.958
GENIE	0.969

In the fake-data study of Fig. 7.13, where GENIE is used as fake data, the total cross-section ratio summing over bins is 0.967 ± 2.55 % (stat.) ± 2.02 % (sys.). The unfolding is therefore working properly, recovering the total truth cross-section ratio of GENIE (0.969 from the table above), with a negligible bias compared to the errors. The uncertainties are evaluated computing the total cross-section ratio of each toy experiment and calculating the variance over toys (Section 6.1).

The water to scintillator total cross-section ratio with the ND280 data in the restricted phase space, summing over bins the unfolded result obtained with the SVD-regularised technique, i.e. Fig. 7.14 plus the "out of range" bin, it is:

$$\sigma^{H_2O}/\sigma^{CH} = 1.01 \pm 2.46\%(\text{stat.}) \pm 1.95\%(\text{sys.}) \qquad (7.14)$$

The uncertainties are evaluated computing the total cross-section ratio of each toy experiment and calculating the variance, and they can be split into the following sources, treated as independent (Section 6.1):

169

	Fractional error
Data statistics	2.38 %
MC statistics	0.63 %
Total statistics	2.46 %
Detector	1.85 %
Interaction model	0.50 %
FSI	0.21 %
Flux	0.29 %
Total systematics	1.95 %

Since the detector uncertainties are the largest one, they have been studied in details. As described in Section 6.2, there are several sources of detector systematics, correlated among each others. Nevertheless they can be studied separately, propagating them to the cross-section result as if they were independent sources, obtaining the following fractional errors:

Detector systematics	Fractional error
Pion secondary interactions	1.47 %
FGD mass	0.95 %
Momentum resolution	0.52 %
TPC track efficiency	0.45 %
Magnetic field distortion	0.43 %
Out of fiducial volume	0.42 %
TPC-FGD matching	0.15 %
TPC PID	0.13 %
Charge mis-identification	0.07 %
Pile-up	0.07 %
Momentum scale	0.07 %
TPC cluster efficiency	< 0.001 %
Sand muons	< 0.001 %

To understand whether the cancellation between FGD1 and FGD2 detector uncertainties is taking place in the ratio, and to quantify how much it is effective, the same table can be computed separately for the numerator (FGD2) and the denominator (FGD1):

Detector systematics	Fractional error		Fractional error	
	FGD1	FGD2	FGD2/FGD1	$\sigma^{H_2O}/\sigma^{CH}$
Pion secondary interactions	1.86 %	1.68 %	0.68 %	1.47 %
FGD mass	0.59 %	0.40 %	0.44 %	0.95 %
Momentum resolution	0.46 %	0.70 %	0.24 %	0.52 %
TPC track efficiency	0.76 %	0.97 %	0.21 %	0.45 %
Magnetic field distortion	0.18 %	0.38 %	0.20 %	0.43 %
Out of fiducial volume	0.59 %	0.70 %	0.19 %	0.42 %
TPC-FGD matching	0.03 %	0.10 %	0.07 %	0.15 %
TPC PID	0.30 %	0.37 %	0.06 %	0.13 %
Charge mis-identification	0.16 %	0.19 %	0.03 %	0.07 %
Pile-up	0.24 %	0.27 %	0.03 %	0.07 %
Momentum scale	0.41 %	0.38 %	0.03 %	0.07 %
TPC cluster efficiency	< 0.001 %	< 0.001 %	< 0.001 %	< 0.001 %
Sand muons	< 0.001 %	< 0.001 %	< 0.001 %	< 0.001 %

As discussed in Section 6.2.5 properly correlating the two FGDs is not trivial. The employed assumptions are quite conservative, but it can be seen in the third column that the cancellation is effective for all the sources. Note that the fractional errors on $\sigma_{water}/\sigma_{scint}$ (fourth column) are larger than the fractional errors of the simple ratio between the two FGDs (third column) because of the second term in Eq. (7.1): a larger water to scintillator fraction would decrease the systematic uncertainties. An improved knowledge of the two FGD detectors and their responses might reduce even further the uncertainties. Anyhow, a limit on the achievable uncertainties is represented by the FGD mass, which is the second largest, giving a $\sim 1\%$ error on the ratio. Indeed the mass systematics cannot cancel more than the current degree, because it is evaluated from the uncertainties on the material densities 'as built', independently for water and scintillator modules (cf. Section 6.2.3.2 and Section 6.2.5): the cancellation in place is due to the presence of identical scintillator modules in both FGDs, but there cannot be cancellation between water and scintillator modules.

Eventually, the total water to scintillator cross-section ratio in $0.2 < E_{QE}(p_\mu, \cos\theta_\mu) < 1.25\,\text{GeV}$, which is the range considered in the T2K oscillation analyses, evaluated by summing over bins in Fig. 7.14 but ignoring the last three bins, it is:

$$\sigma^{H_2O}/\sigma^{CH} = 1.01 \pm 3.50\%(\text{stat.}) \pm 1.87\%(\text{sys.}) \qquad (7.15)$$

As before, the uncertainties are evaluated computing the total cross-section ratio

of each toy experiment and calculating the variance, and they can be split into the following sources, treated as independent (Section 6.1):

	Fractional error
Data statistics	3.40 %
MC statistics	0.84 %
Total statistics	3.50 %
Detector	1.69 %
Interaction model	0.65 %
FSI	0.25 %
Flux	0.38 %
Total systematics	1.87 %

The central value is the same of the one over the whole $E_{QE}(p_\mu, \cos\theta_\mu)$ spectrum, but the uncertainties are larger because of the reduced statistics considered. However, the systematic error is slightly smaller, due to the fact that the detector resolution is worse in the higher energy region. In few other years of data taking, with the increased power of the T2K beam (cf. Fig. 2.4), the statistical error will be significantly reduced.

8

Conclusion

To reach precise measurements of the neutrino oscillation parameters, and consequently hints of CP violation in the lepton sector, oscillation experiments need to have a good understanding of the neutrino interaction model. The main goal of the T2K experiment is the precise measurement of neutrino oscillation parameters. At the same time, the near detector ND280 can be used to provide cross-section measurements that will help to understand the neutrino interaction model. Several ν_μ CC samples from the ND280 detector are currently used in a fit to the oscillation model. In particular, cross sections on water and water to scintillator ratios have the potential to furtherÂ constrain the expected neutrino energy spectrum at Super-Kamiokande, the T2K far detector, it being a water Cherenkov detector. Nevertheless, no measurements of the water cross section have been made so far in the T2K energy range, except for a recent T2K paper [146].

The extraordinary features of the ND280 detector, the good data quality, the thorough event reconstruction and the meticulous simulation, allow to select samples of neutrino events with different topologies and unfold them, i.e. extract information about the true content of the measurement bins by removing the detector smearing and the reconstruction inefficiency. The ND280 tracker volume contains two Fine-Grained Detectors (namely FGD1 and FGD2) which are used as the neutrino interaction target, and which consist of scintillator bars and water modules. Thanks to their design, a cross section on water can be obtained by subtraction of event distributions in the two FGDs.

173

Neutrino cross-section measurements are usually affected by large systematic uncertainties, in particular because the flux systematic is hard to reduce as it is correlated with the neutrino interaction model uncertainties. Nevertheless in a cross-section ratio measurement flux and most of the systematics largely cancel out. Furthermore, a cross-section ratio of ν_μ-CC inclusive samples has the advantage of having small systematics and also the smallest statistical uncertainties.

ν_μ-CC inclusive interactions are selected in FGD1 and in FGD2 sub-detectors, and comparing the two, a water to scintillator cross-section ratio is evaluated as a function of $E_{QE}(p_\mu, \cos\theta_\mu)$, the very quantity which is used in the T2K oscillation analyses. $E_{QE}(p_\mu, \cos\theta_\mu)$ corresponds to the true neutrino energy only for Quasi-Elastic interactions (QE kinematic formula for the neutrino energy). Nonetheless, for any ν_μ-CC interaction, $E_{QE}(p_\mu, \cos\theta_\mu)$ can be simply considered for what it is: a function of the outgoing lepton candidate properties, the muon momentum and the muon direction.

The ν_μ-CC inclusive water to scintillator cross-section ratio has been extracted with two unfolding techniques: (unregularised) matrix inversion and SVD-regularised unfolding. The matrix inversion is known to give unbiased results, but typically carrying large bin-to-bin correlations, oscillation patterns, and huge uncertainties, as noise in the smeared signal is blown up in the inversion. The SVD-based unfolding is basically a regularised matrix inversion, equivalent to a regularised template fit, where a Tikhonov regularisation is re-formulated in terms of the Singular Value Decomposition of the smearing matrix. The regularisation strength is chosen examining the rotated right-hand-side vector obtained in the singular value decomposition, as it unveils which singular values are due to statistical fluctuations, allowing to suppress their spurious, wildly oscillating contributions.

The cross-section ratio results are expressed in the reduced phase-space defined by

$$cos\theta_\mu > 0, \quad p_\mu > 100 \text{ MeV} \tag{8.1}$$

in order to avoid relying completely on the simulation in regions where the efficiency is very low. In this restricted phase space, the water to scintillator cross-section ratio with 5.80×10^{20} protons on target of ND280 data, extracted through the SVD-regularised technique, is shown in Fig. 8.1. The background has been unfolded along with the

174

signal, added as an extra bin in the smearing matrix to take into account the event
migration between signal and background.
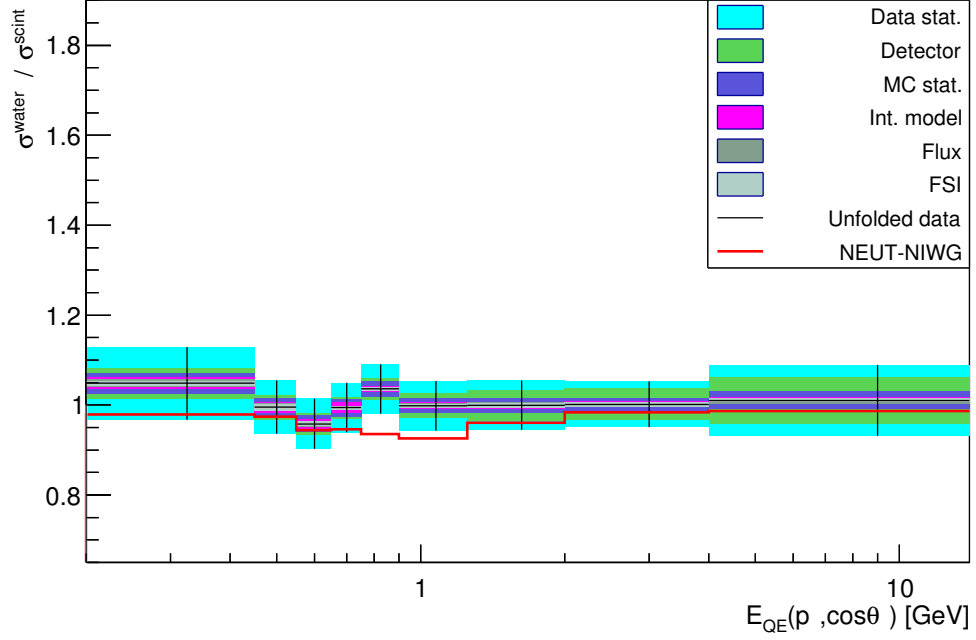
Figure 8.1: Water to scintillator cross-section ratio as a function of $E_{QE}(p_\mu, \cos\theta_\mu)$ unfolding the ND280 data ν_μ-CC inclusive selection with the SVD-regularised technique.

2869 Summing over bins, the total cross-section ratio over the whole $E_{QE}(p_\mu, \cos\theta_\mu)$
2870 range is

$$\sigma^{H_2O}/\sigma^{CH} = 1.01 \pm 2.46\%(\text{stat.}) \pm 1.95\%(\text{syst.}) \qquad (8.2)$$

2871 while in $0.2 < E_{QE}(p_\mu, \cos\theta_\mu) < 1.25$ GeV, which is the range considered in the T2K
2872 oscillation analyses, it is

$$\sigma^{H_2O}/\sigma^{CH} = 1.01 \pm 3.50\%(\text{stat.}) \pm 1.87\%(\text{syst.}) \qquad (8.3)$$

2873 Statistical, detector, flux and cross-section model uncertainties have been propa-
2874 gated to the cross-section results by means of toy experiments. The value given by the
2875 NEUT-NIWG simulation (NEUT generator reweighted with the T2K Neutrino Inter-
2876 action Working Group tuning, cf. Section 6.4.1) is one sigma away from the unfolded

result.

The natural extension of this analysis is extracting the cross-section ratio for exclusive ν_μ-CC channels, in particular for the three samples used in the ND280 fit to the T2K oscillation model: *CC0π*, *CC1π^+* and *CCother* (cf. Section 3.1). Being subsamples of the inclusive selection used in this analysis, the statistical uncertainty will be larger, but the systematics should still cancel to a good degree. Moreover, the T2K beam is being upgraded to increase its power (cf. Fig. 2.4), and ND280 is scheduled to take data up to about four times the current protons on target, thus the statistical error should reduce of a factor two in the near future. The fit to the ND280 near detector data is employed to constrain the flux and cross-section model parameters at the T2K far detector. Therefore, these studies, in particular measurements on water and water to scintillator ratios, are extremely important for both the T2K experiment and the neutrino community, as they contribute to eliminate the uncertainties arising from the carbon/oxygen differences. Future experiments will also find the new cross-section data beneficial. Better constrained cross-section models will result in smaller uncertainties for the oscillation measurements, hence a better chance to measure CP violation in the lepton sector.

References

[1] T2K Collaboration. **T2K Collaboration**.

[2] T2K Collaboration. **Breakthrough prize 2016**. 2015.

[3] Wolfgang Pauli. **Dear radioactive ladies and gentlemen**. *Phys. Today, 31N9*, **27**, 1978.

[4] Chadwick J. **Intensitätsverteilung im magnetischen Spektrum der β - Starhlen von Radium B+C**. *Verh. der Deutschen Physikalischen Ges.*, **16**:383, 1914.

[5] E. Fermi. **Tentativo di una teoria dei raggi β**. *La Ricerca Scientifica*, **2**, 1933.

[6] F. L. Wilson. **Fermi's Theory of Beta Decay**. *American Journal of Physics*, **36**:1150–1160, December 1968.

[7] E. Fermi. **Tentativo Di Una Teoria Dell'emissione Dei Raggi β**. *La Ricerca Scientifica, 4, p. 491-5*, 1933.

[8] E Fermi. **Tentativo di una teoria dei raggi beta**. *Il Nuovo Cimento 11, 1*, 1934.

[9] F. Reines and C. L. Cowan. **Detection of the Free Neutrino**. *Phys. Rev.*, **92**(3):830–831, Nov 1953.

[10] G. Danby, J-M. Gaillard, K. Goulianos, L. M. Lederman, N. Mistry, M. Schwartz, and J. Steinberger. **Observation of High-Energy Neutrino Reactions and the Existence of Two Kinds of Neutrinos**. *Phys. Rev. Lett.*, **9**(1):36–44, Jul 1962.

[11] K. KODAMA ET AL. **Observation of tau-neutrino interactions**. *Phys. Lett.*, **B504**:218–224, 2001.

[12] D. DECAMP ET AL. **Determination of the Number of Light Neutrino Species**. *Phys. Lett.*, **B231**:519–529, 1989.

[13] S SCHAEL, R BARATE, R BRUNELIERE, D BUSKULIC, I DE BONIS, D DÉCAMP, P GHEZ, C GOY, S JÉZÉQUEL, JP LEES, ET AL. **Precision electroweak measurements on the Z resonance**. *Physics Reports A Review Section of Physics Letters*, **427**(5-6):257–454, 2006.

[14] S. CHATRCHYAN ET AL. **Observation of a new boson at a mass of 125 GeV with the {CMS} experiment at the {LHC}**. *Physics Letters B*, **716**(1):30 – 61, 2012.

[15] G. AAD ET AL. **Observation of a new particle in the search for the Standard Model Higgs boson with the {ATLAS} detector at the {LHC}**. *Physics Letters B*, **716**(1):1 – 29, 2012.

[16] Y. FUKUDA ET AL. **Evidence for oscillation of atmospheric neutrinos**. *Phys. Rev. Lett.*, **81**:1562–1567, 1998.

[17] Q. R. AHMAD, R. C. ALLEN, AND T. C. ET AL. ANDERSEN. **Measurement of the Rate of $\nu_e + d \to p + p + e^-$ Interactions Produced by ^{8}B Solar Neutrinos at the Sudbury Neutrino Observatory**. *Phys. Rev. Lett.*, **87**:071301, Jul 2001.

[18] QR AHMAD, RC ALLEN, TC ANDERSEN, JD ANGLIN, JC BARTON, EW BEIER, M BERCOVITCH, J BIGU, SD BILLER, RA BLACK, ET AL. **Direct evidence for neutrino flavor transformation from neutral-current interactions in the Sudbury Neutrino Observatory**. *Physical Review Letters*, **89**(1):011301, 2002.

[19] RAYMOND DAVIS JR, DON S HARMER, AND KENNETH C HOFFMAN. **Search for neutrinos from the sun**. *Physical Review Letters*, **20**(21):1205, 1968.

[20] John Bahcall, Neta Bahcall, and Giora Shaviv. **Present Status of the Theoretical Predictions for the ^{37}Cl Solar-Neutrino Experiment**. *Phys. Rev. Lett.*, **20**:1209–1212, May 1968.

[21] J. N. Bahcall, William A. Fowler, I. Iben, Jr., and R. L. Sears. **Solar neutrino flux**. *Astrophys. J.*, **137**:344–346, 1963.

[22] K. S. Hirata et al. **Experimental Study of the Atmospheric Neutrino Flux**. *Phys. Lett.*, **B205**:416, 1988.

[23] SAGE Collaboration. **Measurement of the solar neutrino capture rate with gallium metal**. *Physical Review C*, **60**(5):055801, 1999.

[24] GALLEX Collaboration. **GALLEX solar neutrino observations: Complete results for GALLEX II**. *Physics Letters B*, **357**(1):237–247, 1995.

[25] K. S. Hirata, T. Kajita, and T. et al. Kifune. **Observation of ^8B solar neutrinos in the Kamiokande-II detector**. *Phys. Rev. Lett.*, **63**(1):16–19, Jul 1989.

[26] E. Lisi, A. Marrone, and D. Montanino. **Probing possible decoherence effects in atmospheric neutrino oscillations**. *Phys. Rev. Lett.*, **85**:1166–1169, 2000.

[27] Lincoln Wolfenstein. **Neutrino oscillations in matter**. *Physical Review D*, **17**(9):2369, 1978.

[28] L. Wolfenstein. **Neutrino oscillations in matter**. *Phys. Rev. D*, **17**:2369–2374, May 1978.

[29] B. Pontecorvo. **Mesonium and antimesonium**. *Sov. Phys. JETP*, **6**:429, 1957.

[30] Bruno Pontecorvo. **Mesonium and antimesonium**. *Zhur. Eksptl'. i Teoret. Fiz.*, **33**, 1957.

[31] Ziro Maki, Masami Nakagawa, and Shoichi Sakata. **Remarks on the unified model of elementary particles**. *Progress of Theoretical Physics*, **28**(5):870–880, 1962.

[32] MAKOTO KOBAYASHI AND TOSHIHIDE MASKAWA. **CP-Violation in the Renormalizable Theory of Weak Interaction**. *Progress of Theoretical Physics*, **49**(2):652, 1973.

[33] CARLO GIUNTI AND CHUNG W KIM. *Fundamentals of neutrino physics and astrophysics*. Oxford university press, 2007.

[34] ZIRO MAKI, MASAMI NAKAGAWA, AND SHOICHI SAKATA. **Remarks on the unified model of elementary particles**. *Prog. Theor. Phys.*, **28**:870–880, 1962.

[35] NICOLA CABIBBO. **Unitary Symmetry and Leptonic Decays**. *Phys. Rev. Lett.*, **10**:531–533, Jun 1963.

[36] HYPER-KAMIOKANDE PROTO-COLLABORATION. **Physics Potential of a Long Baseline Neutrino Oscillation Experiment Using J-PARC Neutrino Beam and Hyper-Kamiokande**. *arXiv preprint arXiv:1502.05199*, 2015.

[37] MATTHEW BASS, DANIEL CHERDACK, AND ROBERT J WILSON. **Future Neutrino Oscillation Sensitivities for LBNE**. *arXiv preprint arXiv:1310.6812*, 2013. LBNE is the predecessor of DUNE.

[38] C. PATRIGNANI ET AL. **Review of Particle Physics**. *Chin.Phys.*, **C40**:100001, 2016.

[39] NOvA COLLABORATION. **NOvA proposal to build a 30 kiloton off-axis detector to study neutrino oscillations in the fermilab NuMI beamline**. *arXiv preprint hep-ex/0503053*, 2005.

[40] K. ET AL. ABE. **Measurement of Neutrino Oscillation Parameters from Muon Neutrino Disappearance with an Off-Axis Beam**. *Phys. Rev. Lett.*, **111**:211803, Nov 2013.

[41] P. ET AL. ADAMSON. **Measurement of Neutrino and Antineutrino Oscillations Using Beam and Atmospheric Data in MINOS**. *Phys. Rev. Lett.*, **110**:251801, Jun 2013.

[42] KamLAND Collaboration. **Precision measurement of neutrino oscillation parameters with KamLAND**. *Physical Review Letters*, **100**(22):221803, 2008.

[43] Daya Bay Collaboration. **Observation of electron-antineutrino disappearance at Daya Bay**. *Physical Review Letters*, **108**(17):171803, 2012.

[44] F. P. et al. An. **Spectral Measurement of Electron Antineutrino Oscillation Amplitude and Frequency at Daya Bay**. *Phys. Rev. Lett.*, **112**:061801, Feb 2014.

[45] RENO Collaboration. **Observation of reactor electron antineutrinos disappearance in the RENO experiment**. *Physical Review Letters*, **108**(19):191802, 2012.

[46] Double CHOOZ Collaboration. **Indication of reactor ν e disappearance in the Double Chooz experiment**. *Physical Review Letters*, **108**(13):131801, 2012.

[47] K. Abe et al. (The T2K Collaboration). **Indication of Electron Neutrino Appearance from an Accelerator-produced Off-axis Muon Neutrino Beam**. *Phys. Rev. Lett. 107, 041801, arXiv:1106.2822 [hep-ex]*, 2011.

[48] Andrei D Sakharov. **Violation of CP invariance, C asymmetry, and baryon asymmetry of the universe**. *Soviet Physics Uspekhi*, **34**(5):392, 1991.

[49] Jiro Arafune, Masafumi Koike, and Joe Sato. **CP violation and matter effect in long baseline neutrino oscillation experiments**. *Physical Review D*, **56**(5):3093, 1997.

[50] KN Abazajian, E Calabrese, A Cooray, F De Bernardis, S Dodelson, A Friedland, GM Fuller, Steen Hannestad, BG Keating, EV Linder, et al. **Cosmological and astrophysical neutrino mass measurements**. *Astroparticle Physics*, **35**(4):177–184, 2011.

[51] KATRIN Collaboration and others. **KATRIN: A next generation tritium beta decay experiment with sub-eV sensitivity for the electron neutrino mass**. *arXiv preprint hep-ex/0109033*, 2001.

[52] A AGUILAR ET AL. **Evidence for neutrino oscillations from the observa-tion of ν^- e appearance in a ν^- μ beam**. *Physical Review D*, **64**(11):112007, 2001.

[53] MINIBOONE COLLABORATION. **First measurement of the muon neutrino charged current quasielastic double differential cross section**. *Physical Review D*, **81**(9):092005, 2010.

[54] MINIBOONE COLLABORATION. **Improved Search for ν^- μ $\rightarrow$ ν^- e Oscillations in the MiniBooNE Experiment**. *Physical review letters*, **110**(16):161801, 2013.

[55] SAMOIL M BILENKY, C GIUNTI, WALTER GRIMUS, AND T SCHWETZ. **Four-neutrino mass spectra and the Super-Kamiokande atmospheric up-down asymmetry**. *Physical Review D*, **60**(7):073007, 1999.

[56] K. ET AL. (T2K COLLABORATION) ABE. **Search for short baseline ν_e dis-appearance with the T2K near detector**. *Phys. Rev. D*, **91**:051102, Mar 2015.

[57] P. ADAMSON ET AL. (THE MINOS COLLABORATION). **Active to Sterile Neutrino Mixing Limits from Neutral-Current Interactions in MINOS**. *arXiv:hep-ex/1104.3922v1*, 2011.

[58] P. ET AL. ADAMSON. **Limits on Active to Sterile Neutrino Oscillations from Disappearance Searches in the MINOS, Daya Bay, and Bugey-3 Experiments**. *Phys. Rev. Lett.*, **117**:151801, Oct 2016.

[59] M. G. ET AL. AARTSEN. **Searches for Sterile Neutrinos with the IceCube Detector**. *Phys. Rev. Lett.*, **117**:071801, Aug 2016.

[60] E. MAJORANA. **Symmetrical Theory of the Electron and the Positron**. *Nuovo Cim. 5, 171-184*, 1937.

[61] SUPERNEMO COLLABORATION. **Probing new physics models of neutrino-less double beta decay with SuperNEMO**. *The European Physical Journal C-Particles and Fields*, **70**(4):927–943, 2010.

[62] CHRISTINE KRAUS AND SIMON JM PEETERS. **The rich neutrino programme of the SNO+ experiment**. *Progress in Particle and Nuclear Physics*, **64**(2):273–277, 2010.

[63] M. AGOSTINI ET AL. **Background free search for neutrinoless double beta decay with GERDA Phase II**. 2017. [Nature544,47(2017)].

[64] GABY R´ADEL AND ROLF BEYER. **NEUTRINO ELECTRON SCATTERING**. *Modern Physics Letters A*, **08**(12):1067–1088, 1993.

[65] K.A. OLIVE ET AL. **Review of particle physics**. *Chin. Phys. C*, **38**, 2014.

[66] JOSEPH A FORMAGGIO AND GP ZELLER. **From eV to EeV: neutrino cross sections across energy scales**. *Reviews of Modern Physics*, **84**(3):1307–1341, Sep 2012.

[67] B. POVH ET AL. *Particles and Nuclei : An Introduction to the Physical Concepts.* Springer-Verlag Berlin Heidelberg, 2008.

[68] R.A. SMITH AND E.J. MONIZ. **Neutrino reactions on nuclear targets**. *Nuclear Physics B*, **43**:605 – 622, 1972.

[69] O. BENHAR. **The Nucleon Spectral Function in Nuclear Matter**. *Nuclear Physics A, 505, 2, Pages 267-299*, 1989.

[70] CALLUM WILKINSON. **NEUT development for T2K and relevance of updated 2p2h models**, 2014. NuFact 2014.

[71] R. ET AL. SHNEOR. **Investigation of Proton-Proton Short-Range Correlations via the $^{12}\mathrm{C}(e,e'pp)$ Reaction**. *Phys. Rev. Lett.*, **99**:072501, Aug 2007.

[72] J NIEVES, I RUIZ SIMO, AND MJ VICENTE VACAS. **The nucleon axial mass and the MiniBooNE quasielastic neutrino–nucleus scattering problem**. *Physics Letters B*, **707**(1):72–75, 2012.

[73] Marco Martini, Magda Ericson, Guy Chanfray, and Jacques Marteau. **Unified approach for nucleon knock-out and coherent and incoherent pion production in neutrino interactions with nuclei**. *Physical Review C*, **80**(6):065501, 2009.

[74] Jan T. Sobczyk. **Multinucleon-ejection model for two-body-current neutrino interactions**. *Phys. Rev. C*, **86**:015504, Jul 2012.

[75] M. Martini, M. Ericson, and G. Chanfray. **Energy reconstruction effects in neutrino oscillation experiments and implications for the analysis**. *Phys. Rev.*, **D87**(1):013009, 2013.

[76] C. H. Llewellyn Smith. **Neutrino Reactions at Accelerator Energies**. *Phys. Rept.*, **3**:261–379, 1972.

[77] NOMAD Collaboration. **A study of quasi-elastic muon neutrino and antineutrino scattering in the NOMAD experiment**. *The European Physical Journal C-Particles and Fields*, **63**(3):355–381, 2009.

[78] MINERνA Collaboration. **Measurement of Muon Neutrino Quasielastic Scattering on a Hydrocarbon Target at E ν 3.5 GeV**. *Physical review letters*, **111**(2):022502, 2013.

[79] R. Smith and E. Moniz. **Neutrino Reactions on Nuclear Targets**. *Nucl. Phys. B 43, 605*, 1972.

[80] Dieter Rein and Lalit M Sehgal. **Neutrino-excitation of baryon resonances and single pion production**. *Annals of Physics*, **133**(1):79–153, 1981.

[81] Dieter Rein and Lalit M Sehgal. **Neutrino-excitation of baryon resonances and single pion production**. *Annals of Physics*, **133**(1):79 – 153, 1981.

[82] GM Radecky et al. **Study of single-pion production by weak charged currents in low-energy ν d interactions**. *Physical Review D*, **25**(5):1161, 1982.

[83] T Kitagaki, H Yuta, S Tanaka, A Yamaguchi, K Abe, K Hasegawa, K Tamai, S Kunori, Y Otani, H Hayano, et al. **Charged-current exclusive pion production in neutrino-deuterium interactions**. *Physical Review D*, **34**(9):2554, 1986.

[84] Callum Wilkinson, Philip Rodrigues, Susan Cartwright, Lee Thompson, and Kevin McFarland. **Reanalysis of bubble chamber measurements of muon-neutrino induced single pion production**. *Physical Review D*, **90**(11):112017, 2014.

[85] KM Graczyk, D Kiełczewska, P Przewłocki, and JT Sobczyk. C_5^A **axial form factor from bubble chamber experiments**. *Physical Review D*, **80**(9):093001, 2009.

[86] MiniBooNE Collaboration. **Measurement of neutrino-induced charged-current charged pion production cross sections on mineral oil at E ν 1 GeV**. *Physical Review D*, **83**(5):052007, 2011.

[87] MINERνA Collaboration. **Charged Pion Production in ν_μ Interactions on Hydrocarbon at E = 4.0 GeV**. *arXiv preprint arXiv:1406.6415*, 2014.

[88] CHARM-II collaboration. **Coherent single charged pion production by neutrinos**. *Physics Letters B*, **313**(1):267–275, 1993.

[89] Y. Kurimoto et al. (SciBooNE Collaboration). **Improved Measurement of Neutral Current Coherent π^0 Production on Carbon in a Few-GeV Neutrino Beam**. *Phys. Rev. D 81, 111102, arXiv:1005.0059 [hep-ex].*, 2010.

[90] K2K collaboration. **Search for coherent charged pion production in neutrino-carbon interactions**. *Physical review letters*, **95**(25):252301, 2005.

[91] K. Hiraide et al. (SciBooNE Collaboration). **Search for Charged Current Coherent Pion Production on Carbon in a Few-GeV Neutrino Beam**. *Phys. Rev. D 78, 112004, arXiv:0811.0369 [hep-ex]*, 2008.

[92] MINERνA COLLABORATION. **Measurement of Coherent Production of** $\pi\pm$**in Neutrino and Antineutrino Beams on Carbon from E** ν **of 1.5 to 20 GeV**. *Physical Review Letters*, **113**(26):261802, 2014.

[93] M. GLÜR, E. REYA, AND A. VOGT. **Parton distributions for high energy collisions**. *Zeitschrift für Physik C Particles and Fields*, **53**(1):127–134, 1992.

[94] A BODEK AND U. K. YANG. **Higher twist, xi(omega) scaling, and effective LO PDFs for lepton scattering in the few GeV region**. *J. Phys.*, **G29**:1899–1906, 2003.

[95] K. ABE ET AL. (THE T2K COLLABORATION). **The T2K Experiment**. *Nucl. Instrum. Meth. A (NIMA) DOI number: 10.1016/j.nima.2011.06.067, arXiv:1106.1238*, 2011.

[96] D. BEAVIS ET AL. **Proposal of BNL AGS E-889**. 1995.

[97] Y. AJIMA ET AL. **Tokai-to-Kamioka (T2K) Long Baseline Neutrino Oscillation Experiment Proposal**, 2006.

[98] K. ABE ET AL. (THE T2K COLLABORATION). **Evidence of Electron Neutrino Appearance in a Muon Neutrino Beam**. *Phys. Rev. D 88, 032002, arXiv:1304.0841 [hep-ex]*, 2013.

[99] K. ABE ET AL. (THE T2K COLLABORATION). **Observation of Electron Neutrino Appearance in a Muon Neutrino Beam**. *Phys. Rev. Lett. 112, 061802, arXiv:1311.4750 [hep-ex]*, 2014.

[100] K. ABE ET AL. (THE T2K COLLABORATION). **First Muon Neutrino Disappearance Study with an Off-axis Beam**. *Phys. Rev. D 85, 031103, arXiv:1201.1386 [hep-ex]*, 2012.

[101] K. ABE ET AL. (THE T2K COLLABORATION). **Measurement of Neutrino Oscillation Parameters from Muon Neutrino Disappearance with an Off-Axis Beam**. *Phys. Rev. Lett. 111, 211803, arXiv: 1308.0465 [hep-ex]*, 2013.

[102] K. ABE ET AL. (THE T2K COLLABORATION). **Precise Measurement of the Neutrino Mixing Parameter** θ_{23} **from Muon Neutrino Disappearance**

in an Off-axis Beam. *Phys. Rev. Lett. 112, 181801, arXiv:1403.1532 [hep-ex]*, 2014.

[103] T2K COLLABORATION. **Measurement of neutrino oscillation parameters from muon neutrino disappearance with an off-axis beam**. *Physical review letters*, **111**(21):211803, 2013.

[104] T2K COLLABORATION. **Measurement of the inclusive ν μ charged current cross section on carbon in the near detector of the T2K experiment**. *Physical Review D*, **87**(9):092003, 2013.

[105] T2K COLLABORATION. **Measurement of the Inclusive Electron Neutrino Charged Current Cross Section on Carbon with the T2K Near Detector**. *Physical review letters*, **113**(24):241803, 2014.

[106] T2K COLLABORATION. **Measurement of the ν_{μ} CCQE cross section on carbon with the ND280 detector at T2K**. *arXiv preprint arXiv:1411.6264*, 2014.

[107] T2K COLLABORATION. **Measurement of the inclusive ν_{μ} charged current cross section on iron and hydrocarbon in the T2K on-axis neutrino beam**. *Phys. Rev. D*, **90**:052010, Sep 2014.

[108] J-PARC TDR. **KEK-Report 2002-13 and JAERI-Tech 2003-044**. *http://hadron.kek.jp/ accelerator/TDA/tdr2003/index2.html*, 2003.

[109] K MATSUOKA, AK ICHIKAWA, H KUBO, K MAEDA, T MARUYAMA, C MATSUMURA, A MURAKAMI, T NAKAYA, K NISHIKAWA, T OZAKI, ET AL. **Design and performance of the muon monitor for the T2K neutrino oscillation experiment**. *Nuclear Instruments and Methods in Physics Research Section A: Accelerators, Spectrometers, Detectors and Associated Equipment*, **624**(3):591–600, 2010.

[110] D BEAVIS, A CARROLL, AND I CHIANG. **Long baseline neutrino oscillation experiment at the AGS**. *Physics Design Report Brookhaven National Lab., Upton, NY.*, **1**, 1995.

[111] C. Giganti (for the T2K Collaboration). **T2K Experiment: Status and Initial Look At the Data**. *22nd Rencontres de Blois, July 17th 2010 (talk)*, 2010.

[112] K. Abe et al. (The T2K Collaboration). **The T2K Neutrino Flux Prediction**. *Phys. Rev. D 87, 012001*, 2013.

[113] E. Ichihara et al. (The SK Collaboration) Y. Fukuda, T. Hayakawa. **The Super-Kamiokande Detector**. *Nucl. Instrum. And Meth. A (NIMA) DOI number: 10.1016/S0168-9002, 00425-X*, 2003.

[114] Pavel A Cherenkov. **Visible emission of clean liquids by action of γ radiation**. *Doklady Akademii Nauk SSSR*, **2**:451, 1934.

[115] et al. (The SK Collaboration) Y. Fukuda. **Measurements of the Solar Neutrino Flux from Super-Kamiokande's First 300 Days**. *Phys. Rev. Lett. 81, 1158.*, 1998.

[116] et al. (The SK Collaboration) Y. Fukuda. **Evidence for Oscillation of Atmospheric Neutrinos**. *Phys. Rev. Lett. 81, 1562.*, 1998.

[117] M. H. Ahn et al. (The K2K Collaboration). **Measurement of Neutrino Oscillation by the K2K Experiment**. *Phys.Rev. D 74, 072003*, 2006.

[118] et al. M. Shiozawa. **Search for Proton Decay Via $p \rightarrow E^+\pi^0$ in a Large Water Cherenkov Detector**. *Phys. Rev. Lett. 81, 3319*, 1998.

[119] et al. Y. Hayato. **Search for Proton Decay Through $p \rightarrow \bar{\nu}K^+$ in a Large Water Cherenkov Detector**. *Phys. Rev. Lett. 83, 1529*, 1999.

[120] K. Abe et al. (The T2K Collaboration). **Measurements of the T2K Neutrino Beam Properties Using the INGRID On-Axis Near Detector**. *Nucl. Instrum. And Meth. A (NIMA) DOI number: 10.1016/j.nima.2012.03.023, arXiv:1111.3119 [hep-ex]*, 2012.

[121] P-A Amaudruz, M Barbi, D Bishop, N Braam, DG Brook-Roberge, S Giffin, S Gomi, P Gumplinger, K Hamano, NC Hastings, et al. **The

T2K fine-grained detectors. *Nuclear Instruments and Methods in Physics Research Section A: Accelerators, Spectrometers, Detectors and Associated Equipment*, **696**:1–31, 2012.

[122] Nicolas Abgrall, B Andrieu, P Baron, P Bene, V Berardi, J Beucher, P Birney, F Blaszczyk, Alain Blondel, C Bojechko, et al. **Time projection chambers for the T2K near detectors**. *Nuclear Instruments and Methods in Physics Research Section A: Accelerators, Spectrometers, Detectors and Associated Equipment*, **637**(1):25–46, 2011.

[123] S Assylbekov, G Barr, BE Berger, H Berns, D Beznosko, A Bodek, R Bradford, N Buchanan, H Budd, Y Caffari, et al. **The T2K ND280 off-axis pi–zero detector**. *Nuclear Instruments and Methods in Physics Research Section A: Accelerators, Spectrometers, Detectors and Associated Equipment*, **686**:48–63, 2012.

[124] D Allan, C Andreopoulos, C Angelsen, GJ Barker, G Barr, S Bentham, I Bertram, S Boyd, K Briggs, RG Calland, et al. **The electromagnetic calorimeter for the T2K near detector ND280**. *Journal of Instrumentation*, **8**(10):P10019, 2013.

[125] S Aoki, G Barr, M Batkiewicz, J Błocki, JD Brinson, W Coleman, A Dabrowska, I Danko, M Dziewiecki, B Ellison, et al. **The T2K side muon range detector (SMRD)**. *Nuclear Instruments and Methods in Physics Research Section A: Accelerators, Spectrometers, Detectors and Associated Equipment*, **698**:135–146, 2013.

[126] D. G. Brook-Roberge. **Measurements of Neutrino Interactions on Water Using a Fine-Grained Scintillator Detector with Water Targets**. *Thesis Dissertation*.

[127] P.-A. Amaudruz et al. (The T2K FGD Collaboration). **The T2K Fine-Grained Detectors**. *Nucl. Instrum. And Meth. A (NIMA) DOI number: 10.1016/j.nima.2012.08.020*, 2012.

[128] J. Kim. **Michel Electrons Analysis in the Fine-Grained Detectors for T2K**. *B.Sc Thesis*.

[129] ET AL. I. GIOMATARIS. **Micromegas in a Bulk**. *Nucl. Instrum. And Meth. A (NIMA) DOI number: 10.1016/j.nima.2005.12.222*, 2006.

[130] T. YUAN FOR THE T2K COLLABORATION. **Measuring the ν_μ Charged Current Quasielastic Cross Section on Water Using T2K's Near Detector**. *Neutrino2014, poster*, 2014.

[131] S. ASSYLBEKOV ET AL. (THE T2K PØD COLLABORATION). **The T2K ND280 Off-Axis Pi-Zero Detector**. *Nucl. Instrum. And Meth. A (NIMA) DOI number: 10.1016/j.nima.2012.05.028*, 2012.

[132] S. AOKI ET AL. (THE T2K SMRD COLLABORATION). **The T2K Side Muon Range Detector (SMRD)**. *Nucl. Instrum. And Meth. A (NIMA) DOI number: 10.1016/j.nima.2012.10.001*, 2012.

[133] RENE BRUN AND FONS RADEMAKERS. **ROOT - an object oriented data analysis framework**. *Nuclear Instruments and Methods in Physics Research Section A: Accelerators, Spectrometers, Detectors and Associated Equipment*, **389**(1):81–86, 1997.

[134] RENE BRUN, FEDERICO CARMINATI, SIMONE GIANI, ET AL. **GEANT detector description and simulation tool**. *CERN program library long writeup W*, **5013**:1993, 1993.

[135] GIUSEPPE BATTISTONI, F CERUTTI, A FASSO, A FERRARI, S MURARO, J RANFT, S ROESLER, AND PR SALA. **The FLUKA code: Description and benchmarking**. In *Hadronic Shower Simulation Workshop(AIP Conference Proceedings Volume 896)*, **896**, pages 31–49, 2007.

[136] MAREK GAZDZICKI, NA61/SHINE COLLABORATION, ET AL. **Ion program of NA61/SHINE at the CERN SPS**. *Journal of Physics G: Nuclear and Particle Physics*, **36**(6):064039, 2009.

[137] YOSHINARI HAYATO. **A neutrino interaction simulation program library NEUT**. *Acta Physica Polonica B*, **40**(9):2477, 2009.

[138] Costas Andreopoulos, A Bell, D Bhattacharya, F Cavanna, J Dobson, S Dytman, H Gallagher, P Guzowski, R Hatcher, P Kehayias, et al. **The GENIE neutrino monte carlo generator**. *Nuclear Instruments and Methods in Physics Research Section A: Accelerators, Spectrometers, Detectors and Associated Equipment*, **614**(1):87–104, 2010.

[139] Y. Hayato. **A Neutrino Interaction Simulation Program Library NEUT**. *Acta Phys. Pol. B 40, 2477*, 2009.

[140] J. Nieves, I. Ruiz Simo, and M. J. Vicente Vacas. **Inclusive charged-current neutrino-nucleus reactions**. *Phys. Rev. C*, **83**:045501, Apr 2011.

[141] Arie Bodek and JL Ritchie. **Fermi-motion effects in deep-inelastic lepton scattering from nuclear targets**. *Physical Review D*, **23**(5):1070, 1981.

[142] The ND280 NuMu Group. ν_μ **CC event selections in the ND280 tracker using Run 2+3+4**. T2K Technical note TN-212, available upon request.

[143] C. Wilkinson, R. Terri, C. Andreopoulos, A. Bercellie, C. Bronner, S. Cartwright, P. de Perio, J. Dobson, K. Duffy, A. P. Furmanski, L. Haegel, Y. Hayato, A. Kaboth, K. Mahn, K. S. McFarland, J. Nowak, A. Redij, P. Rodrigues, F. Sánchez, J. D. Schwehr, P. Sinclair, J. T. Sobczyk, P. Stamoulis, P. Stowell, R. Tacik, L. Thompson, S. Tobayama, M. O. Wascko, and J. Żmuda. **Testing charged current quasi-elastic and multinucleon interaction models in the NEUT neutrino interaction generator with published datasets from the MiniBooNE and MINERνA experiments**. *Phys. Rev. D*, **93**:072010, Apr 2016.

[144] Harrison B. Prosper and Louis Lyons, editors. *Proceedings, PHYSTAT 2011 Workshop on Statistical Issues Related to Discovery Claims in Search Experiments and Unfolding, CERN,Geneva, Switzerland 17-20 January 2011*, Geneva, 2011. CERN, CERN.

[145] K. Abe et al. (The Hyper-Kamiokande Working Group). **Letter of Intent: The Hyper-Kamiokande Experiment — Detector Design and Physics Potential —**. *arXiv:1109.3262*, 2015.

[146] T2K COLLABORATION. **First measurement of the muon neutrino charged current single pion production cross section on water with the T2K near detector**. *Phys. Rev. D*, **95**:012010, Jan 2017.

[147] S OSER. **Elemental composition and masses of FGD XY modules**. T2K Technical note TN-091, available upon request.

[148] D BROOK-ROBERGE AND S OSER. **FGD2 water module masses and elemental composition**. T2K Technical note TN-198, available upon request.

[149] K MAHN AND S OSER. **FGD mass calculation compared to as built**. T2K Technical note TN-122, available upon request.

[150] T2K COLLABORATION. **Measurements of neutrino oscillation in appearance and disappearance channels by the T2K experiment with 6.6 E20 protons on target**. *arXiv preprint arXiv:1502.01550*, 2015.

[151] THE ND280 NuMu GROUP. **CC multiple pion nu-mu event selections in the ND280 tracker using Run 1+2+3+4 data**. T2K Technical note TN-152, available upon request.

[152] J MYSILIK. **Determination of pion secondary interaction systematics for the ND280 tracker ν_μ analysis**. T2K Technical note TN-125, available upon request.

[153] P. A. AMAUDRUZ ET AL. **The T2K Fine-Grained Detectors**. *Nucl. Instrum. Meth.*, **A696**:1–31, 2012.

[154] F DUFOUR, L HAEGEL, T LINDNER, AND S OSER. **Systematics on Out-of-Fiducial-Volume Backgrounds in the ND280 Tracker**. T2K Technical note TN-098, available upon request.

[155] J. LAGODA K. KOWALIK. **The simulations of the beam neutrinos interactions outside the ND280 detector**. T2K Technical note TN-077, available upon request.

[156] T2K COLLABORATION. **T2K neutrino flux prediction**. *Physical Review D*, **87**(1):012001, 2013.

[157] M. FRIEND ET AL. **Flux Prediction and Uncertainty Updates with NA61 2009 Thin Target Data and Negative Focussing Mode Predictions**. Technical Report T2K-TN-217-v5, Multiple institutions, June 2015.

[158] A. BERCELLIE ET AL. **Cross section parameters for the 2014 oscillation analysis**. Technical Report T2K-TN-192-v2.2, Multiple institutions, June 2015.

[159] S SCHMITT. **Data Unfolding Methods in High Energy Physics**. *arXiv:1611.01927v1*, 2016.

[160] J. R. KLEIN AND A. ROODMAN. **Blind analysis in nuclear and particle physics**. *Ann. Rev. Nucl. Part. Sci.*, **55**:141–163, 2005.

[161] A. HÖCKER AND V. KARTVELISHVILI. **SVD Approach to Data Unfolding**. *arXiv:hep-ph/9509307v2*, 1995.

[162] K. TACKMANN AND A. HÖCKER. **SVD-based unfolding: implementation and experience**. *arXiv:1112.2226v1*, 2011.